MAIRA TARIQ

IN VIVO QUANTIFICATION OF COMPLEX NEURITE CONFIGURATIONS USING MAGNETIC RESONANCE IMAGING

IN VIVO QUANTIFICATION OF COMPLEX NEURITE CONFIGURATIONS USING MAGNETIC RESONANCE IMAGING

Development of an advance diffusion-weighted MRI method for microstructure imaging of the human brain

MAIRA TARIQ

A dissertation submitted in partial fulfillment
of the requirements for the degree of

Doctor of Philosophy

of

University College London

March 2018

SUPERVISORS:
Dr. Hui Zhang
Prof. Claudia Gandini Wheeler-Kingshott

AFFILIATION:
Centre of Medical Image Computing
Department of Computer Science
University College London

DECLARATION

I, Maira Tariq, confirm that the work presented in this thesis is my own. Where information has been derived from other sources, I confirm that this has been indicated in the work.

London, March 2018

Maira Tariq

ABSTRACT

Axons and dendrites, collectively termed neurites, are part of the brain microstructure and are integral for normal brain function. Configurations of neurites like axonal fanning/bending or dendritic arbour complexity, which manifest as anisotropic orientation dispersion, are known to be very important during normal brain development and function. *In vivo* studies to characterise how these configurations change for normal development/ageing, function and pathology can help understand the precise changes in microstructure underlying these processes. This can facilitate advancement in the field of neuroscience and development of better diagnosis and prognosis of various brain diseases and disorders.

This thesis concerns the development and evaluation of such an imaging technique, which characterises complex configurations of neurites in the human brain. The proposed technique presents a novel marker of neurite morphology, which specifically quantifies anisotropic orientation dispersion, using *in vivo* diffusion-weighted magnetic resonance imaging (DW-MRI). This is done using standard image acquisition, making the technique feasible for neuroscience and clinical applications. The work presented is the first to enable *in vivo* quantification of anisotropic orientation dispersion.

The first part of the thesis involves the development of the technique to enable quantification of anisotropic orientation dispersion and establishing its *in vivo* feasibility. We call the proposed technique *Bingham-NODDI*. The proposed technique is based on an existing DW-MRI technique called neurite orientation dispersion and density imaging (NODDI), that provides useful indices of neurite morphology, but can not characterise anisotropic orientation dispersion. The *in vivo* feasibility of the proposed model is established by thoroughly evaluating the inherent accuracy and precision of its indices, using *in silico* and *in vivo* data.

In the second part, the proposed technique is applied to a larger cohort to demonstrate its applicability to a greater number of subjects. Normative values of the indices of the proposed technique are reported across the white matter (WM) of the normal human population and power calculations carried out to help design future studies using the technique. Finally, a test-retest imaging

data of multiple subjects is used to establish repeatability and reliability of the indices of the proposed technique. Comparison to a standard DW-MRI model shows that the technique can quantify inter-subject differences but is less robust to noise.

The third part assesses if the proposed technique can characterise the anisotropic orientation dispersion in the grey matter (GM). This is because the assessment in the first two parts shows that for standard imaging data, the technique can only capture anisotropic dispersion in the WM. This is done using high-resolution *ex vivo* and *in vivo* DW-MRI data, which provides better sensitivity to the neurites in the GM.

The aim of this PhD was to develop a model to characterise anisotropic orientation dispersion of neurites, which can ultimately be applied to neuroscience and clinical studies. The proposed work provides an exciting development for better research in neuroscience, by making a step towards improved characterisation of neurites, using standard imaging acquisitions. This will help in making key links between the precise changes in microstructure that result in brain development, ageing and pathology.

IMPACT STATEMENT

In my PhD work, I have proposed an advance model for characterisation of complex configurations of axons and dendrites in the human brain. The proposed model presents a novel marker of the morphology of neurites (collective term for axons and dendrites), which specifically quantifies anisotropic orientation dispersion. The work presented here is the first to enable an *in vivo* quantification of this feature of neurites. The proposed work provides an exciting development in neuroscience research that may be used to make key links between the precise changes in microstructure that result in brain development, ageing and pathology.

The scope of the work presented here was to develop a method to quantify this index of neurite morphology, which can be estimated with standard neuroimaging studies. In this thesis, I present the technical details of the proposed model, including the indices it provides and how they may be useful. I evaluate the proposed model using standard data, showing its feasibility with existing technology. Finally, I apply the proposed method to multiple normal subjects, showing the feasibility for clinical and/or population studies.

The most immediate impact of the presented work is in the field of neuroscience where the proposed model can be used to advance the knowledge of brain microstructure, specifically neurites. Anisotropic orientation dispersion, which can be characterised with the proposed model, is an important feature to characterise, as it is a widespread feature in the brain and provides a subtle marker of neurite morphology. The method developed has been shown to be feasible with standard imaging technology and experiments were done to establish cohort requirements for future studies and the reliability of its indices.

The ultimate impact of the presented work for neuroscience would be to aid early diagnosis and categorise brain diseases based on the characterisation of anisotropic orientation dispersion, which will have a direct impact on the public health. This could easily take decades, but the necessary work for translation of the proposed method for further studies has been carried out as part of this PhD.

To facilitate the use of the proposed method by the clinical and neuroscience community, the model has been made available as an *open source* toolbox. This

is provided as part of the *NODDI* Matlab toolbox[1], which is widely being used and requires no expert knowledge of computational techniques. For the scientific community in general, but specifically in medical imaging, the presented work provides a framework that can be adapted for the development of a new model.

The academic impact of the work presented here is also significant as the work has been disseminated through publications in high impact journals[158,160], as well as several oral and poster presentations at prestigious international conferences[155,156,161–163].

1 Available online at http://nitrc.org/projects/noddi_toolbox

PUBLICATIONS

Some of the ideas and figures in this thesis have appeared previously in the following publications:

Journal articles and book chapters

- Tariq, M., Schneider, T,. Alexander, D. C., Gandini Wheeler-Kingshott, C.A. and Zhang, H.: ***Bingham-NODDI:* mapping anisotropic orientation dispersion of neurites using diffusion MRI**. – *NeuroImage*, 2016, Vol:133, Page 207–223

- Tariq, M., Schneider, T., Alexander, D.C., Wheeler-Kingshott, C.A. and Zhang, H.: **In vivo estimation of dispersion anisotropy of neurites using diffusion MRI**. – *In Medical Image Computing and Computer-Assisted Intervention*, Springer International Publishing, 2014, Page 241–248

Conference publications

- Tariq, M., Zhang, J. and Zhang, H.: **Neurite morphology reveals rich regional microstructural variations in the human brain white matter**. – *Proceedings of the Organization for Human Brain Mapping*, June 2016, Geneva, Switzerland.

- Tariq, M., Kleinnijenhuis, M., van Cappellen van Walsum, A-M., Zhang, H.: **Validation of NODDI estimation of dispersion anisotropy in V1 of the human neocortex**. – *Proc. 23rd Annual Meeting of the International Society for Magnetic Resonance in Medicine*, May 2015, Toronto, Canada.

- Tariq, M., Kleinnijenhuis, M., van Cappellen van Walsum, A-M., Zhang, H.: **Validation of NODDI estimation of dispersion anisotropy in V1 of the human neocortex**. – ***Proceedings of the Organization for Human Brain Mapping***, May 2015, Honolulu, Hawaii.

- Tariq, M., Schneider, T., Alexander, D.C., Wheeler-Kingshott, C.A. and Zhang, H.: **NODDI with dispersion anisotropy**. – ***Proceedings of the Organization for Human Brain Mapping***, June 2014, Hamburg, Germany.

- Tariq, M., Schneider, T., Alexander, D.C., Wheeler-Kingshott, C.A. and Zhang, H.: **NODDI with dispersion anisotropy**. – ***Proceedings of the International Society for Magnetic Resonance in Medicine***, May 2014, Milan, Italy.

Future publications

- Tariq, M., Zhang, J., Thomas, D., Cash, D. and Zhang, H.: **Normative values of the NODDI indices in white matter of the healthy human brain**. – *To be submitted to the MICCAI 2018 workshop on Computational Diffusion MRI (CDMRI)*.

Publications not part of the thesis

- Tariq, M., Schneider, T., Alexander, D.C., Wheeler-Kingshott, C.A. and Zhang, H.: **Scan-rescan reproducibility of neurite microstructure estimates using NODDI**. – *Proceedings of the Annual Meeting of the Medical Image Understanding and Analysis*, 2012, Page 255-61

- Tariq, M., Schneider, T., Alexander, D.C., Wheeler-Kingshott, C.A. and Zhang, H.: **Assessing scan-rescan reproducibility of the parameter estimates from NODDI**. – *Proc. 23rd Annual Meeting of the International Society for Magnetic Resonance in Medicine*, May 2013, Salt Lake City, UT.

- Ferizi, U., Schneider, T., Tariq, M., Wheeler-Kingshott, C.A.M., Zhang, H. and Alexander, D.C.: **The Importance of Being Dispersed: A Ranking of Diffusion MRI Models for Fibre Dispersion Using In Vivo Human Brain Data**. – *In Medical Image Computing and Computer-Assisted Intervention*, Springer International Publishing, 2013, Page 74–81

ACKNOWLEDGMENTS

I would like to thank all the people who have made this thesis possible and to those who have been there for me during this PhD and beyond.

I am extremely thankful to my supervisors Dr. Gary Zhang and Prof. Claudia Wheeler-Kingshott for their support and advice throughout my PhD, which have helped me develop scientific skills and knowledge necessary to make it this far in academia. This has been a great learning experience for me, academically and personally.

In addition, I am extremely grateful to Prof. Serena Counsell, for providing great support during the second year of my PhD and for giving me the opportunity to learn more about the practical and clinical aspects of the research in medical imaging. Particularly her feedback during my first-year viva was of great help.

I would like to acknowledge Dr. Karthik Budidha, Dr. Elisenda Bonet-Carne, Dr. Andrada Savickas, Miss. Jiaying Zhang and Dr. Lebina Shrestha Kakkar for their invaluable feedback on my thesis and for proofreading it. In particular, I would like to thank Dr. Budidha for helping me with the formatting of this thesis and other technical help with putting the thesis together. A special thanks to all of them also for being a great source of support, academically and personally, throughout the last few years. You are all more than friends to me and I will always cherish the great time I've spent getting to know you all and myself through you.

Last but certainly not the least, I would like to thank my parents for their contribution towards my academic and personal accomplishments. I am indebted to them for providing the support and encouragement to excel in education that has helped me come this far.

CONTENTS

I GENERAL INTRODUCTION 1

1 RESEARCH PROBLEM 2

1.1 Introduction . . . 2

1.2 Statement of the problem . . . 5

1.2.1 Project aims . . . 5

1.3 Contributions . . . 6

1.3.1 Development of Bingham-NODDI . . . 6

1.3.2 *In vivo* and clinical feasibility of Bingham-NODDI . . . 6

1.3.3 Assessment of assumptions and propose fitting procedure for Bingham-NODDI . . . 7

1.3.4 Normative values of Bingham-NODDI in the healthy human brain . . . 7

1.3.5 Reproducibility and reliability of Bingham-NODDI indices . . . 8

1.3.6 Bingham-NODDI indices in the grey matter of healthy adult brain . . . 8

1.4 Thesis Overview . . . 9

II BACKGROUND 11

2 IMPORTANCE OF NEURITES IN NEUROSCIENCE 12

2.1 Brain . . . 12

2.1.1 Brain tissue . . . 13

2.2 Microstructure components of the brain . . . 14

2.2.1 Neurites . . . 15

2.2.2 Main fibres of the brain WM . . . 16

2.3 Neurites in healthy and pathological brain . . . 17

2.4 Importance of non-invasive brain imaging . . . 17

3 BRAIN IMAGING WITH MAGNETIC RESONANCE IMAGING 19

3.1 In vivo brain imaging . . . 19

3.2 Diffusion-weighted MRI . . . 20

3.2.1 Diffusion theory . . . 21

3.2.2 Nuclear magnetic resonance . . . 24

3.2.3 Signal generation . . . 24

3.2.4 Acquisition sequence . . . 25
3.2.5 Signal localisation . . . 27
3.2.6 Tissue based contrast . . . 28
3.2.7 Diffusion sensitisation and acquisition . . . 30
4 MICROSTRUCTURE IMAGING 35
4.1 Diffusion as a marker of brain microstructure . . . 35
4.2 Diffusion-weighted MRI modelling . . . 36
4.2.1 Fitting model . . . 37
4.2.2 Acquisition protocol . . . 38
4.2.3 Noise model . . . 39
4.2.4 Fitting algorithm . . . 39
4.2.5 Model comparison . . . 42
4.3 Models of Diffusion-weighted MRI . . . 44
4.3.1 Diffusion signal models . . . 44
4.3.2 Biophysical models . . . 46
4.4 Diffusion-weighted MRI in standard neuroimaging . . . 52
4.4.1 Diffusion Tensor Imaging (DTI) . . . 53
4.4.2 Clinical utility of DTI . . . 54
4.4.3 Limitations of DTI . . . 55
4.5 Microstructure imaging with standard neuroimaging . . . 55
5 CLINICAL MICROSTRUCTURE IMAGING OF NEURITES 57
5.1 Neurite Orientation Dispersion and Density Imaging . . . 57
5.2 NODDI tissue model . . . 58
5.2.1 General NODDI formulation . . . 58
5.2.2 Orientation distribution function . . . 61
5.2.3 Model parameters . . . 61
5.3 NODDI indices of brain microstructure . . . 62
5.3.1 Neurite density index . . . 62
5.3.2 Orientation dispersion index . . . 63
5.4 Acquisition protocol . . . 63
5.5 Clinical applications of NODDI . . . 63
5.6 Limitations of NODDI . . . 64
III METHOD DEVELOPMENT AND EVALUATION 66
6 BINGHAM-NODDI: MAPPING ANISOTROPIC ORIENTATION DISPERSION OF NEURITES 67
6.1 Dispersion anisotropy a measure of complex neurite configurations . . . 68

6.1.1 What is anisotropic orientation dispersion 68
6.1.2 Why quantify orientation dispersion anisotropy 70
6.1.3 Modelling dispersion anisotropy using NODDI 70
6.2 Bingham-NODDI 71
6.2.1 Parameterisation of the ODF in Bingham-NODDI 71
6.2.2 The orientation tensor 74
6.2.3 Implementation of Bingham-NODDI 76
6.2.4 Model parameters 78
6.3 Microstrucutre indices of Bingham-NODDI 78
6.3.1 Dispersion indices of Bingham-NODDI 79
6.3.2 Alternative metrics of Bingham-NODDI 82
6.3.3 Comparison of the two quantifications of Bingham-NODDI indices 83
6.4 Summary and discussion 83
7 BINGHAM-NODDI: *in silico* DATA EXPERIMENTS 85
7.1 Synthetic data 85
7.1.1 Synthetic tissue model 85
7.1.2 Ground truth parameters 85
7.1.3 Acquisition protocol 86
7.1.4 Model fitting procedure 87
7.2 Synthetic data experiment 88
7.2.1 Parameter estimation 88
7.2.2 Protocol comparison 93
7.3 Summary and discussion 95
8 BINGHAM-NODDI: *in-vivo* DATA EXPERIMENTS 98
8.1 Data acquisition and processing 98
8.1.1 *In vivo* data 98
8.1.2 Model fitting procedure 99
8.1.3 Pre-processing 99
8.2 In vivo data experiment 100
8.2.1 Parameter estimation 100
8.2.2 Protocol comparison 104
8.2.3 Model comparison 106
8.3 Summary and discussion 107
9 SIMULATIONS FOR MODEL FITTING AND ASSUMPTIONS OF BINGHAM-NODDI 110
9.1 Optimum fitting procedure for Bingham-NODDI 110
9.1.1 Design 110

9.1.2 Experiments . . . 111
9.1.3 Results . . . 111
9.1.4 Conclusion . . . 111
9.2 Assumption of single fibre population . . . 113
9.2.1 Modelling crossing fibres . . . 113
9.2.2 Discussion . . . 115
9.3 Sensitivity of signal to model parameters . . . 115
9.3.1 Design . . . 117
9.3.2 Sensitivity to neurite radii . . . 117
9.3.3 Sensitivity to intrinsic diffusivity . . . 118
10 METHOD DEVELOPMENT AND EVALUATION: DISCUSSION 120
10.1 Bingham-NODDI to map anisotropic orientation dispersion of neurites . . . 120
10.2 Estimation of neurite morphology using Bingham-NODDI . . . 121
10.3 Existing diffusion MRI models using the Bingham distribution . 122
IV TOWARDS CLINICAL TRANSLATION 124
11 NORMATIVE VALUES OF BINGHAM-NODDI INDICES IN THE WHITE MATTER 125
11.1 Introduction . . . 125
11.2 Methods . . . 126
11.2.1 Cohort and MRI data acquisition . . . 126
11.2.2 Motion and eddy current artefact correction . . . 126
11.2.3 Model fitting . . . 127
11.2.4 Spatial normalisation and region-of-interests . . . 127
11.2.5 Data analysis . . . 128
11.3 Results . . . 129
11.3.1 Population template and WM segmentations . . . 129
11.3.2 Normative values and inter-subject variability . . . 131
11.3.3 ROI analysis . . . 132
11.3.4 Power analysis . . . 135
11.3.5 Regional variability of WM . . . 136
11.3.6 NODDI vs DTI metrics . . . 138
11.4 Discussion . . . 139
11.4.1 Limitations and future work . . . 140
12 REPRODUCIBILITY AND RELIABILITY OF BINGHAM-NODDI INDICES IN THE WHITE MATTER 142
12.1 Introduction . . . 142

12.2 Experiment design . . . 143
12.2.1 Cohort and MRI data acquisition . . . 143
12.2.2 Pre-processing for artefact correction . . . 144
12.2.3 Model fitting procedure . . . 144
12.2.4 Spatial normalisation and region-of-interests . . . 144
12.3 Statistical analysis . . . 145
12.3.1 Agreement of the indices . . . 145
12.3.2 Reliability of the indices . . . 146
12.4 Results . . . 148
12.4.1 Parameter maps . . . 148
12.4.2 Agreement analysis . . . 149
12.4.3 Repeated measures ANOVA . . . 157
12.5 Discussion . . . 164
12.5.1 Reliability of Bingham-NODDI . . . 164
13 CLINICAL TRANSLATION FEASIBILITY: DISCUSSION 167

V ASSESSMENT OF BINGHAM-NODDI IN THE GREY MATTER 169
14 BINGHAM-NODDI: *ex-vivo* DATA EXPERIMENTS 170
14.1 Orientation dispersion anisotropy in the cortex . . . 170
14.2 Sample . . . 171
14.2.1 Data . . . 171
14.3 Model fitting and data analysis . . . 172
14.4 Results . . . 172
14.4.1 Dispersion anisotropy in the cortex . . . 172
14.4.2 Neurite density . . . 174
14.4.3 Comaprison with Watson-NODDI . . . 174
14.4.4 Comparison with fixed diffusivity . . . 175
15 BINGHAM-NODDI IN THE GM USING *in vivo* DATA 178
15.1 Quality of fit comparison . . . 178
15.2 Mapping of dispersion anisotropy index . . . 179
15.3 Discussion . . . 179

VI DISCUSSION AND FUTURE OUTLOOK 183
16 DISCUSSION 184
16.1 Summary of the thesis . . . 184
16.2 Limitations of Bingham-NODDI . . . 186
16.2.1 Assumptions made in Bingham-NODDI . . . 187
16.2.2 Model fitting procedure . . . 189

16.2.3 Reliability of parameter estimation . . . 189
16.2.4 Acquisition protocol . . . 190
16.3 Discussion of the clinical utility . . . 190
17 FUTURE WORK 192
17.1 Modelling crossing fibres with Bingham-NODDI . . . 192
17.2 Relaxing the assumptions of Bingham-NODDI . . . 192
17.3 Acquisition protocol . . . 193
17.4 Validation of Bingham-NODDI . . . 193
17.5 Clinical application of Bingham-NODDI . . . 194
17.6 Future directions for microstructure imaging . . . 194

VII APPENDIX 197
A DIFFUSION-WEIGHTED MAGNETIC RESONANCE IMAGING 198
A.1 NMR . . . 198
A.2 The Bloch equations . . . 199
A.3 Spine echo sequence . . . 200
A.4 Diffusion theory . . . 201
B BINGHAM-NODDI MATHEMATICAL DERIVATIONS 203
B.1 Volume fractions in the NODDI model . . . 203
B.2 Expression for the probability of Bingham distribution . . . 204
B.3 Degrees of freedom of the Bingham matrix **B** . . . 205
B.4 Bingham, a spherical analogue of the 2D Gaussian distribution 206
C BINGHAM-NODDI VS WATSON-NODDI 208
C.1 Estimation of the concentration parameters . . . 208
D NORMATIVE VALUES OF BINGHAM-NODDI INDICES IN THE WM - FURTHER RESULTS 210
D.1 Quality of fit . . . 210
D.2 Variability results . . . 210
D.3 Power calculation results . . . 210
E STATISTICAL METHODS FOR REPRODUCIBILITY ANALYSIS 218
E.1 Reliability . . . 218
E.1.1 Analysis of Variance - ANOVA . . . 219
E.1.2 ANOVA for scan-rescan experiment of NODDI . . . 220
E.1.3 Coefficient of variation . . . 224

Bibliography 229

LIST OF FIGURES

Figure 1.1 Schematics illustrating the various complex orientation configurations of neurites that are found in the brain. . . 4
Figure 2.1 Brain tissue as seen in a dissected human brain, T_1-weighted MRI, and a T_2-weighted MRI. 13
Figure 2.2 Main microstructure components of the neuron 14
Figure 2.3 Groups of axons and dendrites, collectively called *neurites*, typically found in the vast network of neuronal connections in the brain. 15
Figure 2.4 Main fibres of the brain. 16
Figure 3.1 Schematic depicting the diffusion of particles in the brain. 23
Figure 3.2 Illustration of the evolution of $\boldsymbol{M_0}$ in the presence of a magnetic field $\boldsymbol{B}_1(t)$. 25
Figure 3.3 Schematic depicting the SE sequence and how it impacts the $\boldsymbol{M_0}$ in the transverse plane. 26
Figure 3.4 Illustration of the echo planar imaging (EPI) MRI pulse sequence (a) and the corresponding data collection trajectory (b). 28
Figure 3.5 Figure illustrating that the values of TE and TR determine how much the signal decays, which results in a T_1 or T_2 weighted signal. 29
Figure 3.6 Schematic of spin echo experiment in the presence of a pulsed field gradient, as proposed by Stejskal and Tanner. 31
Figure 3.7 A schematic representation of how the PGSE sequence measures the diffusion of water molecules. 32
Figure 4.1 Model fitting for the Ball-Stick model, for a voxel in the CC. 40
Figure 4.2 Overview of a nonlinear fitting procedure, which requires an iterative procedure to estimate the model parameters from the measurements. 43
Figure 4.3 The various models typically utilised in geometric or biophysical modelling with DW-MRI. 48

Figure 4.4 The three-compartment model developed by Stanisz et al. 1997 based on the microstrucutre of the bovine optic nerve. . . . 48
Figure 4.5 Comparison of the angular profile of the orientation distribution function (ODF) of the neuronal processes imaged and the negative log of the diffusion signal (dODF). 51
Figure 4.6 Demonstration of importance of characterising orientation dispersion, for accurate estimation of neurite morphology. . . . 52
Figure 4.7 Demonstration of the dependency on SNR of estimation of anisotropic orientation dispersion, with Ball-Rackets model. . . . 53
Figure 5.1 Breakdown of the total normalised DW-MRI signal as modelled by Watson-NODDI. . . . 59
Figure 5.2 Maps of the Watson-NODDI indices of neurite morphology alongside those for the DTI indices. . . . 62
Figure 6.1 Schematics illustrating anisotropic orientation dispersion of the fibres in the brain, including bending and fanning of fibres. . . . 68
Figure 6.2 The complex orientation configurations of neurites found in the brain. . . . 69
Figure 6.3 Probability density plots for the Bingham distribution, which we use to parameterise the orientation dispersion in Bingham-NODDI. . . . 72
Figure 6.4 Schematic to summarise how the presented indices of Bingham-NODDI vary for various orientation configurations. . . . 81
Figure 7.1 Errors in the estimation of v_{in} and v_{iso} using Bingham-NODDI, for the optimised NODDI protocol (N1). . . . 89
Figure 7.2 As Figure 7.1 but showing the statistics of estimation errors of ODI_P and ODI_S. . . . 90
Figure 7.3 As Figure 7.1 but showing the statistics of estimation errors of ODI_{Tot}. . . . 91
Figure 7.4 As Figure 7.1 but showing the statistics of estimation errors of DA_B and DA_T. . . . 91
Figure 7.5 As Figure 7.1 but showing the statistics of estimation errors of $\hat{\mu}_1$ and $\hat{\mu}_2$. . . . 92

Figure 7.6 As Figure 7.1 but showing the statistics of estimation errors of ODI_{Tot}, using Watson-NODDI. 93
Figure 7.7 Errors in the estimation of ODI_P and ODI_S obtained from the synthetic data experiment using different protocols as indicated by the symbols. 95
Figure 7.8 As Figure 7.7, but for DA_{Tot} 95
Figure 7.9 As Figure 7.7, but for the dispersion anisotropy indices, DA_B and DA_T. 96
Figure 8.1 Axial slices showing maps of the novel parameters ODI_P, ODI_S and ODI_{Tot}, obtained by fitting Bingham-NODDI to the *in vivo* data, along with the maps of ν_{in} and ν_{iso} 101
Figure 8.2 As Figure 8.1, but showing maps of the proposed quantifications of dispersion anisotropy. 103
Figure 8.3 Errors in estimation of the overall dispersion index, ODI_{Tot} using Bingham-NODDI and Watson-NODDI, for various *ground-truth* values of DA_B, for *in vivo* data. . 104
Figure 8.4 Errors for *in vivo* estimation of ODI_P and ODI_S using Bingham-NODDI, for the various *ground-truth* values of the respective parameters. 105
Figure 8.5 As Figure 8.4, but for DA_B and DA_T. 106
Figure 8.6 As Figure 8.4, but for errors in estimation of the orientations, $\hat{\mu}_1$ and $\hat{\mu}_2$. The data is separated according to the ground-truth values of DA_B 107
Figure 8.7 The maps of BIC for fitting with Bingham-NODDI and Watson-NODDI models 108
Figure 9.1 Errors in estimation of some of the model parameters of Bingham-NODDI. 112
Figure 9.2 As Figure 9.1, but for the model parameters for the orientations, obtained from Bingham-NODDI. 112
Figure 9.3 As Figure 9.1, but for the indices of dispersion and dispersion ansitropy derived from Bingham-NODDI. 113
Figure 9.4 The simulated multi-population Bingham-NODDI signal, for the *intra-neurite* and *extra-neurite* compartments, as well as the total signal. 115

Figure 9.5 Values of dispersion and dispersion anisotropy indices estimated by fitting the single population Bingham-NODDI model to the data, as a function of the crossing angle between two populations of equally dispersed fibres. . . . 116
Figure 9.6 Sensitivity of the Bingham-NODDI signal to the changes in values of neurite raddi, α, simulated for several ground truth values of α, as indicated. . . . 117
Figure 9.7 Sensitivity of the Bingham-NODDI signal to the changes in values of intrinsic diffusivity inside the neurites, d_i, simulated for several ground truth values of d_i, as indicated. . . . 118
Figure 11.1 Fractional anisotropy (FA) map of two exemplar subjects in the template space with the corresponding WM ROI segmentations superimposed on them. . . . 130
Figure 11.2 Maps of the Bingham-NODDI parameters, in the template space, for two exemplar subjects and the mean and standard deviation across the cohort. . . . 131
Figure 11.3 Plots showing the distribution of the Bingham-NODDI indices across the adult cohort, for 24 of the WM regions. 134
Figure 11.4 Plot showing the power calculation results for the Bingham-NODDI and DTI metrics . . . 136
Figure 11.5 Plot indicating whether each pair of ROI being compared is statistically the different or not. . . . 138
Figure 11.6 Plot showing the variability in the parameter estimates, quantified as the CV, for the Bingham-NODDI and DTI metrics . . . 139
Figure 12.1 Parameter maps of the DTI indices of FA and MD in the population template space, for mutliple axial slices of two subjects. . . . 149
Figure 12.2 As Figure 12.1, but for Bingham-NODDI indices of ν_{in} and ν_{iso}. . . . 150
Figure 12.3 As Figure 12.1, but for Bingham-NODDI indices of ODI_P and ODI_S. . . . 150
Figure 12.4 As Figure 12.1, but for Bingham-NODDI indices of ODI_{Tot} and DA_B. . . . 151
Figure 12.5 Plot showing the results of the paired t-test for the metrics of Bingham-NODDI and DTI. . . . 152

Figure 12.6 Maps of the mean between-scan differences and the CV_{within} for the DTI metrics of FA and MD in WM ROIs for four slices of the brain. . . . 153
Figure 12.7 As Figure 12.6, but for ν_{in} and ν_{iso} indices of Bingham-NODDI. . . . 154
Figure 12.8 As Figure 12.6, but for ODI_P and ODI_S indices of Bingham-NODDI. . . . 155
Figure 12.9 As Figure 12.6, but for ODI_{Tot} and DA_B indices of Bingham-NODDI. . . . 156
Figure 12.10 Histograms showing the distributions of between-scan differences and the CV_{within} values for each of the parameters of Bingham-NODDI and DTI, in the WM ROIs. 157
Figure 12.11 Variation of CV_{within} for the parameters of Bingham-NODDI and DTI, across several groups of WM tracts. . . 158
Figure 12.12 Maps of the $ICC_{Subject}$ and the MS_{Scan} for the DTI metrics of FA and MD, in WM ROIs for four slices of the brain. . . . 159
Figure 12.13 As Figure 12.12, but for ν_{in} and ν_{iso} indices of Bingham-NODDI. . . . 160
Figure 12.14 As Figure 12.12, but for ODI_P and ODI_S indices of Bingham-NODDI. . . . 161
Figure 12.15 As Figure 12.12, but for ODI_{Tot} and DA_B indices of Bingham-NODDI. . . . 162
Figure 12.16 Histograms showing the distributions of $ICC_{Subject}$ and the MS_{Scan} values for each of the parameters of Bingham-NODDI and DTI, in the WM ROIs. . . . 163
Figure 12.17 Variation of the reliability metric, $ICC_{Subject}$ for the parameters of Bingham-NODDI and DTI, across several groups of WM tracts. . . . 163
Figure 12.18 As 12.17, but for the MS_{Scan}. . . . 164
Figure 14.1 Bingham-NODDI estimation of dispersion anisotropy in the *ex vivo* cortical sample. . . . 173
Figure 14.2 Bingham-NODDI estimation of orientation dispersion indices in the *ex vivo* cortical sample. . . . 173
Figure 14.3 Comparison of the myelin stained histology to the Bingham-NODDI index of neurite density, ν_{in}. . . . 174

Figure 14.4 Comparison of the quality of fit in terms of the *BIC*, between Watson-NODDI, Bingham-NODDI and Bingham-NODDI with diffsivity fixed in the fitting procedure. 175
Figure 14.5 Comparison of the esitmation of the concentration parameter κ, estimated by Watson-NODDI and Bingham-NODDI. 175
Figure 15.1 BIC difference maps to highlight the areas where Watson-NODDI performs worse than Bingham-NODDI and those where Watson-NODDI is sufficient. 179
Figure 15.2 Quality of fit plots for a few voxels from specific regions of the brain tissue. 180
Figure 15.3 DA_B and FA_{OT} weighted RGB images of the dominant orientation $\hat{\mu}_2$ and primary dispersion orientation $\hat{\mu}_2$. . . 181
Figure 15.4 Zoomed in maps of DA_B and FA_{OT} weighted RGB images of the dominant orientation $\hat{\mu}_2$ and primary dispersion orientation $\hat{\mu}_2$, for the HCP subject. 181
Figure C.1 Bingham-NODDI estimation of κ for high ν_{in}. The blue circles represent individual estimates, while the red cross is the mean for estimates for each ground truth value. 208
Figure D.1 Power calculations for Bingham-NODDI indices, for the various effect sizes. 212
Figure D.2 Power calculations for Watson-NODDI and DTI indices, for the various effect sizes. 212

LIST OF TABLES

Table 6.1 The values of the dispersion and dispersion anisotropy indices, corresponding to the various configurations of ODF, specified by the values of κ and β. 80

Table 7.1 The ground-truth parameters used to generate the synthetic data. 86

Table 7.2 The list of imaging protocols used for evaluation of the parameters estimated. 87

Table 9.1 The model parameters for the signal simulated for two orientationally dispersed fibre populations crossing at a seperation angle, θ. 114

Table 11.1 Demographics of the cohort used in the study. 126

Table 11.2 Mean and standard deviation of the normative values of the parameters of Bingham-NODDI, across all the subjects, for the various WM ROIs. 133

Table 11.3 Power cacluations for Bingham-NODDI metrics, for effect size of 10% for each metric. 137

Table D.1 The modified model fitting procedure reduces the percentage of voxels where Watson-NODDI is sufficient. . . 210

Table D.2 Coefficient of variation of the Bingham-NODDI metrics, across all the subjects, for the various WM ROIs. 211

Part I

GENERAL INTRODUCTION

1

RESEARCH PROBLEM

1.1 INTRODUCTION

The most fundamental problem in neuroscience is understanding the brain structure at cellular or microscopic level.This is because the microstructure plays a vital role in normal brain development and ageing, and breakdown of it is linked to various diseases. Neurites are an integral part of the brain microstructure and underpin various brain functions; their integrity is essential for normal brain function. Neurite is a collective term for axons in the white matter WM and dendrites in the grey matter (GM) of the brain, which are projections from the cell body of a neuron.

Traditional histological analysis has helped highlight the importance of neurites, by identifying the links between their morphology to development[40], ageing[80], function[81] and pathology[31,64] of the brain. Specifically, features like the density and orientation dispersion of neurites have been shown to be important. But histological analysis is invasive, providing only local information in the regions sampled, which limits its use specifically for the brain which is formed of an intricate network of neural cells working together. Accessing the details of neurite morphology non-invasively is invaluable as it gives a dynamic view of the brain in health and disease and facilitates research into finding the precise changes in microstructure that underpin normal brain function and disease. Microstructure imaging aims to do this by using *non-invasive* imaging techniques to extract features of microstructure, traditionally accessible with histology. But the challenge for *non-invasive* imaging lies in the scale of the microstructure features of interest as the typical *in vivo* imaging techniques contain hundreds of thousand neurons in a basic area unit[1].

Diffusion-Weighted Magnetic Resonance Imaging (DW-MRI) is a non-invasive imaging technique that is ideal for microstructure imaging as it measures the dispersion of water in the tissue being imaged, making it suitable

to probe microstructure, despite having a resolution in the order of $10^{-}9m^3$ ($1-3mm$ in each dimension). The technique is particularly useful in the brain where neurites restrict the water dispersion to be along their length, providing a unique contrast in terms of their connectivity and orientational variance. So metrics that reflect the microstructural organisation of the brain can be extracted from DW-MRI data. This is generally done by a model, which can estimate indices reflecting the underlying microstructure that would give rise to the water dispersion, as measured by DW-MRI.

The simplest model, that is currently the standard in DW-MRI in the brain is the diffusion tensor imaging (DTI)[22], which provides an estimate of the 3-dimensional diffusion properties of tissue, using a Gaussian diffusion assumption. Despite the Gaussian assumption not holding true for diffusion in the neuronal tissue[149], DTI provides estimates that are sensitive to changes in the microstructure and are widely used in numerous clinical studies[109,139]. But DTI indices lack specificity to microstructure[23,129]; they are affected simultaneously by a number of microstructural changes e.g. demyelination, inflammation, axonal loss, gliosis, which give rise to the same alterations of their values. Thus DTI can not quantify specific measures reflecting how densely packed or coherently organised the neurites are.

Biophysical modelling is now being utilised to address these limitations of DTI. This involves the development of complex models representing the microstructure, in terms of the water dispersion patterns, or diffusion profile, they give rise to. This gives direct estimates of various indices of microstructure morphology, such as their packing density, orientation dispersion or axonal diameters. Numerous biophysical models have been proposed in recent times (see Assaf and Cohen 2009 for a review), but until recently most assumed parallel axons, which is not appropriate to model neurites as they are known to be orientationally dispersed. Modelling this dispersion has been shown to provide better estimates of neurite morphology[63,184].

The first direct approach to estimate specific indices of neurite morphology, by incorporating orientation dispersion in the model was proposed by Jespersen et al. 2007, using DW-MRI with *ex vivo* imaging. The technique enabled estimation of neurite density and their orientation dispersion, which was subsequently validated with detailed histological comparison in Jespersen et al. 2010. Zhang et al. 2012 enabled the *in vivo* mapping of these measures with the development of Neurite Orientation Dispersion and Density Imaging (NODDI)[185]. NODDI has had a huge impact in the field of neuroimaging, as it provides clinically relevant indices of neurite morphology utilising stan-

dard clinical imaging procedures. However, a current limitation of the NODDI model is its inability to characterise other complex configurations, such as multiple neurite populations and anisotropic orientation dispersion of neurites (the various complex configurations of neurites in the brain are shown in Figure 1.1).

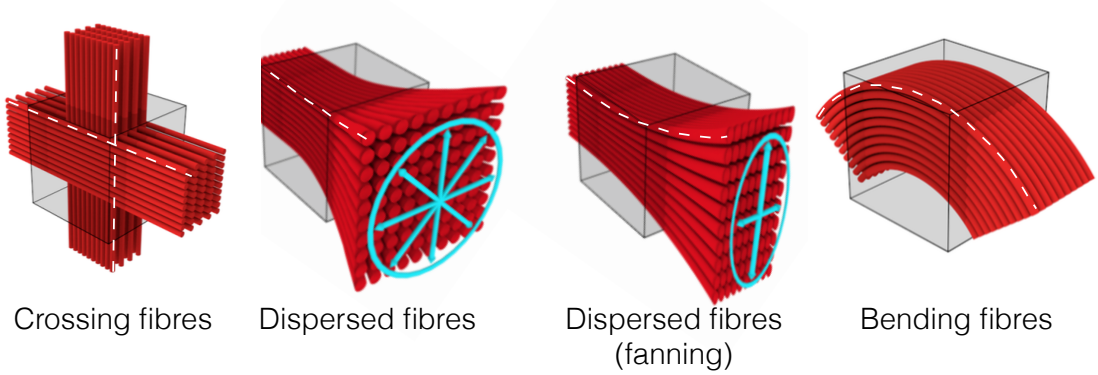

Figure 1.1: Schematics illustrating the various complex orientation configurations of neurites that are found in the brain. These configurations are usually modelled exclusively from each other, e.g. models of orientation dispersion with one fibre population[185], or coherent fibres with multiple populations[168]. These *intravoxel* configurations can be characterised by an *orientation distribution function (ODF)*, shown as the segments of orientations that can be measured by DW-MRI data (white dotted lines). *Figure adapted from Rowe 2014*.

The configuration of interest in this work is the anisotropic orientation dispersion, which arises from fanning or bending of neurites. Such orientation configurations of neurites are widespread in the brain, as shown by histological[32,96,169] and DW-MRI[105,147] data. *In vivo* characterisation of such configurations will provide a more refined measure of neurite morphology, compared to models such as NODDI. These measures can serve as an imaging marker of neurite integrity in normal and pathological brain[85,105], as well as to improve the accuracy of tractography algorithms[138,147]. For example, anisotropic orientations dispersion can be linked to features like dendritic arborization and fanning of bundles of axons, which are associated with normal brain development[19,85] and function play vital role in normal brain function. Thus quantifying anisotropic orientation dispersion of neurites can help enhance our understanding of how the brain develops and ages in terms of its microstructure and the specific changes in its organisation that result in brain disease. A measurement of this quantity has not been demonstrated with NODDI or any other *in vivo* technique. To this end, the aim of the work presented in this thesis is as follows.

1.2 STATEMENT OF THE PROBLEM

Is a technique to noninvasively quantify complex configurations of neurites, specifically anisotropic orientation dispersion, clinically feasible?

1.2.1 *Project aims*

To address the stated research problem, the overall aim of this PhD is to develop a *non-invasive* imaging technique, feasible with standard neuroimaging technology, to estimate complex configurations of neurites in the brain, specifically their anisotropic orientation dispersion. The proposed technique is referred to as Bingham-NODDI, which provides *in vivo* characterisation of such configurations, using DW-MRI. The biophysical model underlying the proposed technique presents a novel marker of neurite morphology, *the dispersion anisotropy index*, which provides a specific quantification of the level of anisotropic orientation dispersion. Bingham-NODDI is the first method to enable *in vivo* quantification of this feature.

To obtain a specific quantification of the dispersion anisotropy index, possible with standard *in vivo* clinical imaging, the NODDI framework is utilised, as it enables *in vivo* quantification of neurite morphology, using standard DW-MRI acquisition. This involves modifying the biophysical model underlying NODDI (also called the NODDI tissue model) to enable characterisation of anisotropic orientation dispersion of neurites. To accomplish this, the specific aims of this PhD are:

1. Develop a technique to characterise anisotropic orientation dispersion
2. Propose a novel measure to quantify this anisotropy
3. Demonstrate the *in vivo* feasibility of the proposed technique, using standard acquisitions
4. Assess model assumptions and make recommendations for model fitting
5. Assess the indices of the proposed model in the WM and GM of a population of healthy adult subjects
6. Establish the clinical feasibility of the proposed technique.

1.3 CONTRIBUTIONS

Following are the main contributions made in the work I carried out during this PhD, to fulfil the aims outlined in Section 1.2. Where contributions were made by others, it is sepcified.

1.3.1 *Development of Bingham-NODDI*

Bingham-NODDI is proposed, which enables enhanced characterisation of neurite orientation dispersion, along with specific indices for quantifying complex neurite configurations that are subtle markers of changes in neurite morphology. A novel index of orientation dispersion anisotropy is also proposed to specifically quantify the level of this feature. This addresses the aims 1 and 2 stated in Section 1.2.

The work for the development of Bingham-NODDI has been published in Tariq et al. 2014a and Tariq et al. 2016a and is entirely my work, but I have had very useful input from the co-authors to refine the writing. The work has also been presented at two major conferences[161,162].

1.3.2 In vivo *and clinical feasibility of Bingham-NODDI*

To demonstrate the *in vivo* feasibility of Bingham-NODDI, the estimability of its indices needs to be established. To achieve this, I analyse their accuracy and precision using a clinically feasible acquisition protocol. I also assess whether making the NODDI model more complex results in overfitting of the data and if the proposed model explains the DW-MRI data better than the original NODDI model, which is referred to throughout this thesis as Watson-NODDI.

Both *in silico* and *in vivo* experiments are used for evaluating the estimability of the model parameters. This evaluation provides an estimate of the inherent variability in estimating the indices of the model, with known ground truth (simulations), as well as real data (*in vivo*). Synthetic data is invaluable to assess the accuracy and precision of the model parameters against a known ground truth, for a rich set of plausible tissue configurations. *In vivo* data evaluation gives a more realistic assessment of the parameter estimation.

The work for evaluation of Bingham-NODDI indices has been published in Tariq et al. 2016a, addressing aim 3 stated in Section 1.2. The *in vivo* data

used for the analysis was acquired by Dr. Torben Schneider at the Institute of Neurology, University College London.

1.3.3 *Assessment of assumptions and propose fitting procedure for Bingham-NODDI*

Here I assess the impact of some of the assumptions made in the proposed model and to obtain the optimum fitting procedure to estimate the model parameters. This includes evaluation of the assumption of a single fibre population per voxel, in the Bingham-NODDI tissue model. Regions of crossing fibres are known to exist in the brain WM and the proposed model can not characterise such configurations.

1.3.4 *Normative values of Bingham-NODDI in the healthy human brain*

I apply the proposed method to high-quality DW-MRI data (Human Connectome Project (HCP) data[1]) acquired on a larger cohort of normal adult subjects. This helps establish the range of values of its indices in the normal adult brain, which are obtained from a very reliable data set. This has clinical utility, for e.g. it is useful to report the anatomical location of areas with microstructure properties significantly different to those in normal population or changes during development in specific areas. I also assess whether the expected variation across the WM tracts is captured by the Bingham-NODDI metrics, as it is known that the fibres in a WM tract are not homogeneous in terms of the microstructure, for example, their packing density and organisation.

This work presenting the normative values of Bingham-NODDI indices has been presented at an international conference[163] and is a step towards 5^{th} and 6^{th} aims of the work. The *in vivo* data used here was acquired by Van Essen et al. 2012, for the HCP. The data processing was carried out by Ms. Jiaying Zhang and I. Ms. Zhang specifically helped me with the template generation and distortion correction of the data. The ananlysis presented here to obtain the mean values and variability of the indices is my own.

1 Available online at http://www.humanconnectome.org/documentation/Q3/

1.3.5 *Reproducibility and reliability of Bingham-NODDI indices*

For the proposed technique to have a clinical use, it needs to be assessed whether the parameters of the underlying model are repeatable and reliable. For this, I carry out a reproducibility study to evaluate if the real microstructural differences (i.e. inter-subject differences) can be seen given the noise in the measurements. To achieve this, scan-rescan DW-MRI data is acquired for multiple subjects. The acquired data has a repeated measurement design so the between-subject and within-subject variance can be separated and it is done using analysis of variance (ANOVA).

The *in vivo* data used here was acquired by Dr. David Cash and Dr. David Thomas, at the Dementia Research Centre (DRC), University College London.. Ms. Zhang helped me with the pre-processing of the data, specifically the template generation.

1.3.6 *Bingham-NODDI indices in the grey matter of healthy adult brain*

A distinct advantage of Bingham-NODDI is that it allows whole brain evaluation of neurites, using standard imaging set-up, and the dispersion anisotropy index is an important characteristic to quantify, for e.g. in the cortical GM[85,147]. However, quantification of features of the microstructure is challenging in the GM with quality and resolution of standard DW-MRIs (the cortical layer is 2-2.6mm thick in normal adults[97], which is comparative to the thickness of a typical DW-MRI voxel[90]). So resolving microstructure in the GM requires a very rich acquisition protocol, particularly for a model as complex as Bingham-NODDI. In order to assess the Bingham-NODDI metrics in the cortical GM, I utilise high-resolution *in vivo* data (used in Section 1.3.4 for assessment in WM), as well as *ex vivo* data acquired on a sample of the human visual cortex, as used in Kleinnijenhuis et al. 2013. I provide a preliminary study assessing the metrics of Bingham-NODDI, specifically the index of dispersion anisotropy in the GM to see if it gives plausible values that correlate with the known microstructure.

The work evaluating Bingham-NODDI indices obtained from *ex vivo* images of human visual cortex were presented at a major conference[155]. The MRI data used was provided by Dr. Michiel Kleinnijenhuis. He acquired the data at the Department of Anatomy of the Radboud University Nijmegen Medical Centre. The histology sample was provided pre-processed by him, but I carried out the analysis on the DW-MRI data.

1.4 THESIS OVERVIEW

The chapters in Part (ii) of the thesis provide the background information relevant for the contributions made as part of the PhD. In Chapter 2 I provide an overview of the brain, with a particular focus on how specific features of the microstructure can inform about the function or abnormalities of the brain. I then discuss why there is a need for a *non-invasive* technique to characterise complex organisations of the neurites for a better understanding of the mechanisms underlying normal brain development and ageing, as well as disease. In Chapter 3 I discuss the various methods to *non-invasively* image the brain, focussing on DW-MRI which is most relevant for the presented work. I then discuss microstructure imaging techniques that have been utilised to enable characterisation/quantification of brain microstructure, in Chapter 4. This includes an overview of the main constituents of such techniques and the various models that have been proposed for *non-invasive* microstructure imaging of the brain. I also outline the importance of techniques like NODDI for the advancement of research and clinical practice in neuroimaging. In Chapter 5 I outline NODDI, the DW-MRI technique I use to quantify brain morphology at the microstructure level and outline the various aspects of the technique, including a detailed description of the mathematical model underlying it.

Part (iii) of the thesis is concerned with the development and evaluation of the proposed technique for *in vivo* quantification of orientation dispersion anisotropy. In Chapter 6 I present the mathematical framework to enable quantification of orientation dispersion anisotropy, which is the work done for contribution 1.3.1. To achieve this, I address the limitation of Watson-NODDI, by relaxing the assumption of isotropic orientation dispersion. I derive indices from the proposed model to quantify the orientation dispersion anisotropy and other features of neurite morphology. In Chapters 7 and 8 I evaluate the clinical feasibility of the proposed model and estimating the orientation dispersion anisotropy, using *in silico* and *in vivo* data. This is the contribution 1.3.2 made in this work. I demonstrate the accuracy and precision of the indices of Bingham-NODDI and assess how well it explains the DW-MRI data, compared to the original NODDI model, using a clinical feasible acquisition protocol. Experiments carried out for contribution 1.3.3 are included in Chapter 9.

Part (iv) is concerned with the contributions 1.3.4 and 1.3.5, which is the work I carried out to establish and facilitate clinical applicability of the proposed method. In Chapter 11 I establish the normative values and carry out power calculations for Bingham-NODDI indices, while in Chapter 12 I demon-

strate the repeatability and reliability of the estimates. Both these studies focus on WM, as it is found that Bingham-NODDI is most useful in neurites of the WM from evaluation of its indices in Chapters 7 and 8, using standard imaging data.

In Part (v) of the thesis I provide a preliminary assessment of Bingham-NODDI in the GM, using very high-quality *in vivo* and *ex vivo* DW-MRI data. Here I assess how well Bingham-NODDI explains the high-quality data utilised, in the cortical GM. Chapter 14 utilises the *ex vivo* data while Chapter 15 the *in vivo* data from Chapter 11 (HCP data).

In Part (vi) I provide a summary of the thesis and a discussion of the main advanatages and limitations of the proposed technique (Chapter 16). I follow this up with the future work required to try and address these limitations (Chapter 17) and take forward the work carried out as part of this PhD.

Part II

BACKGROUND

This part of the thesis details the principles relevant for the contributions made during the PhD This includes the basics of microstructure imaging, specifically the state-of-the-art in computational techniques (biophysical models) in DW-MRI, which are necessary to fully understand and appreciate the context of this thesis and the proposed method.

2

IMPORTANCE OF NEURITES IN NEUROSCIENCE

The integrity of brain microstructure, specifically the neurites, is vital for normal brain function and development. Understanding the changes in neurites underlying normal and pathological brain is thus vital for diagnosis and prognosis of brain pathologies, which pose a significant disease burden.

This chapter establishes the importance of brain microstructurein neuroscience for research and clinical application. In the following sections, we describe the microstructure constituents of the brain, specifically neurites which are the object of interest for this thesis. We finish with a summary of the existing knowledge of how the brain and its microstructure change during normal development and ageing as well as neurological and developmental disorders.

Information in this chapter has been derived from several sources as referenced, including O'Shea 2005 and Johansen-Berg and Behrens 2009.

2.1 BRAIN

Consisting of roughly one billion nerve cells communicating through a hundred trillion interconnections[124], the brain is the most complex organ of the human body. The brain performs a crucial role in the most vital bodily functions, such as pain perception or reacting to changes in blood pressure or oxygenation, as well as being the source of human consciousness. This makes the brain an integral organ for normal functions of the human body. The huge network of cells working and communicating with each other, help the brain function. Disruptions to normal brain function have an immense impact on the human life and substantial economic burden on the society.Thus research in understanding the brain development, ageing and disorders attracts immense interest and has resulted in initiatives to acquire a wealth of imaging data from healthy adults and infants (The Human Connectome Project[1] and

1 http://www.humanconnectomeproject.org/

The Developing Human Connectome Project[2]) as well as longitudinal data for neurodegenerative diseases (The Alzheimer's Disease Neuroimaging Initiative[3]).

2.1.1 *Brain tissue*

The brain is the control centre of the body, playing a vital role in the central nervous system, along with the spinal cord. The functional part of the brain tissue, known as the brain parenchyma, consists of soft tissue which sits in the cerebrospinal fluid (CSF) inside the skull. The CSF mainly provides physical protection and chemical stability to the brain parenchyma but also serves to protect against ischemia by altering the intracranial pressure, as well as flushing out waste e.g. toxins and hormones. The brain parenchyma is composed of two main types of neural tissue, the grey matter (GM) and the white matter (WM), named so due to their distinct macroscopic appearance and colour of the brain tissue, as seen in the dissected brain images in Figure 2.1. The GM at the surface of the brain forms the *cortex*, which surrounds the WM as seen in Figure 2.1. The deep GM regions, seen as intermediate contrasts in the middle of the T_1 and T_2-weighted images shown in Figure 2.1, are made up of neurons from which the deep nerve fibres originate. Deep GM is associated with processing of various vital functions including memory and navigation.

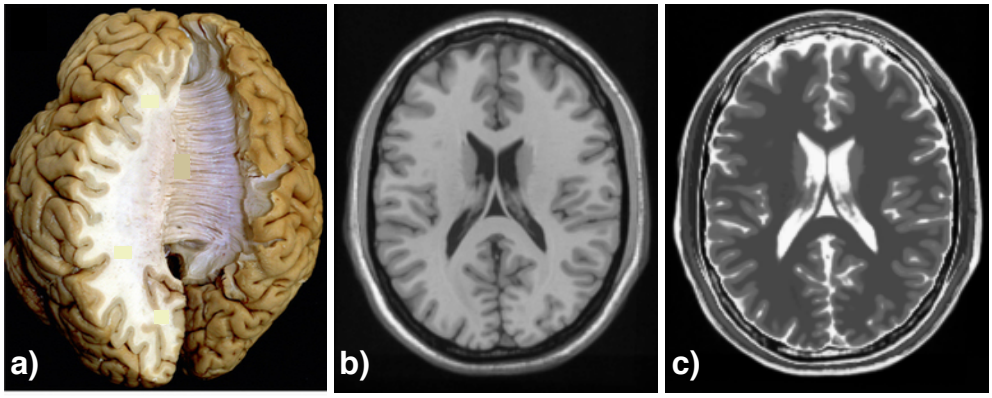

Figure 2.1: Brain tissue as seen in a dissected human brain[119] (a), T_1-weighted MRI (b), and a T_2-weighted MRI (c). The GM is appears darker in the dissected brain, and surrounds the WM tissue, which is lighter in appearance. The GM and WM of the brain can also be distinctly seen as the grey and white regions, respectively, in the T_1-weighted image. In the T_2-weighted image, however, the WM appears darker than the GM. The acquisition of MRI images with various contrasts is described in Chapter 3.

2 http://www.developingconnectome.org/
3 http://adni.loni.usc.edu/

WM is the 'cabling' that connects the various GM regions in the brain to each other and forms the basis of communication between different parts of the brain. WM mainly consists of highly organised and densely packed *axons*, which are a *myelin* covered cylinder-like part of the *neurons*, as shown in Figure 2.2. GM is the main processing part of the brain and consists of the cell bodies of the neurons, which also have projections called *dendrites* (see the cell-bodies in Figure 2.2).

2.2 MICROSTRUCTURE COMPONENTS OF THE BRAIN

The cellular composition of the brain tissue are neurons and glial cells. Glial cells, which include the oligodendrocytes, astrocytes, and microglia, carry out various support functions, like producing myelin, protecting the neurons and maintaining homeostasis. Neurons are the main functional cell in the brain, which form the processing and communication network of the brain.

Neurons are made up of three main constituents: an axon, a soma (cell body) and dendrites, as shown in Figure 2.2. Roughly speaking, the axons are in the WM and the cell bodies (glial and neuron cell bodies), including the dendrites in the GM. The neurons are connected with each other with synapses, which transfer neural signal (action potential) in the form of an electrochemical signal[152].

The non-cellular parts of the brain tissue are made up of neurites, which transport the signals generated and received by the neurons.

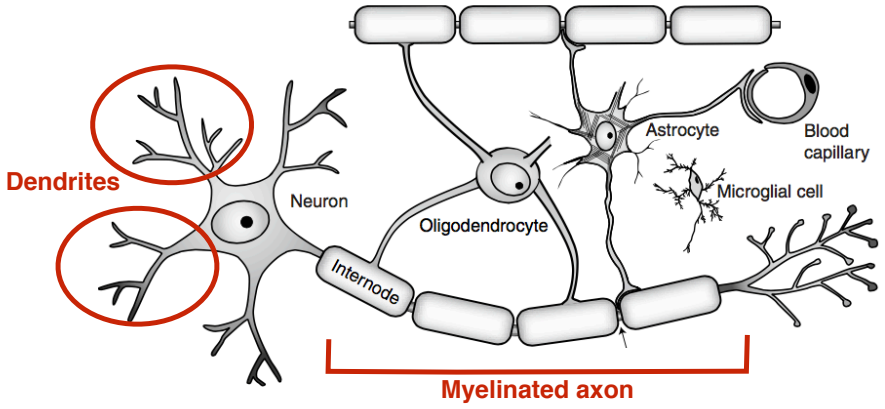

Figure 2.2: Main microstructure components of the neuron. Axons and dendrites, which are long processes extending from the neuron (highlighted in red) underpin the main functions as well as the strucutral integrity of the brain (see main text). *The schematic has been adapted from Edgar and Griffiths 2009.*

2.2.1 *Neurites*

Axons and dendrites are collectively called *neurites* and are cylinder-like projections from neurons. Axons are generally highly organised and densely packed and can extend up to 1m, while dendrites are more orientationally dispersed and less densely packed, as shown in the schematics in Figure 2.3. The main function of the axons is to receive the electrochemical signal from other neurons, often at dendrites.

The major connections formed by the axons are called *axonal pathways*, which are composed of a group of axons, or *fibres*, that connect various functional regions of the brain. Axons are wrapped around in *myelin sheath* (Figure 2.2), which is rich in fat and protein, and greatly improves the efficiency of transfer of the electrical impulses (neural signal). The axon thickness in the brain varies from $0.16 - 9\mu m$[112], as estimated by electron micrograph studies.

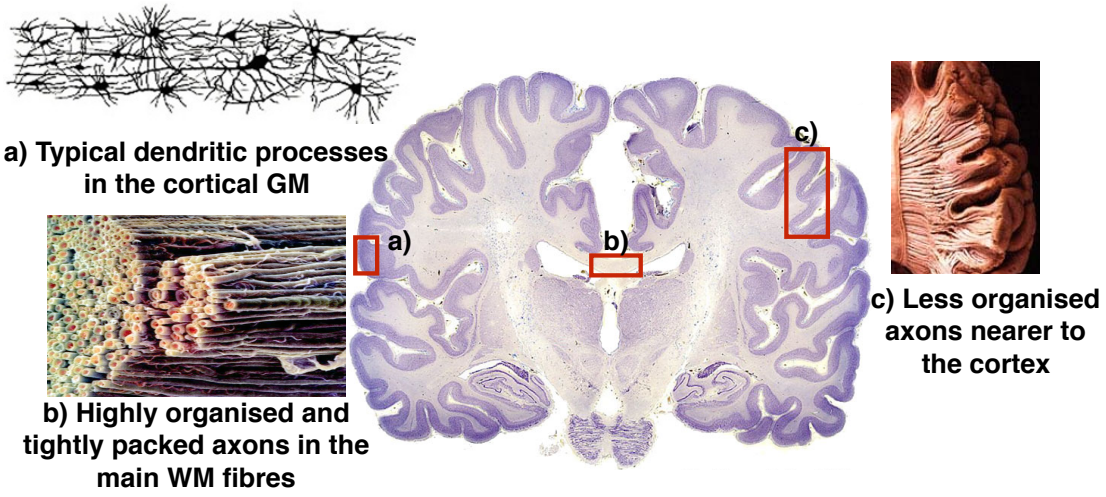

Figure 2.3: Groups of axons and dendrites, collectively called *neurites*, typically found in the vast network of neuronal connections in the brain. The cortical GM is mainly composed of dendrites, which form complex connectivity patterns, shown in a). Axons are generally densely packed and exhibit low orientation dispersion, for example the organisation shown in b), but can also have high orientation dispersion, as shown in c). Note that the images are not to scale. *The images in this figure have been adapted from various sources (The main image: `http://brainmuseum.org/` [accessed in Aug. 2017], a) Leisman et al. 2012, b) `http://www.vetmed.vt.edu/` [accessed in May 2015] and c) `http://brainmind.com/` [accessed in Aug. 2017]).*

The dendrites are organised in a dispersed fashion, which resembles the branches of a tree[152], as shown in Figure 2.3.a), where various interconnected dendritic processes of the cortex are represented. Axons, on the other hand, are usually bundled together to form fibres, which can be densely organised, as

shown in the electron micrograph in Figure 2.3.b) for the central sections of the corpus callosum (CC), or exhibit some orientation dispersion, for example in the fibres extending into the cortex, as shown in Figure 2.3.c).

2.2.2 *Main fibres of the brain WM*

The main WM tracts in the human brain are big bundles of fibres that form major axonal pathways in the brain as shown in Figure 2.4.

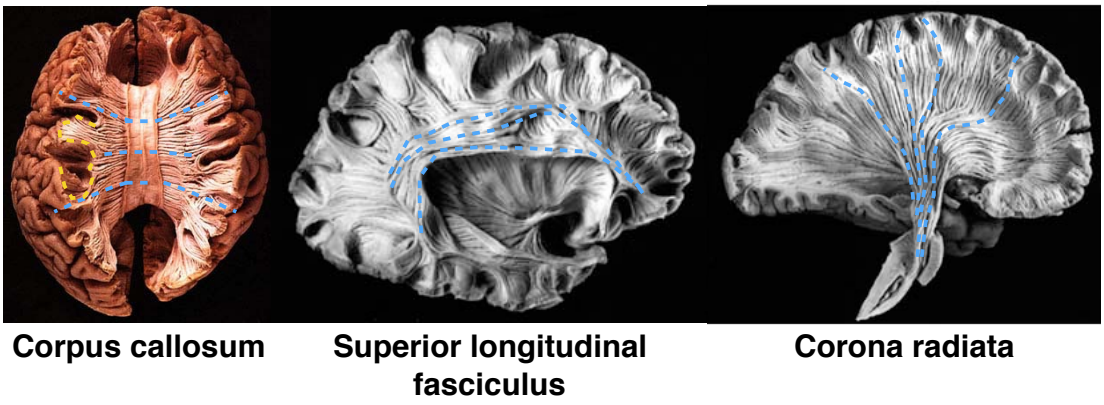

Figure 2.4: Main fibres of the brain. The first image shows a type of commissure, the middle one an association and the last image a projection fibre tract. The dotted lines on each *ex vivo* brain highlight the variety of ways the fibres are arranged in the space, specifically in terms of their orientation dispersion. *Images have been adapted from* `http://brainmind.com/` *[accessed in Aug. 2017].*

These are typically catagorised as follows:

- **Commissure fibres**

  These are the fibres that connect the two brain hemispheres and include the *corpus callosum (CC)*, which is shown in Figure 2.4, and *anterior commissure (AC)*.

- **Association fibres**

  These connect the various cortical regions with each other. Association fibres include the superior longitudinal fasciculus (SLF), as shown in Figure 2.4, as well as the arcuate fasciculus (AF), the cingulum and the U-fibres.

- **Projection fibres**

  The projection fibres connect the regions in the brain stem to the cortical GM. This includes efferent fibres that carry signals from the brain stem

to the cortex (motor) and afferent fibres that carry it from the cortex back to the brain stem (sensory). These fibres include the corona radiata (CR), shown in Figure 2.4, and the internal capsule (IC).

2.3 NEURITES IN HEALTHY AND PATHOLOGICAL BRAIN

Characterisation of the morphology of neurites is an important area of research for neuroscience and clinical studies, due to its links to development, ageing, function, and pathology of the brain.

The *"critical role of dendrites in information processing in the brain"* [153] has been highlighted by the vast amount of work carried out on brain processing, at the cellular level. Dispersion of dendrites is linked with brain development [40] and their density with ageing [80]. Establishment of neuronal pathways and their myelination is characteristic of normal brain development and modification to this process is linked with various neurodevelopmental disorders [172].

Changes in neurite morphology are also linked with various neurological diseases like *multiple sclerosis* [59], *amyotrophic lateral sclerosis* [31], *Alzheimer's disease* [127] and neurodevelopment disorders [47]. Thus by quantifying the physical characteristics of neurites, promising markers of progression of brain diseases can be obtained and used in the diagnosis, prognosis, and treatment of brain disorders.

Histological studies have shown that GM undergoes very significant changes during early brain development [100,101] and abnormal cortical thickness and reduced complexity of the dendritic and axonal processes (i.e. their orientation dispersion) in the cortex are associated with preterm birth [18,19].

So characterisation of neurite morphology, specifically in terms of their orientation distribution and their packing density is very important. There is a need to develop better ways of *in vivo* characterisation of their geometry, which is the subject of this thesis. Advancement in our understanding of the brain microstructure and causes of disruptions to it are greatly dependent on imaging techniques, as discussed in the next chapter.

2.4 IMPORTANCE OF NON-INVASIVE BRAIN IMAGING

The precise changes in brain microstructure that lead to a specific change in function or a certain pathology are not fully understood [43] and require studies that can probe such dynamic processes noninvasively. Non-invasive imaging

techniques that provide direct quantification of such microstructural changes are essential for the advancement of research in neuroscience, as well as clinical practice.

The most accurate and reliable method to image brain microstructure is histological analysis, as it provides high-resolution data representing the exact measure of the microstructure (i.e. there are no models or approximations involved). Histological data is considered the ground truth for existing knowledge on the cellular architecture of the brain. However histological analysis is limited by the invasive nature of the technique, which does not allow for longitudinal studies to be carried out to follow dynamic changes in the brain in normal or pathological conditions. Once the brain has been removed from the body for histological analysis, the imaging analysis is of no use to the subject who has provided the sample and is not directly indicative of brain structure for another subject due to the known inter-subject variability of the brain macro structure as well as the microstructure. There has also been a lack of availability of good quality histological data due to the complex procedures involved.

Non-invasive methods for microstructure imaging are thus vital in neuroscience for better characterisation of the processes involved in brain development, ageing, and disease. One such imaging method is DW-MRI, which is introduced in the next chapter (Chapter 3). The DW-MRI techniques which provide direct quantification of the brain microstructure are discussed in Chapter 4, along with DTI, the current standard in neuroscience for DW-MRI.

3

BRAIN IMAGING WITH MAGNETIC RESONANCE IMAGING

This chapter discusses the various methods utilised in neuroscience to image the brain. The focus is on non-invasive and *in vivo* MRI techniques like DW-MRI, which provide a contrast dependent on the brain microstructure. DW-MRI is sensitive to microstructure and allows us to probe brain tissue, *in vivo* and is a routine for clinical applications like stroke.

Information in this chapter has been derived from several sources, including notes on MRI by Delakis 2008-09 and Shmueli 2011-12, as well as various textbooks on DW-MRI, as referenced.

3.1 IN VIVO BRAIN IMAGING

Development of *in vivo* imaging studies has been invaluable in enhancing our understanding of the dynamic processes of the brain and have allowed longitudinal studies to be carried out, which was not possible with the traditional histological studies.

Magnetic Resonance Imaging (MRI) is one such *in vivo* technique, which provides a dynamic view of the brain. While MRI is one of the most expensive medical imaging techniques and requires a much longer scan time compared to techniques like ultrasound (US) and computed Tomography (CT), it is widely used in neuroscience and clinical studies. This is because MRI is a very rich modality, which can provide several contrasts giving sensitivity to the brain (macro-)structure, function as well as the microstructure. CT is widely used for imaging other parts of the body but is less utilised in the brain as it is ionising, but US is used as a first means of assessing most organs but has very low soft-tissue contrast. MRI, on the other hand, is non-ionising, gives better soft-tissue contrast and there are several MRI techniques that are

non-invasive, as they depend on inherent molecules as contrasts. This makes MRI one of the most widely used techniques for neuroimaging.

Standard MRI techniques, like T_1/T_2-weighted MRI, have enabled studies into understanding the brain maturation and identifying regions of brain injury, as they have a contrast that depends on the underlying tissue. We focus on DW-MRI, which is a suitable technique for our work due to its sensitivity to brain microstructure. In the following sections, we describe the fundamentals of MRI and the theory behind diffusion sensitising of MRI (i.e. DW-MRI), which is the imaging modality used for the presented work.

The following sections summarise the fundamentals of diffusion and how the diffusion profile of water molecules reflects the details of the surrounding microstructure, in the brain. Then we describe the fundamentals of MRI and the theory behind diffusion sensitising of MRI (i.e.DW-MRI).

3.2 DIFFUSION-WEIGHTED MRI

DW-MRI is a powerful non-invasive imaging modality of the MRI that is sensitive to the displacement of water molecules, *in vivo*. The diffusion profile of water provides a unique non-invasive probe to the microstructure, which acts as a barrier to their movement. DW-MRI is sensitive to diffusion providing structural information (for restricted diffusion) in the range of about $0.1 - 100\mu m$[131]. So DW-MRI is particularly applicable to the areas of neuroanatomy, as the scale of the structures involved is in the micrometre range, which is much smaller than the resolution of the conventional MRI techniques (T_1 and T_2 weighted imaging).

The potential for DW-MRI to be utilised in clinical diagnostics was seen very early[108,117]. Various studies have taken advantage of the ability of DW-MRI to allow visualisation of changes at the microscopic level and used it as a tool for clinical diagnosis. Early detection of the onset of a stroke or ischemia has been one of the most successful applications of DW-MRI and has been demonstrated in various human[174], and other animals[48,116]. DW-MRI highlights acute stroke, within the first few hours of onset. This is due to the decrease in the diffusion in the region of the stroke, by almost 50%, but such changes are not visible in conventional MRI until much later[146]. This opens opportunities for development of treatments and prevention techniques, while the brain tissue is still in a viable condition.

3.2.1 *Diffusion theory*

DW-MRI is based on the random motion of particles called the *Brownian motion*, first observed by Brown[30]. Einstein noted that this random motion is related to diffusion, which is a net movement of particles due to a gradient in their concentration (Fick's Law[35]). But the Brownian motion occurs without a net concentration gradient and so is also called self-diffusion.

Einstein described the process of *self-diffusion* in terms of the probability $P(\boldsymbol{r}_0|\boldsymbol{r}_1, t)$[56] of finding a particle at position $\boldsymbol{r}_1$ after diffusing over a time $t = t_1 - t_0$ from an initial position of $\boldsymbol{r}_0$. This probability changes over time due to local fluctuations in concentration and is described by

$$\frac{\partial P(\boldsymbol{r}_0|\boldsymbol{r}_1, t)}{\partial t} = D\nabla^2 P(\boldsymbol{r}_0|\boldsymbol{r}_1, t) \, , \tag{3.1}$$

which is obtained by re-writing Fick's second law of diffusion (Appendix A.4).Here D is the diffusion coefficient of the particles. $P(\boldsymbol{r}_0|\boldsymbol{r}_1, t)$ is also termed the *diffusion propagator*, as it quantifies the likelihood of a molecule diffusing from $\boldsymbol{r}_0$ to $\boldsymbol{r}_1$, over the time t. Solution to Equation (3.1) can be found for specific cases of diffusion, each with specific boundary conditions.

3.2.1.1 *Free diffusion*

Free diffusion is described as self-diffusion when there are no physical restrictions to the movement of particles. For free diffusion in a homogeneous and isotropic medium with initial condition $P(\boldsymbol{r}_0, \boldsymbol{r}_1, 0) = \delta(\boldsymbol{r}_1 - \boldsymbol{r}_0)$ (δ is the Dirac Delta function) and boundary conditions $P \to 0$, as $(\boldsymbol{r}_1 - \boldsymbol{r}_0) \to \infty$, Equation (3.1) can be solved[131] and is given by the Gaussain probability density fucntion (PDF)

$$P(\boldsymbol{r}_0|\boldsymbol{r}_1, t) = \frac{1}{(2\pi)^{\frac{3}{2}}(2Dt)^{\frac{3}{2}}} \exp\left(-\frac{(\boldsymbol{r}_1 - \boldsymbol{r}_0)^2}{4Dt}\right) . \tag{3.2}$$

The mean-squared displacement of the ensemble of freely diffusing particles is then expressed as

$$\langle(\boldsymbol{r}_1 - \boldsymbol{r}_0)^2\rangle = \int_{-\infty}^{\infty} (\boldsymbol{r}_1 - \boldsymbol{r}_0)^2 P(\boldsymbol{r}_0|\boldsymbol{r}_1, t) d\boldsymbol{r}_0 d\boldsymbol{r}_1 = nDt \, , \tag{3.3}$$

where $n = 2, 4, 6$ respectively for $1, 2, 3$ dimensions. Thus for free diffusion in an isotropic medium, the mean-squared displacement is a linear function of time and is independent of the direction, and the diffusion can be quantified experimentally by estimating the diffusion coefficient from a measurement of the mean squared displacement along any direction.

When the medium of diffusion is not isotropic, describing the PDF with scalar diffusion coefficient is not sufficient. To account for orientation dependence of the self-diffusion the tensor form of diffusion coefficient can be used, which gives

$$P(\boldsymbol{r}_0|\boldsymbol{r}_1, t) = \frac{1}{((4\pi t)^3 \det(\mathbf{D}))^{\frac{1}{2}}} \exp\left(-\frac{(\boldsymbol{r}_1 - \boldsymbol{r}_0)^T \mathbf{D}^{-1} (\boldsymbol{r}_1 - \boldsymbol{r}_0)}{4t}\right), \tag{3.4}$$

where $\boldsymbol{D}$ is a *symmetric positive-definite* 3×3 matrix, called the *diffusion tensor*. This form of PDF can be used for anisotropic diffusion as Gaussian (free) diffusion described in a 3-dimensional space and was introduced by Stejskal 1965 and later described as an experimental framework to measure tissue anisotropy by Basser et al. 1994, as detailed in Section 4.4.1.

In the brain, CSF is the fluid surrounding the brain tissue, and exhibits isotropic Gaussian diffusion, as shown by the simulation in Figure 3.1. Such isotropic diffusion can be characterised by a single diffusivity as in Equation (3.2).

3.2.1.2 *Hindered and restricted diffusion*

When there are barriers or physical restrictions to the motion of diffusing particles, the displacement profile of the molecules is dependent on the geometry of the physical barriers as they hinder (permeable membranes) or restrict (non-permeable membrane) the motion of particles.

The brain tissue is highly non-homogeneous, consisting of neurons and glia of varying geometric characteristics (Chapter 2). The diffusion in the neural tissue thus has an apparent diffusion coefficient (ADC), which depends on these microstrucutre components. These diffusion characteristics are very different inside the cells, compared to outside them, as the cell membranes that separate the cell's interior from the exterior form a very impenetrable barrier to diffusion.

The cells in the brain tissue are seperated by $\approx 50\text{nm}$ and the cell sizes are $\approx 1 - 100\mu\text{m}$ and neuronal processes (neurites) are an order of magnitude less than that[95]. Such packing results in a highly tortuous environment outside

the cells for protons to diffuse through, as shown by the blue and red paths in Figure 3.1. Over very short times, the diffusion in this space represents the local intrinsic diffusivity, but at longer diffusion times, the effects of this tortuosity become predominant, reflecting the obstacles to the dispersion of protons[66,106].

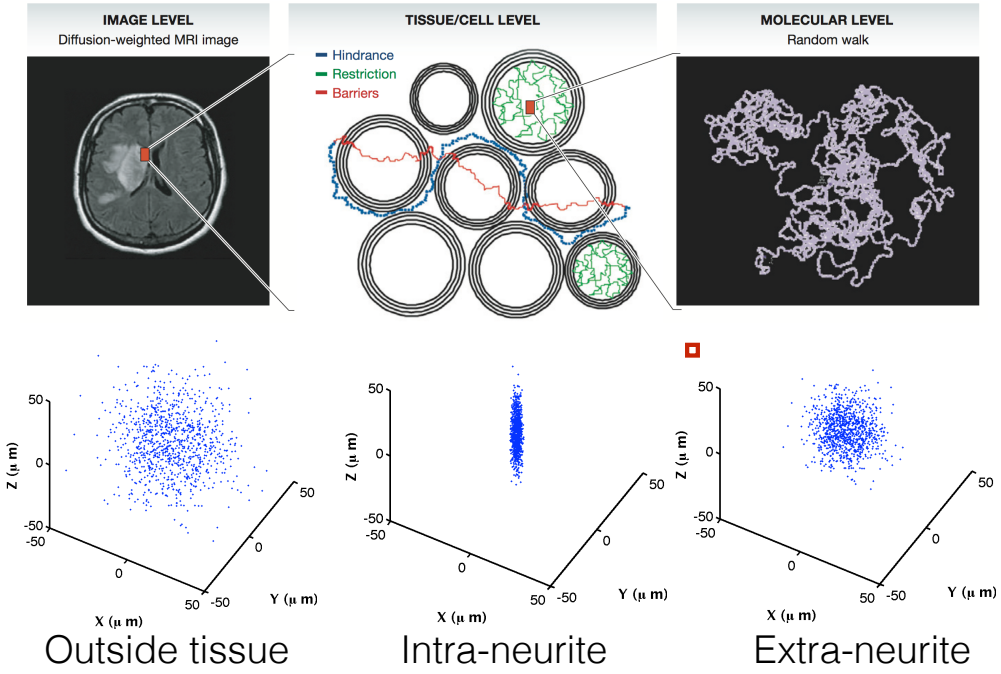

Figure 3.1: Schematic depicting the diffusion of particles in the brain. The top panel shows the displacement of particles in certain parts of the neural tissue, while the bottom panel shows the displacement profile of water molecules within the neurites, or the *intra-neurite space* (restricted diffusion), in the extra-neurite space (hindered diffusion) and CSF (free diffusion). *The displacement profiles were created using Monte-Carlo simulation to depict random motion of a large number of particles using the Camino toolkit*[42] *and the top panel has been adapted from Le Bihan 2014.*

For cells within the impermeable environment of cells and neurites (in the time scale where no exchange happens with the extracellular compartment), the protons are confined within the boundaries and the displacement profile of the particles reflect this, as seen in Figure 3.1. This restricted diffusion in non-Gaussian. The diffusion in the intra-cellular space is thus dependent on the surroudning geomtery as well as the diffusion time.

Thus for diffusion in the neural tissue, the solution to Equation (3.1) is very complicated and the PDF is no longer Gaussian. The PDF thus has to be obtained by considering the specific geometry present in the tissue. Many such solutions for various geometries of interest like spheres and cylinders can be found in literature[44,121].

3.2.2 *Nuclear magnetic resonance*

MRI is based on the phenomenon of nuclear magnetic resonance (NMR), first observed independently by Purcell[133] and Bloch[28] in 1946. NMR is based on the interaction between atomic nuclei with a non-zero spin and charge, and a magnetic field, which results in a transfer of electromagnetic radiation of a certain frequency. The nucleus usually probed in MRI is the Hydrogen ($^1H^+$) in the water, which is abundant in the body ($70-90\%$ of most tissue). Proton or spin is synonymously used instead of the $^1H^+$ nucleus, as it has a single proton with non-zero spin.

Interaction of $\boldsymbol{B}_0$ and the magnetic moment, $\boldsymbol{\mu}$, produces a torque which causes the nucleus to precess about the axis of $\boldsymbol{B}_0$[1]. This results in a circular motion of the magnetic moment, $\boldsymbol{\mu}$ in the plane perpendicular to the main axis of $\boldsymbol{B}_0$ and it rotates with the Larmor frequency,

$$\omega_0 = \gamma \boldsymbol{B}_0 \, . \tag{3.5}$$

In an MRI experiment, we are concerned with the ensemble of nuclei in the typical imaging volume called a *voxel*, where the nuclei take one of their two discrete energy states, up or down, as dictated by the Boltzmann distribution (Appendix A.1). The difference in the occupation of the two energy states creates the equilibrium magnetization $\boldsymbol{M}_0$ in the direction of $\boldsymbol{B}_0$[2], as there are more nuclei in the spin-up than spin-down energy state. Conventionally $\boldsymbol{B}_0$ is applied along the z-axis, which is also called the longitudinal direction and the plane perpendicular to it (x-y plane) is called the transverse plane.

The net magnetisation in each unit of imaging volume describes the macroscopic magnetisation, $\boldsymbol{M} = (M_x, M_y, M_z)$ and is the source of an MRI signal, as described in the next section.

3.2.3 *Signal generation*

In the presence of external magnetic field, the evolution of the net magnetisation, which is the signal measured in MRI, is described by the Bloch equation[28] (see Appendix A.2), which shows that $\boldsymbol{M}_0$ can be manipulated by ap-

1 much like a top spinning around its axis at an angle to the earth's gravitational field, precesses about the gravitational axis

2 there is no net magnetisation in the plane perpendicular to the axis of application of $\boldsymbol{B}_0$, as the precession of individual nuclei are not in phase

plying a magnetic field at the resonant frequency of the precession of the system of nuclei, ω_0. This perturbs the $\boldsymbol{M}_0$ from its equilibrium state (Figure 3.2.a), providing a probe to the different magnetic properties of the sample, as energy is absorbed (excitation) and released (relaxation) by the system of spins.

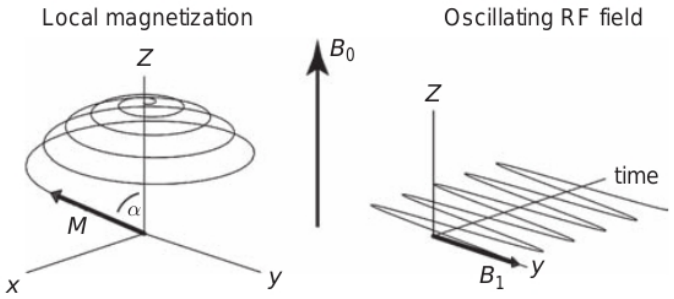

Figure 3.2: Illustration of the evolution of $\boldsymbol{M}_0$ in the presence of a magnetic field $\boldsymbol{B}_1(t)$. Application of $\boldsymbol{B}_1(t)$, oscillating in the transverse plane at Larmor frequency, tips the $\boldsymbol{M}_0$ towards the transverse plane. The oscillating field, $B_1(t)$ is shown in the right and the path taken by the net magnetization as it tips to the transverse plane is shown in the left of the figure. *Figure adapted from Buxton 2009*.

Figure 3.2 shows the evolution of $\boldsymbol{M}(t)$ as it tips to the transverse plane, taking a spiral path described by the Bloch equation (Appendix A.2), as it precesses about the longitudinal plane. The $\boldsymbol{M}(t)$ precessing is the source of MRI signal and is detected as the induced voltage in a coil with the same resonant frequency. The following section describes how this is typically done for MRI of the brain.

3.2.4 *Acquisition sequence*

The MRI acquisition *sequence*, or the *acquisition protocol* detremines the precise evolution of $M(t)$ over time. The data presented in this thesis is acquired using the *spin echo, SE*[75] sequence, so only the SE sequence is described here. The other typical sequence used in brain imaging is the *gradient echo, GE* sequence[57].

The evolution of $M(t)$, for the SE sequence, is shown in Figure 3.3. The $\boldsymbol{M}(t)$ is maximum at the time the excitation pulse is removed, as a result of coherent spin precession, but decays due to their dephasing over time. The excitation pulse rotates $\boldsymbol{M}_0$ by 90°, so is also called the 90° *pulse*. An additional RF pulse flips the position of the spins by 180°. This is called the refocusing pulse as it allows the signal to "re-appear" at a known time, the *time to echo - TE*, so

the signal can be detected. The evolution of the signal as a result of the spins precessing in the transverse plane is explained in Figure 3.3.

The MR signal measured at the end of this sequence is called the spin-echo which is shown in Figure 3.3 and is detected by an RF coil tuned to the frequency of precession of $\boldsymbol{M}(t)$. The whole MR sequence (Figure 3.3) is repeated at time $t = TR$ to acquire more signals. This sequence can be used to probe tissue properties, as detailed in Section 3.2.6, and also made sensitive to diffusion of spins (i.e. DW-MRI), by adding diffusion sensitising magnetic gradients, as described in Section 3.2.7.

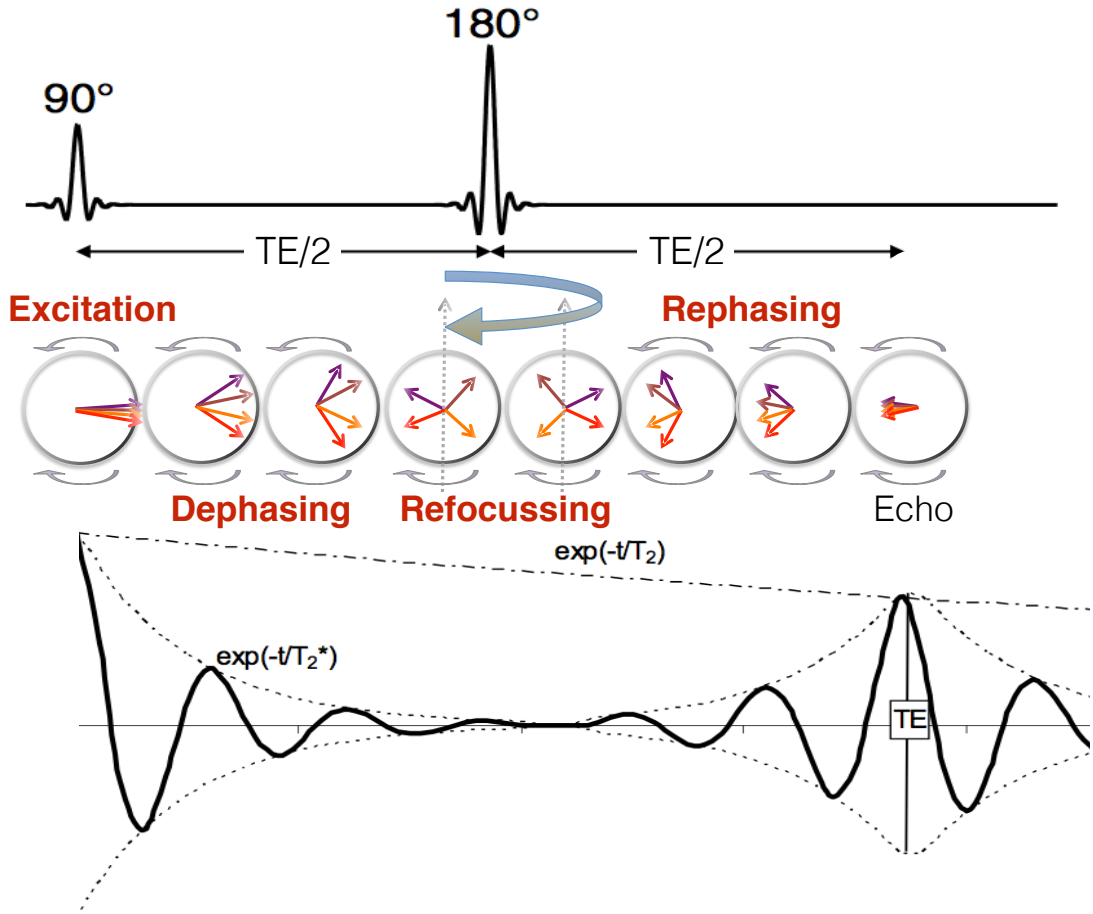

Figure 3.3: Schematic depicting the SE sequence and how it impacts the $\boldsymbol{M}_0$ in the transverse plane. Top: the SE sequence, middle: the evolution of spins in the transverse plane and bottom: the detected signal. The excitation pulse (90°) tips $\boldsymbol{M}_0$ to the transverse plane. With time, phase differences between individual spins (dephasing) and magnetic field inhomogenities (T_2 and T_2^*) cause a reduction in the magnetisation. At a time $\frac{TE}{2}$, the refocusing pulse (180°) flips the spins, leaving the faster (precessing) spins behind the slow ones. At $t = TE$ the spins regain phase coherence, which is the *spin-echo*. *Illustration adapted from Ferizi 2014 and Delakis 2008-09*.

3.2.5 *Signal localisation*

The signal detected by the sequence described until now is an average over the entire sample and needs to be localised to a specific part of the anatomy. This is done by changing the *magnitude* of $\vec{B}_0$ (applying *magnetic field gradients*) along the three principal axes. Since the Larmor frequency (Equation (3.5)) of the spins depends on $\vec{B}_0$, the spins now precess at different frequency depending on their position and the signal from a particular location in the body can be detected with a read-out coil of frequency

$$\omega(\boldsymbol{r}) = \gamma_p(\boldsymbol{B_0} + \boldsymbol{r} \cdot \boldsymbol{G}(\boldsymbol{r})) \,, \tag{3.6}$$

where $\boldsymbol{G} = \frac{dB_z}{dx}i + \frac{dB_z}{dy}j + \frac{dB_z}{dz}k$ represents the gradients applied to modify $\boldsymbol{B}_0$ along the three principal axes. Thus by applying gradients of known magnitude, the resonant frequency of the spins becomes a *spatial label*.

The application of gradients is done in three steps, slice selection, frequency encoding and phase encoding, to image a 3D object or subject.

For slice selection, a gradient in the z-direction is applied, at the same time as the excitation RF pulse. RF pulse will only excite the spins in a specific cross-sectional "slice" which has the resonant frequency within its bandwidth.

The image encoding, i.e. excitation of a specific pixel in the selected slice is then done by applying a frequency encoding gradient in the x-direction and a phase encoding gradient in the y-direction, during the *read out* part of the sequence, i.e. when the MR signal is detected (Figure 3.4). The frequency encoding gradient, G_x makes the oscillation frequency of the spins, linearly dependent on their position along the x-axis. Usually, the phase encoding is done by applying G_y for short time intervals, between the excitation and read-out.

The measured signal in an MRI experiment is complex as it has a phase and magnitude and it is acquired in the *k-space*, which is the Fourier transform of the image space. To reconstruct a 2D image (each excited slice), the k-space is sampled by manipulating the frequency and phase encoding gradients, which represent the x and y coordinates of the k-space. This is generally done line-by-line, where a short G_y gets the spins in each y-location to precess with a certain frequency and a continuous G_x makes these spins precess at a frequency dependent on their location along the x-axis. The signal is acquired at specific intervals during the application of the G_x, so for the same excitation

a single line in the k-space is sampled. For the next k-space line, the same sequence is repeated, but with a G_y of different magnitude. This sequence is not ideal due to the time it takes, so signal decay (relaxation) and subject motion result in lower SNR and distortions of acquired images. For faster acqusition, specifically for DW-MRI, an *echo-planar imaging (EPI)* sequence is used. In EPI, the whole of an excited slice is sample together, by applying successive G_y and G_x of successive opposite polarity to sample the whole k-space, as shown in Figure 3.4.

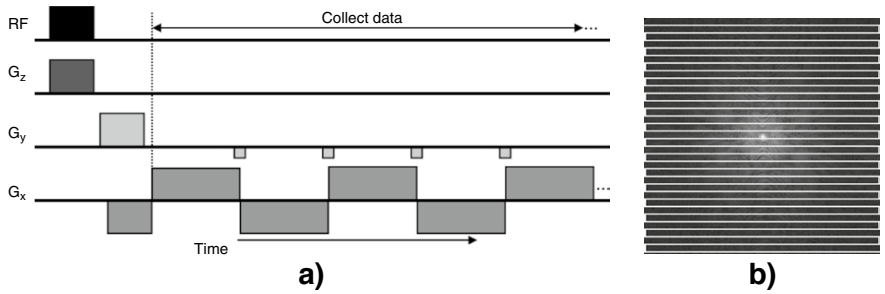

Figure 3.4: Illustration of the echo planar imaging (EPI) MRI pulse sequence (a) and the corresponding data collection trajectory (b). In the EPI pulse sequence the frequency encoding gradient is oscillated and multiple lines of k-space (b) are measured per shot. G_z, G_y and G_x are the slice, phase and read gradients, for signal localisation, as described in the main text. *Illustration adapted from Pipe 2009.*

The complex signal acquired in MRI is affected by noise from several sources, including thermal fluctuations in the hardware. *Signal-to-noise ratio (SNR)* is a measure of the signal quality, which is the ratio of the signal and the standard deviation of the noise. In MRI signal, the SNR depends on the voxel sizes, the number of signal averages, the bandwidth of the signal readout (i.e. thickness of the excited slice) and the number of the k-space sampled in the three dimensions[130].

3.2.6 *Tissue based contrast*

As the spins excited by the oscillating magnetic fields, return to their equilibrium energy states, the signal detected decays according to specific time constants, which depend on the chemical and structural makeup of the surrounding tissue. This tissue-specific response of the spins' magnetisation is termed relaxation. The relaxation time constants are the source of contrast in the MR images, as they vary for different tissues, as well as pathology, and by manipulating the time between the application of pulses, specific contrast can

be achieved, as shown in Figure 3.5. T_1 and T_2 are typically used in brain imaging as sources of contrast and the acquired images are termed T_1-weighted and T_2-weighted MRIs, respectively.

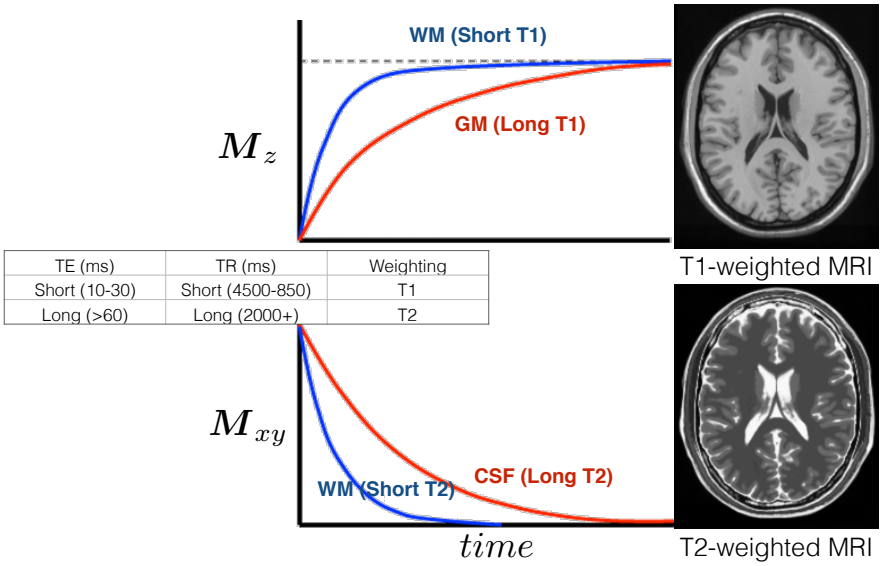

Figure 3.5: Figure illustrating that the values of TE and TR determine how much the signal decays, which results in a T_1 or T_2 weighted signal. The TE and TR values also impact the singal-to-noise ratio (SNR) and a balance needs to be obtained to get good quality signal with suffucient relevant contrast. The typical TE and TR values for spin-echo sequence are also shown.

T_1, the spin-lattice relaxation (or longitudinal recovery) time, is the time taken for the longitudinal component of the magnetization, $M_z(t)$ to recover. The energy, initially absorbed due to the application of the excitation pulse, is released to the lattice surrounding the system of spins (resulting in an increase in sample temperature). $M_z(t)$ recovers its equilibrium position and the magnitude is given by solving the Bloch equations, updated with the effect of relaxation (Appendix A.2, Equation (A.5))

$$M_z(t) = M_0 \left[1 - \exp\left(\frac{-t}{T_1}\right)\right] . \tag{3.7}$$

The T_2 is the spin-spin (or transverse) relaxation time, which describes the de-phasing of the individual spins, as they interact with each other and experience slightly different magnetic environments[3]. The spins precessing at

3 In real systems additional dephasing of spins is caused by $\boldsymbol{B}_0$ inhomogeneities and differences in magnetic susceptibility between tissues, adding static field variations. So the transverse magnetization decays according to: $\frac{1}{T_{2*}} = \frac{1}{T_2} + \frac{1}{T_2'}$

slightly different frequencies result in the decay of the transverse component of the magnetization, $M_{xy}(t)$, which has time dependent behavious as follows:

$$M_{xy}(t) = M_0 \left[\exp\left(\frac{-t}{T_2}\right) \right] . \tag{3.8}$$

3.2.7 *Diffusion sensitisation and acquisition*

MRI can be sensitised to the self-diffusion of water particles, by application of magnetic field gradients, as recognised by Hahn[75], who was the first to note the sensitivity of MRI signal to molecular diffusion. These gradients, termed *diffusion encoding* or *diffusion sensitising* gradients, are applied before the image encoding of an MRI acquisition (Section 3.2.5).

The most commonly used DW-MRI sequence is the *pulsed gradient spin echo (PGSE)* proposed by *Stejskal and Tanner*[150], shown in Figure 3.6, which incudes two diffusion encoding gradients applied around the 180° pulse in the SE sequence. These gradients have magnitude $|\boldsymbol{G}|$, are applied for a duration of δ and have time separation Δ between them.

In PGSE sequence, the 90° pulse is applied at time $t = 0$ (Figure 3.6), and affects the spins, as described in Section 3.2.3. The phase accumulated by spins in the presence of an external magnetic field, at a time t after the application of the 90° pulse, in a SE sequence, is $\phi(t) = \omega_0 t = \gamma \boldsymbol{B}(t)t$. When the external magnetic field is spatially changing (i.e. magnetic field gradients are applied), the angular frequency varies spatially. If this magnetic field gradient, $\boldsymbol{G}$, is applied for a duration δ, a short time t_1 after the 90^0 pulse the phase accumulated by the spins becomes dependent on the position of the spins, and can be measured as an integral over the time the gradient pulse is applied. So the principle of diffusion encoding is similar to that of spatial encoding, described in Section 3.2.5.

A time τ after the 90° pulse, the phase accrued by the i^{th} spin is given by:

$$\phi_i(\tau) = \gamma \boldsymbol{B}_0 \tau + \gamma \boldsymbol{G} \cdot \int_{t_1}^{t_1+\delta} \boldsymbol{r}_i(t)dt . \tag{3.9}$$

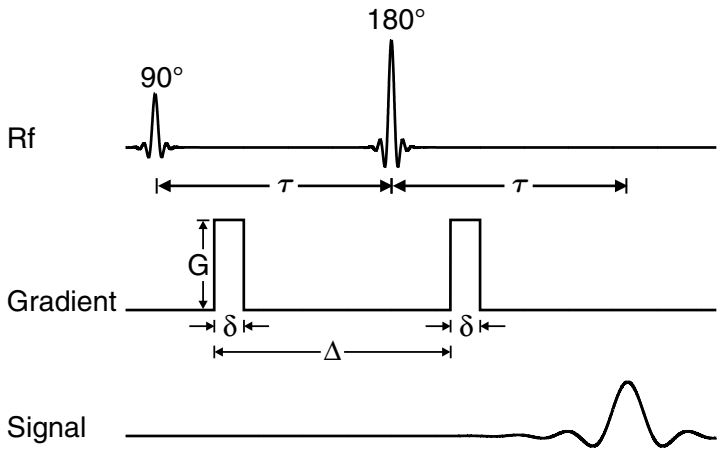

Figure 3.6: Schematic of spin echo experiment in the presence of a pulsed field gradient, as proposed by Stejskal and Tanner. This sequence is also referred to as the pulsed gradient spin echo sequence and is used to sensitise an MRI acquisition to the diffusion of spins, as explained in the main text. *Image adapted from Basser and Ozarslan 2009*

Here the $\cdot$ represents a dot product between $\boldsymbol{G}$ and $\boldsymbol{r}$ The 180^o pulse is then applied at time τ after the excitation pulse, which reverses the phase of the spins. The total phase shift of a particle i after time 2τ is then given by:

$$\begin{aligned}\phi_i(2\tau) &= \left(\gamma B_0 \tau + \gamma \boldsymbol{G} \cdot \int_{t_1}^{t_1+\delta} \boldsymbol{r}_i(t)\,dt\right) - \left(\gamma B_0 \tau + \gamma \boldsymbol{G} \cdot \int_{t_1+\Delta}^{t_1+\Delta+\delta} \boldsymbol{r}_i(t)\,dt\right) \\ &= \gamma \boldsymbol{G} \cdot \left(\int_{t_1}^{t_1+\delta} \boldsymbol{r}_i(t)\,dt - \int_{t_1+\Delta}^{t_1+\Delta+\delta} \boldsymbol{r}_i(t)\,dt\right)\end{aligned} \tag{3.10}$$

Here the effect of the static field gets cancelled out and the phase accrued by a spin is due to that acquired during the application of the two pulse gradients. So for a spin that is stationary throughout the PGSE sequence, the total phase cancels out, but when the spin is not stationary it accumulates a net phase (Equation (3.10)).

Thus for non-diffusing spins, the phase is cancelled due to the *equal duration and magnitude gradient pulses*, and the spins refocus at the TE, as in a typical SE sequence. But if the spin is diffusing, the phase accrued during the first gradient pulse is not the same as that during the second and the phase is not cancelled.

So the signal measured at the end of the PGSE sequence, in presence of diffusion is *attenuated* due to the phase differences between the spins, as illustrated in Figure 3.7. The degree of this dephasing, or *phase dispersion*, is proportional

to the displacement of spins during $\boldsymbol{\Delta}$ in the direction of $\boldsymbol{G}$ and the strength of the gradient applied, i.e.$|\boldsymbol{G}|$.

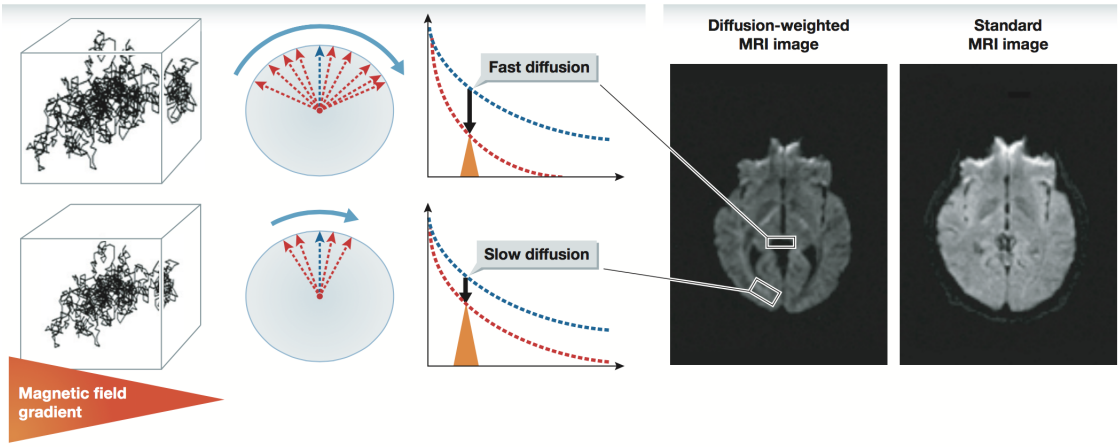

Figure 3.7: A schematic representation of how the PGSE sequence measures the diffusion of water molecules. Two types of samples are shown, one with a lower level of hindrance (top) than the other (bottom). Initially, all the spins within each sample are in-phase. When a PGSE sequence is applied, the spins dephase, according to the level of diffusion in the direction of the applied gradient field. So the level of dephasing is higher for the top sample than the bottom, which the source of contrast in DW-MRI, as shown by the images on the right. *Illustration adapted from Le Bihan 2014*.

The net phase accrued by a diffusing spin according to Equation (3.10) is $\phi_i(2\tau) = \gamma\delta\boldsymbol{G}\cdot(\boldsymbol{r}_0 - \boldsymbol{r}_1) = \boldsymbol{q}\cdot\boldsymbol{x}$, where $\boldsymbol{q} = \gamma\delta\boldsymbol{G}$ is the wavevector, and the magnetic moment of the spin is $Me^{(i\boldsymbol{q}\cdot\boldsymbol{x})}$. Here M is the magnitude of this magnetic moment. This exponential decay due to the phase accumulated is the source of signal in a DW-MRI acquisition, but since the detected signal is from an ensemble of spins, this signal is integrated over all the spins in an imaging voxel and weighted by the probability for a spin to begin at r_0 and move to r_1. So the signal measured at $t = TE$ is

$$A(\boldsymbol{q}) = A(0)\int P(\boldsymbol{x}, t)\exp(-i\boldsymbol{q}\cdot\boldsymbol{x})d\boldsymbol{x}\,, \tag{3.11}$$

where $A(0)$ is the signal without diffusion-weighting and $P(\boldsymbol{x}, t)$ the conditional probability defined in Section 3.2.1, quantifying the probability of particle displacement. So the DW-MRI signal is sampled in the *q-space*, the Fourier transform of which gives the images. This equation is derived from the *Bloch-Torrey* equation[165], which incorporates the diffusion in the standard Bloch equations (Appendix A.2).

In DW-MRI the tunable parameters for the acqusition, $|\boldsymbol{G}|$, Δ, δ are typically combined to give a *diffusion weighting* factor

$$b = \gamma^2 |\boldsymbol{G}|^2 \delta^2 \left(\Delta - \frac{\delta}{3} \right) , \tag{3.12}$$

and it quantifies the sensitivity of the DW-MRI acquisition to the diffusion of particles. This factor is also called the *b-value* and is generally used to describe a specific acquisition, as it contains all the experimentally variable parameters for DW-MRI data. Here $T_d = \left(\Delta - \frac{\delta}{3}\right)$ is the diffusion time which dictates the length scale probed by the diffusion experiment. In free diffusion, the root mean squared displacement of particles over T_d is $\langle \boldsymbol{r} \rangle = 6\boldsymbol{D}T_d$, from Equation (3.3).

For Gaussian diffusion (Section 3.2.1.1) the measured DW-MRI signal is

$$A(\boldsymbol{q}) = A(0) \exp\left(-\boldsymbol{q}^T \boldsymbol{D} \boldsymbol{q} T_d \right) , \tag{3.13}$$

from Equations (3.11) and (3.4).

In a space confined by restricting geometry, the diffusion of particles is a function of the diffusion time, diffusion coefficient and the characteristics (shape, size, orientation distribution etc) of the geometry[131]. Thus the effects of these boundaries must be taken into account, and any estimation made with the Gaussian assumption will not measure the true diffusion characteristics.

In practical DW-MRI, the aim is to recover the probability profile, $P(\boldsymbol{x}, t)$ or its characteristics, or that of the geometries surrounding the diffusing particles, from the acquired signal, $A(\boldsymbol{q})$. For this, assumptions need to be made about the diffusion of particles during the application of the diffusion sensitising gradients. Two common assumptions used are the *short gradient pulse (SGP)* and the *Gaussian phase distribution (GPD)*[121]. In the SGP approximations, it is assumed that no diffusion occurs during the application of the pulses, i.e. $\delta << \Delta$, but this is not attainable in practice, especially with the need to have higher δ for higher diffusion weighting. The GPD assumption accounts for the non-negligible pulse duration of the diffusion sensitising gradients applied. In GPD, it is assumed that the displacment of the spins over time, $\boldsymbol{x}(t)$, and thus their phases, $\phi(t)$, have Gaussian distribution, with variance dependent on the time they are allowed to diffuse[121,151].

Equation (3.13) for free diffusion, holds true for both the SGP and GPD assumptions, but for restricted diffusion, which is not Gaussian, the two approximations give very different forms of $A(\boldsymbol{q})$.

In microstrucutre imaging, the aim is to quantify the microstrucure, based on the diffusion profiles measured by DW-MRI. But the estimation of the $P(\boldsymbol{r}_0|\boldsymbol{r}_1, t)$ from measured diffusion signal is very complicated and several attempts have been made to calculate the diffusion signal in restricted environment[121,131]. Increasingly, the $P(\boldsymbol{r}_0|\boldsymbol{r}_1, t)$ is estimated by modelling, i.e. making various assumptions about the geometry of the surrounding microstructure and the resulting distributions, as discussed in the next chapter.

4

MICROSTRUCTURE IMAGING

Microstructure imaging is a field in neuroscience which aims to obtain indices similar to those derived from traditional histological analysis, using non-invasive and *in vivo* imaging techniques. In DW-MRI this is done using mathematical models that relate the acquired diffusion measurements to the microscopic features of the tissue, providing estimates of histological features of interest. Due to its diffusion-dependant contrast, which reflects the geometry of the underlying microstructure, DW-MRI has been widely used in neuroimaging studies, which has led to exciting developments being made in the field of microstructure imaging.

In this chapter, we introduce the various modelling techniques, based on DW-MRI that are utilised in neuroscience to infer the characteristics of the tissue being imaged. We first give an overview of the various modelling methods of DW-MRI, which includes a) modelling the measured signal to estimate the diffusion profile and b) modelling the microstructure to estimate specific features of microscopic geometry. The focus of this thesis is microstructure imaging with standard clinical imaging, so we give an overview of the relevant microstructure imaging techniques, as well as the current standard in DW-MRI called the DTI. We also describe the framework for estimating parameters of interest from modelling in DW-MRI, as the proposed model in this thesis is based on the same principals.

4.1 DIFFUSION AS A MARKER OF BRAIN MICROSTRUCTURE

The neural tissue in the brain has a characteristic structure which dictates the diffusion profile (the probability $P(\boldsymbol{r}_0|\boldsymbol{r}_1, t)$ defined in Section 3.2.1) of water molecules around them. Due to the longitudinal geometry of neurites, they restrict the diffusion of water inside them hugely in the direction perpendicular to and only hinder it in the direction parallel to their orientation. This

results in a highly restricted and anisotropic displacement profile of water, as seen in Figure 3.1. This restriction is particularly pronounced for axons due to the myelin sheath surrounding them which are impermeable over typical diffusion times employed in DW-MRI[5]. The diffusion pattern in the space surrounding the neurites in the tissue is hindered, as it is a continuous space with cellular structures present. In this extra-neurite space, water molecules exhibit a Gaussian diffusion profile[122], which may be isotropic or anisotropic, depending on the distribution of the neurites (Figure 3.1). The space outside the brain tissue consists of CSF which poses no restriction to the water molecules, resulting in a free diffusion profile as shown in Figure 3.1. The mean path length of the molecules diffusing in the extra-neurite space is much less than those in CSF, due to various barriers present and this can be seen in their displacement profiles.

The overall diffusion of water in biological tissue thus is very complex as it is influenced by a variety of factors. So the diffusion in neural tissue can not be fully characterised by a simple Gaussian, but rather a combination of the various contributions to the measured diffusion signal[149]. The aim of modelling in DW-MRI is to extract useful features of the underlying tissue, in terms of the displacement of water and their geometry. There are two types of models generally used with DW-MRI data in neuroimaging, one where the measured signal is modelled and the second where the underlying microstructure is modelled. But, the underlying principals of extracting parameters of interest from these models are the same, as discussed in the following section.

4.2 DIFFUSION-WEIGHTED MRI MODELLING

Modelling in DW-MRI involves mathematical expressions, described with respect to certain parameters of interest, which are estimated from the measured data. The main components required for estimation of these parameters, the model fitting procedure, are an analytical model to define the relationship between the measured data and the parameters of interest, a set of measurements, an acquisition protocol to acquire these measurements, a noise model to account for the measurement noise in the data and a model fitting algorithm to obtain the best set of parameters that describe the data.

In the following sections, we describe these components in detail, using the Ball-Stick[24] model as an example of a simple model of DW-MRI. We use the DW-MRI data acquired in Zhang et al. 2012, which is acquired on a typical 3T clinical scanner, on a healthy adult male.

4.2.1 *Fitting model*

The fitting model is the mathematical model that relates the DW-MRI signal to the parameters of interest. These *model parameters*, $\boldsymbol{x} = (x_1, .., x_N)^T$, may describe the signal itself or specific features of the microstructure. Usually *metrics* or *indices* are derived from these model parameters, which are more relevant to the particular application. The fitting model is based on some prior belief about the substrate in terms of the expected diffusion profile or the microstructure and their geometry.

A good fitting model must include all the key characteristics that affect the measured signal, so the parameters can be estimated with high confidence. A fitting model is constructed by including the key features of interest, making the assumptions necessary to estimate these features in terms of the model parameters. These assumptions relate to a) the sources of DW-MRI that are accounted for in the model, b) the diffusion properties and c) the geometric features of the substrate of interest. Such assumptions are necessary to make meaningful inferences from the acquired data, which cannot be rich enough to characterise the complexity of neural tissue, due to many practical limitations (see Section 4.2.2).

Ball-Stick model is constructed to estimate the fibre structure in each of the voxels of DW-MRI data. So the model includes only two compartments, one to account for the restrictive and orientationally varying axons (*intra-axonal*) and other for everything else (*extra-axonal*). The Ball-Stick model has the form

$$A = A(0)\left(f\exp\left(-bd(\hat{\boldsymbol{n}}\cdot\hat{\boldsymbol{g}})^2\right) + (1-f)\exp\left(-bd\right)\right), \tag{4.1}$$

where f is the weighting of the signal from the sticks or the *volume fraction* of the intra-axonal compartment, $\hat{\boldsymbol{n}}$ is the fibre direction, d the intrinsic diffusivity of the medium and b the diffusion weighting.

The model parameters of Ball-Stick that are estimated include

- f - volume fraction of the intra-axonal compartment
- d - intrinsic diffusivity in both the compartments
- θ - the elevation angle of $\hat{\boldsymbol{n}}$
- ϕ - the azimuth angle of $\hat{\boldsymbol{n}}$

The index derived from these model parameters for Ball-Sticks is the fibre orientation, $\hat{\boldsymbol{n}}$.

The main assumptions in this model include non-exchanging compartments, Gaussian diffusion of equal magnitude (d) in both compartments, the same relaxation properties of the two compartments and modelling axons as a cylinder with zero radii in each voxel. The assumptions made must be evaluated to test how they impact the parameter estimation, as done for Ball-Stick in Behrens et al. 2003. To relax the assumptions made usually requires data with a rich acquisition which is not feasible in practice, so most models of DW-MRI have several assumptions even on the simplified fitting models.

4.2.2 *Acquisition protocol*

The acquisition protocol gives rise to a specific signal, based on the set of acquisition parameters, $\boldsymbol{y} = (y_1, .., y_M)^T$, that are selected for the MRI scanner. This gives the set of measurements $\boldsymbol{A} = (A(\boldsymbol{y}_1), ..., A(\boldsymbol{y}_K))^T$.

DW-MRI is a very rich imaging modality as its acquisition parameters, Δ, δ, $\hat{\boldsymbol{G}}$ and $|\boldsymbol{G}|$ can be varied used to probe a range of diffusion times ($\Delta - \delta/3$) and the orientation preference of the diffusion. But it is very important to have an optimal set of acquisitions, as it allows to obtain the best signal to probe the various features of interest. A method to obtain the optimal sampling scheme, given certain imaging constraints, is presented in Alexander 2008. For *in vivo* human imaging, these constraints include short acquisition time, power and safety (limit on $|\boldsymbol{G}_{max}|$) and applicability to arbitrary fibre orientations. To enable modelling of arbitrarily orientated microstructure, the *High Angular Resolution Diffusion Imaging (HARDI)*[168] acquisitions are widely used, which aim to sample the q-space as densely as possible, at multiple b-values. An example of a HARDI style acquisition is shown in Figure 4.1.

For our example of Ball-Stick model, we use a protocol with $b = 1000 s/mm^2$, acquired for 30 $\hat{\boldsymbol{G}}$ that are uniformly distributed on a sphere (subset of data acquired in Zhang et al. 2011). In addition, the acquisition also consists of 6 samples without diffusion weighting (i.e. $b = 0 s/mm^2$, which are also referred to as b0 measurements), to account for signal attenuation due to relaxation (i.e. estimate $A(0)$ in Equation (4.1)). The acquired $\hat{\boldsymbol{G}}$ of the acquisition protocol are shown in Figure 4.1 (left).

4.2.3 *Noise model*

Noise in a model is the contribution to the measured signal that can not be explained by the model. In DW-MRI data, this includes noise and artifacts from the acquisition itself but also any real effects not accounted for in the model (i.e. the assumptions made on diffusion or geometric processes). A noise model describes the random contributions to the measured signal.

The acquired MRI data is complex (Section 3.2.5), but typically only the magnitude of the signal is used. This results in the MRI data having Rician noise[73,76]

$$p(\tilde{A}) = \frac{\tilde{A}}{\sigma^2} I_0\left(\frac{A\tilde{A}}{\sigma^2}\right) \exp\left(-\frac{A^2+\tilde{A}^2}{2\sigma^2}\right), \tag{4.2}$$

which is the magnitude of Gaussian noise in the complex and real parts of the signal. Here I_0 is the zeroth order modified Bessel function of the first kind and σ is the standard deviation of the noise of the complex DW-MRI signal. When the SNR is sufficiently high, the Rician noise approximately equals Gaussian. It has been shown that the Rician noise is almost indistinguishable from Gaussian noise, for SNR as low as 5[73].

A noise model is required for the model fitting procedure to get model parameters while accounting for noise in the measured signal. The noise model, characterised in terms of its variance, σ may also be included as parameters to be estimated from the measured data.

In the data used here, there are 6 b0 acquisitions, and the SNR is computed as the mean of these measurements, over their standard deviation (σ). For a single voxel, corresponding to the CC, this gives an SNR $= 23$ (σ= 0.0424), so the noise variability in this data can be assumed to be Gaussian.

4.2.4 *Fitting algorithm*

The model fitting algorithm is used to obtain the set of model parameters that best explain the observed DW-MRI data. The estimated $\boldsymbol{x}$ are obtained based on an *objective fucntion* ($f(\boldsymbol{x})$), which gives an estimate of the difference/distance between the actual measurements and those predicted by the model.

For linear fitting models, $\boldsymbol{x}$ can be estimated by solving $\boldsymbol{A} = G\boldsymbol{x}$, where G is the design matrix, describing the acquisition protocol. Here $f(\boldsymbol{x})$ gives an

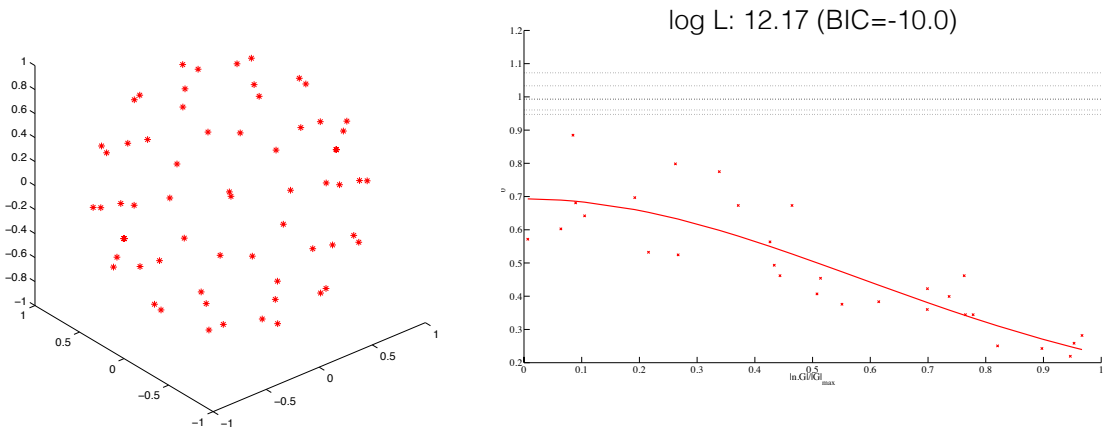

Figure 4.1: Model fitting for the Ball-Stick model, for a voxel in the CC. The acquired $\hat{\boldsymbol{G}}$ are shown as points on a sphere on the left and the acquired DW-MRI data shown on the right (points), with the signal estimated by the model fitting (sold line). The normalised signal (here shown as S/S_0) is plotted against $|n.G|/|G|_{max}$, so from left to right, the $\hat{\boldsymbol{G}}$ is becoming more and more parallel to $\hat{\boldsymbol{n}}$.

estimate of the residuals, i.e. the difference between the predicted signal and the actual measurement.

Given a specific noise model, the optimised parameters, $\tilde{\boldsymbol{x}}$ are found such that the *likelihood* of the measured data is maximised

$$\tilde{\boldsymbol{x}} = \arg\max_{\boldsymbol{x}} L(\boldsymbol{A}|x) \ . \tag{4.3}$$

Here $L(\boldsymbol{A}|x)$ represents the likelihood of the observed data given the set or model parameters, $\boldsymbol{x}$. $\tilde{\boldsymbol{x}}$ are called the *maximum likelihood estimates (MLE)*. $L(\boldsymbol{A}|x)$ has the form of sum of sqaured errors, when the noise is assumed to be independently and identically distibuted Gaussian

$$L_G \propto \sum_{k=1}^{K} \left(A_k - \tilde{A}_k(\boldsymbol{x}, \boldsymbol{y}_k)\right)^2 \ . \tag{4.4}$$

Here K is the number of measurements made, each with unique acquisition parameter sets $\boldsymbol{y}_k$, A_k the true, noise free signal, which when measured has an associated standard deviation of σ_k. $\tilde{A}(\boldsymbol{x}, \boldsymbol{y}_k)$ is the signal predicted from the fitting model, with the model parameters $\boldsymbol{x}$.

For DW-MRI data, the measurement noise is Rician distributed, which gives an alternate form of $L(\boldsymbol{A}|x)$

$$L_R \propto \sum_{k=1}^{K} -2\log\sigma_k + \log I_0\left(\frac{A_k\tilde{A}_k}{\sigma_k^2}\right) + \log A_k - \frac{{A_k}^2 + \tilde{A}_k^2}{2\sigma_k^2} \,. \tag{4.5}$$

Note that in both the Equations (4.4) and (4.5), we have dropped the constant terms and the scaling factors from the equations, as they do not affect the location of the maximum.

If the model parameters are not linearly related to the acquired measurements and are being inferred from the measured DW-MRI data, an iterative optimisation procedure is required, as explained below.

4.2.4.1 *Optimisation algorithm*

The optimisation procedure aims to find the set of model parameters, which best predict the measured data, given the mathematical model. For DW-MRI many combinations of specific microstructure features can give rise to the same signal and it is not possible to acquire data rich enough to be sensitive to all the microstructure features, given the assumptions made. So a nonlinear model fitting procedure is required to obtain indices of the microstructure.

To find the *MLE*, $\tilde{\boldsymbol{x}}$ for the data, an optimisation algorithm is required, which dictates how the parameter space is sampled. They iteratively improve the parameter estimates, until convergence ($\Delta f(\tilde{\boldsymbol{x}}) = 0$). This involves either following the gradient (gradient descent) or the Hessian matrix (Newton method) of $f(\tilde{\boldsymbol{x}})$. The Hessian method is usually better at finding the global minima than using the gradient and can be made less computationally expensive by estimating the Hessian from the Jacobian matrix (Gauss-Newton method).

A typically used optimisation algorithm for solving Equation (4.3) for DW-MRI data is *Levenberg–Marquardt (LM) algorithm*, which is a deterministic optimisation technique, which combines the gradient descent and the Gauss-Newton methods, to give a robust estimation of $\tilde{\boldsymbol{x}}$.

We fit the Ball-Stick model to a single voxel, corresponding to the CC. The corresponding signal is shown as the data points in Figure 4.1 (right). We fit for all the model parameters, using a two-stage fitting algorithm, used in Zhang et al. 2012, where a combination of typical *in vivo* parameter values are used to initialise the search for the MLE. The set of parameters with the highest

probability (highest L_G) from these are then used to find the $\tilde{\boldsymbol{x}}$, using non-linear optimisation.

For the data to fit the Ball-Stick, the set of initial parameter values used are all combinations of $f = [0, 0.25, 0.5, 0.75, 1]$, $d = [1.3, 1.7, 2.1] \times 10^{-9} m^2/s$, which represent a range of typical *in vivo* parameters. The value of $\hat{\boldsymbol{n}}$ is initialised from a DT fit. The set of parameters that best fits the data, determined to be the one with the highest objective function value in Equation (4.4), is $f = 0.5$ and $d = 1.3 \times 10^{-9} m^2/s$. This set of parameters are then used to carry out non-linear optimimisation to find the final set of MLE, using the LM algorithm[1]. This gives $\tilde{\boldsymbol{x}}$: $f = 0.60$, $d = 1.49 \times 10^{-9} m^2/s$, $\theta = 1.18^c$ and $\phi = 2.87^c$ ($\hat{\boldsymbol{n}} = [-0.89, 0.25, 0.38]^T$), which are plausible values in the CC.

The model fitting procedure, for nonlinear optimisation of parameters, is summarised in Figure 4.2.

4.2.5 *Model comparison*

The aim of model comparison to determine the simplest model that explains a given data set. This is done by accounting for the *goodness of fit*, quantified as $f(\boldsymbol{x})$, and the number of parameters that are estimated by the model. A model that is too simple will produce less accurate estimates, but one that is too complex is likely to *over-fit* the data and produce variable results.

Given $\hat{L}(\boldsymbol{A}|\tilde{\boldsymbol{x}})$, the maximum likelihood function, i.e. the solution of Equation (4.3), the Bayesian information criterion (BIC)[140] is defined as

$$BIC = -2\log(\hat{L}(\boldsymbol{A}|\tilde{\boldsymbol{x}})) + K\log(N)\ , \tag{4.6}$$

where K is the number of parameters of the model and N the number of independent and identically distributed measurements. A lower value of BIC reflects a more predictive model. An alternative model comparison metric is the Akaike information criterion (AIC).

$$AIC = -2\log(\hat{L}(\boldsymbol{A}|\tilde{\boldsymbol{x}})) + 2K\ . \tag{4.7}$$

BIC penalises for model complexity more than the AIC (second term in both equations), so is more appropriate as a metric for our purposes, as we

1 using Matlab 2013a inbuilt function: *fmincon*

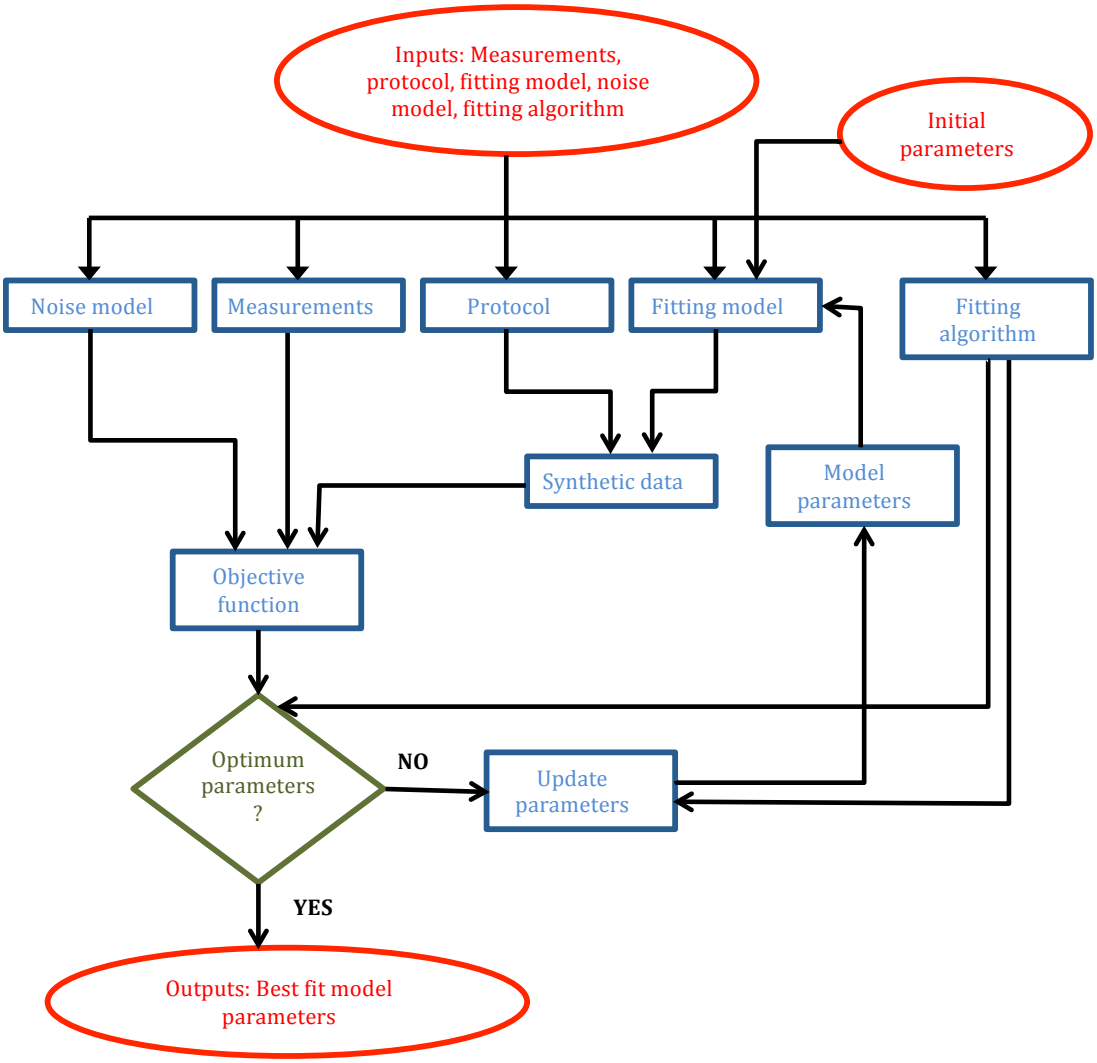

Figure 4.2: Overview of a nonlinear fitting procedure, which requires an iterative procedure to estimate the model parameters from the measurements. The procedure is initialised by a set of $\boldsymbol{x}$ which are used to synthesize the data. Data synthesis requires a set of model parameters, the fitting model, and the acquisition protocol. The objective function is computed for the synthetic signal, $\tilde{A}$, computed for the current set of model parameters and the measured signal, A, given the noise model. If the objective function is *optimal*, the current set of parameters are the optimised ones, but if not optimal, $\boldsymbol{x}$ are updated according to the fitting algorithm, and the process iterated until the optimal set, $\tilde{\boldsymbol{x}}$ are obtained. The decision of whether the objective function is optimal or not depends on the optimisation algorithm being used.

want the simplest model that fits the acquired data the best. Note that since the constant terms have been dropped in Equations (4.4) and (4.5), the precise values of the model comparison terms here would be different in magnitude to when these terms are included.

A framework to select the most appropriate model for a given substrate is presented in Panagiotaki et al. 2012, which ranks multi-compartment models formulated by various combinations of the geometric models in Figure 4.3, according to the quality of fit for the fibres in the WM. The original work presents the framework in *ex vivo* rat brain and shows that three-compartment models, designed for intra/extra-axonal diffusion, best explain multi-shell DW-MRI data. This is subsequently verified for *in vivo* human imaging for the CC in the WM[62] and for orientationally dispersed fibres in Ferizi et al. 2013b.

4.3 MODELS OF DIFFUSION-WEIGHTED MRI

In the following sections, we give a review of the main modelling techniques in DW-MRI, but the focus of the thesis is microstructure imaging, so we only discuss the more widely used approaches for diffusion modelling and the *biophysical models* most relevant to our work.

4.3.1 *Diffusion signal models*

These aim to capture the signal or diffusion characteristics, but not specific microstructure parameters from the DW-MRI data. In this type of models, the diffusion propagator is estimated, which is a characteristic of the underlying microstructure. This can help to make inferences about the microstructure in terms of their diffusion properties, e.g. the density of the tissue through the level of diffusivity or the number of fibre populations, through the profile of the estimated diffusion propagator in spherical space (also known as the *diffusion orientation distribution function (dODF)*).

4.3.1.1 *Gaussian models*

The simplest model of diffusion signal is the *apparent diffusion coefficient (ADC)*, which is based on the assumption of free diffusion in an isotropic, homogeneous environment (with PDF as in Equation (3.2)). This gives a diffusion signal which is mono-exponential and is characterised by a scalar diffusivity ($\boldsymbol{D} = \mathrm{diag}(\mathrm{ADC}, 0, 0)$ in Equation 3.14, i.e. $\mathrm{ADC} = -\frac{\log(A/A_0)}{b}$, with DW-MRI

signal A and non-diffusion weighted signal, A_0. ADC has been widely used in cancer applications[181], but is not an appropriate model for highly anisotropic substrates like the neurites.

Diffusion Tensor Imaging (DTI), introduced by Basser et al. 1994 is the most widely used DW-MRI technique in neuroscience. The main reason for the success of DTI is its simplicity which allows it to be applied within clinical imaging limitations (e.g. time and hardware available), as well as its ability to detect abnormalities in various neural disorders. In DTI a diffusion tensor, $\boldsymbol{D}$, as defined in Section 3.2.1.1 is used, which has six independent terms to describe the diffusion in the 3-dimensional space

$$\boldsymbol{D} = \begin{pmatrix} D_{xx} & D_{xy} & D_{xz} \\ D_{xy} & D_{yy} & D_{yz} \\ D_{xz} & D_{yz} & D_{zz} \end{pmatrix} . \tag{4.8}$$

So DTI assumes Gaussian diffusion where the displacements over time are not the same in all directions. Since $\boldsymbol{D}$ represents the diffusion along particular orientations, positive definitiveness of the tensor ensures that the value is consistent with the physical meaning of diffusivity. The corresponding PDF for $\boldsymbol{D}$ has the form in Equation (3.4) and the diffusion signal has the form of Equation 3.13. The diffusion tensor can be computed experimentally, by sampling the diffusion profile at *at least* six linearly independent directions and an acquisition with no diffusion weighting. For robust estimation of the parameters, in practice about $20-30$ isotropically distributed gradient orientations are sampled[91].

As it is the current clinical standard, we describe the indices of DTI and their clinical utility in detail in Section 4.4.1. The ADC and DTI models are simple and robust, but can only account for a single fibre population and assume Gaussian diffusion. In the next section, we look at some techniques to address these issues.

4.3.1.2 *Non-Gaussian diffusion models*

Diffusion in neural tissue is non-Gaussian (Section 4.1) and the DW-MRI signal departs from a monoexponential decay[149]. Diffusion kurtosis imaging (DKI)[84] was developed to quantify the departure of the diffusion signal from Gaussian, but as it quantifies higher order terms of the diffusion signal, the

estimates are not as robust as DTI but are shown to be correlated to features of the microstructure.

A bi-exponential model can also quantify non-Gaussian diffusion by accounting for two non-exchanging pools with slow and fast diffusion[39].

4.3.1.3 *Multiple fibre models*

Multiple fibre populations are known to exist in a single voxel of the DW-MRI, which may not be orientationally coherent. Advances in DW-MRI acquisition, particularly *High Angular Resolution Diffusion Imaging (HARDI)*[168], have enabled the estimation of dODF (i.e. orientation dependence of $P(\boldsymbol{r}_0|\boldsymbol{r}_1, t)$). There are several techniques that aim to resolve a discrete number of fibre populations (see Seunarine and Alexander 2009 for an overview). Non-parametric techniques like diffusion spectrum imaging[176] and Q-ball imaging[175] use the q-space to estimate the dODF.

Spherical deconvolution methods[166] on the other hand aim to estimate the actual orientation distribution of the fibres by deconvolution of the spherical diffusion signal to get an estimate of the fibre ODF (fODF). The spherical DW-MRI signal is modelled to arise from the convolution of the signal from a single fibre and their orientation distribution in space, assuming each fibre has an identical diffusion profile. This is different from the modelling of ODF from biophysical models (Section 4.3.2), as the specific features of the microstructure are not directly estimated.

These diffusion models provide useful parameters that can capture the trends of interest like the progression of a disease but do not directly correspond to features of the microstructure, which biophysical models described below can.

4.3.2 *Biophysical models*

Biophysical models involve explicit modelling of the features of the microstructure that are important for diagnosis and prognosis of various brain diseases and disorders. The expressions relating the DW-MRI signal to geometry specific parameters form the basis of microstructure imaging. In these models, a mathematical model representing the underlying microstructures is derived and numerical approximations used to relate them to the DW-MRI signal. This allows direct and noninvasive quantification of microstructure features like the axonal radii, their orientation dispersion, and packing density. But

the microstructure of the neural tissue is complex (Section 4.1) and the DW-MRI signal in each voxel contains signal contributions from the different microstructure, which all have different diffusion profiles, giving rise to non-monoexponential signal[149]. So *multi-compartment* models are usually utilised, which account separately for the different geometries, each with characteristic diffusion properties.

In multi-compartment DW-MRI methods, the signal is modelled as a sum of contributions, S_i from N tissue compartments, or pores, each with a relative voxel volume fraction f_i, where f_i is the weighting of the i^{th} compartment, with $0 \leqslant f_i \leqslant 1$ and $\sum_{i=0}^{N} f_i = 1$, usually assuming no exchange between the various compartments, during T_d. Each of the compartments represents the water pool in the specific geometric environment, e.g. the intra-axonal or the intra-neurite space.

Two types of neuronal tissue environments are seen in the duration of a typical DW-MRI acquisition, namely *hindered* and *restricted* diffusion[12], so typical multi-compartment models aim to distinguish these. Various compartments that aim to characterise these environments are shown in Figure 4.3. In the following sections, we describe some of the multi-compartment models developed for the brain, that are most relevant to this thesis.

4.3.2.1 *Models of parallel fibres*

Multi-compartment modelling was pioneered by Stanisz et al. 1997, who developed a mathematical model based on the microstructure of nervous tissue, shown in Figure 4.4. The model is a three-compartment model, which models intra-axonal signal as restricted anisotropic diffusion, extra-axonal space as anisotropic hindered diffusion and isotropically restricted diffusion for water in glial cells. The model also accounted for exchange between the compartments. The authors show good agreement of the estimated values of microstructure features (axon and cell dimensions) with histological measures and the permeability with accepted values. Their biggest contribution of this work was the framework to follow for inferring microstructure of the human brain, from DW-MRI data and demonstration of the need of multi-compartment models through experiments showing a breakdown of mono-exponential signal decay, as Δ was varied.

Subsequently, a lot of work was carried using multi-compartment geometric models to directly relate the diffusion characteristics to the microstructure of interest. Numerous such techniques have been introduced, which are discussed in detail in a review by Assaf and Cohen 2009.

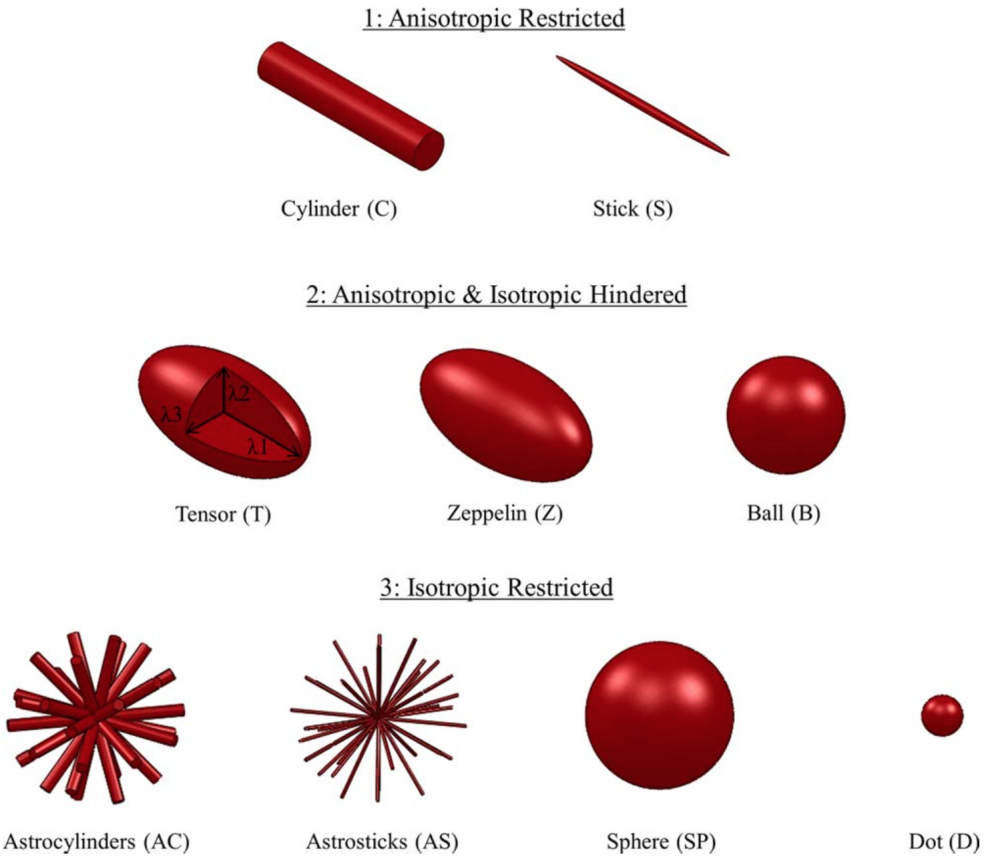

Figure 4.3: The various models typically utilised in geometric or biophysical modelling with DW-MRI. These geometries represent the features of the underlying microstructure e.g. axons can be modelled as cylinders due to their characteristic shape and features of interest like their orientation dispersion and packing density can be extracted using the DW-MRI data. *Image adapted from Richardson et al. 2014*.

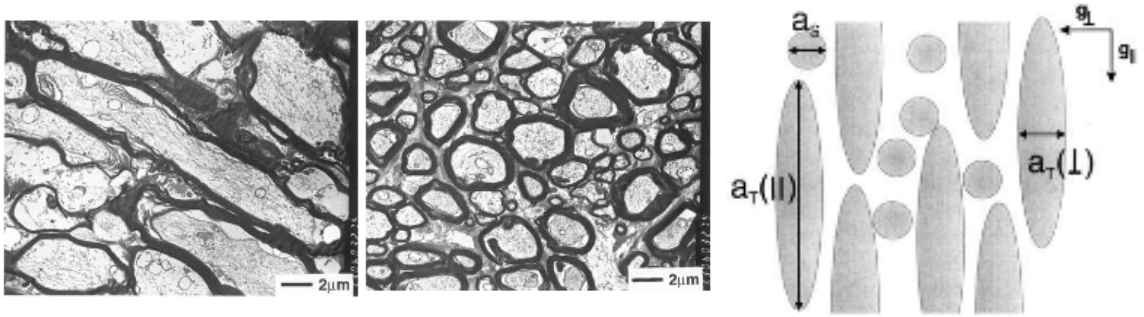

Figure 4.4: The three-compartment model developed by Stanisz et al. 1997 (right) based on the microstrucutre of the bovine optic nerve (left). The model is described in the main text. *Image adapted from Stanisz et al. 1997*.

A simple model which aims to capture the orientational variance of fibre bundles is the Ball-Stick model[24]. The highly restrictive diffusion within and the orientation dependence of the signal from fibres is modelled by a stick compartment and the rest of the signal coming from a Ball compartment, i.e. isotropic Gaussian diffusion. The stick compartment models coherent and straight axons and any signal from the non-parallel fibres are accounted for in the ball compartment.

The *Composite Hindered and Restricted Model of Diffusion (CHARMED)*[14] represents the restricted compartment occupied mainly by neurites, as impermeable parallel cylinders (axons) in a homogeneous space of the hindered compartment (extra-axonal space). The restricted diffusion signal in the intra-axonal compartment is obtained from the *Gaussian Phase Distribution* approximation[121] and the hindered diffusion signal is modelled as Gaussian diffusion by the diffusion tensor, $\boldsymbol{D}$. The model is verified using simulations and *ex vivo* spinal cord data[14]. In subsequent work Assaf and Basser 2005 show that it is possible to obtain reasonable estimates of axonal density using this model, with DW-MRI data acquired on clinical scanners (HARDI acquisition with several b-values (*multi-shell*) to account for arbitrary fibre orientation). But it would take almost an hour to extend the protocol to a whole brain scan. CHARMED was also extended as *AxCaliber* in Assaf et al. 2008 to account for a distribution of axon radii in the neural tissue, which requires $|\boldsymbol{G}|$ too high for standard imaging. Another limitation of these variants of the CHARMED models is that they require measurements perpendicular to the axons, so are not applicable to the whole brain where the dominant orientation of axons varies.

Alexander et al. 2010 present a *Minimal Model of White Matter Diffusion (MMWMD)*, which aims to capture axon diameters and their density, with no assumption on their orientation. To obtained such orientationally invariant indices, the optimised acquisition protocol presented in Alexander 2008 is used, which consists of a four-shell HARDI protocol. The work has been shown to recover known trends of axon radii and density in the CC (WM) for *in vivo* data. *Ex vivo* application[53] shows the importance of high $|\boldsymbol{G}|$ on estimation of the model parameters. The feasibility of the work for standard *in vivo* imaging was shown for the CC, but accurate estimation of the axonal diameters require high gradient strengths and extension to the whole brain would not be practical (scan times).

All these models assume parallel fibres, but they are known to be orientationally dispersed[33] and are abundant in the brain. Such orientationally dis-

persed organisation of the axons and even dendrites can be estimated using models of DW-MRI, as described in the next section.

4.3.2.2 *Models of dispersion*

Jespersen et al. 2007 present an analytical model to incorporate the orientation dispersion of neurites in the brain. Their model is an extension of the CHARMED model, where the restriction compartment is modelled as orientationally dispersed cylinders (so can model both axons and dendrites) and the rest of the signal coming from a compartment with isotropic Gaussian diffusion (extra-neurite). The orientation distribution of the neurites is described as a general distribution, expanded in terms of spherical harmonics. They show in an *ex vivo* baboon brain, the accurate quantification of the density and orientation dispersion of the neurites. However, the method put forward in the work is not clinically feasible due to the high b-values used (up to $15,000 s/mm^2$) and the long scan time. This method has been shown in Jespersen et al. 2010 to be a more accurate measure of dendrite density compared to DTI, as well as being able to capture a realistic map of the orientation dispersion of neurites, by comparing to estimates made by light and electron microscopy.

Subsequent work by Jespersen et al. 2012 presents a generic framework for the model in Jespersen et al. 2010. They establish the precise relationship between the anisotropy as measured by the diffusion signal and that arising from the actual orientation dispersion of neurites. They also use optical imaging to capture dendritic structure and estimate the scatter matrix of the underlying ODF, to demonstrate the relationship in a model-independent way, as shown in Figure 4.5. The results show that the scatter matrix (covariance of multivariate normal distribution) can provide a good summary of the true orientation distribution and the measured diffusion anisotropy is a confounded measure of the actual neurite orientation dispersion.

MMWMD is extended by Zhang et al. 2011 where the axons are modelled with orientation dispersion, parameterised with the Watson distribution. Experiments with synthetic data show that the estimated axon diameters are more accurate compared to when the orientation dispersion is not modelled, as shown in Figure 4.6. They also show that assuming parallel fibres underestimates the axonal density while overestimating their diameters. The model is also applied to *in vivo* DW-MRI data, demonstrating a good agreement to the histology, compared to studies with the assumption of parallel fibres. But the use of standard imaging shows limited sensitivity to the estimation of ax-

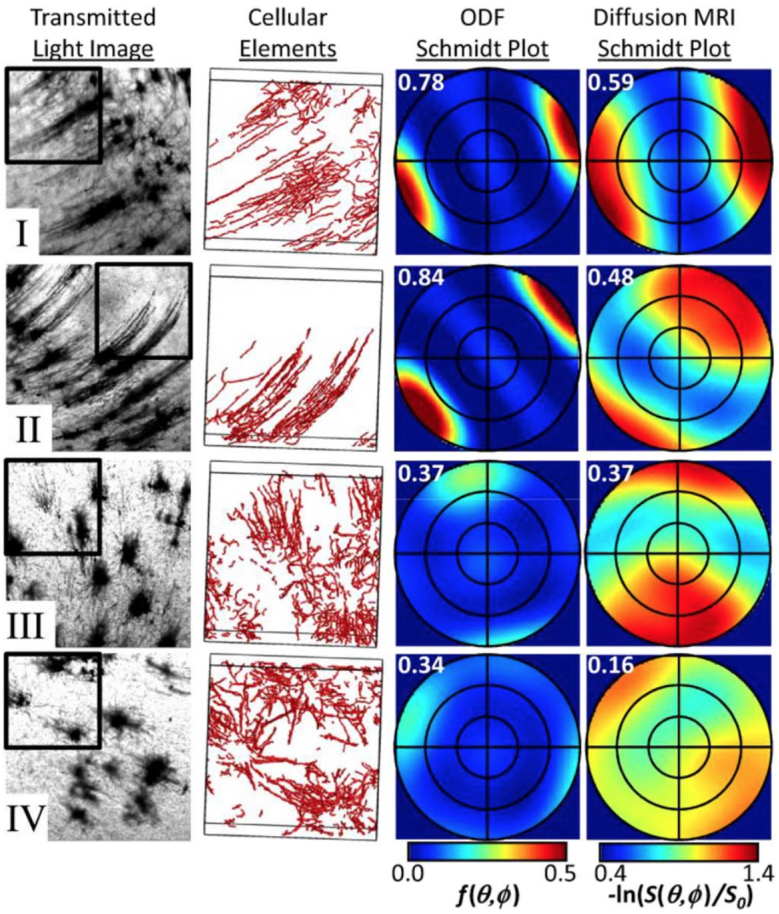

Figure 4.5: Comparison of the angular profile of the orientation distribution function (ODF) of the neuronal processes imaged and the negative log of the diffusion signal (dODF). *Image adapted from Jespersen et al. 2012*.

onal diameters $< 10\mu m$ Alexander 2006, but only less than 1% of fibres are $> 3\mu m$[79].

Sotiropoulos et al. 2012 present a model that aims to capture orientation dispersion anisotropy, which is a special case of the model presented by Kaden et al. 2007. The focus of both studies is connectivity estimation for tractography and not estimation of microstructure-specific indices, but the findings, specifically of Sotiropoulos et al. 2012, are relevant to this work. Sotiropoulos et al. 2012 proposed the *Ball-Rackets* model that extends the Ball-Stick model to capture within-voxel fanning and bending, by explicitly model the effect of these configurations on diffusion signal, using the Bingham distribution. They utilise simulations to establish the accuracy of the model to estimate the orientation dispersion and compare to other nonparametric techniques for estimating the ODF (or diffusion ODF). The key findings of their work that are relevant to this thesis are that estimation of anisotropic orientation dispersion requires data with a high SNR (> 30) (Figure 4.7) and estimating multiple fibre populations while accounting for anisotropic orientation dispersion gives

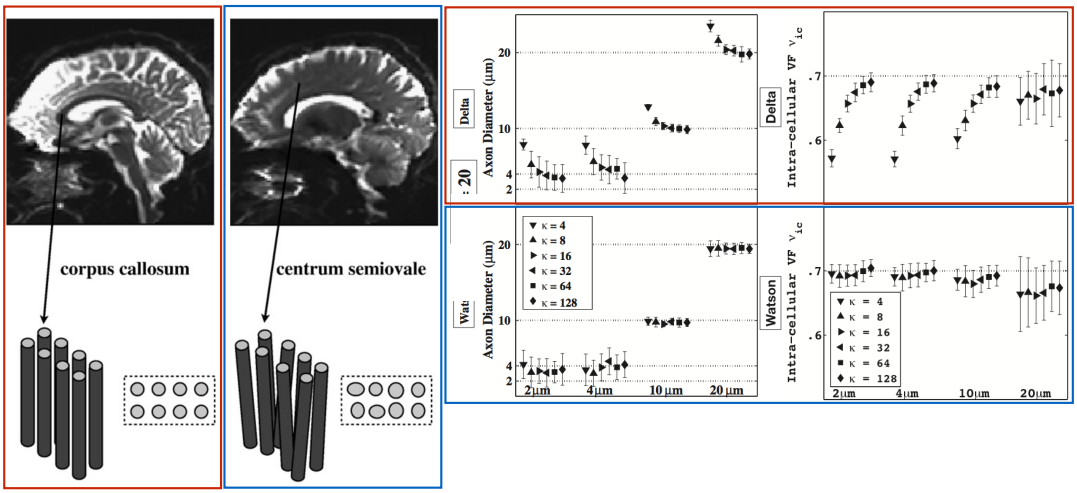

Figure 4.6: Demonstration of importance of characterising orientation dispersion, for accurate estimation of neurite morphology. Here the results are shown for estimation of the diameter and density of neurites. *Image adapted from Zhang et al. 2011*.

very unstable estimates (requires SNR > 30 and $b = 3000 s/mm^2$). The second finding is consistent with the results from Kaden et al. 2007.

4.4 DIFFUSION-WEIGHTED MRI IN STANDARD NEUROIMAGING

DTI[22] is the most widely used DW-MRI model in neuroimaging, with indices sensitive to features of the microstructure. But geometric models are more useful in practice as they explicitly estimate features of the microstructure that are important for diagnosis and prognosis of various brain diseases and disorders. Currently, the big hurdle for geometric models from being used in standard neuroimaging studies is that they require acquisitions which are not feasible with the typical neuroimaging setup. This includes the scan time, the MRI hardware (e.g. field and/or gradient strengths) and the acquisition sequence required.

In the following section, we discuss the clinical standard DW-MRI technique, the DTI, in detail, specifically the immense utility of it in clinical neuroscience. This is followed by a discussion of the geometric models of DW-MRI which are clinically feasible, specifically NODDI, which is a model central to the work presented in this thesis

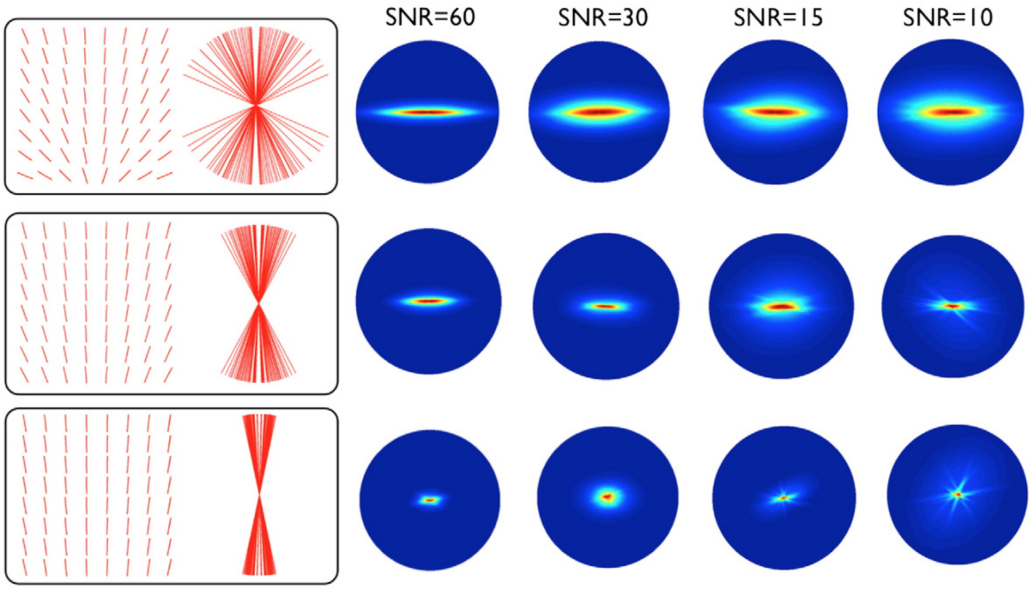

Figure 4.7: Demonstration of the dependency on SNR of estimation of anisotropic orientation dispersion, with Ball-Rackets model. The signal is simulated using segments of neurite orientations, shown in the left of the image. The estimated ODF is shown as a spherical density map, where the colour represents the density of orientations. *Image adapted from Sotiropoulos et al. 2012*.

4.4.1 *Diffusion Tensor Imaging (DTI)*

DTI is the most widely used DW-MRI technique in neuroscience for clinical and research studies, despite its simplicity. The indices derived from DTI are very simple and robust and allow visualisation of underlying geometric changes in the brain microstructure, making them a useful clinical tool.

4.4.1.1 *Parameters derived from DTI*

By decomposing $\boldsymbol{D}$ into its *principle components*, indices are derived which summarise diffusivity properties of the tissue being imaged. These estimates include *mean diffusivity*, *anisotropy* and *dominant orientation of diffusion*. If the *eigenvalues* of the $\boldsymbol{D}$ are sorted as: $\lambda_1 \geqslant \lambda_2 \geqslant \lambda_3$ and the corresponding *eigenvectors* are given by $\{\boldsymbol{e}_i\}_{i=1,2,3}$, then $\boldsymbol{D}$ can be described as:

$$\boldsymbol{D} = \lambda_1 \hat{\boldsymbol{e}}_1 \hat{\boldsymbol{e}}_1^T + \lambda_2 \hat{\boldsymbol{e}}_2 \hat{\boldsymbol{e}}_2^T + \lambda_3 \hat{\boldsymbol{e}}_3 \hat{\boldsymbol{e}}_3^T \, . \tag{4.9}$$

Since $\boldsymbol{D}$ is symmetric and positive definite the eigenvalues always exist and are positive. *Mean diffusivity* is the average diffusivity or ADC over each of the

orthogonal directions and is measured as an average of the three eigenvalues of the diffusion tensor:

$$MD = \frac{\lambda_1 + \lambda_2 + \lambda_3}{3} = \frac{Tr(\boldsymbol{D})}{3} \tag{4.10}$$

Where $Tr(\boldsymbol{D})$ is the *trace* of the tensor. The anisotropy of the diffusion tensor *DT* is a measure of how directional the diffusion is. It is measured as the variance of the three eigenvalues about their mean, normalised to the sum of all the eigenvalues i.e:

$$FA(\boldsymbol{D}) = \sqrt{\frac{3}{2}\frac{\sum_{i=1}^{3}(\lambda_i - \frac{1}{3}Tr(\boldsymbol{D}))^2}{\sum_{i=1}^{3}{\lambda_i}^2}} \tag{4.11}$$

FA ranges from 0 to 1, representing isotropic and perfectly anisotropic diffusion, respectively. The principal direction of diffusion, which usually corresponds to the main fibre orientation, is a unit vector, given by the eigenvector of the biggest eigenvalue, i.e. $\boldsymbol{e}_i$

MD is a measure of the overall mean-square displacement of the diffusing molecules and thus allows visualisation of any restrictions to the normal motion of these molecules. FA is related to the degree of organisation of the structure surrounding the diffusion molecules, particularly oriented structures, and is a measure of the degree of anisotropy of the diffusion. The main fibre orientation derived from the DT is a useful measure of the macroscopic organisation and connectivity of different regions of the anatomy. MD and FA provide diffusion characteristics which relate to tissue, specifically WM integrity, and orientation.

4.4.2 *Clinical utility of DTI*

DTI has been shown to be clinically useful in the diagnosis of various disease of the white matter like Multiple sclerosis[178], Alzheimer's disease and schizophrenia. DTI has been invaluable to visualise the early organisation of WM bundles[78], maturation of brain[132], as well as probing brain injury[171]. For the preterm brain, DTI metrics have been correlated with delayed brain maturation[19] and difference in volume of various sub-cortical GM regions[18], compared to term-born infants. Brain connectivity is also shown to be affected

due to preterm birth[17], utilising DTI based tractography. Detailed reviews of the use of DTI technique for several clinical applications like neurological disorders and infection, fibre tracking, development studies, ischemia, neurotrauma, and tumours are given in[139] and[109].

4.4.3 *Limitations of DTI*

DTI greatly simplifies the underlying diffusion of the water in neural tissue, which has been shown to deviate from mono-exponential behaviour[149]. It is widely accepted that the Gaussian model underlying the DTI is not valid in neuronal tissue[128], particularly for high b-values.

Another disadvantage of DTI is the lack of specificity of the model to microstructure. DTI measures are affected simultaneously by a number of microstructural changes (e.g. demyelination, inflammation, axonal loss, gliosis), which give rise to the same alterations of their values[23]. Thus DTI can not quantify specific measures such as changes in axonal/dendritic density or their complexity in terms of the organisation (i.e. dispersion). Such measures have the potential to provide greater insight into tissue architecture and pathology.

4.5 MICROSTRUCTURE IMAGING WITH STANDARD NEUROIMAGING

To address the limitations of DTI, discussed in Section 4.4.1, the multi-compartment geometric models of neuronal tissue, as discussed in Section 4.3.2 were developed. These models, also called *biophysical models*, provide indices that relate to the geometric features of the microstructure. These indices are related to specific features of brain microstructure, unlike DTI indices, which can change in the same way due to various alterations of the microstructure. However, there is a lack of microstructure imaging techniques that are feasible for *in vivo* studies with existing standard technology, limiting the advances in the field of neuroscience, particularly for neurites.

Many techniques aim to measure the axonal density and their radii (see Section 4.3.2), but it has been found that axon radius is a very hard parameter to estimate and requires very comprehensive protocols, with high diffusion weighing (b-values), which are not clinically feasible. Modelling neurites as arbitrarily oriented cylinders, rather than parallel cylinders has been shown to improve the estimation of their density and diameters[87,183].

Despite the lack of clinical feasibility, the result that orientation dispersion and density of neurites can be estimated well by DW-MRI data is promising and has motivated subsequent work for *in vivo* estimation of orientation dispersion of neurites, resulting in the development of NODDI. NODDI is a multi-compartment model which estimates the neurite density and their orientation dispersion just like Jespersen et al. 2007, but has been designed to be clinically feasible by making several assumptions in the tissue model (details in Chapter 5). This includes assuming neurites as sticks, to remove the neurite radius estimation from the model, which is hard to estimate with standard imaging.

NODDI is particularly useful to study brain microstructure as unlike most other DW-MRI techniques, it allows modelling of the GM as well as the less coherent WM, with its index of neurite orientation dispersion, making it applicable to study all brain tissue. Due to lack of *in vivo* techniques that are applicable to all brain tissue, changes in GM during brain development or pathologies are not as well understood as the major WM structures.

Thus *in vivo* measurement of the morphology of neurites using NODDI can help us advance our knowledge of brain cytoarchitecture. Microstructure imaging of neurites, specifically using NODDI is discussed in the next chapter, where a detailed mathematical description of the NODDI tissue model is also provided.

5

CLINICAL MICROSTRUCTURE IMAGING OF NEURITES

This chapter discusses NODDI a DW-MRI technique for microstructure imaging of neurites, with a clinically feasible acquisition. Clinical feasibility is a particular focus of the work presented here and is important as it allows a technique to be widely adopted into studies with a big cohort, without the need of special hardware or software updates.

Indices provided by NODDI are being rapidly adopted in clinical and research studies and help identify the precise cellular components that are affected by brain pathologies and the dynamic changes at the neuronal level that characterise them.

Neurites cannot be modelled to have a parallel configuration, as dendrites are orientationally dispersed and while axons can be thought of having a higher level of orientational coherence, they have been shown to exhibit orientation dispersion[63,184], as illustrated in Figures 2.3 and 2.4. NODDI[185] is the only technique to date, that has been demonstrated to be clinically feasible, providing useful indices of neurite morphology, while accounting for their orientation dispersion.

5.1 NEURITE ORIENTATION DISPERSION AND DENSITY IMAGING

NODDI aims to estimate the integrity of the axons and dendrites, in the human brain. The NODDI framework utilises microstructure sensitive data from DW-MRI, combined with a biophysical tissue model quantifying how this data relates to the specific features of the microstructure, as detailed in the following sections.

5.2 NODDI TISSUE MODEL

In this section, we describe the tissue model underlying the NODDI framework. In the first subsection, we detail the general NODDI formulation, with particular emphasis on the multi-level compartmentalisation of the NODDI tissue model. The second subsection details the specific parameterisation of the ODF to allow estimation of orientation dispersion of neurites and the model parameters estimated by the model fitting procedure.

5.2.1 *General NODDI formulation*

NODDI is underpinned by a two-level multi-compartment model, as shown in Figure 5.1, where all compartments are assumed to be non-exchanging. The total normalised signal, A, is modelled as the signal contribution from the tissue and non-tissue components of the brain, weighted by their respective relaxation-weighted volume fractions (Appendix B.1)

$$A = (1 - \nu_{iso})A_{tissue} + \nu_{iso}A_{iso} \ . \tag{5.1}$$

The non-tissue compartment represents the free diffusing water in the brain (e.g. CSF) and is modelled by free isotropic diffusion, with diffusivity d_{iso} (i.e. the ADC model described in Section 4.3.1.1). The volume fraction of this compartment is denoted by ν_{iso} and that of the tissue compartment by $(1 - \nu_{iso})$.

The second level models the signal from tissue compartment, A_{tissue}, comprising the GM and WM. A_{tissue} is the sum of the signal originating from inside the neurites (intra-neurite) and that from the space outside them (extra-neurite), weighted by their respective volume fractions

$$A_{tissue} = \nu_{in}A_{in} + (1 - \nu_{in})A_{en} \ , \tag{5.2}$$

where A_{in} and A_{en} are the normalised signal from the intra-neurite and extra-neurite compartments, respectively. The intra-neurite volume fraction gives an estimate of the density of neurites and we denote it by ν_{in}, while the extra-neurite volume fraction is $(1 - \nu_{in})$, by construction.

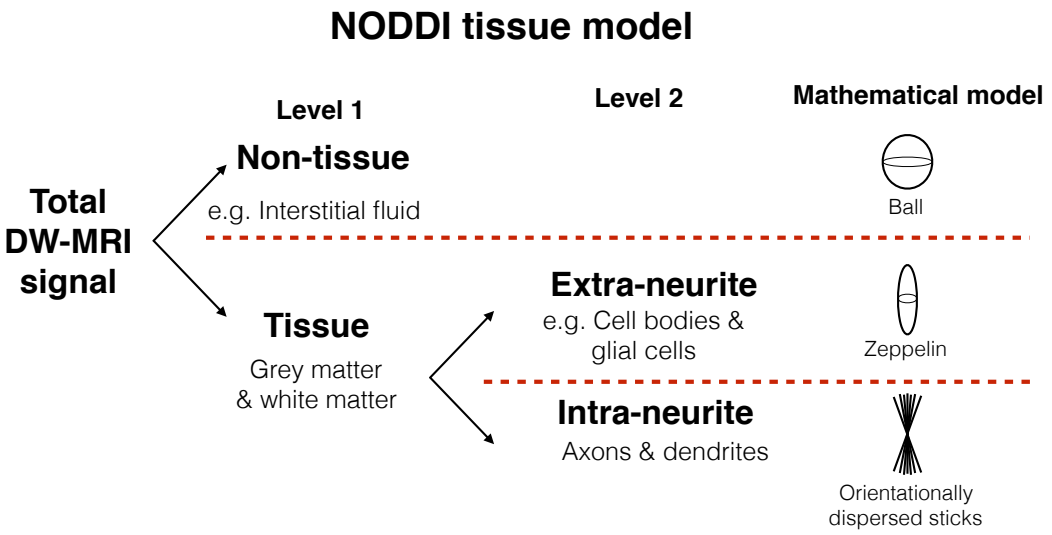

Figure 5.1: Breakdown of the total normalised DW-MRI signal as modelled by Watson-NODDI. The contributions of the tissue and non-tissue components of the brain are modelled separately. The tissue signal is further broken down to account for the signal originating from the highly restricted neurites and the hindered space outside the neurites. The non-tissue compartment is modelled by isotropic Gaussian diffusion. The intra-neurite compartment models the neurites as orientationally dispersed sticks, while the space around the neurites is prescribed an anisotropic diffusion model, as detailed in the main text.

The intra-neurite signal, A_{in}, is computed as the signal from inside a neurite weighted by an orientation distribution function (ODF), $f : \mathbb{S}^2 \to \mathbb{R}^+$. Neurites are modelled as sticks because, in the typical time scale of DW-MRI experiments, the membrane of neurites restricts the water diffusion to be along their length[38]. Thus, the diffusion signal from a neurite along an orientation $\hat{n}$ is the attenuation due to this length-wise unhindered diffusion, parallel to the direction of applied gradient, i.e. $e^{-bd_i(\hat{q}\cdot\hat{n})^2}$. Here b is the diffusion-weighting factor, $\hat{q}$ the gradient direction and d_i the intrinsic diffusivity inside the neurites. To account for the orientational dispersion of neurites, we sum this attenuation over all possible orientations, given a certain density of neurites along each orientation, $\hat{n}$. So

$$A_{in} = \int_{\mathbb{S}^2} f(\hat{n}) e^{-bd_i(\hat{q}\cdot\hat{n})^2} \, d\hat{n} \,, \tag{5.3}$$

where $f(\hat{n})\, d\hat{n}$ is the probability of neurites with orientations within $d\hat{n}$, an infinitely small cone of orientations centred about $\hat{n} \in \mathbb{S}^2$.

To account for the hindrance due to the presence of neurites, the extra-neurite signal, A_{en}, is modelled as signal attenuation due to anisotropic Gaussian diffusion, i.e.

$$A_{en} = e^{-b\hat{q}^T \boldsymbol{D}_{en} \hat{q}} , \tag{5.4}$$

where $\boldsymbol{D}_{en}$ is the diffusion tensor representing the diffusion characteristics in the extra-neurite space. We model the effect of orientationally dispersed neurites on A_{en} by taking into account the following two observations: a) the dispersion of neurites has an effect on the diffusion in the extra-neurite space, with the diffusion perpendicular to the dominant orientation of neurites being greater if they have high dispersion, b) neurites hinder the diffusion in the surrounding space and this hindrance is greater if the neurite density in that space is greater. The observation a) implies that the extra- and intra-neurite spaces are coupled by the orientation distribution of neurites, $f(\hat{n})$. Thus

$$\boldsymbol{D}_{en} = \int_{S^2} f(\hat{n}) \boldsymbol{D}(\hat{n}) \, d\hat{n} \tag{5.5}$$

represents the diffusion tensor in the extra-neurite space in the presence of orientationally dispersed neurites, where $\boldsymbol{D}(\hat{n})$ is a cylindrically symmetric tensor, with principal diffusion orientation $\hat{n}$, parallel diffusivity $d_{\parallel}$ and perpendicular diffusivity, $d_{\perp}$. $\boldsymbol{D}(\hat{n})$ represents the canonical configuration of perfectly parallel neurites along $\hat{n}$. We assume that for the canonical configuration modelled by $\boldsymbol{D}(\hat{n})$, the parallel diffusivity in the extra-neurite space is the same as the intrinsic diffusivity inside neurites, i.e. $d_i = d_{\parallel}$. To account for b), a tortuosity model is used to estimate $d_{\perp}$, for a given neurite density. For randomly placed parallel cylinders, this gives $d_{\perp} = d_{\parallel}(1 - v_{in})$ [154].

Note that due to the multi-level compartmentalisation of NODDI, when $v_{iso} \approx 1$, the tissue parameters, describing the intra- and extra- neurite signals, can take any value without affecting the total signal (see Equation (5.1)). Thus, the tissue parameters are indeterminate for such cases.

The mathematical description of the NODDI signal model allows any orientation distribution function to be used. The next section describes the orientation distribution function used in the original work [185].

5.2.2 *Orientation distribution function*

The orientation distribution function, $f(\hat{n})$, used in NODDI is Watson distribution[113]. Watson distribution is a probability density function, described by the probability along an orientation $\hat{n}$:

$$f(\hat{n}) = \frac{1}{M\left(\frac{1}{2}, \frac{p}{2}, \kappa\right)} e^{\kappa(\hat{\mu}^T \hat{n})^2}, \tag{5.6}$$

where M is a confluent hypergeometric function of the first kind, $\hat{\mu}$ is the mean orientation and κ the concentration parameter that quantifies the coherence of the orientations about $\hat{\mu}$. Watson distribution belongs to a class of probability density functions for axial data (orientational rather than directional) called Bingham distribution, which is the spherical analogue of 2-dimensional Gaussian probability density function (See Section 6.2.1 for details).

Watson distribution models the orientation distribution as being isotropically dispersed about $\hat{\mu}$, with the probability decreasing exponentially as $\hat{n}$ and $\hat{\mu}$ become less parallel (i.e. the angle between $\hat{n}$ and $\hat{\mu}$ approaches $N\pi$ radians). In general: $-\infty \leqslant \kappa \leqslant \infty$, but for NODDI it is restricted to: $0 \leqslant \kappa \leqslant \infty$. This avoids girdle distributions ($\kappa < 0$), which have no meaning in modelling neurites.

5.2.3 *Model parameters*

The complete set of parameters included in the NODDI tissue model are:

- v_{in}: intra-neurite volume fraction
- $d_{\parallel}$: intrinsic free diffusivity
- κ: concentration parameter of Watson distribution
- $\hat{\mu}$: dominant orientation of Watson distribution, characterised by the angles $\theta \in [0, \pi]$, $\phi \in [0, 2\pi]$
- v_{iso}: isotropic volume fraction
- d_{iso}: isotropic diffusivity

In the original work presenting NODDI[185], the model parameters estimated from the data are v_{in}, v_{iso}, κ, θ and ϕ. The diffusivities are fixed to their

typical values *in vivo*: $d_{\parallel} = 1.7 \times 10^{-3} mm^2 s^{-1}$ and $d_{iso} = 3.0 \times 10^{-3} mm^2 s^{-1}$. So only 5 parameters are estimated, which is comparable to the 6 estimated for the DTI.

5.3 NODDI INDICES OF BRAIN MICROSTRUCTURE

The microstructure indices provided by NODDI include an estimate of neurite density and their orientation dispersion, quantified as the intra-neurite volume fraction, ν_{in}, and the orientation dispersion index, ODI, respectively.

These parameter maps are useful for whole brain visualisation of the microstructure of the brain tissue and thus are a useful tool to identify key features of the microstructure in various regions of the brain.

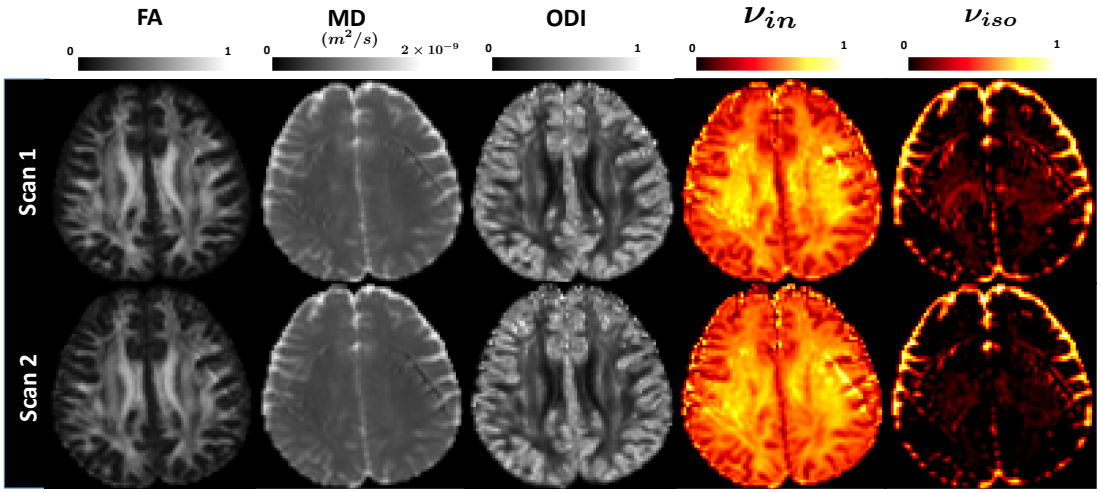

Figure 5.2: Maps of the Watson-NODDI indices of neurite morphology (columns 3-4) alongside those for the indices DTI (columns 1-2). *The images have been adapted from Tariq et al. 2012*.

5.3.1 *Neurite density index*

The neurite density index, ν_{in}, quantifies the packing density of neurites, which is highest in core WM regions like the corpus callosum (CC) and less in the GM, as shown in Figure 5.2.

5.3.2 *Orientation dispersion index*

To quantify the dispersion of neurites about $\hat{\mu}$ an orientation dispersion index is used:

$$\mathrm{ODI} = \frac{2}{\pi}\arctan(1/\kappa). \tag{5.7}$$

ODI is defined in this way to obtain a quantity which, unlike κ, describes dispersion and is finite, making it suitable to visualise. ODI has a value close to 1 for highly dispersed orientation distribution, e.g. dendrites in GM, and $\mathrm{ODI} \to 0$ for highly coherent neurites e.g the parallel axons in the CC, as shown in Figure 5.2.

5.4 ACQUISITION PROTOCOL

The NODDI acquisition protocol has been determined using the experiment design optimisation procedure in Alexander 2008. The optimisation was carried out using typical parameters of human brain parenchyma and accounting for the hardware and time limitation of clinical scanning, as described in Zhang et al. 2012.

The optimised NODDI protocol consists of two high angular resolution diffusion imaging (HARDI)[168] shells, with $b = 711 s/mm^2$ and $b = 2855 s/mm^2$, with 30 and 60 gradient directions sampled, respectively. To ensure the same diffusion time for the different measurements, which supports the assumption of neurites as sticks, the gradient strength is changed to achieve a different diffusion weighting (b-value), while all other acquisition parameters of the DW-MRI sequence (Δ, δ, TE, TR) are kept constant. In addition, 9 b0 images are also acquired to factor out the signal attenuation due to the relaxation of transverse magnitisation (i.e. T_2 decay described in Section 3.2.6). A more comprehensive four-shell protocol was used in the original publication[185] to assess the *in vivo* results of the optimised protocol against.

5.5 CLINICAL APPLICATIONS OF NODDI

NODDI has had a rapid uptake in the field of neuroimaging as it allows quantification of microstructure changes in both GM and WM, with a clinically feasible imaging protocol. Clinical studies have been carried out using NODDI

for applications including normal brain development and ageing[25,36,120], neurological disorders[54,102,111,125,125,164,180] and brain connectivity[111]. All these studies find that the microstructure specific indices provided by NODDI are clinically relevant. For example, in a study of focal cortical dysplasia, Winston et al. 2014 show that NODDI parameters consistently identify the regions of dysplasia more conspicuously, compared to the changes observed from other MRI modalities. Kunz et al. 2014 use NODDI to assess brain development and show that its indices capture the specific features of the microstructure that change in the major WM pathways during brain development, including fibre density, myelination and orientation distribution of neurites. Lemkaddem et al. 2014 demonstrate the use of NODDI in connectivity studies and show that the alteration of brain networks in temporal lobe epilepsy is a result of changes in neurite density and orientation dispersion, quantified by NODDI.

NODDI is particularly useful to study brain microstructure as unlike most other DW-MRI techniques, it allows modelling of the GM as well as the less coherent WM, with its index of neurite orientation dispersion, making it applicable to study all brain tissue. Due to lack of *in vivo* techniques that are applicable to all brain tissue, changes in GM during brain development or pathologies are not as well understood as the major WM structures. For example, histological studies have shown that GM undergoes very significant changes during early brain development[100,101] and abnormal cortical thickness and reduced complexity of the dendritic and axonal processes in the cortex are associated with preterm brain[18,19]. Thus *in vivo* measurement of the morphology of neurites using NODDI can help us advance our knowledge of brain cytoarchitecture.

5.6 LIMITATIONS OF NODDI

The clinical utility and impact of NODDI are immense, however, there are certain limitations of the technique that have an impact on the metrics estimated by the model. NODDI was developed with the clinical applicability in mind and thus constitutes of the simplest tissue model that can be reliably estimated with the standard neuroimaging setup, in terms of hardware and acquisition time. Most of these are related to the assumptions made in the tissue model underlying the technique and are listed below:

1. The neurite orientations are assumed to be isotropically dispersed.
2. The neurites are assumed to be cylinders with zero radii (*sticks*).

3. The intrinsic diffusivity is assumed constant and fixed to empirically estimated values.

4. A tortuosity assumption is used to compute the diffusivity in the extra-neurite space

5. Requires nonlinear optimisation to estimate the microstructure parameters.

6. Requires acquisition which is plausible with standard hardware but requires non-standard acquisition protocol.

7. Assumes one neurite population per imaging voxel.

These limitations are discussed in detail in Chapter 16. The limitation of NODDI that is relevant to achieve the objective of this work is that the neurite orientations are assumed to be isotropically dispersed. NODDI models the orientation distribution of neurites with the Watson distribution[113], which constrains the dispersion about the dominant orientation to be isotropic. Thus in its current form, it can not characterise anisotropic orientation dispersion.

In Part (iii) we extend the NODDI formalism to enable the characterisation of anisotropic orientation dispersion and present specific indices for assessing complex neurite configurations.

Part III

METHOD DEVELOPMENT AND EVALUATION

This part of the thesis is concerned with the development of a technique to enable quantification of dispersion anisotropy. We present the precise mathematical framework for quantification of orientation dispersion anisotropy. Then we evaluate the clinical feasibility of estimating this feature. We demonstrate the accuracy/precision of the indices of the proposed model, using a clinically feasible acquisition protocol.

6

BINGHAM-NODDI: MAPPING ANISOTROPIC ORIENTATION DISPERSION OF NEURITES

This chapter presents *Bingham-NODDI* as a clinically-feasible technique for estimating the anisotropic orientation dispersion of neurites. The proposed method can further the existing knowledge of the brain in health and disease, as it presents a novel index of neurite morphology by modelling complex features of the geometry of neurites.

Neurites are orientationally dispersed and it is important to model this dispersion, as discussed in Chapter 5. These orientationally dispersed neurites exhibit many complex orientation configurations in the human brain, which include multiple fibre populations, that may be crossing or kissing within an imaging voxel, as shown in the Figure 1.1. A lot of work has been carried out to characterise complex neurite configurations such as crossing and kissing[2,8,50,167], with *ex vivo* and *in vivo* studies. A feature of complex orientation configuration of neurites that has not been widely explored is anisotropic orientation dispersion, which is the subject of the work presented here.

The proposed model, *Bingham-NODDI* enables estimation of anisotropic orientation dispersion. Characterisation of such complex neurite configurations is very important to understand normal brain development, as well as the changes in microstructure that happen due to neurological disorders, e.g. preterm birth[19,85]. Measurement of these novel indices of the proposed model will facilitate investigations of changes in the GM and WM underlying normal development and ageing or pathology.

We quantify anisotropic orientation dispersion of the neurites in terms of the principal components of the Bingham distribution, which describe the extent of orientation dispersion about the dominant orientation, separately along the primary and secondary dispersion orientations. We present indices derived from the parameters of the Bingham distribution to quantify anisotropic orientation dispersion, along with the standard NODDI indices of neurite morphol-

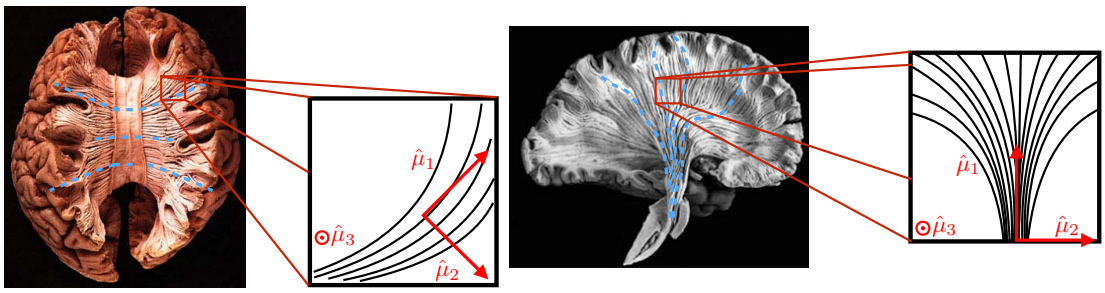

a. Bending configuration

b. Fanning configuration

Figure 6.1: Schematics illustrating anisotropic orientation dispersion of the fibres in the brain, including bending (a) and fanning (b) of fibres. Such configurations can be interpreted as orientations dispersed about a mean orientation, $\hat{\mu}_1$, with the highest dispersion in the plane of fanning, characterised by $\hat{\mu}_1$ and $\hat{\mu}_2$ and the least in the plane perpendicular to it, defined by $\hat{\mu}_1$ and $\hat{\mu}_3$. The existence of such fibre configurations has been confirmed with histological and DW-MRI data, as detailed in the main text. Watson-NODDI assumes isotropic orientation dispersion, so can not characterise such configurations. *The brain dissection images have been adapted from* `http://brainmind.com/` *[accessed in Aug. 2017].*

ogy. The novel indices of Bingham-NODDI allow us to distinguish the changes in overall dispersion from dispersion anisotropy.

6.1 DISPERSION ANISOTROPY A MEASURE OF COMPLEX NEURITE CONFIGURATIONS

6.1.1 *What is anisotropic orientation dispersion*

Anisotropic orientation dispersion is a feature of neurite configuration in the brain, arising from fanning and bending fibres. In such fibre configurations, the dispersion about the dominant orientation is the highest in the plane of fanning and bending but the lowest in the plane perpendicular to it, giving rise to anisotropic dispersion, as illustrated in Figure 6.1.

Anisotropic orientation dispersion configurations have been shown to be extensive in the brain. Kleinnijenhuis et al. 2013 show extensive bending/-fanning of fibres into the cortex. Budde and Annese 2013 also show sharp bending/fanning of fibres into the cortex, as well as a high dispersion in the medial and lateral regions of the corpus callosum (CC). Türe et al. 2000 show the fanning fibres of the corticospinal tracts (CST), as they pass through the internal capsule.

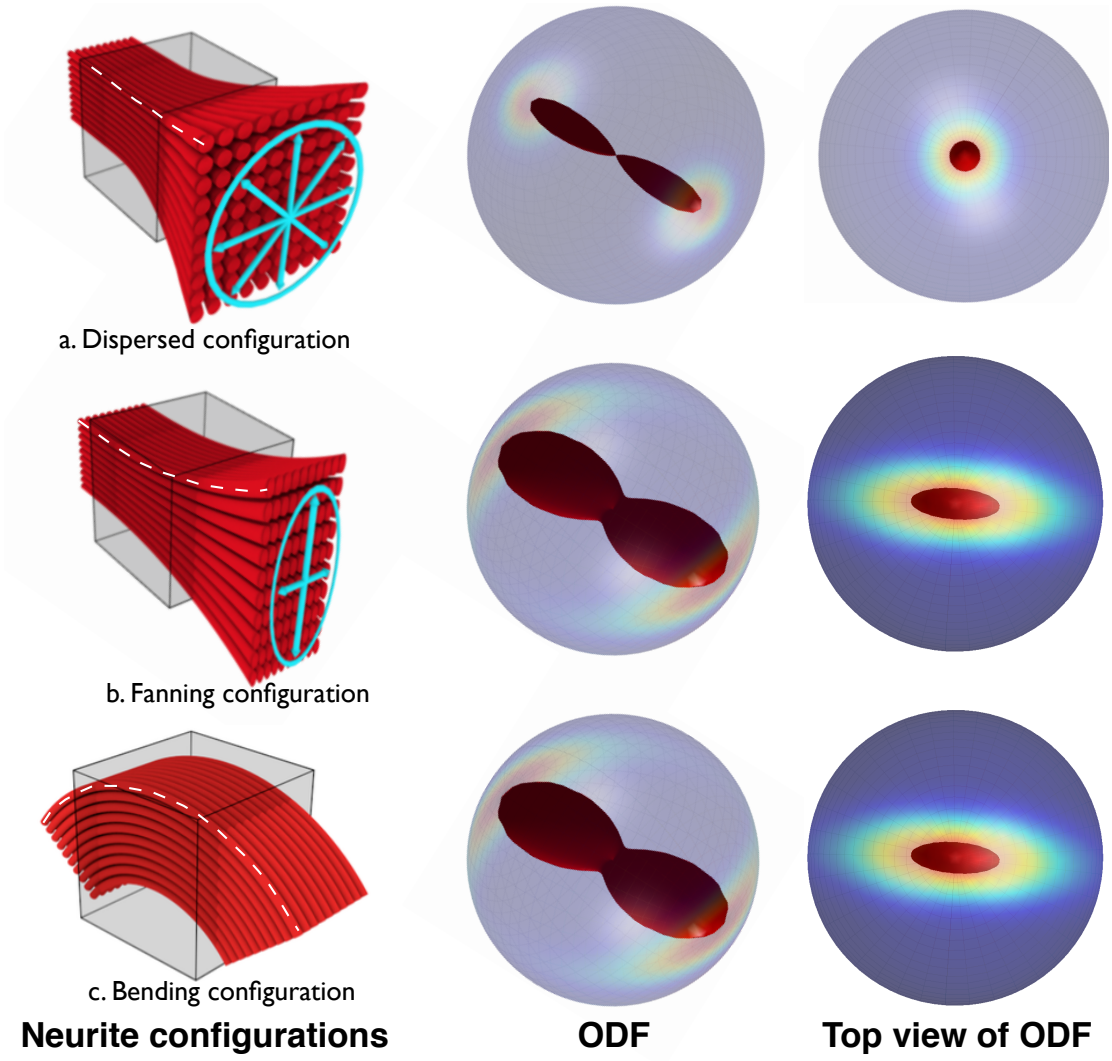

Figure 6.2: The complex orientation configurations of neurites found in the brain. The 1st column shows the within-voxel pattern of neurites (single-population), which are modelled as cylindrical segments in DW-MRI models (at voxel-level, we see a continuum of orientations, centered on a mean orientation, $\hat{\mu}_1$ [85,147], as in Figure 4.7), depicted by the white dotted lines here. The next two column shows how each of these configurations can be represented as an orientation distribution function (ODF) in 3D. The ODF can be represented in terms of a lobed structure where the radius is scaled by the value of the ODF or by a heat map representing the density in a particular orientation on the sphere. The last column shows the top view of the ODF for each of the configurations, which is the view usually shown in this thesis. Watson-NODDI can only capture the isotropic orientation dispersion configuration, while Bingham-NODDI is able to capture all such configurations. *Figure adapted from Rowe 2014*.

6.1.2 *Why quantify orientation dispersion anisotropy*

Anisotropic orientation dispersion of neurites is an important microstructure feature to characterise, as specific quantification of this anisotropy, a *dispersion anisotropy index*, can provide a marker of microstructure morphology, that can capture subtle changes in neurite configurations. Fanning/bending fibres, which exhibit anisotropic orientation dispersion, have been shown to be abundant in the human brain as highlighted by histological[32,96,169] and DW-MRI studies[105,147]. A quantification of such anisotropy has not been demonstrated *in vivo* with NODDI, which quantifies the overall orientation dispersion only (Section 5.3), or any other *in vivo* technique. An index of orientation dispersion anisotropy of neurites can highlight subtle changes in neurite morphology, which may not alter the overall dispersion. So quantification of such anisotropy not only provides a more comprehensive description of the orientation dispersion of neurites but may also serve as a marker of subtle microstructural changes in pathology[105]. Characterising anisotropic orientation dispersion can also enhance tractography[105,138].

Anisotropic orientation dispersion has been characterised in some DW-MRI studies, but a specific quantification of dispersion anisotropy has not been presented, which is the feature we are interested in. Studies incorporating characterisation of anisotropic orientation dispersion include Cook et al. 2004, Kaden et al. 2007, Sotiropoulos et al. 2012, but the focus has been on mapping brain connectivity while our aim is to estimate biophysically meaningful parameters. As shown in Lazar et al. 2005, the eigenvalues of the diffusion tensor (DT), specifically the difference $\lambda_2 - \lambda_3$, can be used to reflect the level of dispersion anisotropy in WM tracts, but the metrics derived from the DT do not provide a direct index of microstruture[129].

6.1.3 *Modelling dispersion anisotropy using NODDI*

NODDI has had rapid adoption in neuroimaging, enabling key advances in the field of microstructure imaging. NODDI is underpinned by an acquisition protocol feasible for standard clinical scanners and a tissue model that allows quantification of microstructure changes in both GM and WM, making it feasible for research and clinical studies for the whole brain. Numerous studies in neuroimaging research and preliminary clinical studies demonstrate the utility of the NODDI metrics to quantify microstructural basis of normal brain development and ageing, as well as various brain pathologies. Thus *in vivo*

measurement of the morphology of neurites using NODDI can help advance our knowledge of brain cytoarchitecture.

But a limitation of NODDI is that it can not characterise complex neurite configurations such as those arising from fanning and bending axons. NODDI models orientation distribution of neurites with the Watson distribution (Section 5.1), which constrains the dispersion about the dominant orientation, $\hat{\mu}_1$, to be isotropic (Figure 6.3.a). Thus fanning and bending configurations cannot be accurately modelled by Watson-NODDI and can affect the accuracy of estimation of other NODDI parameters.

We propose a method that extends the NODDI formalism to enable the characterisation of anisotropic orientation dispersion and specifically quantify this anisotropy. NODDI provides a suitable framework for developing a technique to estimate anisotropic orientation dispersion of neurites, using standard DW-MRI acquisition. Feasibility of NODDI for standard neuroimaging setup, including hardware and scan times, was assessed in Zhang et al. 2012. The results demonstrated that it is possible to non-invasively estimate the NODDI indices of neurite morphology over the whole brain.

6.2 BINGHAM-NODDI

We propose Bingham-NODDI, which is an advance microstructure imaging technique extending the NODDI tissue model, to enable *in vivo* estimation of orientation dispersion anisotropy, using a clinically feasible imaging protocol.

The Bingham-NODDI tissue model has the same general formulation as the original NODDI model, described in Section 5.2.1. In the following sections, we describe how we quantify the anisotropic orientation dispersion of neurites in Bingham-NODDI[1].

6.2.1 *Parameterisation of the ODF in Bingham-NODDI*

The Bingham distribution is used to quantify the orientation distribution of neurites in Bingham-NODDI. As shown in Figure 6.3, the Bingham distribution can capture anisotropic orientation dispersion of varying levels, as well as isotropic dispersion, since Watson is a special case of the Bingham distribution.

The Bingham distribution[26,67] is a parametric orientation distribution, which is the spherical analogue of a two-dimensional Gaussian distribution.

1 The work described here has been published[160] and presented at conferences[161,162]

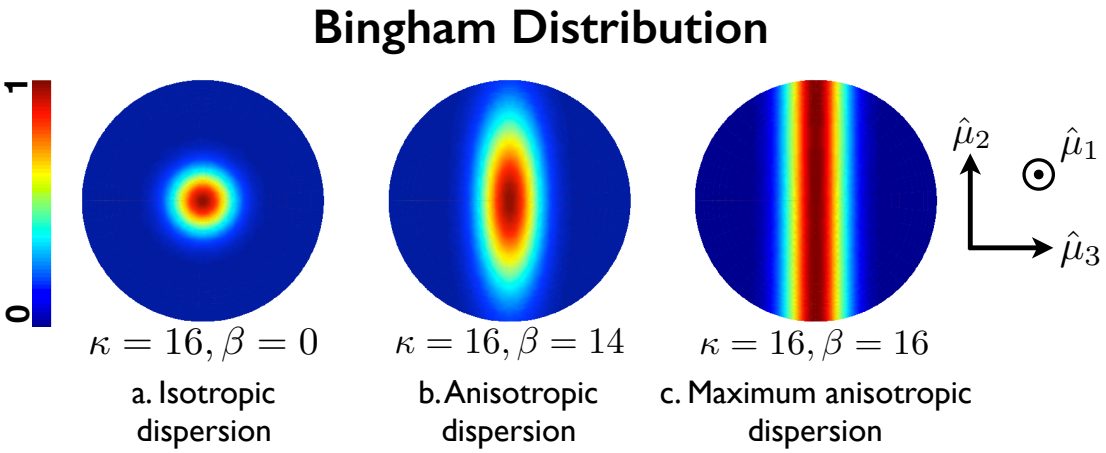

Figure 6.3: Probability density plots for the Bingham distribution, which we use to parameterise the orientation dispersion in Bingham-NODDI. The density plots represent increasing anisotropic dispersion about $\hat{\mu}_1$. The primary dispersion orientation, $\hat{\mu}_2$, represents the orientation with the largest dispersion extent about $\hat{\mu}_1$, while $\hat{\mu}_3$ represents that with the least. The vectors $\hat{\mu}_1$, $\hat{\mu}_2$ and $\hat{\mu}_3$ are mutually orthogonal, so $\hat{\mu}_3$ is fixed for a specific $\hat{\mu}_1$ and $\hat{\mu}_2$ (their cross product). Figure 6.3.a is a special case of the Bingham distribution, where the dispersion is isotropic and is called the *Watson distribution*. (Note that in each of the density plots, the orientation density is normalised with respect to the maximum value and the plots show the top view of the distribution on a sphere.)

The probability density of an orientation along $\hat{n}$ for the Bingham distribution is defined in terms of a 3×3 symmetric matrix, $\boldsymbol{B}$

$$f(\hat{n}; \boldsymbol{B}) = \frac{1}{c_B} \exp\left(\hat{n}^T \boldsymbol{B} \hat{n}\right) . \tag{6.1}$$

Since $f(\hat{n}; \boldsymbol{B})$ is a probability density function, the condition

$$\int_{S^2} f(\hat{n}; \boldsymbol{B})\, d\hat{n} = 1 \tag{6.2}$$

is satisfied, and c_B, the normalisation constant is determined by

$$c_B = {}_1F_1\left(\frac{1}{2}; \frac{3}{2}; \boldsymbol{B}\right) , \tag{6.3}$$

where ${}_1F_1$ is the confluent hypergeometric function of the first kind. Equation (6.1) can be re-writen (Appendix B.2) as:

$$f(\hat{n};\mathbf{B}) = \frac{1}{c_B} exp\left(\kappa_1(\hat{\mu}_1\cdot\hat{n})^2 + \kappa_2(\hat{\mu}_2\cdot\hat{n})^2 + \kappa_3(\hat{\mu}_3\cdot\hat{n})^2\right) , \tag{6.4}$$

where $(\hat{\mu}_i\cdot\hat{n})$ denotes the dot product of two vectors (measuring how parallel the vectors are).

We can obtain a geometrically interpretable form of the Bingham distribution by expressing $\boldsymbol{B}$ in terms of its eigendecomposition

$$\boldsymbol{B} = \boldsymbol{Q}\boldsymbol{D}\boldsymbol{Q}^{-1} = \begin{pmatrix}\hat{\mu}_1 & \hat{\mu}_2 & \hat{\mu}_3\end{pmatrix}\begin{pmatrix}\kappa_1 & 0 & 0\\ 0 & \kappa_2 & 0\\ 0 & 0 & \kappa_3\end{pmatrix}\begin{pmatrix}\hat{\mu}_1^T\\ \hat{\mu}_2^T\\ \hat{\mu}_3^T\end{pmatrix} , \tag{6.5}$$

such that the diagonal terms reflect the concentrations about the principal axes, $\hat{\mu}_1$, $\hat{\mu}_2$ and $\hat{\mu}_3$. Here $\boldsymbol{Q}$ and $\boldsymbol{D}$ are the matrices of eigenvectors and eigenvalues of $\boldsymbol{B}$, respectively, and $\kappa_1 \geqslant \kappa_2 \geqslant \kappa_3$ represent the concentration of orientations along the corresponding principal axes, as shown in Figure 6.3. Symmetry of $\boldsymbol{B}$ implies that $\boldsymbol{Q}$ is an orthogonal matrix (i.e. $\boldsymbol{Q}^{-1} = \boldsymbol{Q}^T$) and $\hat{\mu}_1$, $\hat{\mu}_2$ and $\hat{\mu}_3$ are mutually orthogonal unit vectors that can be parameterised in terms of Euler's angles, $\theta \in [0,\pi]$, $\phi \in [0,2\pi]$ and $\psi \in [0,\pi]$.

As the Bingham distribution is invariant to the addition of arbitrary constants to its eigenvalues[113], by choosing $-\kappa_3$ as the constant (Appendix B.3), Equation (6.1) can be rewritten as

$$f(\hat{n};\boldsymbol{B}) = \frac{1}{c_B} exp\left(\kappa(\hat{\mu}_1\cdot\hat{n})^2 + \beta(\hat{\mu}_2\cdot\hat{n})^2\right) , \tag{6.6}$$

where $\kappa = \kappa_1 - \kappa_3$ and $\beta = \kappa_2 - \kappa_3$. Bingham distribution thus has only 5 degrees of freedom, two associated with the concentrations and three with the orientations.

A more intuitive description of the orientation distribution is achieved by re-writing Equation (6.1) in a form that is analogous to the two-dimensional Gaussian distribution

$$f(\hat{n};\boldsymbol{B}) = \frac{e^{\kappa}}{c_B} exp\left(-\frac{(\hat{\mu}_2\cdot\hat{n})^2}{1/(\kappa-\beta)}\right) exp\left(-\frac{(\hat{\mu}_3\cdot\hat{n})^2}{1/\kappa}\right) , \tag{6.7}$$

where $1/(\kappa - \beta)$ and $1/\kappa$ represent the dispersion about the dominant orientation $\hat{\mu}_1$, along the axes $\hat{\mu}_2$ and $\hat{\mu}_3$, respectively (see Appendix B.4 for derivation). These dispersion parameters are analogous to the variance parameters of the Gaussian distribution and inversely proportional to the concentration parameters κ and β. Since $\kappa \geqslant \beta$, the dispersion extent along $\hat{\mu}_3$ is less than or equal to that along $\hat{\mu}_2$, as shown in the density plot in Figure 6.3. Thus we refer to $\hat{\mu}_2$ as the *primary dispersion orientation*, and $\hat{\mu}_3$ as the *secondary dispersion orientation*.

The estimability of the Bingham distribution and thus the determination of the corresponding orientations and the concentration/dispersion parameters depends on the specific geometry of the underlying orientation distribution of neurites. For the case where $\kappa > \beta > 0$, anisotropic dispersion exists about $\hat{\mu}_1$ (Figure 6.3.b), all the orientations are well-defined and estimable. When the dispersion is isotropic about $\hat{\mu}_1$ (Figure 6.3.a), the orientations $\hat{\mu}_2$ and $\hat{\mu}_3$ are not distinguishable and thus are arbitrarily defined. Similarly, when the dispersion is completely anisotropic, i.e. $\kappa = \beta > 0$ (Figure 6.3.c), $\hat{\mu}_1$ and $\hat{\mu}_2$ become indistinguishable and arbitrarily defined. For an isotropic orientation distribution ($\kappa = \beta = 0$), none of the orientations is uniquely defined.

6.2.2 *The orientation tensor*

An orientation tensor, $\boldsymbol{T}$ is defined as the second moment (also known as the scatter matrix) of an ODF. In the case of a Bingham distribution,

$$\boldsymbol{T} = \int_{S^2} f(\hat{n}; \boldsymbol{B}) \hat{n}\hat{n}^T \, d\hat{n} \, , \tag{6.8}$$

i.e. $\boldsymbol{T}$ is the outer product of each vector in the distribution with itself, weighted by the probability along that vector and summed for all vectors:

$$\boldsymbol{T} = \begin{pmatrix} \sum_i x_i^2 & \sum_i x_i y_i & \sum_i x_i z_i \\ \sum_i x_i y_i & \sum_i y_i^2 & \sum_i y_i z_i \\ \sum_i x_i z_i & \sum_i y_i z_i & \sum_i z_i^2 \end{pmatrix} \, . \tag{6.9}$$

We can see that $\hat{n}\hat{n}^T$ is a symmetric matrix, which is expected since

$$(\hat{n}\hat{n}^T)^T = \hat{n}\hat{n}^T \,, \tag{6.10}$$

as $\boldsymbol{A}\boldsymbol{B}^T = \boldsymbol{B}^T\boldsymbol{A}^T$ and a symmetric matrix has the property: $\boldsymbol{A}^T = \boldsymbol{A}$.

6.2.2.1 *Eigenvalues of the orientation tensor*

As $\boldsymbol{T}$ is symmetric, it can be expressed in a diagonalised form

$$\boldsymbol{T} = \begin{pmatrix} \hat{\mu}_1 & \hat{\mu}_2 & \hat{\mu}_3 \end{pmatrix} \begin{pmatrix} \tau_1 & 0 & 0 \\ 0 & \tau_2 & 0 \\ 0 & 0 & \tau_3 \end{pmatrix} \begin{pmatrix} \hat{\mu}_1^T \\ \hat{\mu}_2^T \\ \hat{\mu}_3^T \end{pmatrix} \,, \tag{6.11}$$

where the eigenvectors $\hat{\mu}_1$, $\hat{\mu}_2$ and $\hat{\mu}_3$ are identical to those of matrix **B** in the Bingham distribution and τ_1, τ_2 and τ_3 are the eigenvalues. $\tau_1 + \tau_2 + \tau_3 = 1$ due to constancy of the trace ($\mathrm{Tr}(\boldsymbol{T}) = 1 = \mathrm{Tr}(\hat{n}\hat{n}^T)$).

In the coordinate system the axes of which are the principal eigenvectors of $\boldsymbol{T}$, the Bingham distribution has a simple form

$$f(\hat{n}; \boldsymbol{B}) = \frac{1}{c_B} \exp\left(\kappa(\hat{\mu}_1 \cdot \hat{n})^2 + \beta(\hat{\mu}_2 \cdot \hat{n})^2\right) = \frac{1}{c_B} \exp\left(\kappa \cos^2\theta + \beta \sin^2\theta \cos^2\phi\right) \,, \tag{6.12}$$

while

$$\hat{n}\hat{n}^T = \begin{pmatrix} \cos^2\theta & \sin\theta\cos\theta\sin\phi & \sin\theta\cos\theta\cos\phi \\ \sin\theta\cos\theta\sin\phi & \sin^2\theta\cos^2\phi & \sin^2\theta\sin\phi\cos\phi \\ \sin\theta\cos\theta\cos\phi & \sin^2\theta\sin\phi\cos\phi & \sin^2\theta\sin^2\phi \end{pmatrix} \,. \tag{6.13}$$

The particular components of $\boldsymbol{T}$ can be computed by integrating each component of $f(\hat{n}; \boldsymbol{B})\hat{n}\hat{n}^T$, over the unit sphere. It can be shown that for $i \neq j$, $\boldsymbol{T}_{ij} = 0$

($\int_0^{2\pi} \cos\theta d\theta = 0$ for all non-squared terms), so the diagonal components of $\boldsymbol{T}$ are equal to the respective eigenvalues, such that

$$\tau_1 = \boldsymbol{T}_{11} = \frac{1}{c_B} \int_0^{2\pi} d\phi \int_0^1 d\cos\theta \exp\left(\kappa \cos^2\theta + \beta \sin^2\theta \cos^2\phi\right) \cos^2\theta \,, \quad (6.14)$$

and

$$\tau_2 = \boldsymbol{T}_{22} = \frac{1}{c_B} \int_0^{2\pi} d\phi \int_0^1 d\cos\theta \exp\left(\kappa \cos^2\theta + \beta \sin^2\theta \cos^2\phi\right) \sin^2\theta \cos^2\phi \,, \quad (6.15)$$

these are $\frac{\partial c_B}{\partial \kappa}$ and $\frac{\partial c_B}{\partial \beta}$, repsectively, while $\tau_3 = 1 - \tau_1 - \tau_2$.

6.2.3 *Implementation of Bingham-NODDI*

The Bingham-NODDI model has been implemented in Matlab, as part of the *NODDI* Matlab toolbox[2]. In the implementation of Bingham-NODDI, we express the intra- and extra-neurite signals in terms of c_B, the normalisation constant of the Bingham distribution. We compute c_B using the numerical approximation implemented by Koev and Edelman 2006.

To compute A_{in}, we substitute Equation (6.1) into Equation (5.3)

$$\begin{aligned} A_{in} &= \frac{1}{c_B} \int_{S^2} \exp\left(\hat{n}^T \boldsymbol{B} \hat{n} - b d_i (\hat{q} \cdot \hat{n})^2\right) d\hat{n} \\ &= \frac{1}{c_B} \int_{S^2} \exp\left(\hat{n}^T \left(\boldsymbol{B} - b d_i \hat{q}\hat{q}^T\right) \hat{n}\right) d\hat{n} \\ &= \frac{1}{c_B} \int_{S^2} \exp\left(\hat{n}^T \boldsymbol{Q} \hat{n}\right) d\hat{n} \end{aligned} \quad (6.16)$$

As $c_B = \int_{S^2} \exp\left(\hat{n}^T \boldsymbol{B} \hat{n}\right) d\hat{n}$ (from Equation 6.2), A_{in} can be computed as

$$A_{in} = \frac{c_Q}{c_B} = \frac{{}_1F_1\left(\frac{1}{2}; \frac{3}{2}; \boldsymbol{Q}\right)}{{}_1F_1\left(\frac{1}{2}; \frac{3}{2}; \boldsymbol{B}\right)} \,, \quad (6.17)$$

2 http://nitrc.org/projects/noddi_toolbox

i.e. by working out the normalisation coefficients c_Q and c_B of the Bingham distributions, with the symmetric matrix $\boldsymbol{Q} = \boldsymbol{B} - bd_i\hat{q}\hat{q}^T$, and $\boldsymbol{B}$, respectively. This is an expression similar to those derived by Kaden et al. 2007 and Sotiropoulos et al. 2012.

To compute A_{en} we substitute Equation (6.1) into Equation (5.5) to express $\boldsymbol{D}_{en}$ in terms of the parameters of the Bingham distribution. $\boldsymbol{D}_{en}$ can be expressed in terms of its eigenvalues and eigenvectors as

$$\boldsymbol{D}_{en} = \begin{pmatrix} \hat{\mu}_1 & \hat{\mu}_2 & \hat{\mu}_3 \end{pmatrix} \begin{pmatrix} d_{\hat{\mu}_1} & 0 & 0 \\ 0 & d_{\hat{\mu}_2} & 0 \\ 0 & 0 & d_{\hat{\mu}_3} \end{pmatrix} \begin{pmatrix} \hat{\mu}_1^T \\ \hat{\mu}_2^T \\ \hat{\mu}_3^T \end{pmatrix} , \tag{6.18}$$

where $d_{\hat{\mu}_n}$ represents the diffusivity along the nth eigenvector of $\boldsymbol{D}_{en}$. Using Equation 5.5, this gives

$$d_{\hat{\mu}_1} = d_\perp + \int_{S^2} (d_\parallel - d_\perp)(\hat{\mu}_1 \cdot \hat{n})^2 f(\hat{n})\, d\hat{n} . \tag{6.19}$$

And $\frac{\partial c_B}{\partial \kappa} = \int_{S^2} (\hat{\mu}_1 \cdot \hat{n})^f(\hat{n})\, d\hat{n}$. So the diffusivities along the principal eigenvectors of $\boldsymbol{D}_{en}$ can be obtained by taking the partial derivative of c_B with respect to the corresponding concentration parameter

$$d_{\hat{\mu}_1} = d_\perp + (d_\parallel - d_\perp)\frac{\partial c_B}{\partial \kappa} , \tag{6.20}$$

$$d_{\hat{\mu}_2} = d_\perp + (d_\parallel - d_\perp)\frac{\partial c_B}{\partial \beta} . \tag{6.21}$$

We compute these derivatives numerically, using finite differences. The diffusivity along $\hat{\mu}_3$ is then

$$d_{\hat{\mu}_3} = d_\parallel + 2d_\perp - d_{\hat{\mu}_1} - d_{\hat{\mu}_2} , \tag{6.22}$$

using the fact that $\mathrm{Tr}(\boldsymbol{D}_{en}) = \mathrm{Tr}(\boldsymbol{D}(\hat{n})) = d_\parallel + 2d_\perp$.

6.2.4 *Model parameters*

Bingham-NODDI has the following model parameters:

- ν_{in}: intra-neurite volume fraction
- $d_{\parallel}$: intrinsic free diffusivity
- κ: concentration parameter of Bingham distribution
- β: concentration parameter of Bingham distribution
- $\hat{\mu}_1$: dominant orientation of Bingham distribution, characterised by the angles $\theta \in [0, \pi]$, $\phi \in [0, 2\pi]$
- $\hat{\mu}_2$: Primary dispersion orientation, characterised by the angle $\psi \in [0, \pi]$
- ν_{iso}: isotropic volume fraction
- d_{iso}: isotropic diffusivity

As shown in Section 6.2.1, the Bingham distribution has 5 degrees of freedom and only one angle is required to determine $\hat{\mu}_2$, once $\hat{\mu}_1$ is known. Thus only two extra parameters need to be determined for the orientation dispersion quantification for Bingham-NODDI compared to Watson-NODDI, namely the concentration parameter β and the angle, ψ.

The total number of model parameters estimated for Bingham-NODDI, when the diffusivities are fixed to typical values, as for Watson-NODDI (see Section 5.2.3), are 7. This includes ν_{in}, ν_{iso}, κ, β, θ, ϕ and ψ.

6.3 MICROSTRUCUTRE INDICES OF BINGHAM-NODDI

Metrics of neurite density, free water volume fraction, and dominant orientation are the same as Watson-NODDI as we only manipulate the probability distribution function used to characterise the orientation distribution of neurites in NODDI.

6.3.1 *Dispersion indices of Bingham-NODDI*

We quantify the dispersion characteristics of neurites using Bingham-NODDI, by generalising the orientation dispersion index (ODI) for Watson-NODDI[185]. We quantify the dispersion extent along $\hat{\mu}_2$ with the parameter

$$\mathrm{ODI}_P = \frac{2}{\pi} \arctan\left(\frac{1}{\kappa - \beta}\right) , \tag{6.23}$$

and that along $\hat{\mu}_3$ with

$$\mathrm{ODI}_S = \frac{2}{\pi} \arctan\left(\frac{1}{\kappa}\right) , \tag{6.24}$$

which both range between 0 and 1 for lowest and highest orientation dispersion, respectively. In the case of Watson distribution (Fig6.3.a), where $\beta = 0$, ODI_P and ODI_S are equal and reduce to ODI.

Table 6.1 summarises how these dispersion indices vary for a few configurations of the ODF, including the three configurations shown in the density plots in Figure 6.3. As the value of β is increased for the same κ, resulting in an increase in anisotropic dispersion, ODI_P increases while ODI_S remains constant. Thus, while their absolute values indicate the level of dispersion, the relative values of ODI_P and ODI_S are an indicator of dispersion anisotropy. The dispersion characteristics can also be represented in terms of the dispersion angles, α_P and α_S, quantifying the angle associated with the spread along $\hat{\mu}_2$ and $\hat{\mu}_3$ (see Table 6.1). Quantification of dispersion in terms of dispersion angles is valuable as it allows comparison of different ODFs, independent of their parameterisation.

An alternative representation of an ODF, with anisotropic orientation dispersion, is by describing it using the orthogonal measures of the overall dispersion and dispersion anisotropy. These enable separate quantification of the level of dispersion and that of anisotropic dispersion unlike ODI_P and ODI_S. These measures are described in the following sections.

6.3.1.1 *Overall dispersion index*

To estimate the overall orientation dispersion, we observe that the overall spread or dispersion of a multivariate normal distribution can be quantified

	ODI_P	ODI_S	ODI_{Tot}	DA_B	DA_T	α_P	α_S
$\kappa = 4, \beta = 0$	0.16	0.16	0.16	0	0	59.59°	59.59°
$\kappa = 4, \beta = 2$	0.30	0.16	0.22	0.5	0.19	81.36°	59.59°
$\kappa = 4, \beta = 4$	1	0.16	1	1	0.73	87.66°	59.59°
$*\kappa = 16, \beta = 0$	0.04	0.04	0.04	0	0	22.92°	22.92°
$\kappa = 16, \beta = 8$	0.08	0.04	0.06	0.5	0.04	34.66°	22.92°
$*\kappa = 16, \beta = 14$	0.30	0.04	0.11	0.91	0.35	81.36°	22.92°
$*\kappa = 16, \beta = 16$	1	0.04	1	1	0.94	87.66°	22.92°

Table 6.1: The values of the dispersion and dispersion anisotropy indices, corresponding to the various configurations of ODF, specified by the values of κ and β. The dispersion angles are an alternative way to represent the level of dispersion in an ODF and are quantified here as the angles corresponding to 95% spread along $\hat{\mu}_2$ and $\hat{\mu}_3$ and labelled as α_P and α_S, respectively. The configurations corresponding to the density plot in Figure 6.3 are highlighted by *. (ODI_P, ODI_S *&* ODI_{Tot} *are the primary, secondary and total dispersion indices, while* DA_B *&* DA_T *are the two dispersion anisotropy indices, as described in the main text.*)

as the determinant of its covariance matrix. Thus, we propose to estimate the total dispersion by

$$|\Sigma_{Bing}| = \sqrt{\left(\frac{1}{\kappa - \beta}\right)\left(\frac{1}{\kappa}\right)}\,, \tag{6.25}$$

which can be mapped to a finite range, similar to ODI_P and ODI_S, giving a measure of total dispersion

$$ODI_{Tot} = \frac{2}{\pi}\arctan\left(|\Sigma_{Bing}|\right)\,. \tag{6.26}$$

For Watson distribution, the overall orientation dispersion reduces desirably again to ODI. Thus for isotropic dispersion, the ODF can be completely parameterised by a single dispersion index, as done in Zhang et al. 2012. ODI_{Tot} reflects the level of overall dispersion and as shown in Table 6.1, it increases with increasing ODI_P or ODI_S (decreasing κ or increasing β).

6.3.1.2 *Dispersion anisotropy index*

We propose to measure the dispersion anisotropy of neurites with Bingham-NODDI using the index

$$\mathrm{DA_B} = \frac{2}{\pi} \arctan\left(\frac{\beta}{\kappa - \beta}\right) , \tag{6.27}$$

which has the value of 0 when $\beta = 0$ (isotropic dispersion) and 1 when $\kappa = \beta$, regardless of the actual magnitude of κ and β. $\mathrm{DA_B}$ provides a measure sensitive to changes in anisotropic dispersion, which may not change the overall dispersion. Thus $\mathrm{DA_B}$ is a useful measure to quantify the anisotropy, even in the WM tracts as coherent as the CC, which bends sharply.

Figure 6.4 summarises how the overall dispersion $\mathrm{ODI_{Tot}}$ and the orientation dispersion anisotropy $\mathrm{DA_B}$ vary with different combinations of values of the primary and secondary orientation dispersion indices ($\mathrm{ODI_P}$ and $\mathrm{ODI_S}$). The relative values of $\mathrm{ODI_P}$ and $\mathrm{ODI_S}$ reflect the level of dispersion anisotropy, while $\mathrm{ODI_{Tot}}$ changes with both $\mathrm{ODI_P}$ and $\mathrm{ODI_S}$.

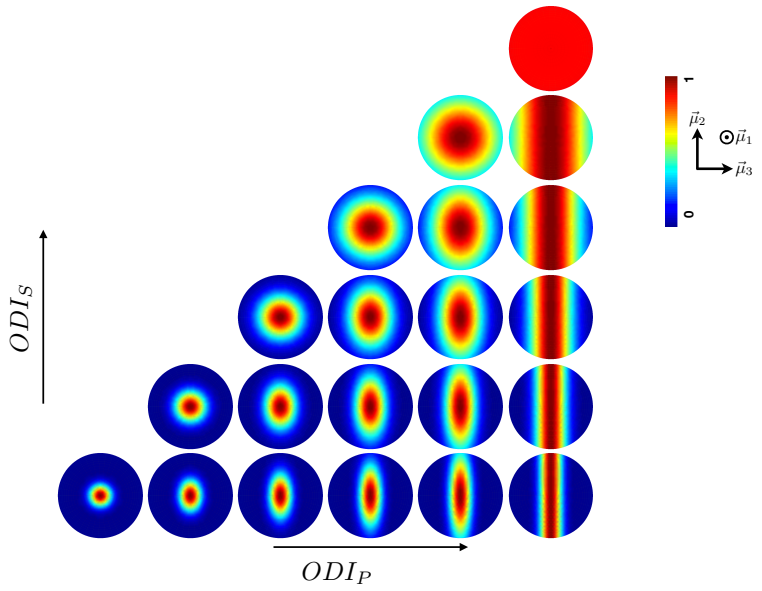

Figure 6.4: Schematic to summarise how the presented indices of Bingham-NODDI vary for various orientation configurations. The relative values of the primary and secondary orientation dispersion indices indicate the level of orientation dispersion anisotropy, as when $\mathrm{ODI_P}$ is increased, while keeping $\mathrm{ODI_S}$ constant (going from left to right within the same row), $\mathrm{DA_B}$ also increases. When the difference in the dispersion extent along the two dispersion orientations is maximum, $\mathrm{DA_B}$ is maximum. $\mathrm{ODI_{Tot}}$ changes when either $\mathrm{ODI_P}$ or $\mathrm{ODI_S}$ change.

6.3.2 *Alternative metrics of Bingham-NODDI*

We can summarise the orientation distribution of the neurites in each voxel in terms of the Orientation Tensor (OT), similar to the 3-D rendering of the diffusion tensors (DT)[22] to describe the diffusion characteristics. This provides a visualisation of the orientation distribution of neurites, as well as provide summary metrics to quantify the orientation distribution of neurites.

6.3.2.1 *Orientation coherence indices*

As τ_1 and τ_2 reflect the relative concentrations of neurites along $\hat{\mu}_1$ and $\hat{\mu}_2$, respectively, we call these the *Orientation Coherence Indices (OCI)*. We can use OCI to quantify the dispersion of neurites as they have a finite range, unlike κ and β, which range between 0 and ∞. The orientation dispersion indices defined here and in Zhang et al. 2012, describe the dispersions and thus have an inverse relationship with τ_1 and τ_2. ODI is an arbitrary transformation to map κ to a finite range from $0 \to \infty$ to $1 \to 0$.

6.3.2.2 *Dispersion anisotropy index*

To quantify the dispersion anisotropy of neurites, we can define the planarity measure[179] of the *orientation tensor,* $\boldsymbol{T}$

$$\mathrm{DA}_T = \frac{(\tau_2 - \tau_3)}{\tau_1} \,. \tag{6.28}$$

$\boldsymbol{T}$ is the second moment of an ODF and τ_1, τ_2 and τ_3 are its eigenvalues, which are functions of κ and β, as described in Section 6.2.2.1. DA_T ranges from 0 for isotropic dispersion, to 1 for maximum dispersion anisotropy. Intuitively, DA_T is a product of the overall dispersion, ODI_{Tot} and DA_B. Thus this quantification of anisotropic dispersion assigns lower value to very coherent tracts like the CC, despite differences in the primary and secondary dispersion values.

6.3.2.3 *Fractional anisotropy index*

Similarly to Jespersen et al. 2012, we can utilise the fractional anisotropy of $\boldsymbol{T}$, which is analogous to that of the diffusion tensor, i.e.:

$$\mathrm{FA}_{OT} = \sqrt{\frac{3}{2}\frac{(\tau_1 - \bar{\tau})^2 + (\tau_2 - \bar{\tau})^2 + (\tau_3 - \bar{\tau})^2}{{\tau_1}^2 + {\tau_2}^2 + {\tau_3}^2}} \,, \tag{6.29}$$

where τ_i denote the eigenvalues of $\boldsymbol{T}$ and $\bar{\tau} = \mathrm{Tr}(OT)/3 = 1/3$. FA_{OT} defines the anisotropy of the orientation tensor and thus quantifies the extend of coherence in the distribution of neurites about the dominant orientation, $\hat{\mu}_1$.

6.3.3 *Comparison of the two quantifications of Bingham-NODDI indices*

It's worthwhile to compare how DA_B differs from the dispersion anisotropy index, DA_T proposed in Tariq et al. 2014a.

DA_B is an important measure because it is orthogonal to the overall dispersion measure ODI_{Tot} and quantifies specifically the anisotropy in the orientation dispersion of neurites, unlike DA_T, which is weighted by the overall dispersion. We can see this from Table 6.1 where both DA_B and DA_T change with change in dispersion anisotropy, but when κ and β are changed with their ratio remaining the same (for e.g. $\kappa = 4, \beta = 2$ to $\kappa = 16, \beta = 8$), DA_B remains constant while DA_T decreases. Thus, DA_B reflects purely the dispersion anisotropy about $\hat{\mu}_1$, while DA_T reflects the change in dispersion as well as the anisotropy. Anisotropic dispersion can thus be identified as the difference between ODI_P and ODI_S but quantified directly by the value of DA_B.

6.4 SUMMARY AND DISCUSSION

This chapter describes the proposed method to allow a comprehensive description of the neurite orientation dispersion to characterise complex features of neurite configuration, like dendritic arborizations and fanning/bending of bundles of axons. We propose a NODDI model that incorporates the Bingham distribution[26,67] to enable the quantification of dispersion anisotropy in neurite orientation distributions.

We modify the ODF used to model the dispersion of neurites in NODDI and a specific index to characterise anisotropic orientation dispersion is proposed. Indices are presented to quantify orientation dispersion anisotropy, as well as the overall dispersion, which are based specifically on the ODF used here and some based on generic ODFs. Watson-NODDI can only estimate the overall dispersion and will not be sensitive to changes in dispersion anisotropy, while Bingham-NODDI can capture this subtle difference in the orientation distribution.

We quantify anisotropic orientation dispersion of the neurites in terms of the principal components of the Bingham distribution, which describe the extent

of orientation dispersion about the dominant orientation, separately along the primary and secondary dispersion orientations. We present indices derived from the parameters of the Bingham distribution to quantify anisotropic orientation dispersion, along with the standard NODDI indices of neurite morphology. The novel indices of Bingham-NODDI allow us to distinguish the changes in overall dispersion from dispersion anisotropy. Discussion of the main limitations of the proposed model are in Chapters 10 and 16.

In the following chapters, we assess the accuracy and precision of the indices of Bingham-NODDI using *in silico* and *in vivo* DW-MRI data.

7

BINGHAM-NODDI: *IN SILICO* DATA EXPERIMENTS

This chapter presents an evaluation of the Bingham-NODDI indices using *in silico* data. The aim is to assess parameter estimation against known ground truth and to establish *in vivo* feasibility with a standard acquisition protocol. DW-MRI data is synthesised to obtain the signal corresponding to known ground-truth, which is used to evaluate the estimated parameters against. Bingham-NODDI is characterised in terms of its estimability, the choice of acquisition protocol on the estimability, and its performance relative to Watson-NODDI.

The following sections describe how the synthetic data is generated, the model fitting procedure to obtain estimated parameters of the proposed model and finally the evaluation of their estimability.

7.1 SYNTHETIC DATA

7.1.1 *Synthetic tissue model*

Diffusion signal is synthesised using a multi-compartment model as in Zhang et al. 2011, which simulates signals for various neurite densities and diameters while accounting for their orientation dispersion. The Bingham distribution is substituted as the ODF to generate DW-MRI signals expected from neurite substrates with orientation dispersion anisotropy.

7.1.2 *Ground truth parameters*

Data is simulated for all possible combinations of the set of parameters shown in Table 7.1, with the restriction $\kappa \geqslant \beta$ (by definition of the Bingham distribution), to test Bingham-NODDI for various configurations of tissue microstruc-

Parameter	Ground-truth values
v_{in}	{0.2, 0.4, 0.6, 0.8}
v_{iso}	{0.0}
α	{0.25, 0.5, 1, 2} μm
κ	{0, 1, 2, 3, 4, 5, 6, 7, 16}
β	{0, 1, 2, 3, 4, 5, 6, 7, 16}
$\hat{\mu}_1$ and $\hat{\mu}_2$	250 uniform random rotations

Table 7.1: The ground-truth parameters used to generate the synthetic data. v_{in} and v_{iso} represent the intra-neurite and isotropic volume fractions, while κ and β are the concentration parameters of the Bingham distribution. $\hat{\mu}_1$ represents the dominant orientation and $\hat{\mu}_2$ the primary dispersion orientation. α denotes the axon radii.

ture expected from the GM and WM in the human brain. A total of 180,000 different combinations of ground truth parameters are evaluated.

The ground truth parameters consist of various non-zero axon radii to evaluate the consequence of not modelling the axon radii in Bingham-NODDI. 250 uniform random rotations of the Bingham distribution are obtained, for each tissue configuration, to see if there is any bias in estimates due to the orientational variance of neurites. The random rotations are obtained using the method in Shoemake 1992.

Rician noise is added to the simulated signals, to represent the typical clinical SNR of 20. This is done by adding random numbers sampled from a Gaussian distribution, with $\bar{\mu} = 0$, $\sigma = 0.05$ to the real and imaginary (set to zero here) part of the synthesised signal. The magnitude of this complex signal is then taken to represent MRI signal with added Rician noise.

7.1.3 *Acquisition protocol*

Synthetic data is generated for each instantiation of the ground truth parameters using the four-shell protocol utilised in Zhang et al. 2012 and detailed in Table 7.2 (explained in Section 8.1.1). We assess the optimised NODDI protocol, N1 as well as subsets of it with fewer orientations sampled (N2 and N3). The comparison is done with two single shell protocols (S1 and S2), which represent standard b-values acquired for DW-MRI with clinical scanners.

Protocol	Settings
All	Full data set (180)
N1	$b = 711 s/mm^2 (30)$ & $b = 2855 s/mm^2 (60)$
N2	$b = 711 s/mm^2 (15)$ & $b = 2855 s/mm^2 (30)$
N3	$b = 711 s/mm^2 (10)$ & $b = 2855 s/mm^2 (20)$
S1	$b = 1000 s/mm^2 (30)$
S2	$b = 2000 s/mm^2 (60)$

Table 7.2: The list of imaging protocols used for evaluation of the parameters estimated. All denotes the complete four-shell protocol, while the rest of the protocols are two-shell (N1, N2 and N3) and single-shell (S1 and S2) subsets of it. The number in brackets denote the number of gradient orientations sampled for the diffusion-weighted acquitision for each protocol. The total acquisitions at $b = 0 s/mm^2$ are 12 (3 b0s are utilsied for each HARDI shell).

7.1.4 *Model fitting procedure*

The *NODDI* Matlab toolbox[1] is used for fitting the model to the synthetic, which provides the maximum likelihood estimates using the two-stage fitting procedure described in Zhang et al. 2012. In the first stage, a crude estimate of the parameters is obtained from a grid of parameters representing typical *in vivo* tissue configurations. In the second stage, the parameters are refined by utilising a Gauss-Newton optimisation scheme (LM algorithm[2]), to obtain the maximum likelihood parameters. The toolbox is modified to include the Bingham distribution as the ODF, which uses the numerical implementation proposed by Koev and Edelman 2006, to compute the hypergeometric function in Equation (6.3).

Diffusivities are fixed to typical values of $d_i = 1.7 \times 10^{-9} m^2 s^{-1}$ and $d_{iso} = 3.0 \times 10^{-9} m^2 s^{-1}$, and it is assumed that $d_{\parallel} = d_i$, as in Zhang et al. 2012. The noise level for model fitting is estimated for each set of synthesised signal, as the standard deviation of the measurements at $b = 0$. The only explicit constraint in the fitting procedure is applied to κ and β values ($\leqslant 64$), for numerical stability of the implementation[99]. But this is not a practical issue, as it is shown in Zhang et al. 2011 that at very high levels of coherence, the difference in diffusion signal is negligible.

From the estimated parameters of Bingham-NODDI, namely ν_{in}, κ, β, ν_{iso}, S_0, θ, ϕ, ψ, the indices ODI_P, ODI_S, ODI_{Tot}, DA_B and the parameters of $\mathbf{T}$ are

1 http://nitrc.org/projects/noddi_toolbox
2 using Matlab 2013a inbuilt function: *fmincon*

computed, using the expressions described in Section 6.3.1. Watson-NODDI is also fitted to the synthetic and *in vivo* datasets for model comparison analysis.

7.2 SYNTHETIC DATA EXPERIMENT

The synthetic data experiment fits the Bingham-NODDI model to the simulated measurements, using known model parameters. The approach allows determination of the accuracy and precision of parameter estimation in the most idealised conditions to assess the intrinsic ability to estimate the model parameters, undersampling constraints imposed by the measurement procedure. The simulated data is obtained as detailed in section 7.1, which uses the same parameterisation of the ODF as Bingham-NODDI, but models neurites with non-zero radii.

For a meaningful evaluation of the tissue parameters, the estimated indices are assessed separately for GM and WM regions. This is done by separating the synthetic data representing typical values of the parameters for each tissue.The sets of parameter combinations that belong to each tissue type are learned from the parameters estimated from the *in vivo* data (chapter 8).

7.2.1 *Parameter estimation*

7.2.1.1 *Design*

The estimates from Bingham-NODDI fitting to the large set of tissue configurations described in Section 7.1 are used for parameter estimation analysis. For each model parameter, the absolute estimation errors are pooled over instances of the tissue configurations with the same orientation-invariant parameters but different orientations. The mean and the standard deviation of the pooled errors are computed to quantify the accuracy and precision of the model parameters.

The results are shown for estimation based on the two-shell protocol (N1) optimised for Watson-NODDI in Zhang et al. 2012, as it is currently the standard *in vivo* protocol for NODDI. The results for the other protocols (not shown) exhibit similar trends. The parameter estimation with Watson-NODDI fitting is also evaluated to compare with Bingham-NODDI results.

7.2.1.2 *Results for Bingham-NODDI parameters*

Figure 7.1 summarises the error statistics of estimating the volume fraction parameters. The results show that both parameters can be estimated accurately and precisely (compared to the level of noise) with only a weak dependence on ν_{in}, κ and β. The estimability reduces slightly for lower ν_{in}. This is expected as the reduction in the fraction of restricted diffusion results in increased signal attenuation, which lowers the effective SNR. The weak dependence of the estimability on the concentration parameters reflects the reduced accuracy and precision in estimating large values of κ and β (results not shown). The underestimation of κ and/or β when they take large values is compensated by a slight overestimation of ν_{in}.

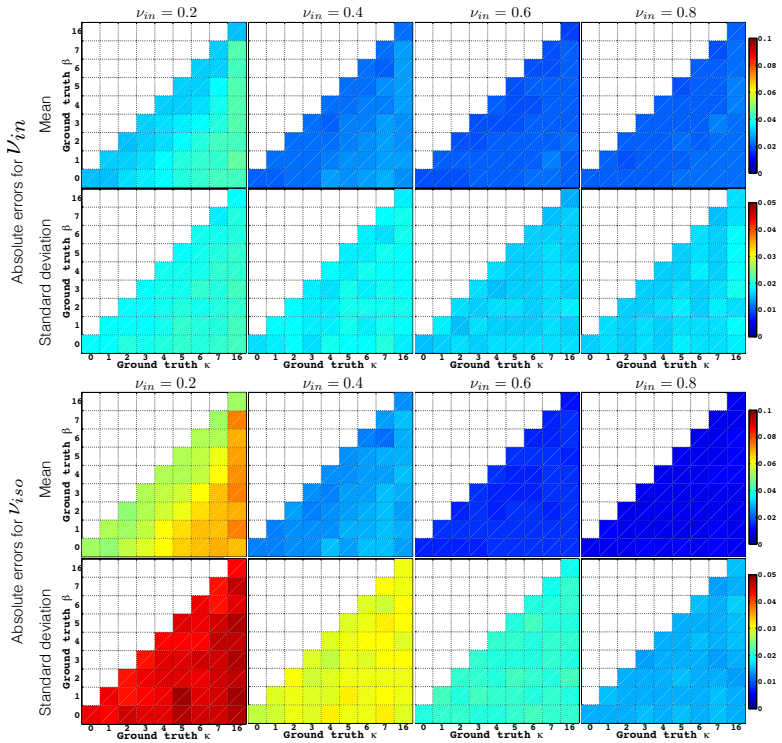

Figure 7.1: [Errors in the estimation of ν_{in} (top panel) and ν_{iso} (bottom panel) using Bingham-NODDI, for the optimised NODDI protocol (N1). Each panel shows the mean (top row) and the standard deviation (bottom row) of the absolute errors. Each column corresponds to the ground-truth value of ν_{in}, as indicated. Each pixel corresponds to one combination of ground-truth κ and β values.

Figures 7.2 and 7.3 summarise the error statistics of estimating the orientation dispersion indices of Bingham-NODDI. We find that for most of the plausible neurite configurations, the dispersion indices can be determined accurately and precisely. The results show that the estimability of ODI_P, ODI_S and ODI_{Tot} depends strongly on ν_{in} and the underlying orientation distribution of neurites. The estimation of ODI_P and ODI_{Tot} is also affected by the

level of anisotropic dispersion. For all the parameters, the estimability reduces for lower values of ν_{in}, which is expected as reduced ν_{in} means the measured signal has weaker orientation dependence.

The errors and variability for estimation of the dispersion indices are high when the underlying ODF is isotropic. This is expected due to noise-induced anisotropy (also seen for the DT in Pierpaoli et al. 1996), when the underlying ODF is isotropically distributed either about all orientations ($\kappa = 0$) or one of the orientations ($\beta = 0$ or $\kappa = \beta$). The error and variability are the highest at the corresponding singularities for the specific orientation dispersion index. These findings are consistent with the estimation of ODI for Watson-NODDI[185], which was found to be the hardest for the highest level of overall dispersion (corresponds to $\kappa = 0$, where all dispersion parameters are hard to estimate).

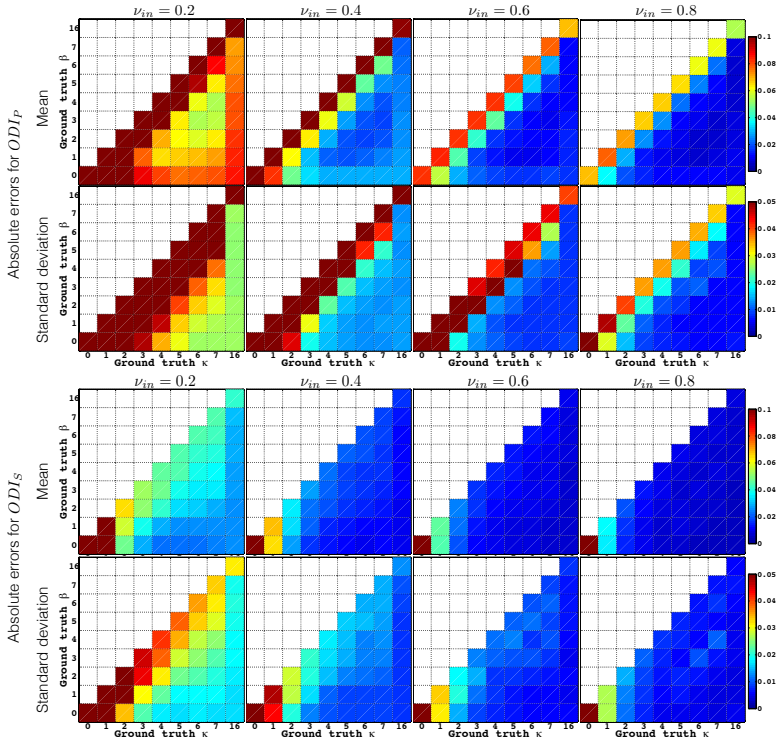

Figure 7.2: As Figure 7.1 but showing the statistics of estimation errors of ODI_P and ODI_S.

Figure 7.4 summarises the estimability of the dispersion anisotropy indices DA_B and DA_T. Our results indicate that dispersion anisotropy is harder to estimate than the metrics of dispersion, but the estimation errors and variability are still modest. We find that the estimation of the anisotropy parameters also depends strongly on ν_{in}, as well as the underlying ODF. Like the dispersion indices, the estimation of the anisotropy indices is harder when ν_{in} is low, as well as when the ODF is isotropically dispersed. The estimation of DA_B is

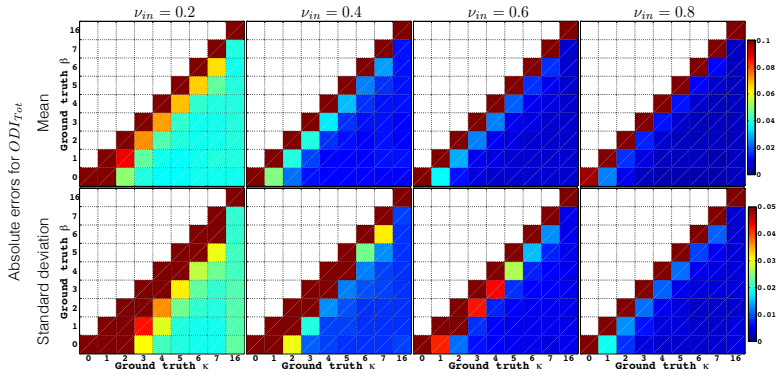

Figure 7.3: As Figure 7.1 but showing the statistics of estimation errors of $\mathrm{ODI}_{\mathrm{Tot}}$.

hardest when $\beta = 0$, and for DA_T when $\kappa = \beta$ and $\kappa = 0$, which correspond to an isotropic ODF at the singularity for the specific index. The estimation of DA_B is also compromised when κ is high, corresponding to poor estimability of κ and β (results not shown). We note that DA_T has much lower errors and variability than DA_B, which is expected as $\mathbf{T}$ is a second order approximation of the Bingham distribution.

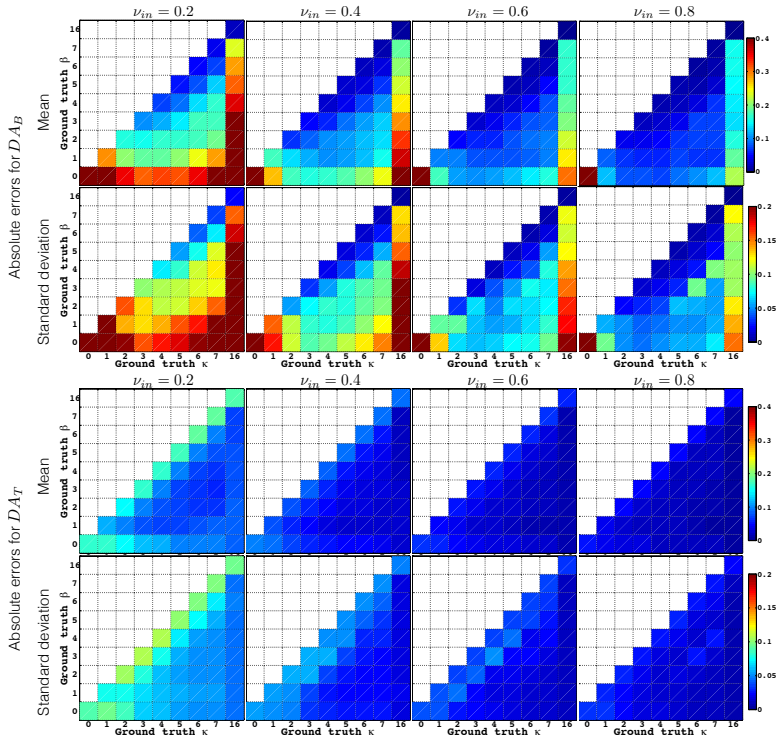

Figure 7.4: As Figure 7.1 but showing the statistics of estimation errors of DA_B and DA_T.

The errors and standard deviations for estimating the orientations $\hat{\mu}_1$ and $\hat{\mu}_2$ are shown in Figure 7.5. These errors are quantified as the angles between the estimated and the ground-truth orientations. We find that the orientations of the Bingham distribution can be estimated accurately and precisely, for all

configurations for which they are well-defined. For $\hat{\mu}_1$ the bias and variability of the estimates is very low for most combinations of the concentration parameters and is high only when $\kappa = \beta = 0$ and $\kappa = \beta > 0$, i.e. for configurations where $\hat{\mu}_1$ is not well defined (see Figure 6.3.c). The estimation of $\hat{\mu}_2$ is more variable, especially for very low ν_{in}. The configurations where the errors and variability are consistently high are also the ones where $\hat{\mu}_2$ is not well defined i.e. $\kappa = \beta = 0$, $\kappa = \beta > 0$ (Figure 6.3.c) and when $\beta = 0$ (Figure 6.3.a). Increasing ν_{in} reduces the errors and variability for estimation of both the orientations, in the regions where they are well-defined.

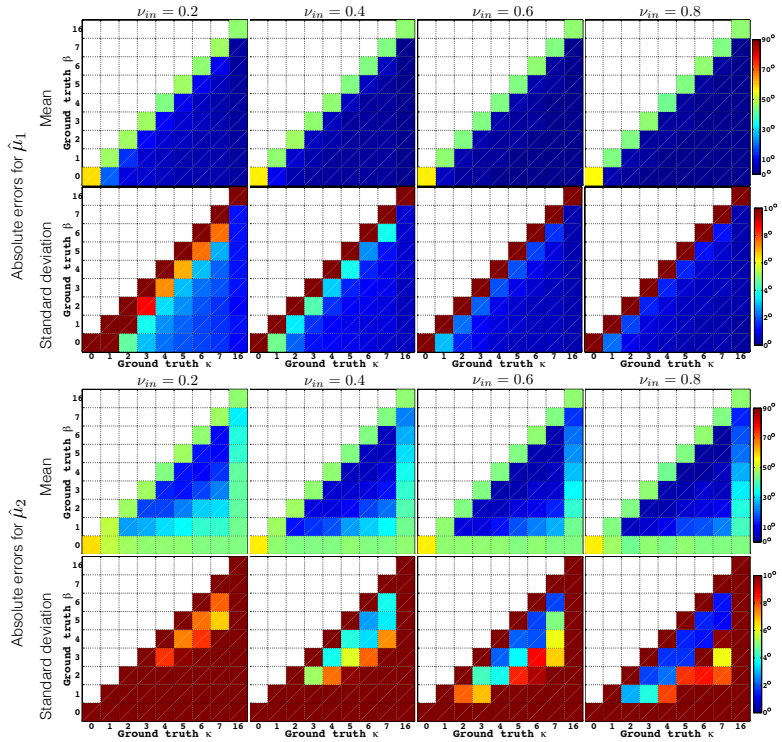

Figure 7.5: As Figure 7.1 but showing the statistics of estimation errors of $\hat{\mu}_1$ and $\hat{\mu}_2$. The errors correspond to the mean angles between the estimated and the ground truth orientations, for each pool.

7.2.1.3 *Results for Watson-NODDI parameters*

The interesting finding from the estimability analysis on the Watson-NODDI parameters is that the simplified ODF does not have a significant impact on the estimation of its parameters. The estimability of the volume fractions, overall dispersion, and the dominant orientation, estimated from Watson-NODDI, shows very similar errors and variability to those estimated using Bingham-NODDI, with the same trends with respect to the ground-truth ν_{in}, κ and β values. However, for low ν_{in} the estimation of ODI_{Tot} using Watson-NODDI has less variability compared to Bingham-NODDI (comparing Figures 7.3 and

7.6). Thus, Watson-NODDI provides an accurate estimation of the volume fractions, the dominant orientation, and the overall dispersion, but we are unable to determine dispersion anisotropy about $\hat{\mu}_1$, or characterise the dispersion extent along $\hat{\mu}_2$ and $\hat{\mu}_3$ separately.

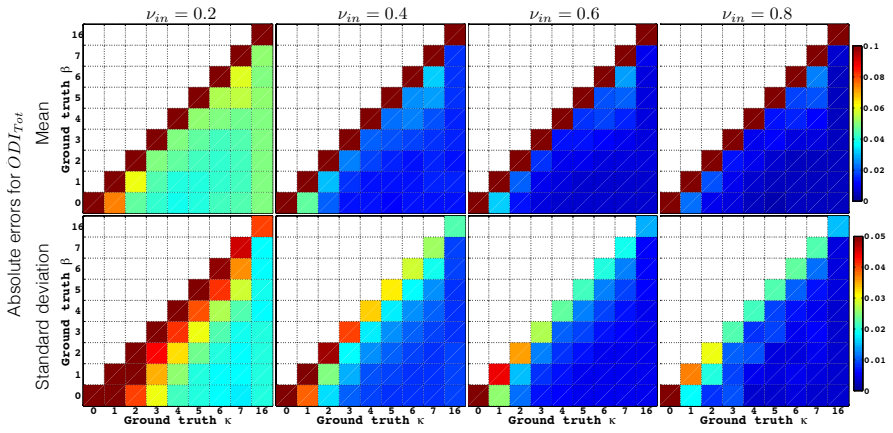

Figure 7.6: As Figure 7.1 but showing the statistics of estimation errors of $\mathrm{ODI}_{\mathrm{Tot}}$, using Watson-NODDI.

It is additionally seen that the Bingham-NODDI estimation of the primary orientation dispersion is more accurate compared to that of Watson-NODDI, but also more variable (see simulation results in Appendix C).

7.2.2 *Protocol comparison*

The aim of the protocol comparison is to assess if it is possible to accurately and precisely estimate the Bingham-NODDI parameters, using the optimised NODDI protocol, **N1**. It is also assessed if the acquisition can be further reduced without affecting the quality of estimated parameters, as found true for Watson-NODDI in Zhang et al. 2012. The evaluation of the four-shell protocol (**All**) is included to determine if using the estimates from this protocol as a pseudo ground-truth for the *in vivo* experiment is a sensible thing to do.

7.2.2.1 *Design*

The estimated parameters obtained from fitting Bingham-NODDI are compared to the data acquired using the protocols listed in Table 7.2, separately for data representing each set of tissue configurations. To assess the protocols in a way that is relevant for *in vivo* data, the synthetic data is grouped into classes representative of the GM and WM tissue.

For each tissue type, parameter estimation is evaluated by pooling together the data with least variability in the estimation errors, as determined by the

estimability analysis in Section 7.2.1. The mean and standard deviations of the errors are plotted for all the parameters, for each pool of ground truth values.

The estimation of the orientations was found to be dependent on the level of orientation dispersion anisotropy (Section 7.2.1), for all ν_{in}. So the orientations are evaluated with respect to the ground truth value of DA_B. The results are presented for the novel parameters of Bingham-NODDI, as well as $\hat{\mu}_1$, as the errors are evaluated here with respect to the varying levels of anisotropy.

7.2.2.2 *Results*

The results for the estimation of ν_{in} and ν_{iso} are consistent with the findings for the original model Zhang et al. 2012, namely that a multi-shell protocol is required to accurately estimate the volume fractions.

The errors in estimation of ODI_P, ODI_S and ODI_{Tot} are summarised in Figures 7.7 and 7.8. It can be seen that a single shell with a high b-value is sufficient to estimate the dispersion indices accurately and increasing the number of gradients sampled in the protocol increases the accuracy of the estimates made. The higher values of dispersion are harder to estimate, and the errors and variability are higher for GM, i.e. low ν_{in}. All these trends are consistent with those for ODI in Zhang et al. 2012.

The results for the estimation of DA_B and DA_T are shown in Figure 7.9. The results show that as with the dispersion indices, a single-shell protocol is sufficient to estimate dispersion anisotropy, although the errors are larger in magnitude. Similar to the dispersion indices, the ground-truth value of the DA_B has an impact on the estimation and higher bias and variance is seen when the dispersion about $\hat{\mu}_1$ is completely isotropic or anisotropic, as expected (Section 6.2.1). The estimation of DA_T follows the same pattern in estimability for the various protocols and ground-truth values, but as $\mathbf{T}$ is a second order approximation of the ODF, the estimates are more stable.

Errors in estimation of the orientations, quantified as the mean angle between the estimated and the true orientation, are shown in Figure 7.7. As with the dispersion indices and the dispersion anisotropy measures, the orientations can be accurately estimated with a single-shell protocol. However, for a very high level of dispersion anisotropy, all the protocols perform equally, which is expected as both $\hat{\mu}_1$ and $\hat{\mu}_2$ are not well defined for very high dispersion anisotropy (Figure 6.3.c). Similarly, the protocol used has very little effect on estimation of $\hat{\mu}_2$ for isotropic dispersion about $\hat{\mu}_1$, where $\hat{\mu}_2$ is not well defined (Figure 6.3.a).

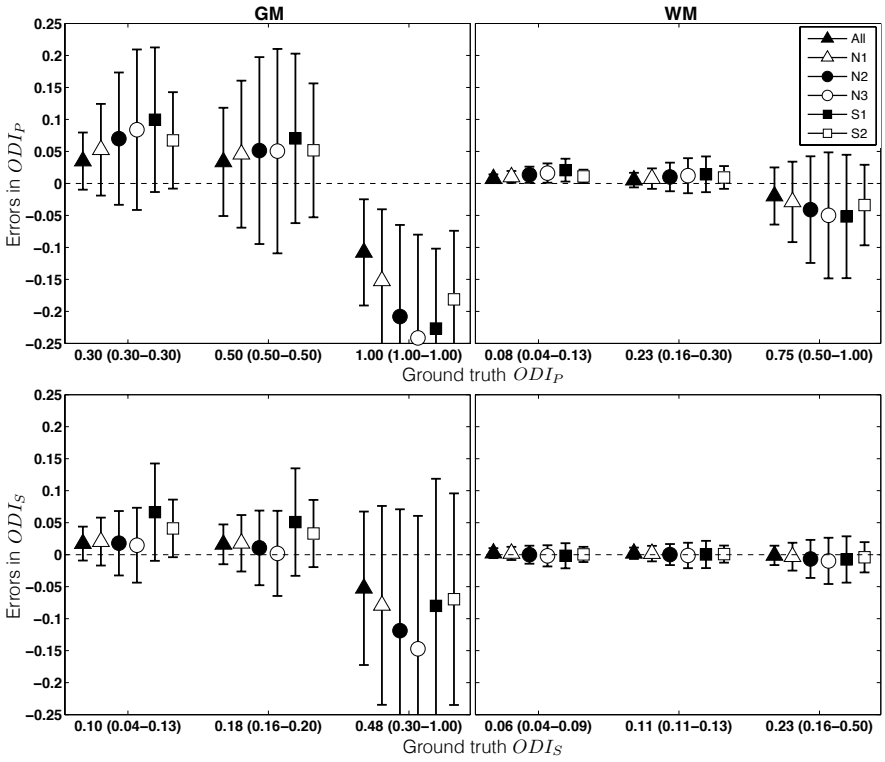

Figure 7.7: Errors in the estimation of $\mathrm{ODI_P}$ and $\mathrm{ODI_S}$ obtained from the synthetic data experiment using different protocols as indicated by the symbols. The results are shown separately for parameters representing the GM and WM tissue, obtained using Bingham-NODDI, for the various ground-truth values of the respective parameters. The ground-truth values shown are the mean values in each pool, with the range of included values in the brackets.

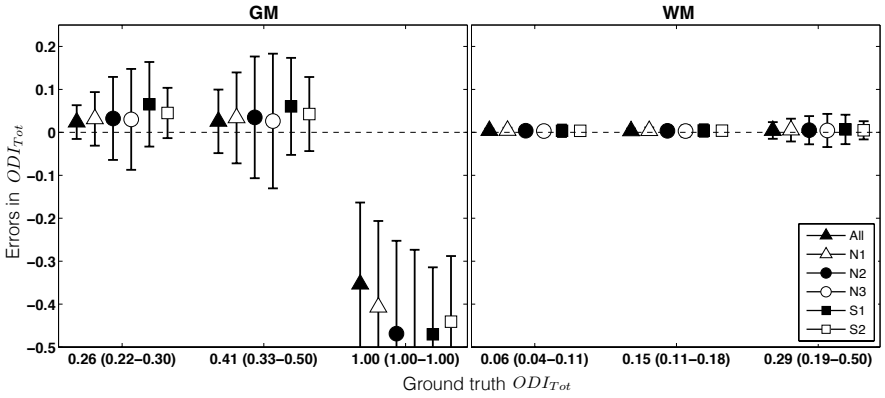

Figure 7.8: As Figure 7.7, but for $\mathrm{DA_{Tot}}$

7.3 SUMMARY AND DISCUSSION

Here we have presented experiments to systematically evaluate the ability of the proposed model to recover the key parameters of anisotropic orientation dispersion with standard NODDI protocol, using *in silico* data.

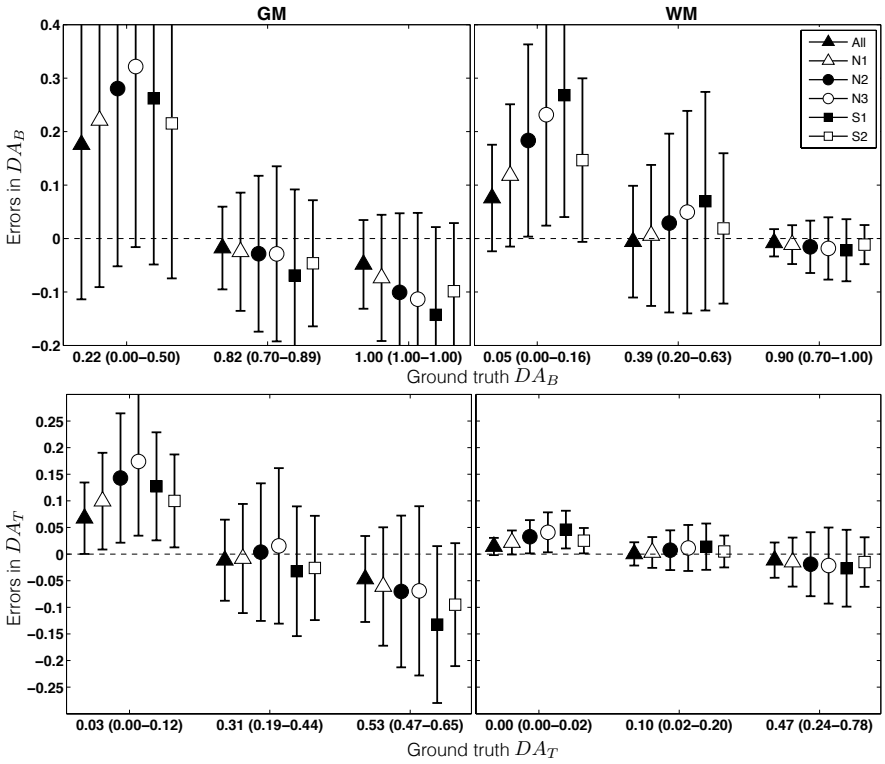

Figure 7.9: As Figure 7.7, but for the dispersion anisotropy indices, $\mathrm{DA_B}$ and $\mathrm{DA_T}$.

The results demonstrate that the parameters of the proposed model can be estimated without additional acquisition requirements over the standard NODDI protocol. Thus anisotropic dispersion can be determined with a clinically feasible data. We additionally find that the original NODDI model is robust to the effects of anisotropic orientation dispersion when the quantification of anisotropic dispersion is not of interest.

Estimation of the dispersion indices of Bingham-NODDI follow trends consistent with the Watson-NODDI dispersion index. A single shell with a high b-value is sufficient to estimate the dispersion indices accurately and increasing the number of gradient orientations sampled increases the accuracy of the estimates. The anisotropy measures also have the same trends in protocol comparison as the dispersion indices, but the errors are higher in magnitude. For the orientations, the same trends are seen as for the dispersion indices, except when they are not well-defined (Figure 6.3.c for $\hat{\mu}_1$ and Figure 6.3.a and c for $\hat{\mu}_2$), where the errors and variability are very high and the protocol used has very little impact on parameter estimation.

A limitation of the presented *in silico* experiments is that the synthetic signal is simulated using a more complex version of the fitted model, rather than synthesising the tissue itself, for example by using Monte-Carlo (MC) simula-

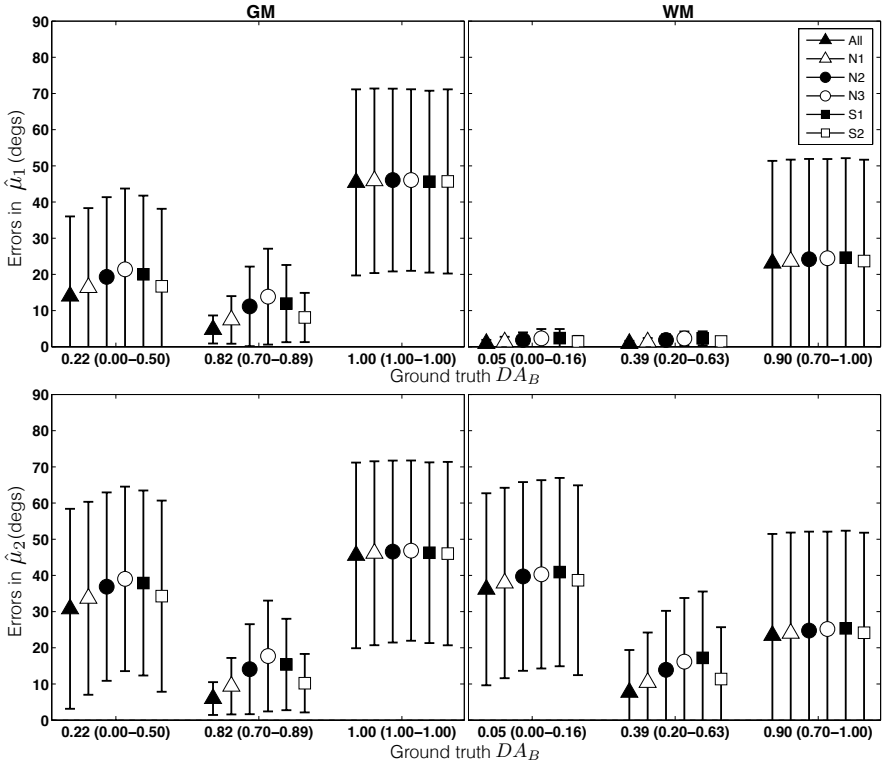

Figure 7.10: As Figure 7.7, but for errors in estimation of the orientations, $\hat{\mu}_1$ and $\hat{\mu}_2$, quantified as the angle between the ground-truth and the estimated orientation. The data is separated according to the ground-truth values of DA_B

tions. The reason is the current unavailability of a framework to incorporate orientation dispersion within a tissue substrate for MC simulations.

Another limitation of the presented simulations is that the parameters are only evaluated for $v_{iso} = 0$, i.e. regions with a partial volume of the WM with CSF are not represented in the simulations. It would be very interesting to assess how the model parameters behave in the presence of higher volume fraction of an isotropic compartment, a practical issue usually encountered in DW-MRI studies[77]. Adding an isotropic compartment in the synthetic data potentially would also make the model fitting less stable and it would be interesting to assess any such impact.

Further discussion of the results of this chapter is in Chapter 10. The next chapter carries out a similar evaluation of the estimability of the model parameters of Bingham-NODDI, using *in vivo* data of a healthy volunteer.

8

BINGHAM-NODDI: *IN-VIVO* DATA EXPERIMENTS

This chapter presents an evaluation of the Bingham-NODDI indices using *in vivo* data acquired on a healthy adult volunteer, to determine the suitability of Bingham-NODDI for the characterisation of brain tissue microstructure. The aim is to establish *in vivo* feasibility of the proposed model and assess parameter estimation with standard acquisition protocol.

8.1 DATA ACQUISITION AND PROCESSING

This section describes the data acquired for *in vivo* assessment of Bingham-NODDI indices, as well as the model fitting procedure and the pre-processing applied to the data.

8.1.1 In vivo *data*

The DW-MRI data acquired for Zhang et al. 2012 is used in this study, which consists of data acquired for one healthy volunteer (male, 35 years), with informed consent and approval of the local research ethics committee. The *in vivo* images were acquired on a $3\boldsymbol{T}$ Philips Achieva clinical scanner with $|\boldsymbol{G}|_{max} = 60\text{mT/m}$, using a 32-channel head coil. The acquisition consists of a rich four-shell HARDI protocol, of which the optimised NODDI protocol is a subset. The acquisition uses an EPI readout with matrix size 112×112, over a field of view (FOV) of $224 \times 224\text{mm}^2$ and slice thickness of 2mm. This results in Isotropic voxels of 2mm are obtained in 25 minutes for optimised NODDI protocol, and another 25 minutes for the additional HARDI shells.

The NODDI protocol consists of two HARDI shells, the first with $b = 711\text{s/mm}^2$ and 30 gradient directions and the second with $b = 2855\text{s/mm}^2$

and 60 gradient directions, with 9 b=0 images[1]. The echo time TE=78ms and repetition time TR=12.5s are the same for all measurements (see Zhang et al. 2012). The two additional HARDI shells consist of $b = 1000 s/mm^2$ and $b = 2000 s/mm^2$, with 30 and 60 gradient directions, respectively. Different b-values are achieved by varying the gradient strength while holding the diffusion time constant. This minimises the sensitivity of acquired data to axon diameters, making the protocol suitable for our model of zero-radius cylinders for neurites.

The full four-shell protocol is used as a pseudo *ground-truth* to test the *in vivo* performance of the model, as done in Zhang et al. 2012. Additionally, parameters estimated for various subsets of the full data-set are evaluated, to determine whether the Bingham-NODDI indices can be estimated using a reduced orientation sampling scheme. The various combinations of protocols compared are detailed in Table 7.2.

8.1.2 *Model fitting procedure*

The model fitting procedure used is the same as used for *in silico* data evaluations, described in Section 7.1.4. Briefly, this involves the two-stage fitting procedure to obtain the maximum-likelihood estimates of the model parameters[185], with diffusivities fixed to typical values.

8.1.3 *Pre-processing*

A mask is manually drawn on the acquired data, to extract the brain parenchyma, using ITK-SNAP[182]. Only the regions within this mask are used for fitting the models. For a meaningful evaluation of the tissue parameters, the parameters are assessed separately for GM and WM regions.

A very simple scheme, utilising the DT metrics, is used to segment the brain parenchyma, to get the broad trends in the GM and WM regions. The CSF is taken to be regions where the MD $\geqslant$ 80% of the free diffusivity in the brain ($d_{iso} = 3.0 \times 10^{-9} m^2 s^{-1}$). The WM and GM are then partitioned in the remaining voxels, using the linearity of the DT[179]. GM regions are segmented as the ones with linearity below 0.2 and the remaining are partitioned as the WM

1 For a standard scanner with $|\boldsymbol{G}|_{max} = 40 mT/m$, the optimised protocol would consist of reduced b-values of $700 s/mm^2$ and $2000 s/mm^2$, as discussed in Zhang et al. 2012

8.2 IN VIVO DATA EXPERIMENT

8.2.1 *Parameter estimation*

The aim of parameter estimation analysis is to evaluate the *in vivo* estimation of the Bingham-NODDI parameters, by looking at the plausibility of the parameter maps and the statistics of parameter estimation.

8.2.1.1 *Parameter maps*

Parameter maps are assessed to check if the Bingham-NODDI indices, particularly the novel ones, are sensible in specific tissue regions of the brain. Emphasis is on the regions where the dispersion is expected to be the highest and lowest, as well as regions where the dispersion anisotropy is expected to exist. The maps obtained using the estimates from the four-shell protocol are shown.

Results

Figures 8.1 and 8.2 show a qualitative analysis of Bingham-NODDI, in the form of the parameter maps of the *in vivo* fitting. The maps demonstrate the *in vivo* feasibility of Bingham-NODDI as sensible values of parameters are obtained, which reveal that dispersion anisotropy is widespread in the brain, specifically the peripheral WM. The slices show the cross-section of the corpus callosum (CC), corona radiata (CR) (regions in blue in the RGB map, on either sides of the CC), a region known to exhibit fanning as it extends from the internal capsule to the various cortical areas, as well as several peripheral WM tracts.

The RGB maps of $\hat{\mu}_1$ are consistent with the dominant orientations maps expected from DTI fit. The RGB maps are weighted by FA_T, the fractional anisotropy metric for the orientation tensor, $\mathbf{T}$[85]. The FA_T shows a pattern very similar to FA of the DTI, but there are non-negligible intensities even in regions with very high orientation dispersion. The maps of volume fractions representing the intra-neurite and the isotropic compartments are shown in rows 2 and 3 of Figure 8.1, which show a spatial pattern consistent with that obtained by fitting Watson-NODDI in Zhang et al. 2012. The maps of the novel dispersion indices ODI_P, ODI_S and ODI_{Tot} (highlighted in yellow in Figure 8.1) also show patterns consistent with ODI for Watson-NODDI. ODI_P has higher dispersion values throughout the brain tissue, compared to ODI_S, particularly in regions where complex neurites are expected to be present. For example in the CR, as it gets closer to the cortex (see regions of

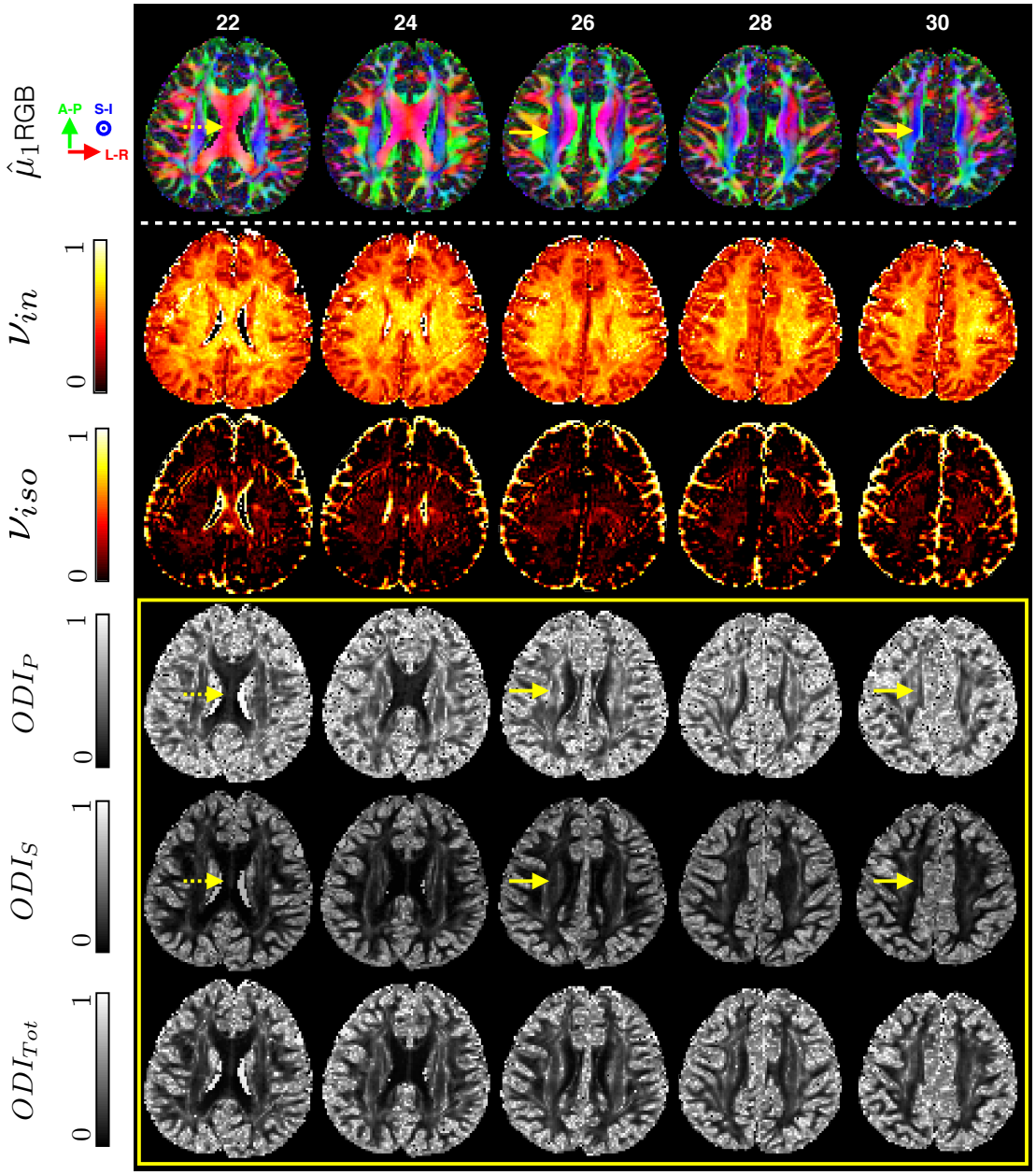

Figure 8.1: Axial slices showing maps of the novel parameters $\mathrm{ODI_P}$, $\mathrm{ODI_S}$ and $\mathrm{ODI_{Tot}}$ (highlighted in yellow), obtained by fitting Bingham-NODDI to the *in vivo* data, along with the maps of ν_{in} and ν_{iso} (2^{nd} and 3^{rd} rows). Corresponding RGB maps of dominant orientation ($\hat{\mu}_1$) are shown as anatomical reference (row 1). The RGB maps are weighted by $\mathrm{FA_T}$, the overall anisotropy metric for the orientation tensor, $\mathbf{T}$[85]. The dashed arrows indicate the CC, while the solid arrows highlight regions of CR across various slices.

the CR annotated with arrows on slice 26 and 30 in Figure 8.1), as well as the tracts near the cortex. This pattern of anisotropy is consistent with findings by Lazar et al. 2005, who use DTI on human data, and Sotiropoulos et al. 2012, who utilise a multi-compartment model similar to Bingham-NODDI, fitted to macaque data. The CC shows low values of ODI_P and ODI_S, as expected.

Anisotropic dispersion is quantified by DA_B and DA_T in Figure 8.2. High values of dispersion anisotropy indices are seen in various WM tracts, including the CR, the external capsule (EC) and the superior longitudinal fasciculus (SLF), highlighted by arrows in Figure 8.2. This is consistent with previous studies exploring the anisotropy of WM tracts in the human brain[105], showing that dispersion anisotropy is a widespread feature of the WM. Since DA_B maps pure anisotropy, even a region as coherent as the CC has high values (dashed arrow in Figure 8.2), consistent with the known bending of the tract. The higher values in the DA_T map are consistent with DA_B, but there is a greater contrast between the various regions with anisotropic dispersion, depending on whether they have high overall dispersion or not. For e.g. the CC has a lower DA_T compared to regions like the CR. Such a mapping is suited for tractography, where the extent of dispersion is very important to correctly trace streamlines and higher anisotropy significantly change the ODF only when the overall dispersion is high. As expected, the DA_B map shows higher variability in estimates compared to DA_T.

Crossing fibres are not explicitly modelled in Bingham-NODDI, but regions of two fibres crossing are also seen to have higher values of DA_B (e.g. the crossing of CR and CC). However, three crossings appear to have low values of DA_B, e.g. where the CR and CC cross the SLF, which is similar to findings in Kaden et al. 2007. Examples of crossings between two and three fibre populations are highlighted in Figure 8.2.

The primary dispersion orientations, $\hat{\mu}_2$, estimated by Bingham-NODDI (Figure 8.2, row 2) match very well with the secondary eigenvalues of the DTI and follow the findings in Lazar et al. 2005. Some incoherence in the estimation of $\hat{\mu}_2$ can also be seen in the midsagittal plane. Lazar et al. 2005 suggest that this corresponds to regions of high axial symmetry ($\hat{\mu}_2$ is degenerate in this case). We think it could also be a result of low SNR in the deep-lying brain regions.

8.2.1.2 *Quantitative analysis*

Here an explicit comparison of the performance of the *in vivo* estimates obtained from the Bingham-NODDI and Watson-NODDI models is carried out,

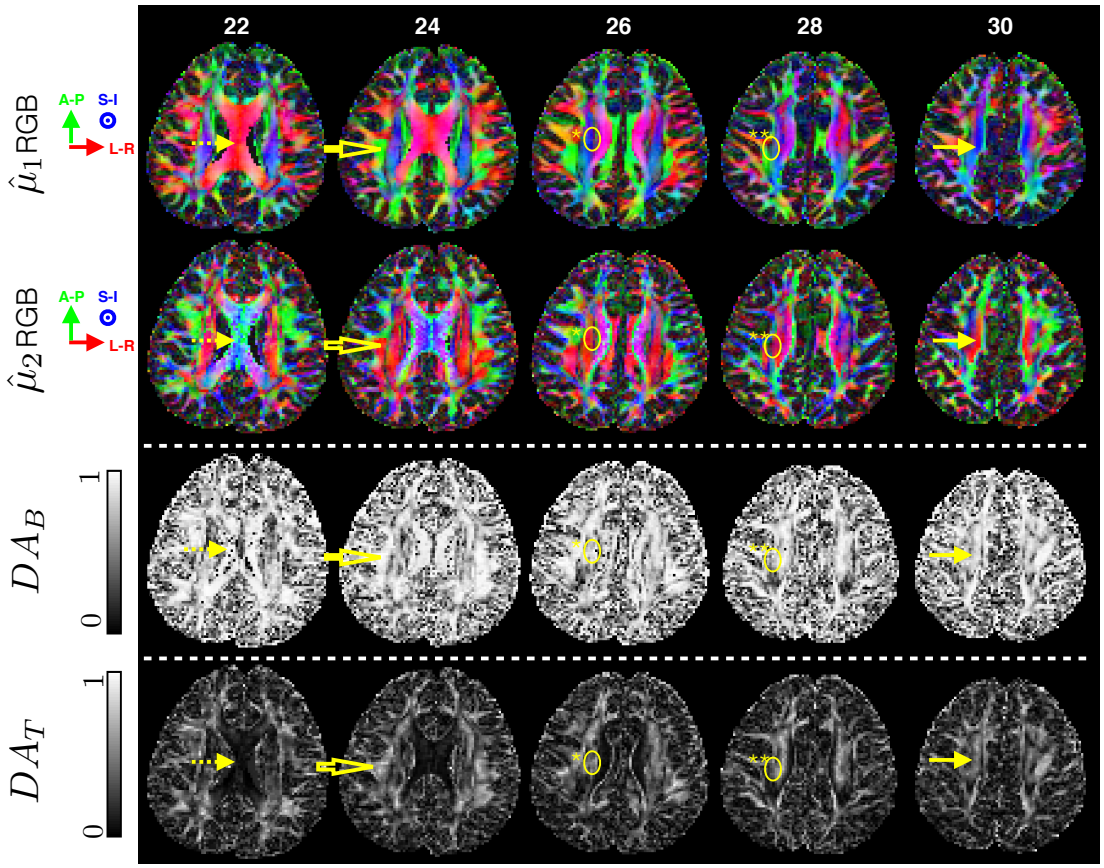

Figure 8.2: As Figure 8.1, but showing maps of the proposed quantifications of dispersion anisotropy. The RGB maps of $\hat{\mu}_2$ weighted by FA_T are also shown. The dashed arrows indicate the CC, the solid arrows the CR and the un-filled arrows highlight the SLF. Regions of crossings are highlighted with circles, with * indicating a crossing with two fibre populations and ** with three.

using the statistics of estimation of comparable parameters. This is to evaluate how important it is to model anisotropic dispersion and if modelling for this anisotropy affects the accuracy and precision of the parameters.

Design

The accuracy and precision of the estimates obtained by fitting to data from **N1**, the standard *in vivo* NODDI protocol, is compared for the two NODDI models. In particular, the consequence of not including dispersion anisotropy in the NODDI model is quantified. Towards this end, the results are stratified according to the level of dispersion anisotropy determined by the value of DA_B. This DA_B is estimated by fitting the *in vivo* data from the four-shell protocol, which is the *"ground-truth"* for *in vivo* analysis. The plotted errors and variability represent the difference in paramter values estimated using **N1** and the *"ground-truth"*, for a particular range of *"ground-truth"* values of DA_B.

Results

The quantitative comparison of the estimates of the two models reveals that the estimation of v_{in}, v_{iso} and $\hat{\mu}_1$ (results not shown) is the same for the two models, regardless of the level of anisotropic dispersion, while the estimation of ODI_{Tot} gets slightly worse for Watson-NODDI for higher levels of dispersion anisotropy (Figure 8.3). The Watson-NODDI estimates are overall comparable to Bingham-NODDI ones, as concluded also from the synthetic data experiment, with a slight increase in bias for ODI_{Tot}, specifically notable for GM. Thus, Watson-NODDI is able to reliably estimate the volume fractions, the overall dispersion and the dominant orientation of the neurites, but Bingham-NODDI provides extra information by separately quantifying ODI_P and ODI_S, to enable quantification of anisotropic orientation dispersion.

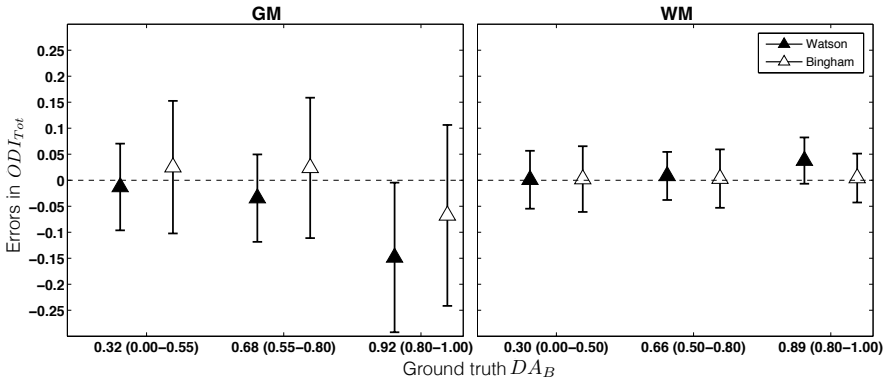

Figure 8.3: Errors in estimation of the overall dispersion index, ODI_{Tot} using Bingham-NODDI and Watson-NODDI, for various *ground-truth* values of DA_B, for *in vivo* data. The results are shown for GM and WM, obtained by fitting the two-shell NODDI protocol (N1). The *"ground-truth"*values shown are the mean values in each pool, with the range of those values indicated in brackets.

8.2.2 *Protocol comparison*

A protocol comparison, similar to that for synthetic data, is done to establish if the Bingham-NODDI parameters can be estimated *in vivo* with the standard NODDI protocol, **N1** and if the protocol can be further reduced without impacting the accuracy and precision of the estimates. The obtained results are compared to those for the synthetic data in Section 7.2.2.

8.2.2.1 *Design*

The protocol comparison for the *in vivo* data is carried out in the same way as for the synthetic data, but the estimates from the four-shell protocol (All) are used as the pseudo *"ground-truth"*to compute the errors. As shown in Sec-

tion 7.2.2, the estimation of all the parameters is highly accurate and reliable for the four-shell protocol, except for the orientations, when they are indeterminate. The statistics are pooled for the various *"ground-truth"* values of each parameter, which correspond roughly to the values used for synthetic data.

8.2.2.2 *Results*

Figures 8.4-8.6 show the plots of the statistics computed for the novel parameters of Bingham-NODDI, separately for the GM and WM tissue. All the results are consistent with the findings from the synthetic data experiment and show that the parameters of the model are estimable with the N1 protocol (results for ν_{in} and ν_{iso} not shown). We notice that for all the parameters, the estimation appears to be more variable for *in vivo* than the synthetic data. This is likely explained by the fact that the NODDI model remains an imperfect representation of the measured data.

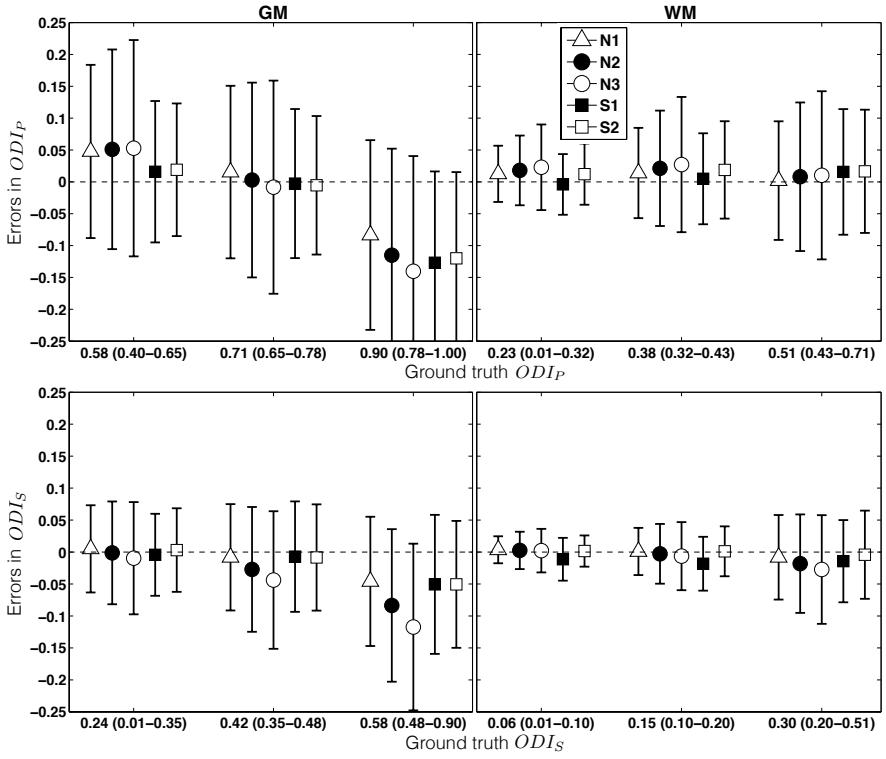

Figure 8.4: Errors for *in vivo* estimation of $\mathrm{ODI_P}$ and $\mathrm{ODI_S}$ using Bingham-NODDI, for the various *ground-truth* values of the respective parameters. The results are shown separately for GM and WM. The various protocols are indicated by the symbols.

The results obtained for the estimation of the dispersion indices and the orientations show that a single-shell protocol is sufficient for their estimation, consistent with the synthetic data experiment (Section 7.2.2). But the errors for estimating $\hat{\mu}_1$ and $\hat{\mu}_2$ appear to be not as high as seen for the synthetic data,

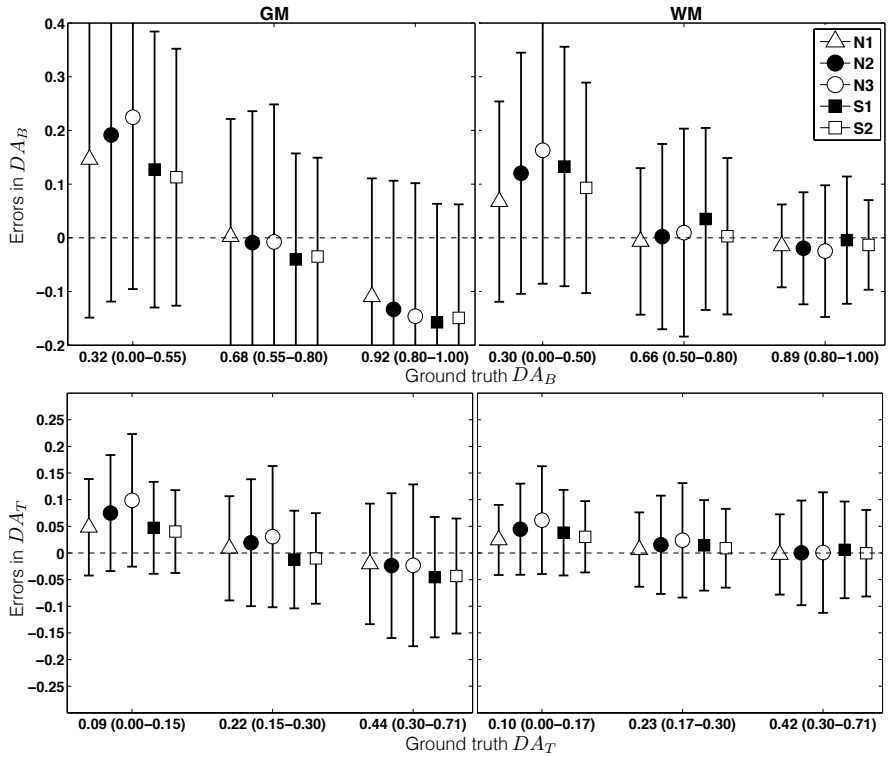

Figure 8.5: As Figure 8.4, but for DA_B and DA_T.

for highest DA_B, as well as for lowest DA_B for $\hat{\mu}_2$ estimation. This is because the *in vivo* data does not show orientation distribution configurations where κ is exactly equal to β or $\kappa = 0$.

8.2.3 *Model comparison*

8.2.3.1 *Design*

To assess how well the two models explain the data a model comparison is carried out. A standard model selection criterion, the Bayesian Information Criterion (BIC)[140], is used, which quantifies the quality of fit to the data while accounting for model complexity (number of parameters). A lower value of BIC corresponds to a model which provides a better fit for the acquired data and thus explains the data better.

8.2.3.2 *Results*

Figure 8.7 shows the BIC maps for Bingham-NODDI and Watson-NODDI. The maps clearly show that Bingham-NODDI explains the data better than Watson-NODDI, in a significant proportion of the voxels.

The raw BIC maps (Figure 8.7, rows 2 and 3) highlight that Bingham-NODDI is the preferred model in most WM regions, but in GM and the very coherent

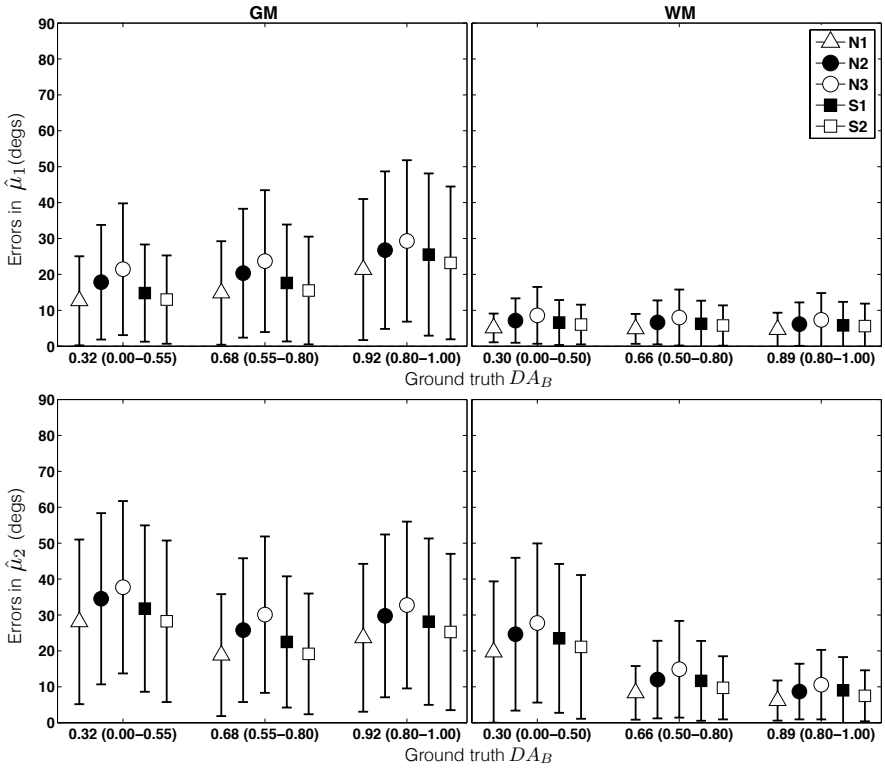

Figure 8.6: As Figure 8.4, but for errors in estimation of the orientations, $\hat{\mu}_1$ and $\hat{\mu}_2$. The data is separated according to the ground-truth values of DA_B

WM regions (e.g. midsagittal CC) Watson-NODDI is sufficient. The higher BIC values in the Watson-NODDI fit correspond to regions of WM with expected fanning/bending configurations. The maps of difference in BIC values between the two models (Figure 8.7, rows 4 and 5) highlight these findings clearly.

8.3 SUMMARY AND DISCUSSION

Here we have presented an *in vivo* evaluation of the Bingham-NODDI parameters, in terms of their estimability and plausibility of their values, using various imaging protocols. We demonstrate the accuracy/precision of the indices of the proposed model and show that the model explains the DW-MRI data better than Watson-NODDI, using a clinical feasible acquisition protocol. The results for the various protocols are consistent with the findings from the synthetic data experiment and show that the parameters of Bingham-NODDI are estimable with the optimised NODDI protocol (N1 in Table 7.2). It can be noted that for all the parameters, the estimation appears to be more variable for *in vivo* than the synthetic data. This is likely explained by the fact that the

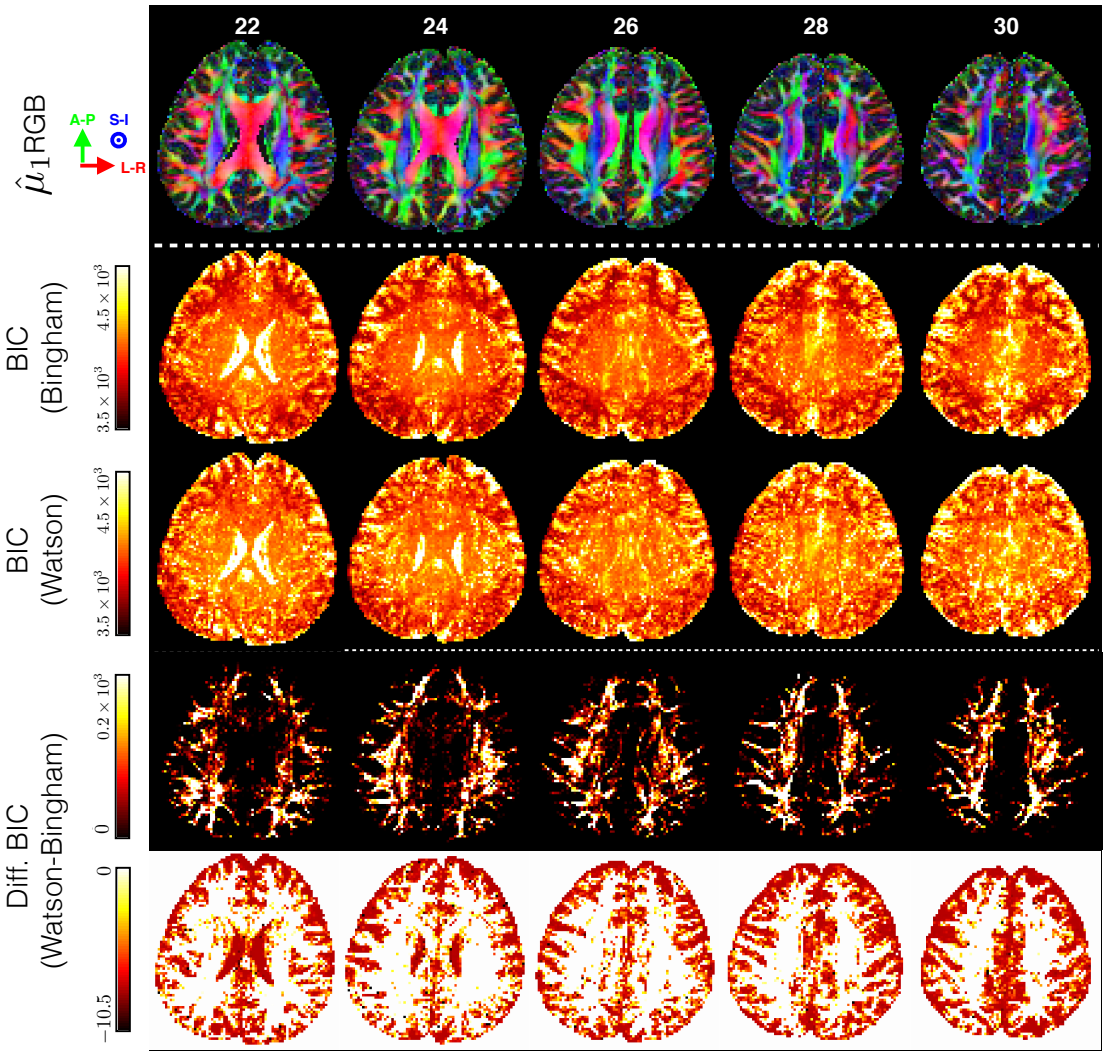

Figure 8.7: The maps of BIC for fitting with Bingham-NODDI and Watson-NODDI models (2^{nd} and 3^{rd} rows). The last two rows show the difference BIC maps to highlight the areas where Watson-NODDI performs worse than Bingham-NODDI (4^{th} row) and those where Watson-NODDI is sufficient (5^{th} row). For clarity, the BIC difference map has been modified to show the positive and negative intensities separately. The number of negative values in the difference map correspond to regions where Watson-NODDI is sufficient, but a small number also represent voxels where the fitting procedure gets stuck in local minima (see discussion in Section 9.1).

NODDI tissue model remains an imperfect representation of the measured data.

A limitation of the presented results is that the model is only evaluated on single subject data. This is because this presents a feasibility study only, and application of Bingham-NODDI to a cohort of healthy subjects is carried out in Part (iv) of the thesis.

9

SIMULATIONS FOR MODEL FITTING AND ASSUMPTIONS OF BINGHAM-NODDI

This chapter includes the experiments to determine the optimum fitting procedure for Bingham-NODDI and also assess the impact of the various model assumptions on the parameter estimation.

9.1 OPTIMUM FITTING PROCEDURE FOR BINGHAM-NODDI

The fitting procedure used for experiments in Chapter 7 and 8 may not be optimal for fitting Bingham-NODDI with standard clinical data, specifically in the GM. We find that for a small but non-negligible number of the voxels, the objective function indicates that Watson-NODDI fits the data better than Bingham-NODDI, corresponding mainly to the regions of partial volume between GM or WM and CSF.

As Bingham-NODDI should fit the data at least as well as Watson-NODDI, this indicates that our fitting procedure is getting stuck in local minima for these voxels. We can improve the fitting procedure in these regions by using the Watson-NODDI fit as the starting point for Bingham-NODDI. Experiments in this section focus on establishing the optimum fitting procedure for Bingham-NODDI.

9.1.1 *Design*

It is expected that using the Watson-NODDI estimates will improve the model fitting for Bingham-NODDI. Here we test various other options to figure out the best overall fitting procedure, including the orientations, and whether they are fixed or fitted. Following are the various fitting procedures tested here

1. Watson-NODDI starting values and orientations from DTI fit, which are fixed during Bingham-NODDI fitting

2. Watson-NODDI starting values, including $\hat{\mu}_1$ and $\hat{\mu}_2$ from DTI
3. Watson-NODDI starting values and orientations from DTI fit, which are fitted during Bingham-NODDI fitting
4. Watson-NODDI starting values, including $\hat{\mu}_1$ and $\hat{\mu}_2$ from DTI, which are then fitted during the Bingham-NODDI fitting
5. fitting without any initialisation

9.1.2 *Experiments*

We use the same data set tissue substrate and the ground truth parameters, as used for the *in silico* experiments in Chapter 7.

9.1.3 *Results*

The errors in the estimation of the model parameters and the indices derived are shown in Figures 9.1- 9.3. We find that the fitting procedure using Watson-NODDI initial parameters, performs the best, particularly for the fitting of the dispersion and dispersion anisotropy parameters, when DTI orientations are used, which are then fitted by Bingham-NODDI. This fitting procedure consistently provides the best estimates for all the parameters, getting not only the most accurate and precise estimates but also taking significantly less time compared to the original fitting procedure.

We also analyse the quality of fit of some of the estimates (results not shown), with consistent findings.

9.1.4 *Conclusion*

From the experiments, we find that the optimal fitting procedure for Bingham-NODDI is to initialise using the orientations from the linear DTI fit and the rest of the parameters from the Watson-NODDI fit. The β parameter is simply initialised as a fraction of the κ estimated by Watson-NODDI.

From here on, we use this fitting procedure to carry out the model fitting for Bingham-NODDI.

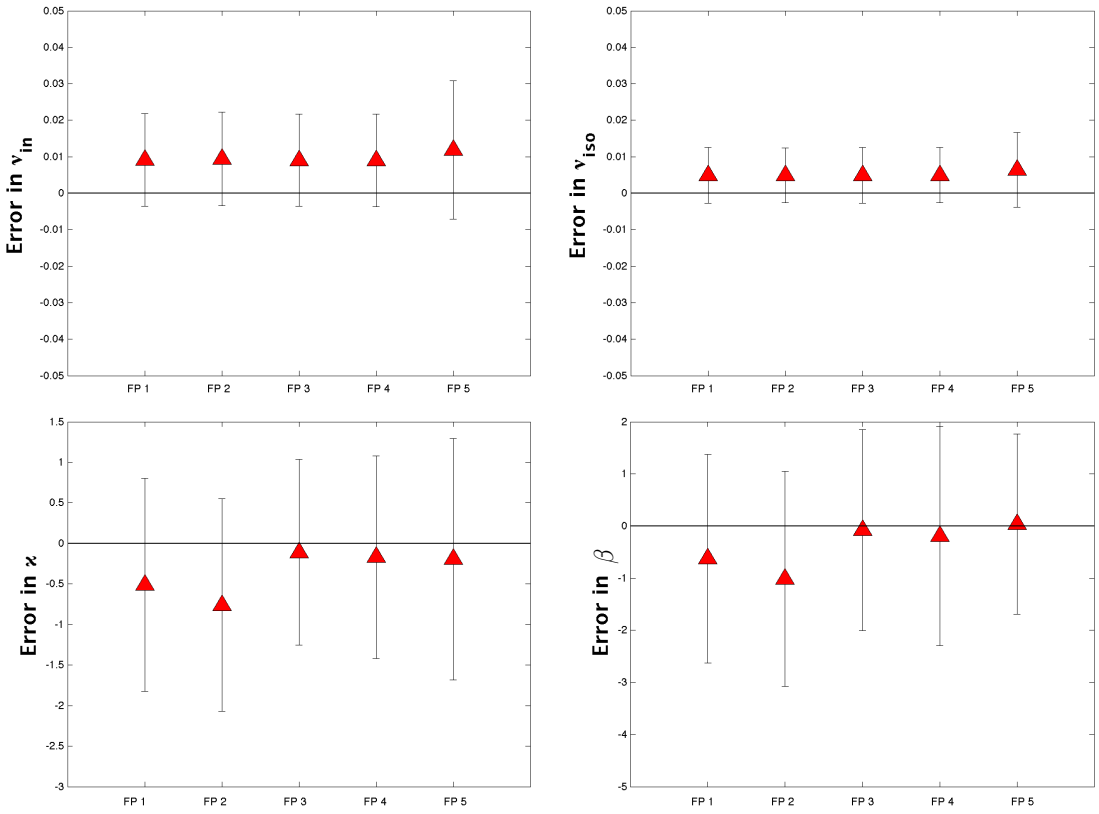

Figure 9.1: Errors in estimation of some of the model parameters of Bingham-NODDI. The 'FP N' indicate the N^{th} fitting procedure as details in the main text.

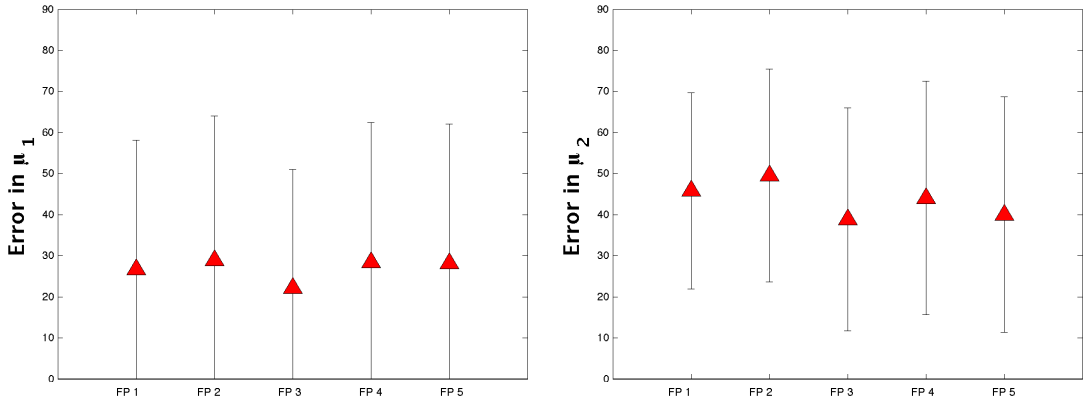

Figure 9.2: As Figure 9.1, but for the model parameters for the orientations, obtained from Bingham-NODDI.

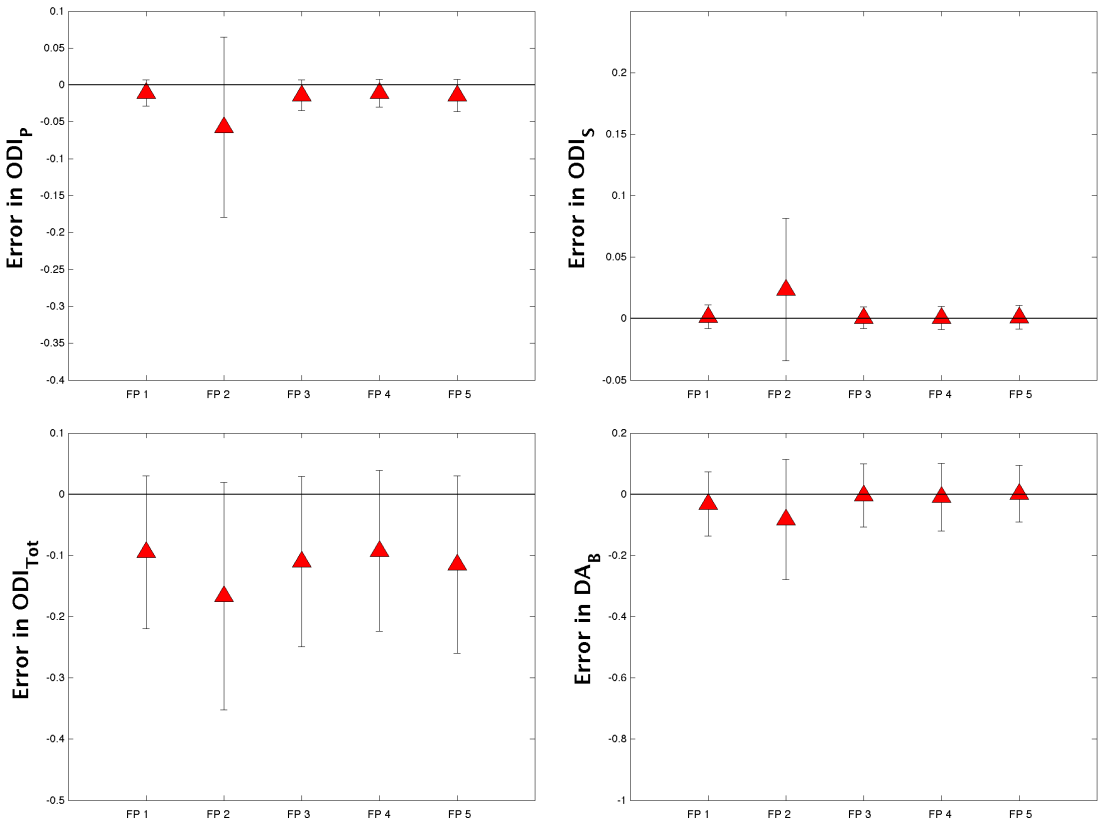

Figure 9.3: As Figure 9.1, but for the indices of dispersion and dispersion ansitropy derived from Bingham-NODDI.

9.2 ASSUMPTION OF SINGLE FIBRE POPULATION

A key limitation of the proposed model is not explicitly estimating crossing fibres. Our primary aim is to provide simple and robust indices of microstructure and attempting to resolve multiple fibre populations will introduce instability in parameter estimation as discovered by Sotiropoulos et al. 2012. Nevertheless, we find that the model correctly identifies crossing regions with high orientation dispersion and some with high anisotropic dispersion (see the parameter maps in Figure 8.2).

This section evaluates how the dispersion and dispersion anisotropy indices are affected by the presence of crossings, which is a very plausible configuration in the human brain. This will allow better interpretation of *in vivo* maps presented in Chapter 8.

9.2.1 *Modelling crossing fibres*

To evaluate how the existence of multiple fibre populations affects the estimation of anisotropic orientation dispersion, using Bingham-NODDI, diffusion

Parameter	Ground-truth values
f_1-f_2	{0.5-0.5, 0.7-0.3}
ν_{in}	{0.7}
ν_{iso}	{0.0}
κ	{32}
β	{0, 16}
θ (radians)	{0-$\frac{\pi}{40}$-$\frac{\pi}{2}$}

Table 9.1: The model parameters for the signal simulated for two orientationally dispersed fibre populations crossing at a seperation angle, θ.

signal is simulated by explicitly modelling crossing fibres, in the presence of dispersion.

9.2.1.1 *Design*

We simulate a very simple case of two fibre populations crossing, where each population has the same level of orientation dispersion, as well as dispersion anisotropy. We add an extra compartment with Bingham-distributed sticks, to get a three compartment tissue model and simulate substrate with two very similar characteristics, with varying crossing angles.

We simulate data with high neurite density and orientation coherence, with isotropic and anisotropic orientation dispersion. The exact ground truth parameters utilised are as summarised in Table 9.1.

The signal simulated for each of the four set of tissue configurations is shown in Figure 9.4, for three crossing angles.

Rician noise is added to the simulated signals, at SNR $= 20$, as done in Chapter 7. The Bingham-NODDI parameters are estimated using the same fitting procedure as used for the *in vivo* evaluation (Chapter 8).

9.2.1.2 *Results*

The effect on the dispersion parameters estimated using Bingham-NODDI, which is a single-fibre dispersion model, are shown in Figure 9.5. As expected, increasing the crossing angle between the two fibre populations results in an increase in the estimated dispersion and dispersion anisotropy indices. In particular, the estimation of DA_B is very variable when two fibre populations exist, with a small crossing angle ($\theta < 45°$). While the values of the estimated indices have high errors compared to the ground truth values, the increase in orientation dispersion and anisotropy with increasing crossing angle is right. This is because the underlying orientation configuration, when assuming a

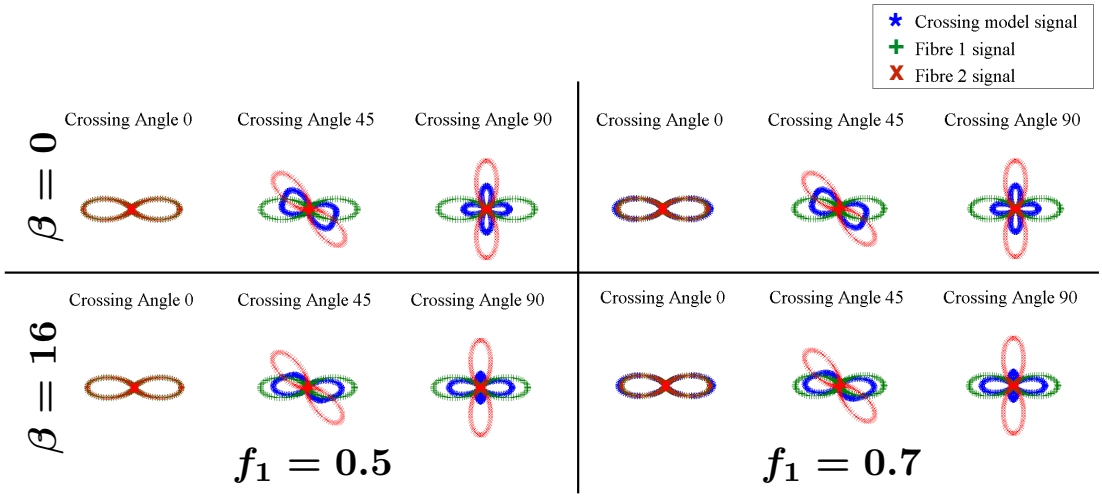

Figure 9.4: The simulated multi-population Bingham-NODDI signal, for the *intra-neurite* and *extra-neurite* compartments, as well as the total signal. The first row represents neurite configurations with no dispersion anisotropy ($\beta = 0$), while the second row represents those with dispersion anisotropy ($\beta = 16$). The relative volume fractions of the two populations are $[0.5, 0.5]$ for the first column, and $[0.7, 0.3]$ for the second column.

single-fibre population, as Bingham-NODDI does, is actually becoming more and more orientationally dispersed and anisotropic.

9.2.2 *Discussion*

We find that as expected, and noted from the *in-vivo* experiments, increasing the crossing angle between the two fibre populations results in an increase in the estimated dispersion and dispersion anisotropy indices. This is important for neuroimaging studies as a higher DA_B or DA value does not necessarily reflect the existence of dispersion anisotropy and would need to be validated by other means like fMRI or histological data. However, for typical clinical applications, this may not be a problem as a difference from the normal value in a region would still be highlighted. This does take away from the main benefit of microstructure imaging, which is to precisely indicate the microstructure changes underlying brain development, function, or pathology.

9.3 SENSITIVITY OF SIGNAL TO MODEL PARAMETERS

The Bingham-NODDI tissue model assumes a fixed intrinsic diffusivity inside and outside the neurites, as well as neurites with zero radii (neurites modelled as sticks). These assumptions are required for wider applicability of the model as these parameters are hard to be estimated with standard clinical

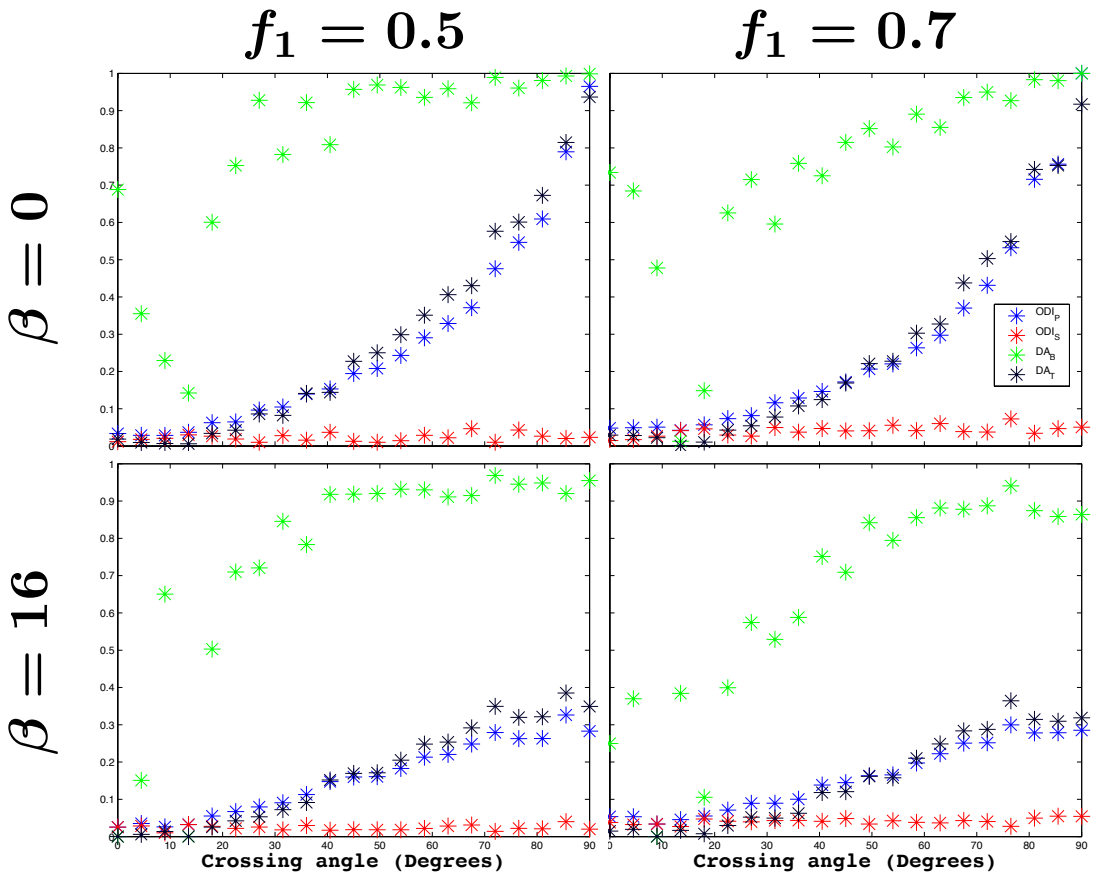

Figure 9.5: Values of dispersion (ODI_P, ODI_S) and dispersion anisotropy (DA_B, DA_T) indices estimated by fitting the single population Bingham-NODDI model to the data, as a function of the crossing angle between two populations of equally dispersed fibres ($\kappa = 32$). The first row represents neurite configurations with no dispersion anisotropy ($\beta = 0$), while the second row represents those with dispersion anisotropy ($\beta = 16$). The relative volume fractions of the two populations are $[0.5, 0.5]$ for the first column, and $[0.7, 0.3]$ for the second column.

imaging[6,184]. However, intrinsic diffusivity inside and outside the neurites and the neurite radii are important parameters to be estimated in neuroscience and clinical applications.

Here we assess how sensitive a very rich DW-MRI acquisition is to change in these parameters, which is important for reliable estimation of these parameters. The results are not included here, but we provide a summary of the findings below.

9.3.1 *Design*

Synthetic signal is produced using the model described in Section 7.1.1, which is a Bingham-NODDI model, with neurites modelled with non-zero radii. The specific parameter values simulated are: $\kappa = 16$, $\beta = 0$, $\nu_{in} = 0.8$, $\nu_{iso} = 0$. We use a very rich acquisition protocol, with 6 b-values and with 60 diffusion directions ($\hat{\boldsymbol{G}}$) for each (the protocol used in Chapter 14) to simulate the signal. The sensitivity of the signal to both the neurite radii and intrinsic diffusivity is assessed for several ground truth values of each parameter, as described in the following sections.

9.3.2 *Sensitivity to neurite radii*

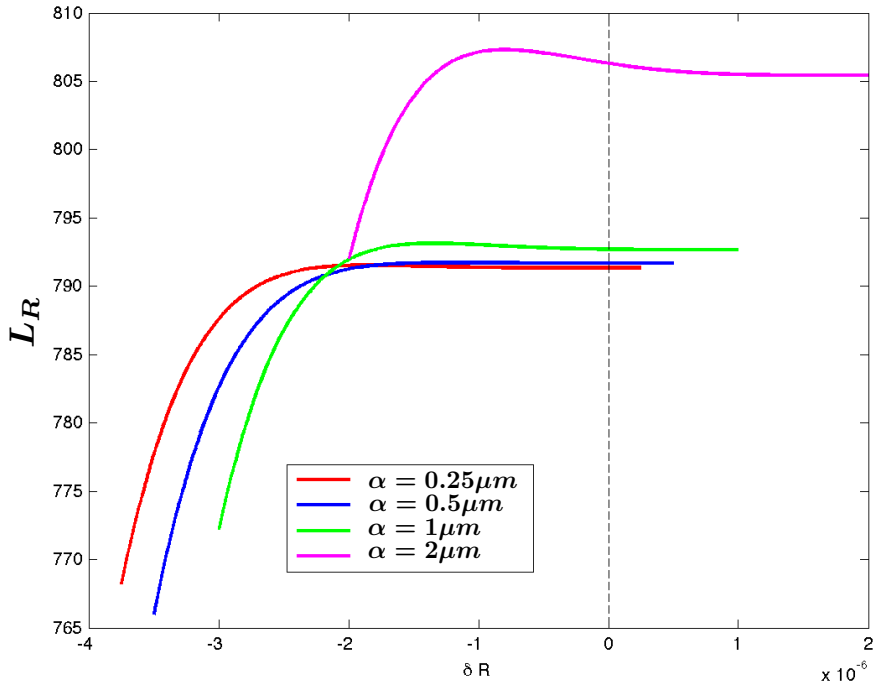

Figure 9.6: Sensitivity of the Bingham-NODDI signal to the changes in values of neurite raddi, α, simulated for several ground truth values of α, as indicated.

The ground truth values simulated for the radius parameter are $\alpha = [0.25, 0.5, 1, 2]\mu m$. The sensitivity of the Bingham-NODDI signal to changes in neurite radius is estimated by computing the objective function (Equation (4.5)) for each of the ground truth signals and signal synthesised, with Rician noise, for the same set of parameter values, while the radius parameter is varied between $\alpha_p = [0 : 0.01 : 4]\mu m$. The diffusivities values are $d_i = 1.7 \times 10^{-9} m^2 s^{-1}$ and $d_{iso} = 3.0 \times 10^{-9} m^2 s^{-1}$. This simulates how sensitive the signal is to small perturbations in the estimated values of α.

The results in Figure 9.6 clearly show that even with the very rich protocol used here, the radius parameter does not change the underlying signal sufficiently, for it to be reliably estimated. The sensitivity of the signal increases with the ground truth value of the radii, as expected.

9.3.3 *Sensitivity to intrinsic diffusivity*

The sensitivity for intrinsic diffusivity is evaluated for the ground truth values $d_i = [1, 1.3, 3] \times 10^{-9} m^2 s^{-1}$. The radius and isotropic diffusivity values are set to $\alpha = 0\mu m$ and $d_{iso} = 3.0 \times 10^{-9} m^2 s^{-1}$. The objective function is computed for d_i, as done for α, by perturbing the values $d_i p = [0.25 : 0.5 : 5] 10^{-9} m^2 s^{-1}$

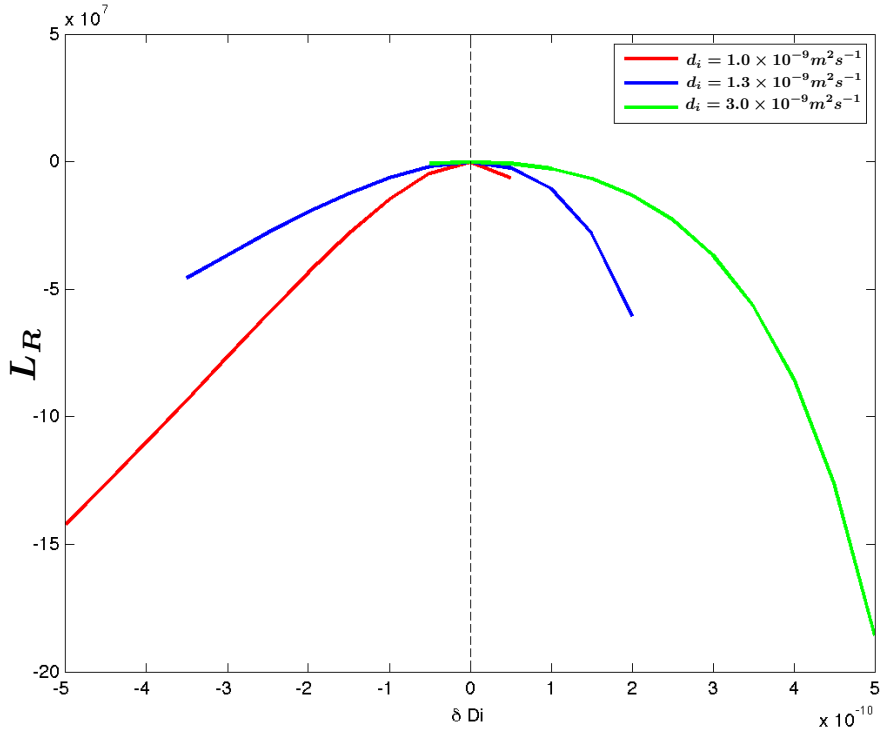

Figure 9.7: Sensitivity of the Bingham-NODDI signal to the changes in values of intrinsic diffusivity inside the neurites, d_i, simulated for several ground truth values of d_i, as indicated.

The results are shown in Figure 9.7 and show that the simnulated signal is sensitive to changes in d_i and so the parameter can be reliably estimated for with a rich DW-MRI protocol. The sensitivity of the signal is higher for lower values of diffusivity, as expected.

9.3.4 *Discussion*

We assessed the sensitivity of the neurite radii and intrinsic diffusivity parameters on the Bingham-NODDI signal synthesised with the very rich protocol. We use a tissue substrate with very high neurite density and coherence and no dispersion anisotropy, cases for which the parameters are found to be most estimable.

We find that the synthesised signal is sensitive to changes in diffusivity, but not the neurite radii, with the high-quality data we used. So the signal acquired itself needs to be very rich to enable estimation of neurite radii, with the standard PGSE acquisition sequence.

The other assumptions and the main limitations of Bingham-NODDI are discussed in Chapter 16, along with a discussion of the implications of these assumptions.

10

METHOD DEVELOPMENT AND EVALUATION: DISCUSSION

This chapter provides a discussion of the findings from the *in silico* (Chapter 7) and *in vivo* (Chapter 8) experiments carried out for evaluating Bingham-NODDI indices of neurite morphology.

10.1 BINGHAM-NODDI TO MAP ANISOTROPIC ORIENTATION DISPERSION OF NEURITES

Here we have presented Bingham-NODDI, a generalisation of the Watson-NODDI model, to characterise the anisotropic orientation dispersion of neurites, which provides a more accurate representation of the orientation distribution of neurites in the human brain. Characterisation of anisotropic orientation dispersion is important as it can serve as a useful marker of brain pathologies, reflecting very subtle changes in the orientation dispersion of neurites, as detailed in the motivation of the work (Chapter 1) and Chapter 6.

We use the Bingham distribution, allowing us to derive the parameters to separately quantify the dispersions extent along the primary and secondary dispersion orientations, as detailed in Chapter 6. Thus, we can distinguish the changes in overall dispersion from dispersion anisotropy and independently quantify these with the indices ODI_{Tot} and DA_B, respectively. It is conceivable that a change in the orientation dispersion of neurites occurs such that there is little or no change in the overall dispersion, but the level of dispersion anisotropy is altered. Watson-NODDI can only estimate the overall dispersion and will not be sensitive to such a change while Bingham-NODDI can capture this subtle difference in the orientation distribution.

DA_B is useful as it provides a marker specific to changes in the anisotropy of the orientation dispersion of neurites. However, DA_B is harder to estimate compared to other indices of Bingham-NODDI. An alternative quantification

of anisotropy is DA_T, which has utility in tractography and is very robust. However, it is a second-order approximation of the ODF and cannot represent higher order variations in the ODF. DA_T is defined for any generic ODF and thus may be utilised to quantify anisotropic dispersion for an alternative parameterisation of the ODF, while DA_B is specifically defined for the Bingham distribution.

10.2 ESTIMATION OF NEURITE MORPHOLOGY USING BINGHAM-NODDI

The results demonstrate the *in vivo* feasibility of the proposed model and show that the model provides sensible estimates of neurite microstructure, with a clinically feasible protocol. The error analysis on the Bingham-NODDI parameters reveals that they have good estimability. The errors and variability of estimates are commensurate with the level of noise in the synthetic and *in vivo* data. Cases, where the errors and standard deviations are high, correspond generally to degenerate cases (one or more the model parameters are not well defined).

We show that a two-shell HARDI protocol is sufficient to estimate the indices of Bingham-NODDI, as with Watson-NODDI. Thus, the estimation of Bingham-NODDI parameters is possible with a clinically feasible imaging protocol. However, the parameters DA_B and $\hat{\mu}_2$ are harder to estimate and unlike Watson-NODDI, a reduced-orientation sampling scheme like N2 and N3 are not feasible for Bingham-NODDI. This is expected as the Bingham distribution represents a more complex ODF compared to the Watson distribution and having more orientations sampled would allow better characterisation of this ODF. But having fewer data points for these schemes also has an impact on the estimation.

Increasing the angular resolution of the acquisition protocol is expected to make the estimation of these parameters more accurate and reliable, however, the configurations where $\hat{\mu}_2$ is not well defined, would not become estimable even with a protocol with higher orientation sampling. Obtaining a very high orientation sampling is not yet clinically feasible with existing imaging sequences, but emerging technologies such as multi-band imaging[60] will make it possible to acquire more data per unit time, enabling higher orientation sampling in the same acquisition time.

Model comparison, with BIC, reveals that Bingham-NODDI is the preferred model in most WM regions of the brain. We significantly improve the fitting in these regions by adding just two parameters to NODDI, which originally

has one less parameter than the standard DTI model. Watson-NODDI is sufficient for most of the GM, which is expected as the dendrites are in general isotropically dispersed, and where dispersion anisotropy does exist (e.g. pyramidal neurons) it might be too minute to be discerned with our data. Since for data with standard clinical resolution, Bingham-NODDI does not appear to give any clear advantage over the standard NODDI model, the assessments carried out in the rest of the thesis is focussed on WM regions only. It might be possible to obtain better fit in the GM with higher resolution data. Follow-on work will investigate this further with the state-of-the-art acquisition, such as the Human Connectome Project (HCP) data[1] (see Part (iv) of the thesis).

Interestingly, the accuracy of most of the NODDI parameters is not affected by the simplified ODF model used in Watson-NODDI. This includes the volume fractions v_{in} and v_{iso}, the overall dispersion ODI_{Tot}, as well the dominant orientation $\hat{\mu}_1$. Thus, any studies which have already been carried out with Watson-NODDI are still valid, but the data may be reanalysed using Bingham-NODDI, to obtain a richer characterisation of orientation dispersion and quantify dispersion anisotropy, without any additional acquisition requirements.

In previous work[160], we explored the quantification of anisotropic orientation dispersion of neurites, in terms of $\mathbf{T}$, as described in Section 6.3.1.2. The alternative parameters for quantification of dispersion are the coherence parameters τ_1 and τ_2, and DA_T for dispersion anisotropy. The evaluation of estimability of these parameters revealed that they are more reliable compared to the indices of anisotropic dispersion proposed here (results not shown). This is expected as these parameters are derived from the second order approximation of the actual ODF and thus can provide a useful summary metric for the overall orientation dispersion.

10.3 EXISTING DIFFUSION MRI MODELS USING THE BINGHAM DISTRIBUTION

Bingham distribution has been used in various diffusion MRI techniques[41,93,147], but the focus has been on mapping brain connectivity while our aim is to estimate biophysically meaningful parameters. The key distinction in this work over these approaches is the use of multi-shell data, as in Zhang et al. 2012, which enables estimation of microstructure at the same time as the fibre dispersion parameters. This work is the first to present a specific quantification of anisotropic dispersion and provides a thorough evaluation

1 Available online at http://www.humanconnectomeproject.org/data/

of its estimability, while previous studies only explore the level of dispersion anisotropy, using DTI[105] or multi-compartment models[93,147], but do not explicitly quantify this feature.

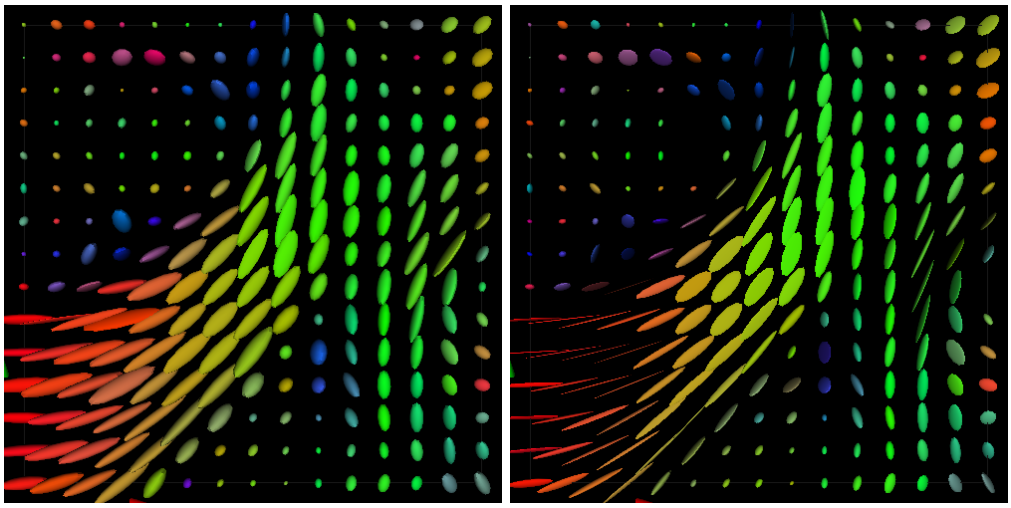

(a) Diffusion tensors (b) Orientation tensors

Figure 10.1: Plot of the diffusion tensors (a) and the orientation tensors (b), corresponding to the fibres of the *genu of the corpus callosum (GCC)*.

As shown in Lazar et al. 2005, the eigenvalues of the diffusion tensor (DT), specifically the difference $\lambda_2 - \lambda_3$, can be used to reflect the level of dispersion anisotropy in WM tracts. Our results are consistent with their findings and there is no significant difference in the orientations estimated by Bingham-NODDI and the three eigenvalues of the DT, as seen qualitatively in Figure 10.1. However, the DT and the ODF in Bingham-NODDI represent fundamentally different physical properties. DT represents the diffusion profiles associated with the underlying microstructure and the ODF represents the orientation dispersion pattern of the neurites. Similarly, DA_B and $\lambda_2 - \lambda_3$ are fundamentally different. DA_B is specific to the orientation distribution; the latter is influenced by DA_B but also by other features like neurite density. Thus, DA_B will be useful to highlight changes specifically in the dispersion of neurites, as a result of brain injury or disruption to normal brain development, which may not be seen by the DT or its anisotropy measure, as many confounding factors can contribute to changes in the diffusion characteristics.

Part IV

TOWARDS CLINICAL TRANSLATION

This part of the thesis is concerned with experiments to evaluate if the proposed method can be used as a tool in neuroimaging studies. This usually requires the ability of the metrics produced to distinguish subjects or ROIs, drawn from for example patient and healthy population or tissue. The focus here is on the white matter of the brain, as standard data only gives sensitivity to quantify dispersion anisotropy in the white matter.

11

NORMATIVE VALUES OF BINGHAM-NODDI INDICES IN THE WHITE MATTER

In this chapter, we present a preliminary study to obtain the normative values of Bingham-NODDI indices in the WM of the adult human brain using state-of-the-art *in vivo* DW-MRI data set and evaluate their variability across the population. We use the high-quality *in vivo* data from the Human Connectome Project (HCP)[1] of multiple subjects and establish the range of Bingham-NODDI indices in the core WM regions-of-interest (ROIs) of normal adults. Because of the quality of this dataset, the presented results could be used as a benchmark for the evaluation of successful setup of Bingham-NODDI data acquisition. This is an important step towards translating this technique to future neuroscience and clinical studies.

11.1 INTRODUCTION

For clinical and neuroscience translation of Bingham-NODDI, it is important to evaluate the variability of its indices across the normal population. Here, we do this by applying Bingham-NODDI to a larger cohort of data to establish the range of values of its indices in the normal adult brain, as well as how variable these are, across the core WM regions of the brain. The normative values and the calculated inter-subject variability are used for power calculation to establish the number of subjects required for future clinical studies utilising the model.

We use diffusion MRI data collected for the HCP, which provides high-quality images obtained from the normal adult population. This gives reliable and highly reproducible estimates of the model parameters. So results from this work can be used as a reference for future studies utilising the NODDI models and the reported power calculations will help design such studies.

1 Available online at http://www.humanconnectome.org/documentation/Q3/

	Total (F/M)	Mean Age (Years)	Median Age (Years)
All subjects	34 (17/17)	28.85 ± 4.36	28.50

Table 11.1: Demographics of the cohort used in the study.

Here, the preliminary results of normative values and the inter-subject variability of the Bingham-NODDI metrics are presented in specific WM regions of interest (ROIs), which are compared to the variability of the indices from Watson-NODDI and DTI.

11.2 METHODS

11.2.1 *Cohort and MRI data acquisition*

Diffusion MRI data acquired for the Human Connectome Project (HCP), Q3 release, was used to generate the normative values of Bingham-NODDI. 34 subjects, balanced for gender, were randomly selected, with age distribution representing the normal adult population, as specified in Table 11.1.

The HCP data consists of high-quality diffusion imaging data acquired on a Siemens 3T Skyra scanner, with $G_{Max} = 100 mT/m$, using a 64-channel, tight-fitting brain array coil. The diffusion data was acquired over 3 HARDI shells, with b=[1000, 2000, 3000]s/mm^2, each with 90 gradient orientations and 18 images at b=0. The other imaging variables were set as described in the documentation[2].

Complete details of the acquisition parameters and preprocessing can be found in Sotiropoulos et al. 2013.

11.2.2 *Motion and eddy current artefact correction*

The HCP data is expected to have susceptibility artifacts as high gradient strengths are used to acquire the diffusion data, as well as eddy artifacts due to EPI acquisition. Motion artifacts are also expected to make a significant contribution to the acquired images due to the high gradient strength used. The data has been made available with motion and eddy current distortions corrected, as detailed in Glasser et al. 2013.

2 Available online at https://www.humanconnectome.org/storage/app/media/documentation/q3/Q3_Release_Reference_Manual.pdf

In addition, gradient non-linearities in acquired data are higher than with conventional 3T scanners and result in distortions in the data. These distortions are corrected by warping the images to the estimated gradient field information[92]. This means that the actual gradient strength and orientation of the DW-MRI acquisition is not the same as in the protocol files and needs to be corrected. So, the gradient information was corrected using the estimated gradient fields provided with the data[3].

11.2.3 *Model fitting*

The NODDI model was fitted to the data using the NODDI Matlab Toolbox[4] , with modification to include the Bingham-NODDI model. Watson-NODDI parameters were obtained using the optimisation procedure described in Zhang et al. 2012. To make the Bingham-NODDI fitting more stable and efficient, the maximum-likelihood parameters from the Watson-NODDI fit were used to initialise the fitting. Details of the model fitting procedure are given in Chapter 9 and some example voxel fits are shown in Appendix D.

The diffusion tensor model[22] was also fit to the data to help with spatial normalisation of the maps (see Section 11.2.4) and to obtain the scalar metrics, FA and MD, for comparison to NODDI metrics. The DTI was fit to the complete three-shell data for consistency with the NODDI metrics.

11.2.4 *Spatial normalisation and region-of-interests*

To compute statistics of the estimated metrics across the cohort, the acquired images were spatially normalised with respect to a study-specific template. The study-specific template was generated from a subset of the data, with age distribution and gender representative of the whole cohort, to minimise bias in the template. This is because template generation is very computationally expensive for data of this quality, but as the cohort is from a healthy adult population, the results are not expected to be affected by this. WM ROIs were also defined in the normalised space, to report the normative values and their variability in specific core WM tracts.

The study-specific template for spatial normalisation was generated using a tensor-based registration algorithm introduced in Zhang et al. 2006. This

3 Matlab code available at https://www.humanconnectome.org/storage/app/media/documentation/q3/HCP_Q3_Release_Appendix_II.pdf

4 Available online at https://www.nitrc.org/projects/noddi_toolbox/

method takes advantage of the orientation information in the diffusion tensors to register the WM tracts and has been shown to provide more accurate alignment, compared to the typically used scalar-based normalisation[16,173]. The tensor-based normalisation was carried out using the DTI-TK[5], which uses the iterative process described in Zhang et al. 2006.

We use a subset of the data rather than the whole cohort to reduce the computational load of generating a population template. This is reasonable for the cohort used as it consists of healthy subjects of very similar age and the subset used has the same age and gender distribution as the whole cohort.

We use the segmentations from the ICBM-DTI-81 WM atlas[115], to define the WM ROIs in the normalised space. The atlas provides segmentation of 48 core WM tracts, which are created using diffusion MR data and thus based on the same contrast as our data. We warp the segmentations to the template space, using the segmentation propagation method, as implemented in NiftyReg toolbox[114].

To obtain all the parameter maps in a normalised space, the diffusion tensors obtained from the diffusion data of each subject were non-rigidly registered to the study-specific template, using DTI-TK. The resulting transformation was then used to warp the Bingham-NODDI maps to the template space.

11.2.5 *Data analysis*

11.2.5.1 *Normative values and inter-subject variability*

The normative maps of Bingham-NODDI were produced as the mean parameter value in each voxel, across the 34 subjects and the inter-subject variability as the standard deviation, from the parameter maps in the template space. All maps were reconstructed in 1mm isotropic resolution for accurate delineation of WM ROIs.

The normative values and inter-subject variability are also reported for each of the WM ROIs and the distribution of these metrics plotted to visualise the normative values and distribution of the indices in each of the ROIs. The normative values and inter-subjects variability are calculated as the mean and standard deviation across the subjects of the mean parameter value in each ROI.

5 Available online at http://dti-tk.sourceforge.net

11.2.5.2 *Power analysis*

Power analysis was carried out to obtain the minimum required sample size to detect specific effect sizes, for each of the ROIs and all the evaluated parameters, given the obtained normative values and inter-subject variability. We compute the number of subjects required to measure effect size of 10%, 5% and 2% (using Matlab 2013a inbuilt functions). These values were chosen as each parameter is expected to have different effect size for several applications, as well as various ROIs. For example Kelly et al. 2016 found an effect size of about 10% for ODI and 2% for v_{in} for group comparison of normal controls and very preterm infants, for major WM tracts.

11.2.5.3 *Regional variability of WM*

To assess the regional variability of the Bingham-NODDI metrics in the adult human brain, the obtained normative values in each of the core WM ROIs are compared to each other to check for statistically significant differences. We expect the microstructure across the various WM regions to show considerable variability due to functional specialisation[136] and want to determine which metrics of our model enable the best discrimination of these differences. We compare the mean values in each of the ROIs with all others, using a two-tailed paired t-test (using Matlab 2013a inbuilt functions).

11.3 RESULTS

11.3.1 *Population template and WM segmentations*

The study-specific template generated, as described in Section 11.2.5.1, consists of well-delineated core WM tracts, as shown by the fractional anisotropy (FA) map for two exemplar subjects, transformed to the template space in Figure 1. Some of the ROIs are shown superimposed on the FA maps in the template space for the two subjects in Figure 11.1, which show a good alignment of the segmentations to the WM ROIs.

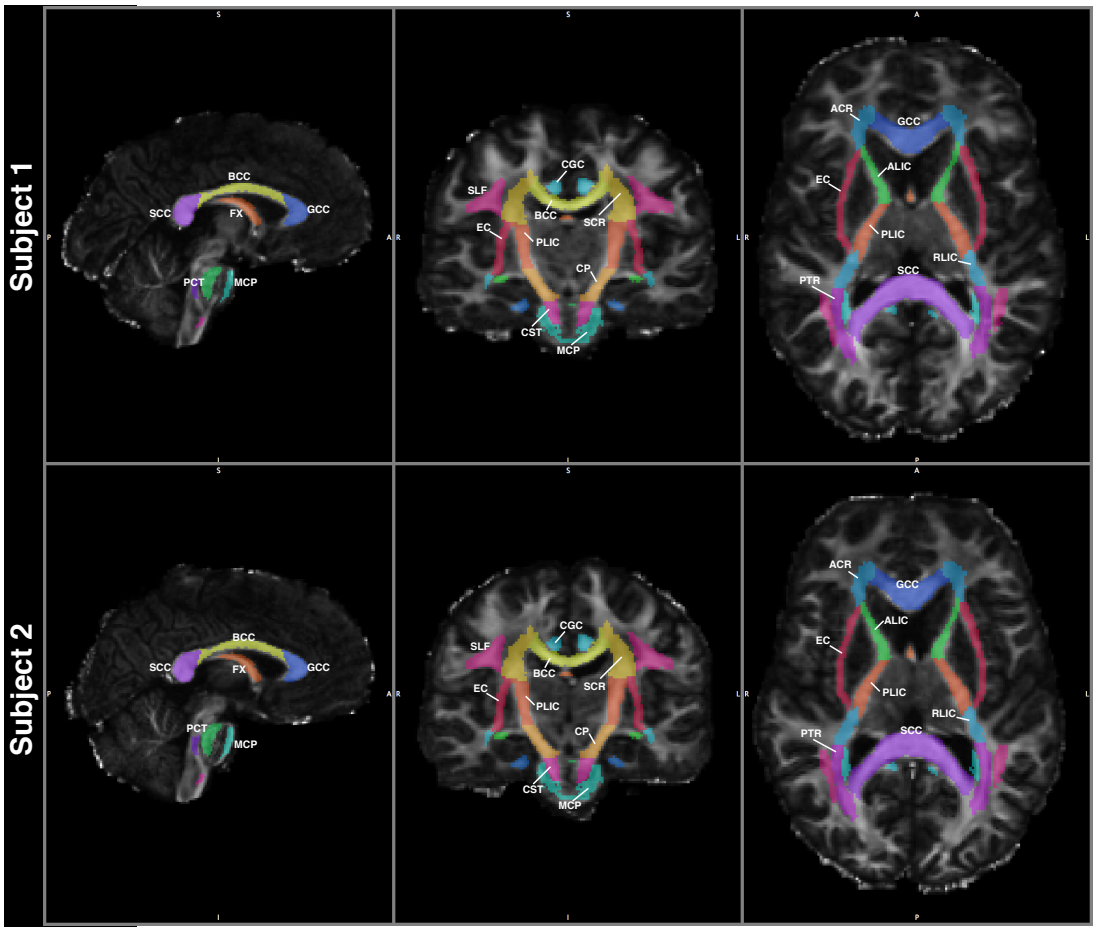

1	Middle cerebellar peduncle	MCP	10	Superior cerebellar peduncle	SCP	19	Sagittal stratum	SS
2	Pontine crossing tract	PCT	11	Cerebral peduncle	CP	20	External capsule	EC
3	Genu of corpus callosum	GCC	12	Anterior limb of internal capsule	ALIC	21	Cingulum (cingulate gyrus)	CGC
4	Body of corpus callosum	BCC	13	Posterior limb of internal capsule	PLIC	22	Cingulum (hippocampus)	CGH
5	Splenium of corpus callosum	SCC	14	Retrolenticular part of internal capsule	RLIC	23	Fornix (cres) / Stria terminalis	FX/ST
6	Fornix	FX	15	Anterior corona radiata	ACR	24	Superior longitudinal fasciculus	SLF
7	Corticospinal tract	CST	16	Superior corona radiata	SCR	25	Superior fronto-occipital fasciculus	SFO
8	Medial lemniscus	ML	17	Posterior corona radiata	PCR	26	Inferior fronto-occipital fasciculus	IFO
9	Inferior cerebellar peduncle	ICP	18	Posterior thalamic radiation	PTR	27	Uncinate fasciculus	UNC

Figure 11.1: Fractional anisotropy (FA) map of two exemplar subjects in the template space with the corresponding WM ROI segmentations superimposed on them (see legend). The ROIs show good alignment with the WM tracts they represent in the individual subjects. There are some areas where the ROI exceeds the boundary of the tracts, resulting in some non-ROI voxels included at the boundaries (see SLF for example). This increases the variability of the parameters in an ROI within each subject.

11.3.2 *Normative values and inter-subject variability*

11.3.2.1 *Parameter maps*

Bingham-NODDI parameter maps of two exemplar subjects, in the normalised space, are shown in Figure 11.2, along with the normative parameter and the inter-subject variability maps.

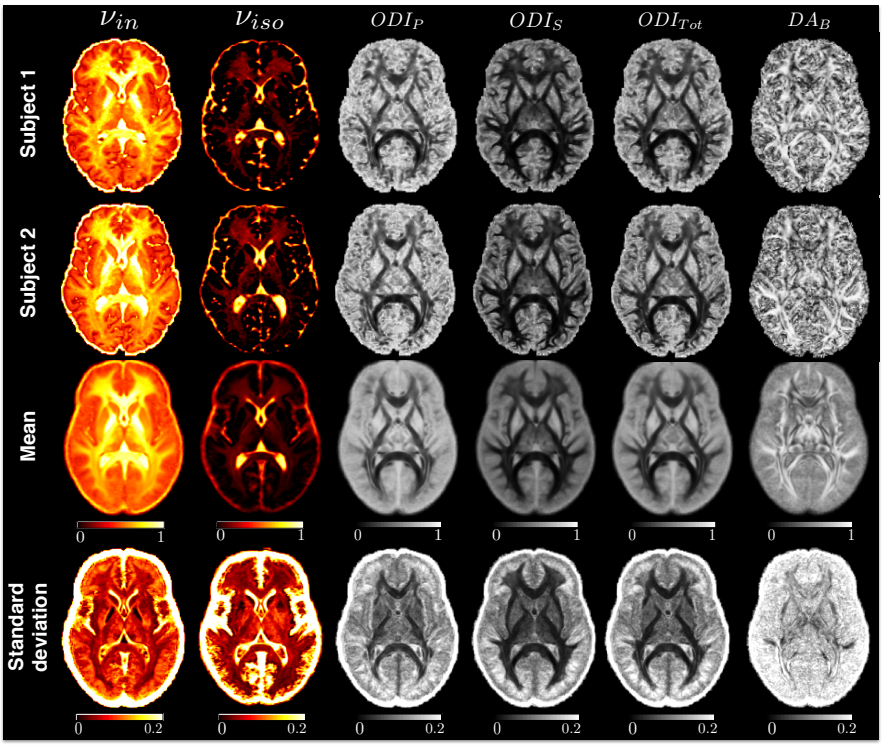

Figure 11.2: Maps of the Bingham-NODDI parameters, in the template space, for two exemplar subjects (rows 1&2) and the mean and standard deviation (rows 3&4) across the cohort. A good cross-subject alignment is apparent in the normalised maps as they are of good quality and have the expected pattern of variation across the WM, where the main fibres can be easily identified. There is low inter-subject variability in parameter values in WM as seen by the comparable contrast between single-subject maps and group means. We also see expected contrast in the mean parameter maps, showing the WM microstructure indices estimated by the model are consistent across the subjects. Even for DA_B, which is known to be harder to estimate[158] i.e. higher values in the peripheral WM compared to deep WM regions.

The pattern of variability across the WM tracts for Bingham-NODDI metrics is consistent with analysis on lower resolution MRI data of single subject[158] and comparable for the various subjects, but there are slight differences in the specific values. For all the subjects, the main WM tracts like the CST, CC and the IC have highest neurite density and low dispersion values, while the

more lateral WM tracts, which are less coherent, like ACR/PCR and the EC have lowest neurite density and high overall dispersion. Tracts known to have extensive fanning or bending like the CR, the SLF, and the PTR have higher anisotropic dispersion values.

A good cross-subject alignment is apparent for most of the tracts in the ROIs, as seen by the comparable contrast between single-subject maps and the group means (normative maps). The WM tracts in the ROIs are easily identifiable in the normative map as well and show good correspondence with the individual subject maps in terms of regional variation. Even for DA_B, which is known to be harder to estimate[158], we see expected contrast in the mean maps, i.e. higher values in the peripheral WM compared to the main WM regions.

There is low inter-subject variability in parameter values in WM, shown by the low values of standard deviation in most regions in the WM. The regions with particularly high variability are the peripheral WM regions where inter-subject differences are expected to be more apparent. The highest variability is seen for DA_B and the lowest for ν_{in}, which is consistent with the findings of parameter estimability analysis in Tariq et al. 2016a.

11.3.3 *ROI analysis*

Table 11.2 summarises the obtained normative values and their standard deviations over the volunteers, in the WM ROIs, for the Bingham-NODDI metrics, while Figure 11.3 provides a visualisation of the distribution of values across the population. For bilateral tracts, the means shown are averaged over the left and right tracts.

The neurite density metric ν_{in} shows high mean values (0.55-0.9) as expected in the WM, while the dispersion parameter values are much lower (ODI_{Tot}<0.35) and the anisotropy measure is fairly high in the WM regions. The trends of the various metrics are visualised in the box and whisker diagram, where the values for various ROIs are sorted with respect to the mean value of each of the parameters.

We see that individual parameters vary across the various WM regions and the pattern of this variation is as expected. The pattern of change of the two dispersion parameters is similar, but the subtle changes in microstructure are captured specifically by the anisotropy measure DA_B. The overall dispersion ODI_{Tot} and DA_B change independently from each other, seen specifically in the more peripheral WM structures.

	ν_{in}	ν_{iso}	ODI_P	ODI_S	ODI_{Tot}	DA_B
MCP	0.833 ± 0.037	0.180 ± 0.017	0.407 ± 0.019	0.184 ± 0.017	0.283 ± 0.019	0.576 ± 0.026
PCT	0.862 ± 0.059	0.227 ± 0.035	0.428 ± 0.048	0.220 ± 0.026	0.319 ± 0.039	0.504 ± 0.038
GCC	0.843 ± 0.049	0.159 ± 0.016	0.284 ± 0.016	0.129 ± 0.013	0.192 ± 0.014	0.548 ± 0.047
BCC	0.744 ± 0.043	0.153 ± 0.018	0.251 ± 0.013	0.112 ± 0.011	0.168 ± 0.012	0.570 ± 0.046
SCC	0.790 ± 0.038	0.154 ± 0.021	0.238 ± 0.013	0.073 ± 0.009	0.126 ± 0.010	0.710 ± 0.033
FX	0.750 ± 0.064	0.330 ± 0.101	0.237 ± 0.068	0.113 ± 0.043	0.163 ± 0.058	0.586 ± 0.055
CST	0.853 ± 0.050	0.224 ± 0.034	0.395 ± 0.039*	0.160 ± 0.028	0.263 ± 0.036	0.602 ± 0.033*
ML	0.701 ± 0.044	0.173 ± 0.042	0.275 ± 0.031*	0.136 ± 0.023*	0.194 ± 0.028*	0.515 ± 0.053*
ICP	0.726 ± 0.042*	0.177 ± 0.047	0.336 ± 0.026*	0.140 ± 0.015*	0.216 ± 0.021*	0.607 ± 0.029
SCP	0.775 ± 0.041*	0.326 ± 0.041	0.230 ± 0.023*	0.098 ± 0.017	0.148 ± 0.021*	0.590 ± 0.033*
CP	0.885 ± 0.031	0.210 ± 0.021*	0.242 ± 0.014*	0.105 ± 0.013*	0.154 ± 0.014*	0.590 ± 0.042*
ALIC	0.817 ± 0.036	0.126 ± 0.029*	0.339 ± 0.018*	0.160 ± 0.016*	0.233 ± 0.017*	0.562 ± 0.044
PLIC	0.843 ± 0.032*	0.138 ± 0.027*	0.277 ± 0.016*	0.099 ± 0.010*	0.161 ± 0.011*	0.652 ± 0.043*
RLIC	0.749 ± 0.045*	0.157 ± 0.028*	0.300 ± 0.016*	0.102 ± 0.014*	0.174 ± 0.014	0.670 ± 0.053*
ACR	0.748 ± 0.036*	0.152 ± 0.017*	0.458 ± 0.024	0.207 ± 0.016*	0.322 ± 0.018	0.581 ± 0.037*
SCR	0.735 ± 0.028*	0.133 ± 0.018*	0.426 ± 0.025*	0.165 ± 0.012*	0.275 ± 0.016	0.652 ± 0.039*
PCR	0.627 ± 0.029	0.126 ± 0.019*	0.395 ± 0.028*	0.140 ± 0.013*	0.240 ± 0.019*	0.674 ± 0.035*
PTR	0.653 ± 0.032	0.132 ± 0.019*	0.295 ± 0.016*	0.094 ± 0.011*	0.166 ± 0.012*	0.689 ± 0.043
SS	0.696 ± 0.040	0.181 ± 0.022*	0.320 ± 0.026	0.101 ± 0.015	0.181 ± 0.018	0.697 ± 0.059
EC	0.617 ± 0.032	0.084 ± 0.022	0.436 ± 0.018*	0.170 ± 0.012*	0.288 ± 0.016*	0.642 ± 0.023*
CGC	0.677 ± 0.041	0.105 ± 0.019*	0.378 ± 0.028	0.169 ± 0.019	0.259 ± 0.024	0.588 ± 0.029
CGH	0.628 ± 0.054*	0.126 ± 0.034	0.394 ± 0.039*	0.194 ± 0.032	0.282 ± 0.039	0.555 ± 0.041*
FX/ST	0.737 ± 0.049*	0.195 ± 0.031*	0.320 ± 0.026*	0.130 ± 0.019	0.208 ± 0.024	0.572 ± 0.051*
SLF	0.717 ± 0.028*	0.128 ± 0.014*	0.434 ± 0.016*	0.140 ± 0.010*	0.257 ± 0.014*	0.715 ± 0.020
SFO	0.795 ± 0.044	0.135 ± 0.022*	0.388 ± 0.025	0.213 ± 0.017*	0.290 ± 0.020*	0.480 ± 0.037*
IFO	0.554 ± 0.031*	0.047 ± 0.019*	0.339 ± 0.031*	0.153 ± 0.015*	0.231 ± 0.022*	0.569 ± 0.036*
UNC	0.661 ± 0.056*	0.294 ± 0.104	0.260 ± 0.033*	0.105 ± 0.026*	0.164 ± 0.032	0.612 ± 0.063*

Table 11.2: Mean and standard deviation of the normative values of the parameters of Bingham-NODDI, across all the subjects, for the various WM ROIs. *Abbreviations: GCC - Genu of Corpus Callosum, BCC - Body of Corpus Callosum, SCC - Splenium of Corpus Callosum, CST - Corticospinal tract, ALIC - Anterior limb of internal capsule, PLIC - Posterior limb of internal capsule, ACR - Anterior corona radiata, SCR - Superior corona radiata, PCR - Posterior corona radiata, PTR - Posterior thalamic radiation, EC - External capsule, SLF - Superior longitudinal fasciculus.* * *indicates where the left and right parts of a tract are statistically different according to the specific estimated index.*

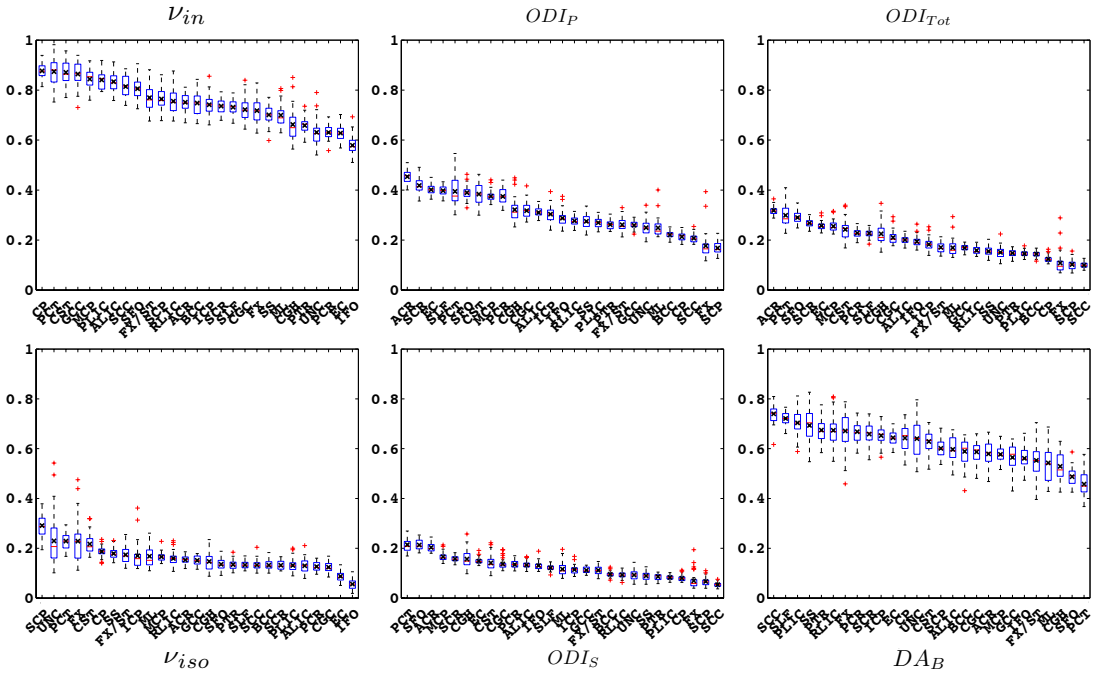

Figure 11.3: Plots showing the distribution of the Bingham-NODDI indices across the adult cohort, for 24 of the WM regions. The first column shows the values for the volume fractions parameters, the middle column, the dispersion parameters, while the last shows the orthogonal measures of total dispersion and dispersion anisotropy. Each of the plots is sorted in ascending order of the specific parameter values, giving an insight into the variation of the metrics. We see that individual parameters vary across the various WM regions and the pattern of this variation is as expected. The pattern of change of the two dispersion parameters is similar, but the subtle changes in microstructure are captured specifically by the anisotropy measure DA_B. The overall dispersion ODI_{Tot} and DA_B change independently from each other, seen specifically in the more peripheral WM structures. For each plot, the box represents the interquartile range, with the medians marked by red horizontal lines and the mean values by the black 'x'. The red '+' signs indicate the outliers

For ν_{in} the highest values are seen for the WM regions in the pyramidal tract, specifically CP, CST, and PLIC, as well as in MCP, which is a part of the brain stem. Lowest ν_{in} values are seen for the more peripheral WM including the CGH and IFO and PCR and EC, which are expected to have lower neurite density as the axonal projections usually disperse to reach various cortical regions. Such peripheral regions have the highest overall dispersion values, while the main WM tracts like the SCC, PLIC, and CP have the lowest dispersion values. The anisotropy metric, DA_B, has highest values in the SLF, SCC, SS, and PTR, which are all part of projection or association fibres close to the cortex and are expected to exhibit anisotropic dispersion. The lowest values are seen in the GCC, ML, PCT and the SFO which are all part of the main WM tracts, away from the cortical projections and thus have little anisotropy.

The inter-subject variability is the highest for ν_{in} and DA_B and the lowest for the dispersion parameters. The coefficient of variation, on the other hand, has the opposite trend, as the mean values of ν_{in} and DA_B are much higher than the other parameters of Bingham-NODDI. The highest variability seems to be associated with the estimation of all of the parameters in the FX and the UNC and the lowest with the main WM tracts like the CC and CR.

If the differences in means of the left and right sides are statistically significant, it is indicated by an asterisk next to the mean values listed in Table 11.2. Most bilateral tracts have significant differences between the right and left sides, with at least one of the Bingham-NODDI metrics.

11.3.4 *Power analysis*

The power analysis results are summarised in Table 11.3 for Bingham-NODDI indices. As expected the cohort requirements increase with reduced effect size, but the relative sample requirement across the various parameters remain the same. For example, ODI_S and ν_{iso} require a very large number of subjects even for a relatively large effect size of 10%, while ν_{in} requires the smallest cohort size. For an effect size of 10%, corresponding to change of 0.01 for each of the Bingham-NODDI metrics, the cohort size is around 20, which is comparable to requirements for the DTI metrics (Figure 11.4) and the original NODDI model (results not shown), except for the very noisy ROIs specifically the FX.

In terms of the specific WM ROIs the FX and UNC, which are two of the smallest ROIs require the highest number of subjects for all of the parameters, followed by CST, ML, and SCP, the regions in the most medial parts of the

brain and in general have the lowest signal-to-noise ratio (SNR) due to distance from the receiver coils.

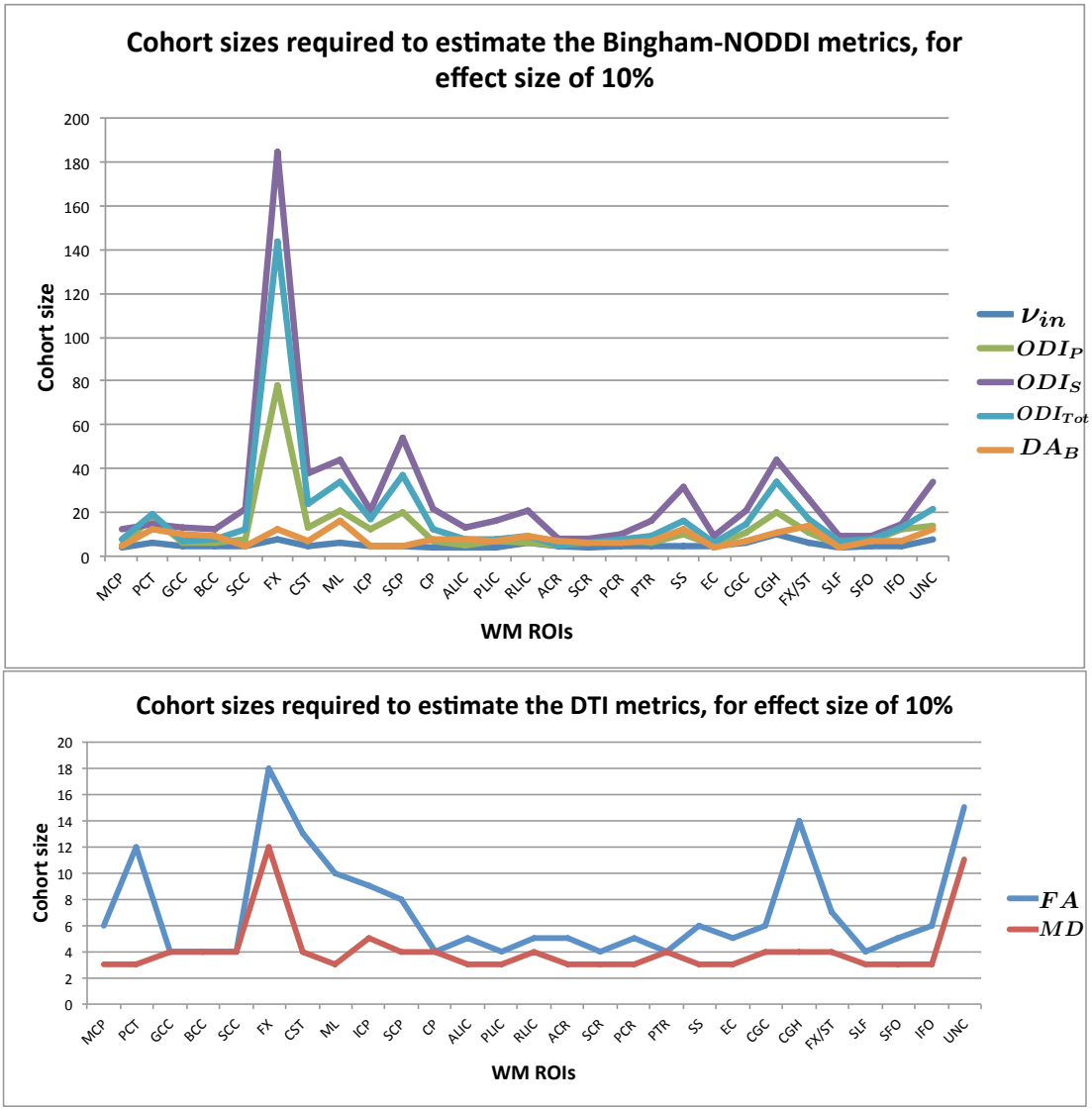

Figure 11.4: Plot showing the power calculation results for the Bingham-NODDI and DTI metrics

11.3.5 *Regional variability of WM*

To determine how well the metrics of Bingham-NODDI differentiate the various ROIs we compare the mean value in each ROI with all others. This analysis is summarised in Figure 11.5, where the colours indicate whether the paired values are statistically different or not. The ROIs are sorted according to the mean value for each parameter, as in Figure 11.3. For the highest differentiation between the various ROIs, we expect the plot to have values of 0 along the

	ν_{in}	ν_{iso}	ODI_P	ODI_S	ODI_{Tot}	DA_B
MCP	4	9	4	9	6	4
PCT	6	21	12	13	14	7
GCC	5	11	5	10	7	8
BCC	5	14	5	10	6	8
SCC	5	17	5	15	8	4
FX	8	76	67	118	102	10
CST	5	21	10	26	17	5
ML	6	49	13	25	19	11
ICP	5	58	7	12	10	5
SCP	5	15	11	26	19	5
CP	4	11	5	14	9	7
ALIC	4	45	5	10	7	7
PLIC	4	32	6	11	6	6
RLIC	6	27	5	17	7	8
ACR	5	12	5	8	5	6
SCR	4	16	6	7	6	6
PCR	5	19	7	9	7	5
PTR	5	19	5	13	7	6
SS	5	14	8	21	11	8
EC	5	56	4	7	5	4
CGC	6	29	7	13	9	5
CGH	8	59	10	24	17	7
FX/ST	6	22	8	20	13	9
SLF	4	12	4	6	5	3
SFO	5	24	6	8	6	7
IFO	5	130	9	10	10	6
UNC	8	101	16	51	33	11

Table 11.3: Power cacluations for Bingham-NODDI metrics, for effect size of 10% for each metric. The values for effect size 5% and 2% are shown in Appendix D

diagonal only. So the plots where the dark values are most tightly packed (i.e. the null hypothesis is mostly rejected), gives the best regional variability across the various WM regions. From the plots, it appears that ν_{in} and ODI_{Tot} provide the most regional variation amongst the Bingham-NODDI metrics, while the DA_B provides the least.

Another interesting finding from these results is how well the parameters group the specific fibres of the WM (see Section 2.2.2 for the categories of WM fibres). In general, the association fibres are best grouped with the Bingham-NODDI metrics, followed by the projections fibres. Overall the regional differences seen with the Bingham-NODDI metrics is similar to those of DTI metrics (results included in the Appendix D, Figure D.3).

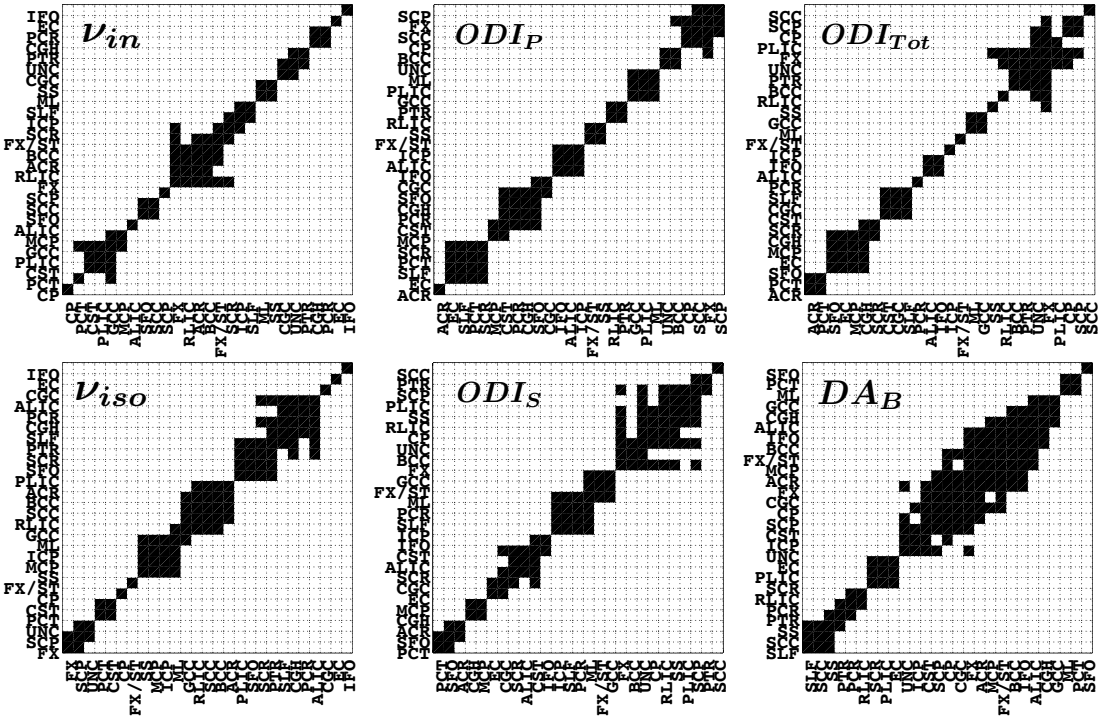

Figure 11.5: Plot indicating whether each pair of ROI being compared is statistically the different (white) or not (black).

11.3.6 *NODDI vs DTI metrics*

To determine how the NODDI models compare to the standard DTI model fit, we compare the variability of the metrics using the coefficient of variation (CV), which represents the relative standard deviation as a percentage, enabling comparison across different variables. Tables D.2, D.4 and D.6 in Appendix D report the CV of the Bingham-NODDI, Watson-NODDI and the DTI models, respectively. A direct comaprison of the CV of the Bingham-NODDI

and DTI metrics is shown in Figure 11.6. As expected, the variability of the corresponding parameters of the two NODDI models is consistent. The orientation dispersion parameters have higher variability compared to ν_{in} and the dispersion anisotropy index, DA_B. In general, the NODDI metrics have higher CV compared to DTI. This is the finding for multi-shell fit for DTI and using a more standard $b = 1000 mm s^{-1}$ gives a slightly lower CV. This is expected as a single-shell acquisition is better than multi-shell for Gaussian diffusion.

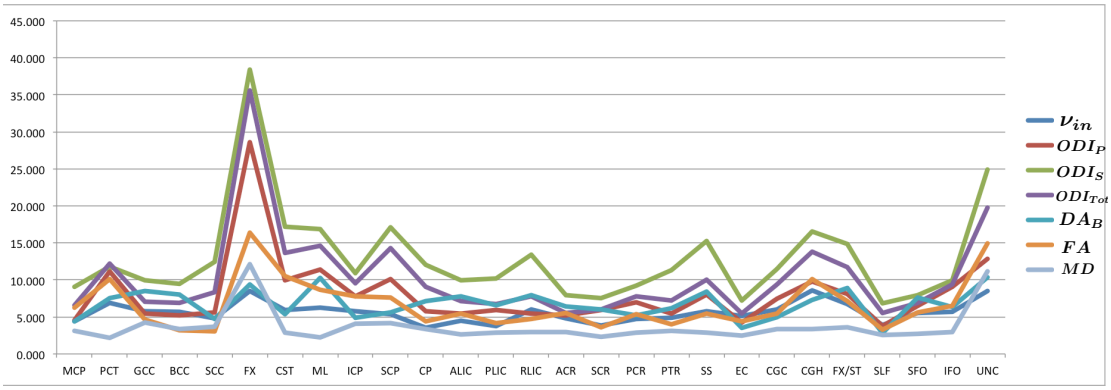

Figure 11.6: Plot showing the variability in the parameter estimates, quantified as the CV, for the Bingham-NODDI and DTI metrics

11.4 DISCUSSION

In this work, we use a larger cohort to establish the range of values of Bingham-NODDI indices in the normal adult brain, as well as how variable these are across the different WM regions. Such an assessment is important to establish the range of values of the model's parameters expected in the normal adult brain. The reported results of the power calculations will help design future studies to measure differences across groups in a neuroscience or clinical study, using indices of Bingham-NODDI.

Our results demonstrate the regional variation of neurite morphology captured by the indices of Bingham-NODDI. The modest inter-subject variability of the indices means that we can utilise the model for interesting clinical applications, e.g. to see how these parameters change over time, by comparison to normative values in pre-term population[94,102], or to use the reported sample sizes in the power calculation to help design the studies for neuroscience or clinical studies.

We see expected regional variation in the Bingham-NODDI parameters across the cohort. For example, highest ν_{in} is seen for major WM tracts like

CC, CST, and ALIC/PLIC and lowest for peripheral WM structures like the CR, EC, and SLF, which is consistent with the known packing density of their axons. DA_B is high in regions with expected complex fibres (CR, SLF, PLIC) and low in regions with a fairly isotropic dispersion of axons (CC, FX, CST). The results also highlight that DA_B is highly variable within the WM ROIs.

The normative values we report are also consistent with existing publications. The mean values of the Watson-NODDI parameters in the adult population are very similar to those reported in Kodiweeraa and Wu 2016, despite a different acquisition protocol used, and with those in Chung et al. 2016. In general, the variability of the metrics is lower for our results, most likely due to the use of high-quality images.

The DTI values, on the other hand, are fairly different to those reported in these studies. This difference is reduced when single shell ($b = 1000s/mm^2$) data is used to fit DTI and the ROIs are eroded, as expected. The results for Watson-NODDI and DTI parameters are included in the Appendix D for reference. DA_B and ν_{in} have cohort requirements very similar to the DTI metrics. The cohort size required for the dispersion metrics of Bingham-NODDI, ODI_P, ODI_S and ODI_{Tot} is reasonably close to DTI metrics for all ROIs, except the FX and UNC.

11.4.1 *Limitations and future work*

The presented results utilise WM ROIs manually segmented on single-shell diffusion MRI data, which are registered to the population template generated from multi-shell data. A limitation of this approach is that the registration is not perfect and introduces some errors in the reported results. As can be seen also from the overlap of the segmentations on the individual subjects' parameter maps (Figure 11.1), sometimes the voxels outside of the actual tract are included in the ROI. This can be avoided by applying erosion to the ROI segmentations, which is an approach adopted in many publications but was not utilised here. We found that while it improved the results of some of the parameters (for e. g.the FA values in the CC were much higher and a lot closer to the literature accepted values, when erosion was applied), it results in the number of voxels reducing by a lot, especially for the small tracts such as the FX and the UNC (up to 80% fewer voxels) reducing the statistical power of the reported results. This is directly evident in the variances and power calculations for these tracts, which increase after erosion.

Work extending the presented study to include the superficial WM regions, like the ROIs in Oishi et al. 2008, as well GM regions is the next natural direction for this study. But the normalisation method used here works well only for the core WM regions, as seen from the higher variability in the other brain regions and thus needs improvement for the peripheral WM and GM alignment.

We established the cross-sectional variability here, which is important, but to evaluate whether the variability reported reflects true structural differences and not noise or imaging artifacts, we need a reproducibility study where the noise contributions can be separated from the inter-subject variability. Such a study is the subject of the next chapter, which reveals how differentiable the indices of Bingham-NODDI are from noise.

12

REPRODUCIBILITY AND RELIABILITY OF BINGHAM-NODDI INDICES IN THE WHITE MATTER

In this chapter, we present a pilot study to evaluate the test-retest reproducibility and reliability of Bingham-NODDI metrics. This is an important step towards establishing the technique as a useful tool for neuroimaging studies. A method with reproducible indices can be utilised with a high confidence to differentiate between various groups like healthy and control or male and female, which are some of the criteria utilised for common neuroscience studies. This requires an assessment of the various sources of variability in the estimation of the model parameters. Such an assessment can determine if the real microstructural differences (i.e. between-subject differences) are distinguishable given the noise in the measurements (i.e. within-subject variability) and thus, demonstrate the clinical applicability of Bingham-NODDI.

12.1 INTRODUCTION

Every measurement has an error associated with it, which results in the estimated values varying from the true value. In clinical practice, measurements are made to aid diagnosis and prognosis by assessing how close they are to the typical or normal values of the quantity being measured. Thus from the clinical perspective, it is important for a method of measurement to be not only accurate, i.e close to the true value, but also precise, i.e. have low variability associated with its estimate. A reproducibility study is thus an important step towards establishing a new method, like Bingham-NODDI, as a clinically useful technique. In this work, we compare the reproducibility of Bingham-NODDI and DTI metrics, to see how the proposed method compares to the standard DW-MRI technique, using a pilot study utilising scan-rescan data acquired on healthy subjects.

If the estimates made by a technique differ from one subject to another at a level comparable to noise, then the method has a very low discriminative power. This implies that the technique will not be very useful in practice as a difference in two measurements can be attributed to noise rather than actual differences in the quantity being measured. So if we can show that Bingham-NODDI is able to *reliably* estimate its parameters, it can become a useful clinical tool and the estimates made can act as markers for specific disease progression. The *in vivo* accuracy of Bingham-NODDI parameters has already been established in Tariq et al. 2016a (Chapters 7 and 8), while Tariq et al. 2016b looks at their inherent variability or precision (Chapter 11). Here we look at how reliable these metrics are by employing a test-retest experiment where multiple subjects are scanned twice, within a short time period. We have already demonstrated a good agreement of NODDI estimates in a pilot study on a single subject in Tariq et al. 2012 and shown that the precision of NODDI estimates is comparable to that of DTI indices. In this study, we want to establish the reliability or the discriminative power of NODDI estimates.

We carry out an ANOVA procedure on test-retest diffusion MRI data acquired on multiple healthy subjects, which enables separation of the within- and between-subject variability. Since we have just two measurements on each subject, a simple t-test is sufficient to assess whether the differences in means of the scan-rescan estimates are statistically the same or not. But we want to evaluate the reliability of Bingham-NODDI metrics, which requires estimation of the within- and between-subject variability as well as the noise. So we employ a repeated measures ANOVA to compute the between-subject and within-subject variability, which gives us a measure of the reliability of the metrics being assessed. We also assess the agreement of the metrics as we have multiple measurements (MR images) for the same subjects, where we expect no real differences in the indices, as the time between the two scans is short. We also report the coefficient of variation (CV) to allow comparison to other studies.

12.2 EXPERIMENT DESIGN

12.2.1 *Cohort and MRI data acquisition*

The cohort for this pilot study consists of 10 healthy adults, of which 6 are males, with mean age $\mathbf{32.1 \pm 6.08}$years. *In-vivo* diffusion MRI data was acquired on a $3\boldsymbol{T}$ Siemens Trio scanner, with $|\boldsymbol{G}|_{max} = 40\mathrm{m}\boldsymbol{T}/\mathrm{m}$. The data is

acquired as a repeated measures design where each subject is scanned twice, with roughly 40 minutes between the two scans (volunteers were taken out of the scan between the two sessions). The short time between the two scans for each subject mean that effects like thermal drifts and other long-term changes in the scanner are not captured. This is suitable for our assessment as we want to assess only the variability in the estimates due to thermal noise and patient-related noise (movement, physiological noise), and are not interested in scanner-specific effects.

The DW-MRI data is obtained using the optimised NODDI protocol for a scanner with $|\boldsymbol{G}|_{max} = 40 mT/m$, i. e.with b-values of $700 s/mm^2$ and $2000 s/mm^2$, as recommended in Zhang et al. 2012. An additional b-value of $300 s/mm^2$ is acquired for better estimation of the isotropic compartment. The three b-values are acquired for 8, 32 and 64 gradient orientations, respectively, with an additional 15 acquisitions with no diffusion weighting for signal normalisation. TR= 7s and TE= 91.6ms are same for all measurements and the diffusion gradient strength is varied to get the different b-values.

12.2.2 *Pre-processing for artefact correction*

To correct for motion artefacts and eddy current distortions, we utilise the *eddy*[9] tool, from the *FSL* analysis libraries[83]. The data acquired has very little motion and some eddy current artifacts and *eddy* gives results which reduce both, with minimum impact on results when data has no artifacts[70].

12.2.3 *Model fitting procedure*

The NODDI model was fitted to the data using the NODDI Matlab Toolbox[1] , with modification to include Bingham-NODDI model. Bingham-NODDI fitting was initialisated from the Watson-NODDI and DTI estimates, as done for experiments in Chapter 11 (described in Section 9.1).

12.2.4 *Spatial normalisation and region-of-interests*

To compute statistics of the estimated metrics across the cohort, the acquired images were spatially normalised with respect to a study-specific template. This was done by first creating a subject-specific template, by registering the

1 Available online at: https : //www.nitrc.org/projects/noddi$_t$oolbox/

two scans per subject. The resulting subject-specific templates are then registered with each other to create the final study-specific template.

The spatial normalisations are all carried out using the tensor-based registration process implemented in DTI-TK[2], as also done for the *HCP* data in Chapter 11. All the subjects are used to generate the study-specific template as the current data is of standard quality and has slightly less homogeneous data compared to the *HCP* data.

We report the reproducibility of the Bingham-NODDI metrics across the key WM tracts, using the WM ROIs defined in Mori et al. 2008.

12.3 STATISTICAL ANALYSIS

We are interested in applying Bingham-NODDI as a tool to differentiate normal subjects from a patient population, as well as a tool for accurately obtaining connectivity between different regions of the brain via tractography. Thus we want to quantify the reliability of its indices. High reliability corresponds to the estimation of parameters with low inherent variability (or noise), such that the differences in measurements can be associated with true microstructural differences with high confidence. We, therefore, are interested in estimating the different sources of variability in the estimation of Bingham-NODDI indices.

We assess both the agreement or reproducibility, which quantifies the precision of the metrics (i.e. the difference in two measurements with the same true value) and the reliability of the indices, which quantifies how well it can distinguish real differences in metrics, i.e. between-subject differences. We use various statistical methods to assess the reproducibility and reliability of the estimates, as detailed in the following sections. Main metrics of Watson-NODDI and DTI are also assessed along with those of Bingham-NODDI.

12.3.1 *Agreement of the indices*

We quantify the agreement between the indices estimated from the scan-rescan data, as a simple and quick way to assess how well the corresponding metrics for the same subject match each other.

To assess the agreement of the indices we quantify whether the indices obtained from the two scans of the same subject are statistically the same or not

2 Available online at: http://dti-tk.sourceforge.net

and compute the within-subject variability. This is done by quantifying the *coefficient of variation (CV)*, which is a measure of the dispersion of the variables about the mean, given by

$$CV = \sigma_k/\mu \times 100 \,, \tag{12.1}$$

where σ_k is the within-subject (between-scan) variance

We do a paired t-test to verify that the scans from the two subjects are statistically the same, i.e. are obtained from the same set of subjects and quantify their variability as the coefficient of variation.

12.3.2 *Reliability of the indices*

Reliability is a measure used to quantify the reproducibility of a parameter, and is defined in Bartlett and Frost 2008 as a measure that relates the *measurement error* to variability in true value due to differences *between subjects*. To separate these sources of variance in the estimated parameters of the models, we use ANOVA.

Numerous quantifications of reliability have been reported, which all provide dramatically different values[118,144]. So it is very important to not only report the computed value, with details of how it is computed, but also the actual variances calculated, as the reliability is a sample specific quantification.

12.3.2.1 *ANOVA*

An ANOVA is a specific form of General Linear Models (GLMs) where the response (measured) variable is modelled as a linear combination of one or more sources of variability, as well as noise (details in Appendix E). The j^{th} measurment made on the i^{th} subject has the form

$$Y_{ij} = \mu + \pi_i + \alpha_j + \epsilon_{ij} \,, \tag{12.2}$$

where μ is the grand mean of all measurment, π_i the effect of i^{th} subject and α_j the effect of j^{th} scan, while ϵ_{ij} models the contribution of random noise. Here $1 \leqslant i \leqslant n, 1 \leqslant j \leqslant k$, where n is the number of subjects and k the number of measurements/scans on each subject. The random effects of interest as well as the noise are normally distributed: α_j $N(0, {\sigma_n}^2)$, β_j $N(0, {\sigma_k}^2)$ and ϵ_{ij} $N(0, {\sigma_e}^2)$.

In this model, the response variable Y_{ij} is modelled to be different from the population mean μ, by the subject, scan and noise effects. An interaction term $(\pi\alpha)_{ij}$, between the scan and subject, is also sometimes included in the model.In order to separate this *interaction* effect from the noise ϵ_{ij}, we would have to take multiple scans for each subject, on each day. Thus the variance of the interaction term, ${\sigma_I}^2$ and the variance of the noise, σ^2 are not separable in our experiment design, without multiple scans during each session on each subject. The contributions to Y_{ij} from its constituents in Equation (12.2) are estimated from the acquired data, by partitioning the *sum-squares*, the sum of squared differences from the mean[187]

$$SS_n = \sum_{i=1}^{n} k(\bar{Y_{i.}} - \bar{Y_{..}})^2, \tag{12.3}$$

for between-subject effect, and

$$SS_k = \sum_{i=1}^{n}\sum_{j=1}^{k} (Y_{ij} - \bar{Y_{i.}})^2, \tag{12.4}$$

for within-subject effect. Here $\bar{Y_{..}}$ is the grand mean of the data and $\bar{Y_{i.}}$ and $\bar{Y_{.j}}$, the means across the two effects of interest, respectively. The corresponding degrees of freedom are $(n-1)$ and $(k-1)n$, respectively for the subject and scan effect. These *sum-squares* and degrees of freedom are used to compute the variances associated with the subject (σ_k) and scans (σ_k), as detailed in Appendix E.

In GLMs the mean response can be modelled as a combination of population characteristics that are assumed to be shared by all individuals (fixed effects) and subject-specific ones that are unique to particular individuals (random effects). The choice of whether an effect is treated as a fixed or random effect depends on whether the interest lies in the behaviour of only the particular instance of effect (fixed) or the underlying population (random). We consider the subjects as random effect as we are interested in the variability associated with the underlying population of all healthy adult subjects.

Each scan obtained in this experiment can be considered a specific instance as the associated scanner noise depends on many factors including the time of scan (e.g. if scan happens after a long day of scanning, the heating of gradient coils causes a drift in the signal), various artifacts from eddy currents, magnetic susceptibility gradients, noise as well as cardiac pulsation. So it would

be desirable to treat the scan effect as a random variable too, but it can not be separated from the measurement error, with only single scan acquired at each "session".

One-factor ANOVA is suitable for our experiment design, as with just one scan per session for each subject, the effect of the specific scan cannot be separated from the noise variation. As detailed in Shrout and Fleiss 1979b and Müller and Büttner 1994, since each rater, or in our case the specific instance of the scan (i.e. the various contributing factors to the scan acquired e.g. scanner drift, hardware heating, etc. which have a different contribution to the data, each time it is acquired even on the same scanner), only "rates" each of the subjects once, we should use a one-way ANOVA. Our data has a repeated measures design so the within-subject measures are correlated, giving more statistical power compared to an independent measures design.

12.3.2.2 *Metrics of reliability*

The reliability of estimating a parameter Y_{ij} can be quantified as the *intra-class correlation coefficient* or *ICC*. Using the process described in Müller and Büttner 1994 for our experiment design, the reliability should be computed as follows:

$$ICC_{subject} = \frac{{\sigma_n}^2}{({\sigma_n}^2 + \sigma^2)}, \tag{12.5}$$

where $0 \leqslant ICC_{subject} \leqslant 1$, with 1 representing a perfectly reliable parameter. This quantification provides one of the most conservative estimates of ICC, so the values quoted here may be less compared to other work, but the relative values of ICC for DTI and NODDI estimates should remain the same as other work, e.g. Tariq et al. 2013. We also compute the corresponding metrics for the scan/noise component, $MS_{scan} = \sigma$, which is the variability due to the within-subject differences. Unlike the $ICC_{subject}$, MS_{scan} should be as small as possible for a particular metric to be more reliable.

12.4 RESULTS

12.4.1 *Parameter maps*

Figures 12.1-12.4 show the parameter maps for the Bingham-NODDI and DTI metrics, in the template space, for both scan session of two of the subjects. The

maps provide a visual assessment of the artifact removal and normalisation process.

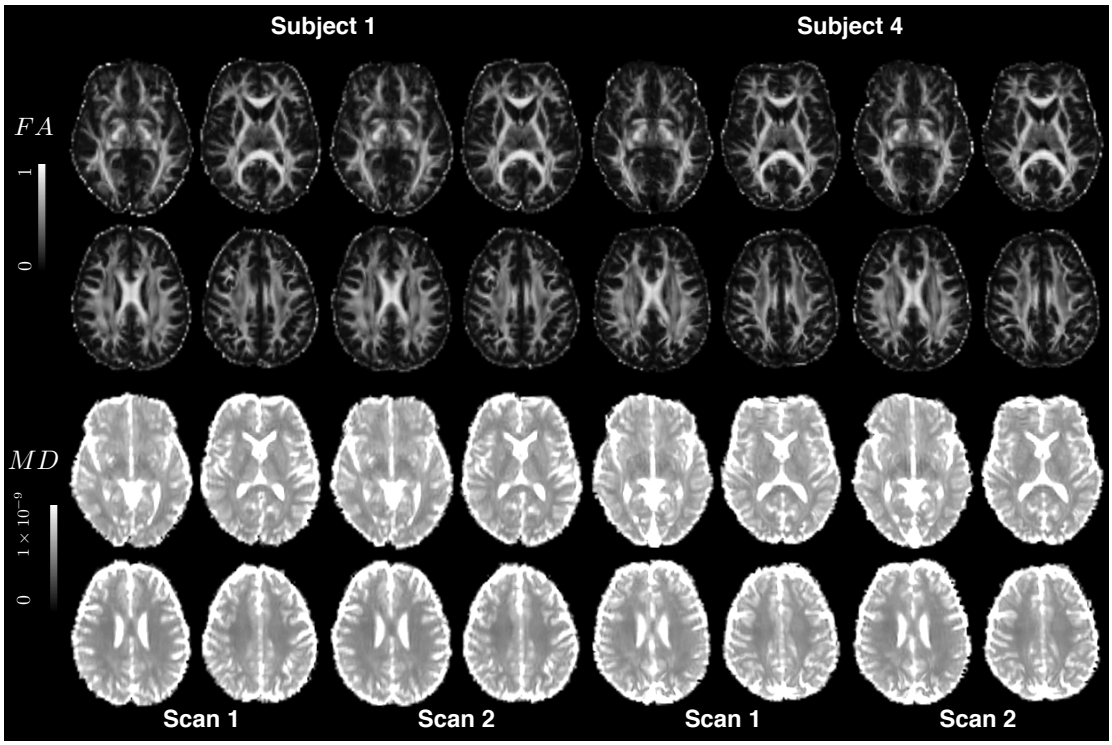

Figure 12.1: Parameter maps of the DTI indices of FA (top) and MD (bottom) in the population template space, for mutliple axial slices of two subjects.

Overall the maps show consistent patterns, even between different subjects, particularly in the core WM regions, indicating good normalisation of the images.

Looking at the scan-rescan data for each subject, we found that the data for one of the subjects is very noisy (intensities very different in the two scans even after registration), so it is removed from further analysis. An interesting finding is that the NODDI metrics, for both models, are affected by this difference but not the DTI ones. So DTI metrics are not sensitive to underlying differences in intensities of the acquisition. The intensity differences in the raw images and the estimated parameters for the excluded subject and a few more are shown for reference in Appendix F.

12.4.2 *Agreement analysis*

12.4.2.1 *Paired t-test*

The statistical analysis shows that for the majority of WM ROIs the estimated parameters are the same, for all the models (results not shown).

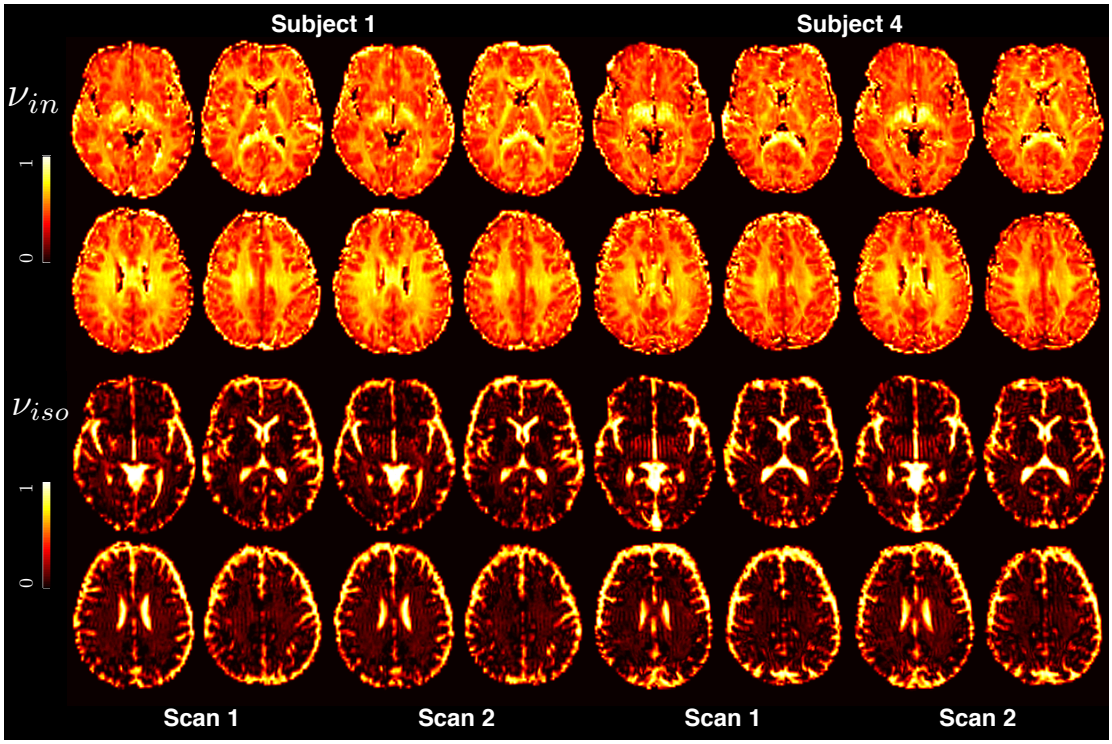

Figure 12.2: As Figure 12.1, but for Bingham-NODDI indices of ν_{in} and ν_{iso}.

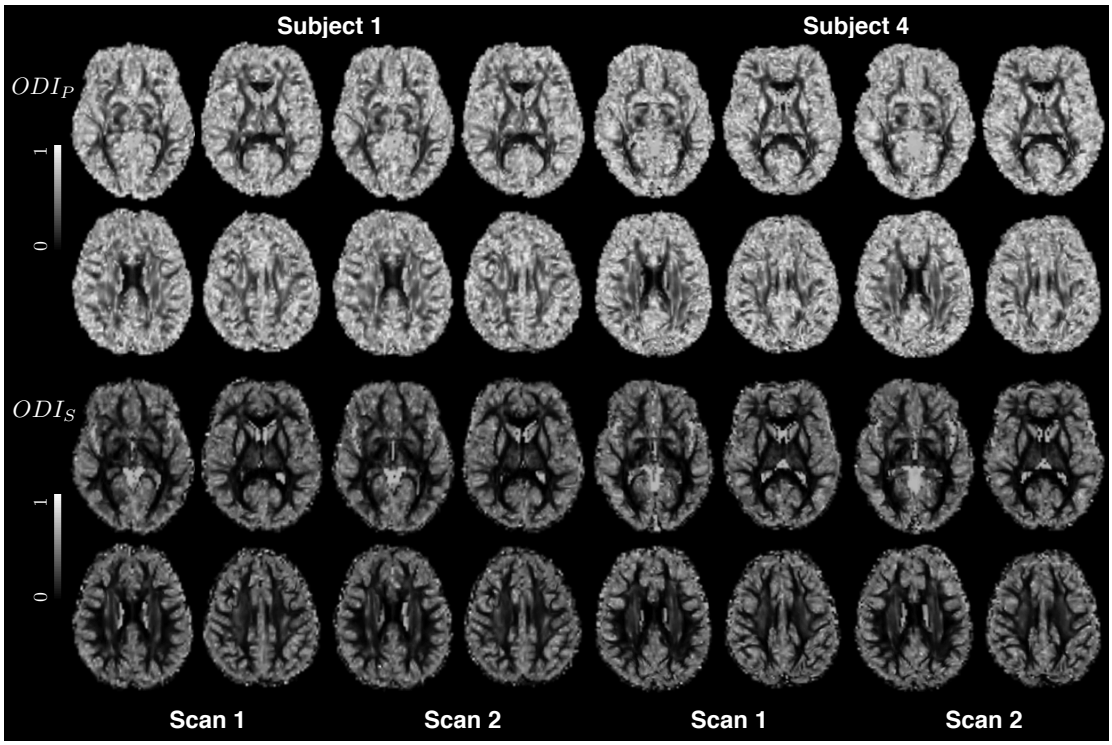

Figure 12.3: As Figure 12.1, but for Bingham-NODDI indices of ODI_P and ODI_S.

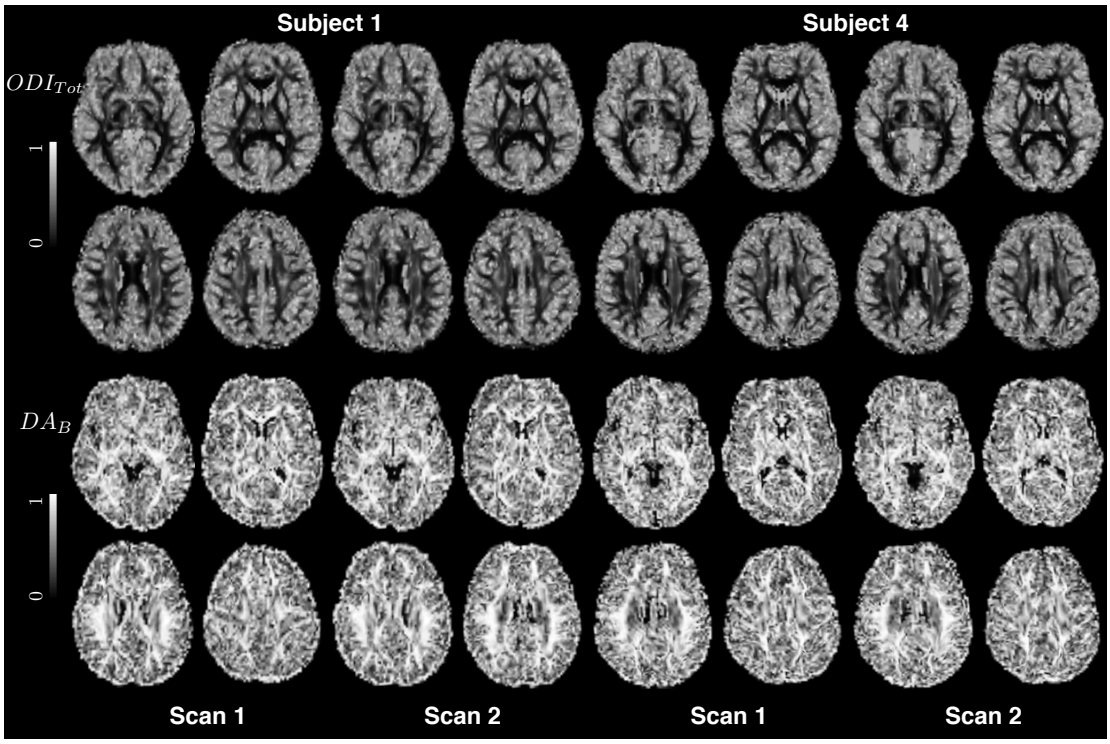

Figure 12.4: As Figure 12.1, but for Bingham-NODDI indices of ODI_{Tot} and DA_B.

Figure 12.5 summarises the findings of the paired t-test computed for the metrics of both Bingham-NODDI and DTI. The plotted values show whether, for each of the WM ROI, the alternative hypothesis is true (white) or false (black), signifying statistically different values in the ROI for that parameter. Thus for most of the parameters, the estimates are statistically the same.

The values on the right of the plot show the percentage of voxels in all the WM ROIs, with statistically significant differences for each parameter. Interestingly, the DTI parameters show the highest amount of statistically significant differences. Overall, the metrics are statistically the same across the two scans, for all parameters.

12.4.2.2 *Coefficient of variation*

Figures 12.6-12.9 show the mean of the absolute differences between the two scans of each subject and the within-subject CV (CV_{within}) computed from it, representing the differences as a percentage of the mean values of the parameters, in the WM ROIs being evaluated.

Figure 12.10 shows the distribution of the mean differences and the CV_{within} for all the parameters and the trends verify the overall findings from the maps of within-subject variability.

In general the Bingham-NODDI metrics have higher within-subject variability and CV_{within} compared to DTI ones, consistent with the results in Chap-

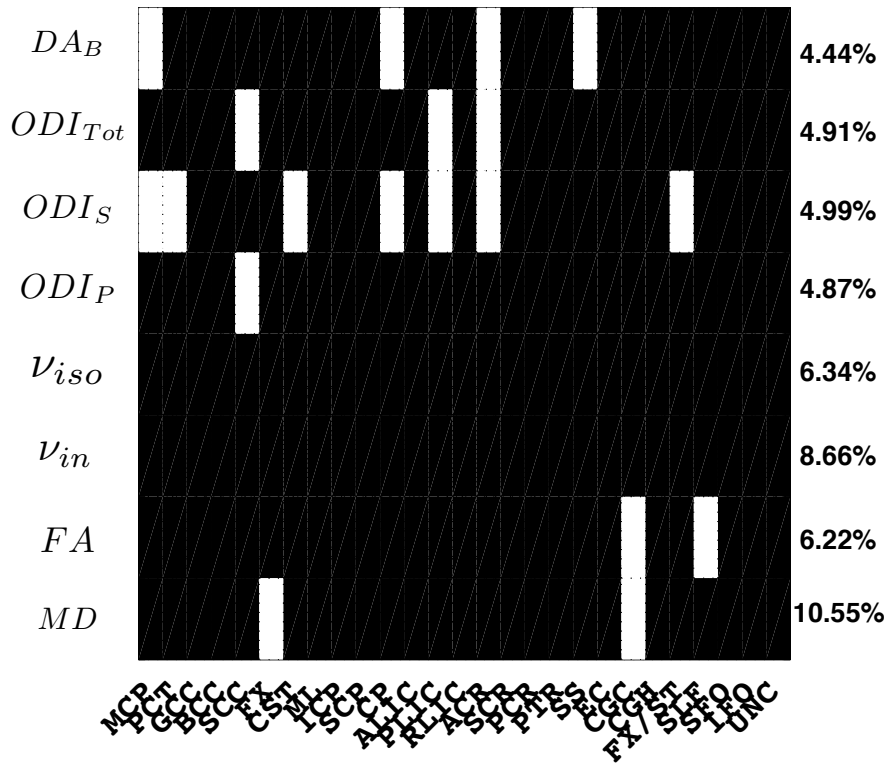

Figure 12.5: Plot showing the results of the paired t-test for the metrics of Bingham-NODDI and DTI. Here white values depict that the alternative hypothesis is true, i.e. the paired values of the specific model parameter are statistically different for that ROI. The values on the right of the plot show the percentage of voxels in all the WM ROIs, with statistically significant differences for each parameter. For example, for FA, only two of the ROIs show statistically significant differences across the two scan (CGC and SLF), and for 6.22% of the voxels in the whole WM.

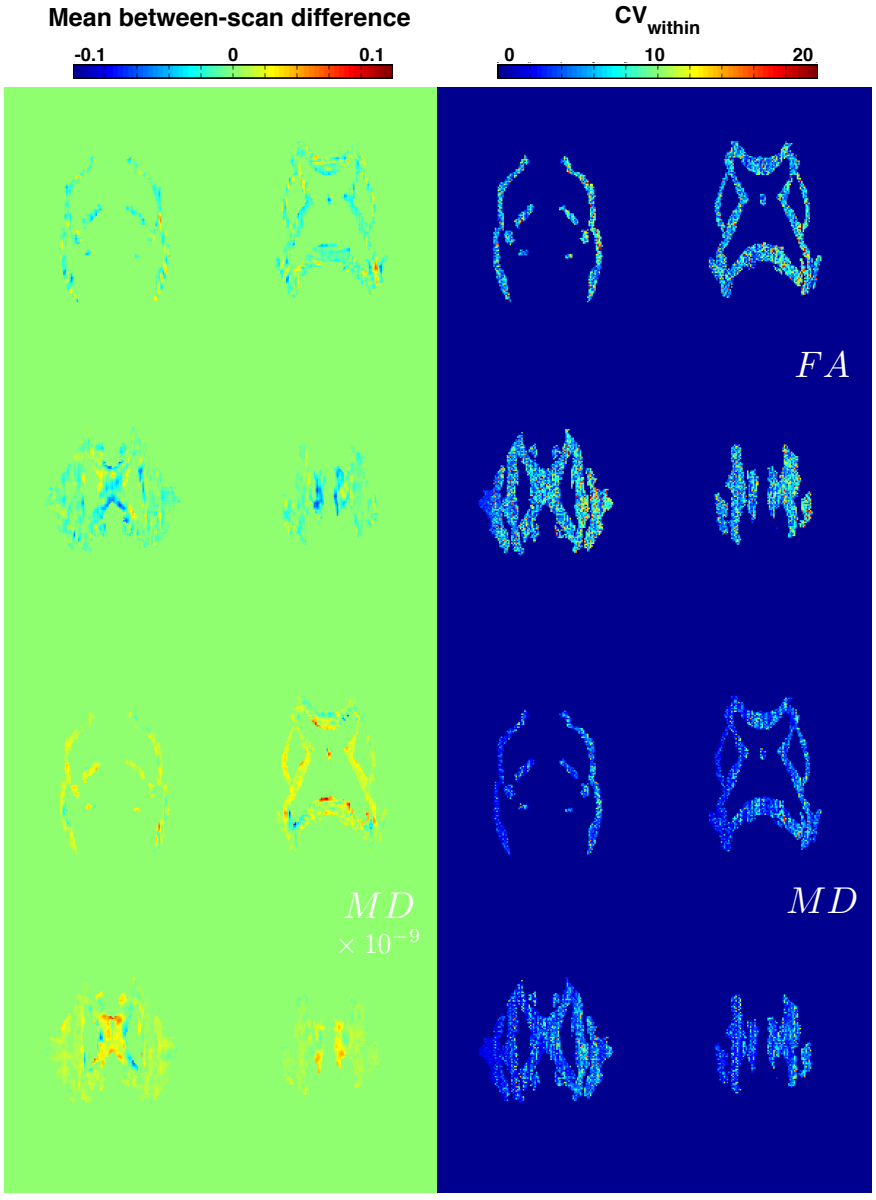

Figure 12.6: Maps of the mean between-scan differences and the CV_{within} for the DTI metrics of FA (top) and MD (bottom) in WM ROIs for four slices of the brain.

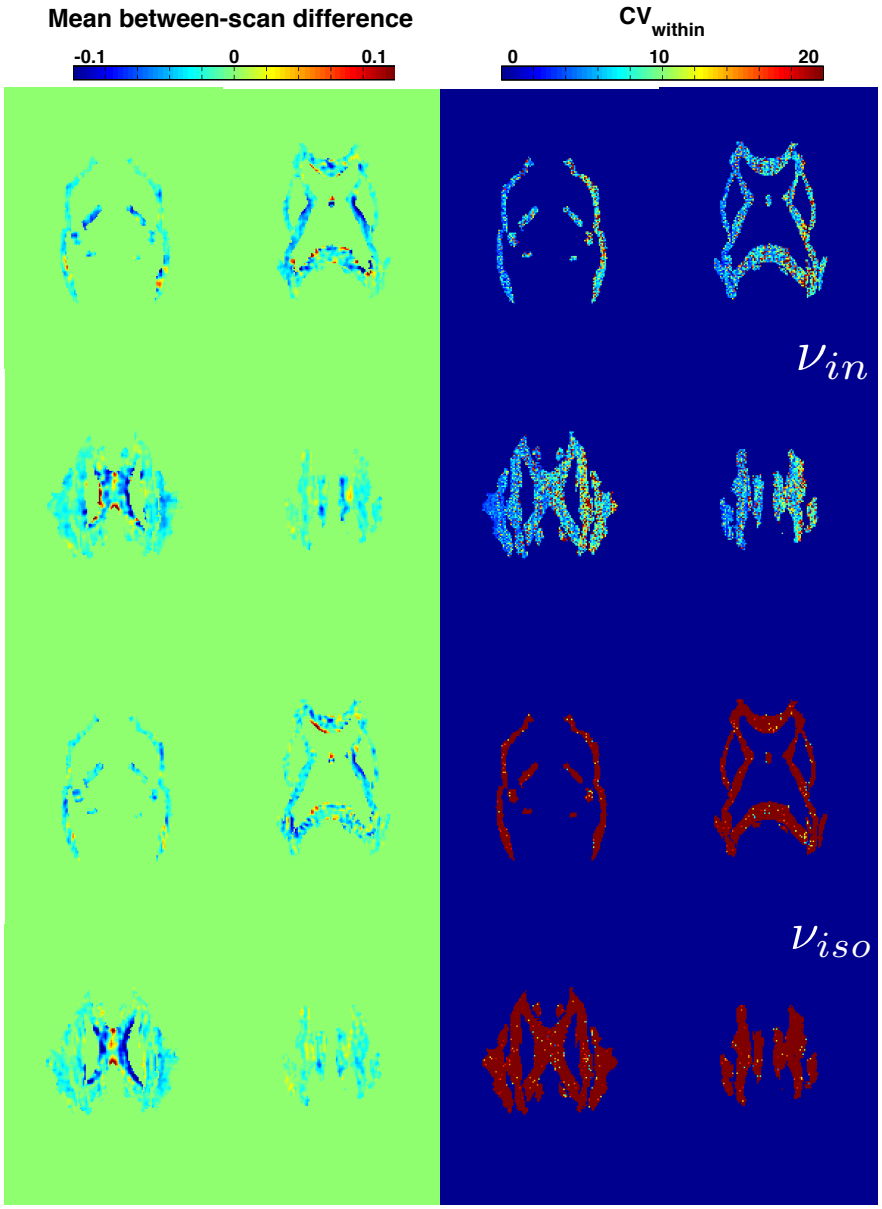

Figure 12.7: As Figure 12.6, but for ν_{in} (top) and ν_{iso} (bottom) indices of Bingham-NODDI.

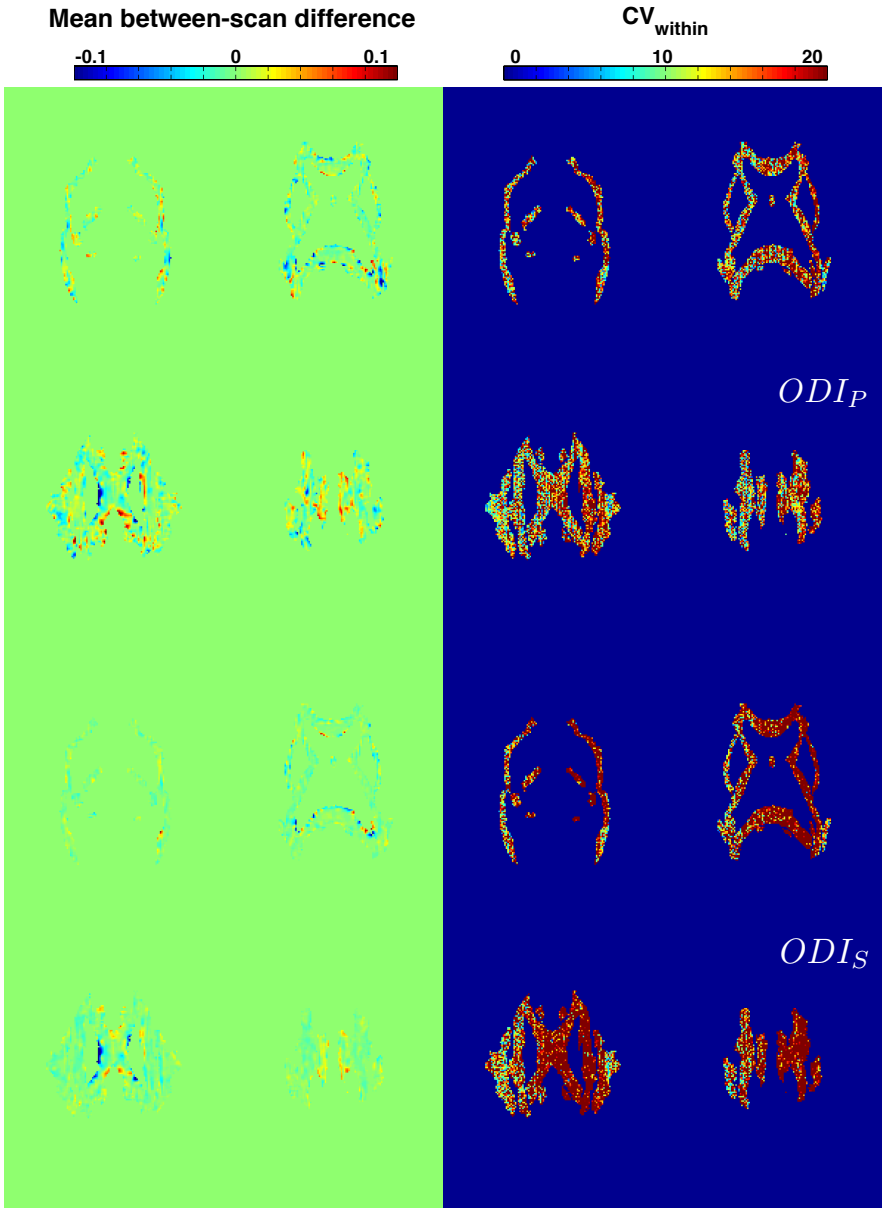

Figure 12.8: As Figure 12.6, but for ODI_P (top) and ODI_S (bottom) indices of Bingham-NODDI.

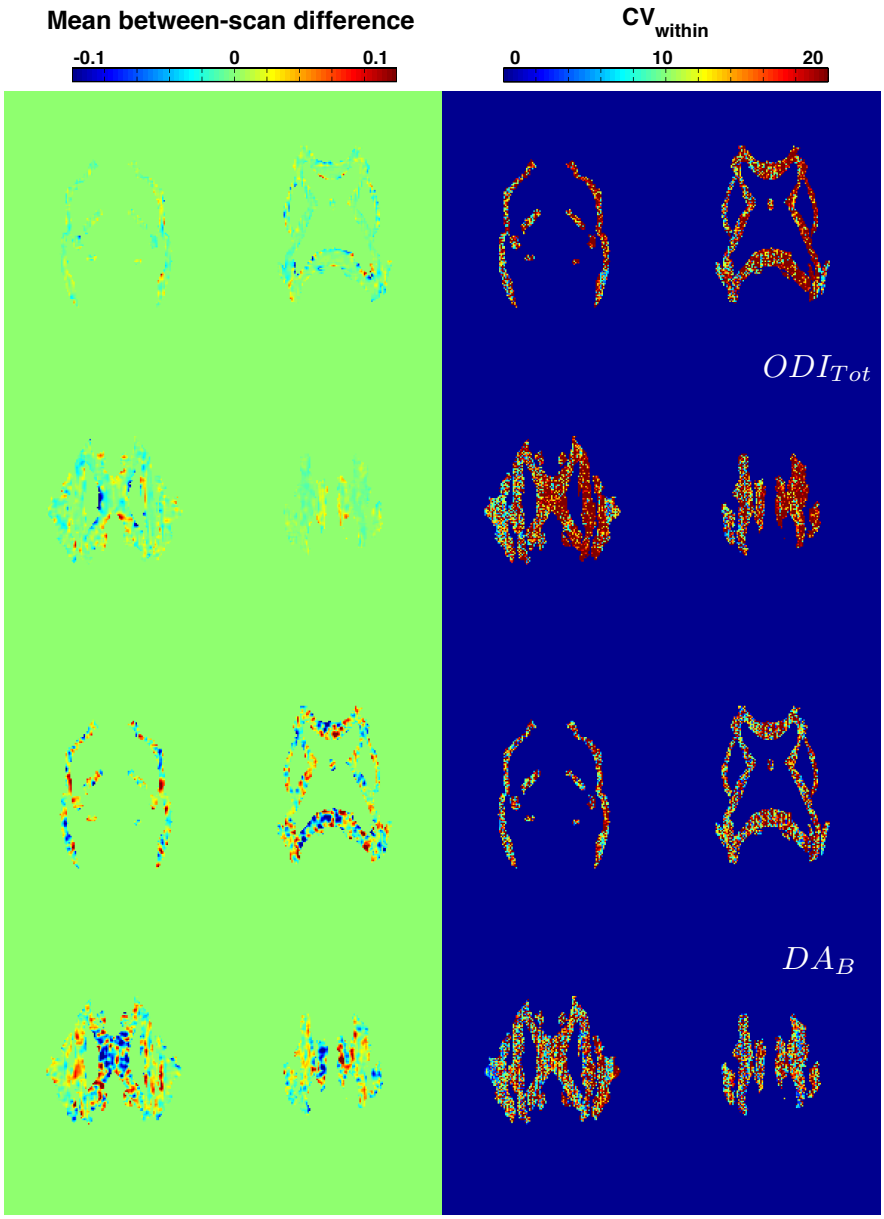

Figure 12.9: As Figure 12.6, but for $\mathrm{ODI_{Tot}}$ (top) and $\mathrm{DA_B}$ (bottom) indices of Bingham-NODDI.

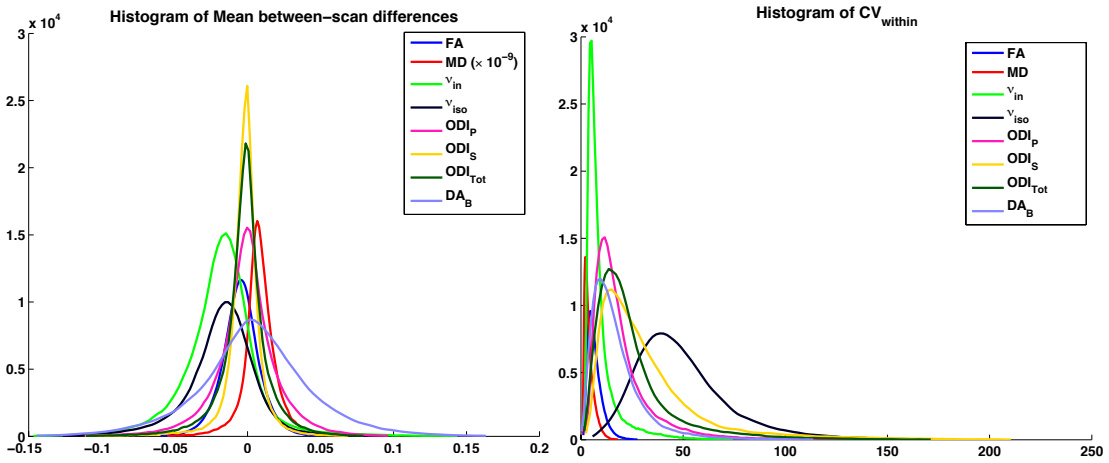

Figure 12.10: Histograms showing the distributions of between-scan differences (left) and the CV_{within} values (right) for each of the parameters of Bingham-NODDI and DTI, in the WM ROIs.

ter 11. This is expected even though the number of estimated parameters is the same for both the models, as the Bingham-NODDI fitting procedure requires nonlinear optimisation of several parameters while fixing a few to a suitable value as well (e.g. diffusivities).

Amongst the parameters relevant in the WM, FA has the lowest within-subject variability apparent from both the quantities plotted in Figures 12.6-12.9, while ODI_{Tot} and ODI_S have the highest. ν_{in} has the lowest variability amongst the Bingham-NODDI metrics. In general, ν_{iso} has the highest, while MD has the lowest variability. But this is expected in the WM, as ν_{iso} simply accounts for the isotropic volume fraction (and has in general very low values in the WM), while MD changes very little in the WM. FA has the lowest mean differences between-session as well as the CV_{within}.

For metrics of both Bingham-NODDI and DTI, the CV_{within} seems to be dependent on the physical location of the ROI. The right side of the tracts seem to show higher between-scan differences.

The plots in Figure 12.11 show how the within-subject differences computed here vary across the various groups of WM tracts. This includes the brain stem, the commissures and the association and projection fibres. The plots show that the CV_{within} of a parameter does not change for different WM ROIs, and the pattern of CV_{within} across the various parameters is the same for all ROIs.

12.4.3 *Repeated measures ANOVA*

The results for the one-way ANOVA are shown in Figures 12.12- 12.15. It is clear from the results that overall the Bingham-NODDI metrics are less repro-

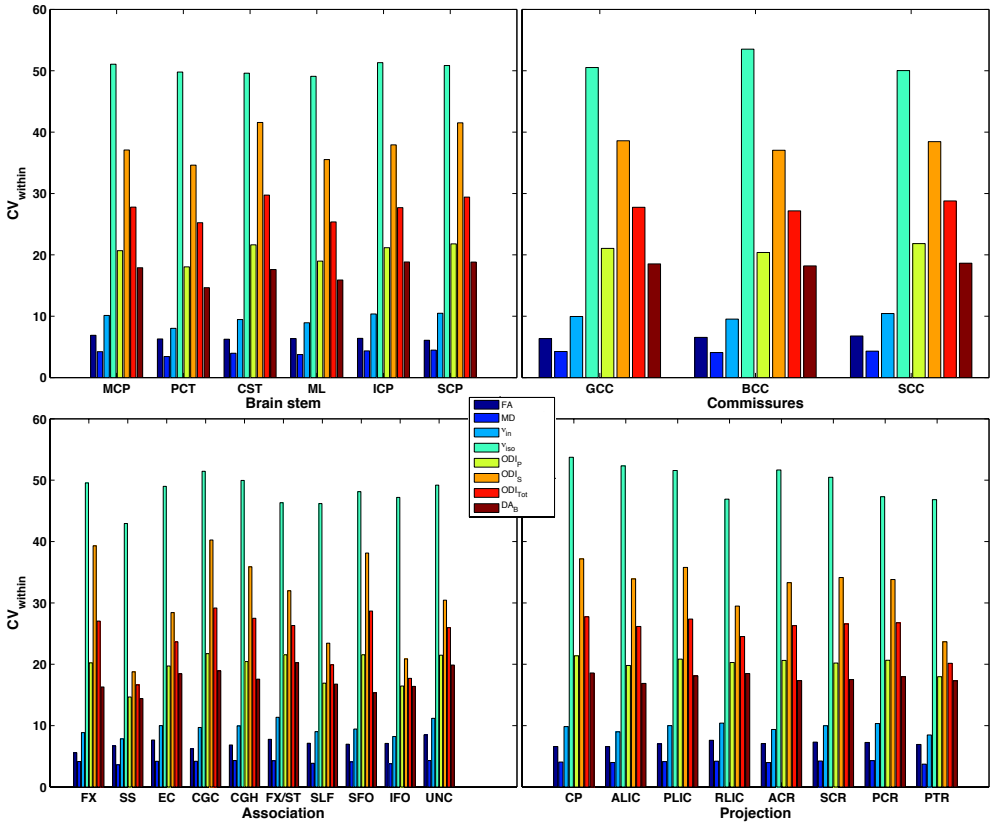

Figure 12.11: Variation of CV_{within} for the parameters of Bingham-NODDI and DTI, across several groups of WM tracts.

ducible than the DTI ones. It is also seen from the results that the Bingham-NODDI metrics are not as robust as the DTI ones, as the contribution to the variability of the metrics from noise (MS_{scan}) is higher.

Figure 12.16 presents a comparison of the reliability statistics across all the metrics evaluated. The plots clearly show the robustness to noise and superior reliability of the DTI metrics, consistent with the findings of independent studies on the NODDI model[37].

A breakdown of the reliability metrics in terms of the kind of WM tracts is shown in Figures 12.17 and 12.18, which again shows inferior reproducibility of Bingham-NODDI compared to DTI. In particular, the reliability of ν_{in} is very low, while DA_B is the least robust amongst all the parameters, as the noise contribution (MS_{Scan}) is very high. These results also show that the reproducibility of the various parameters is consistent across the various tracts.

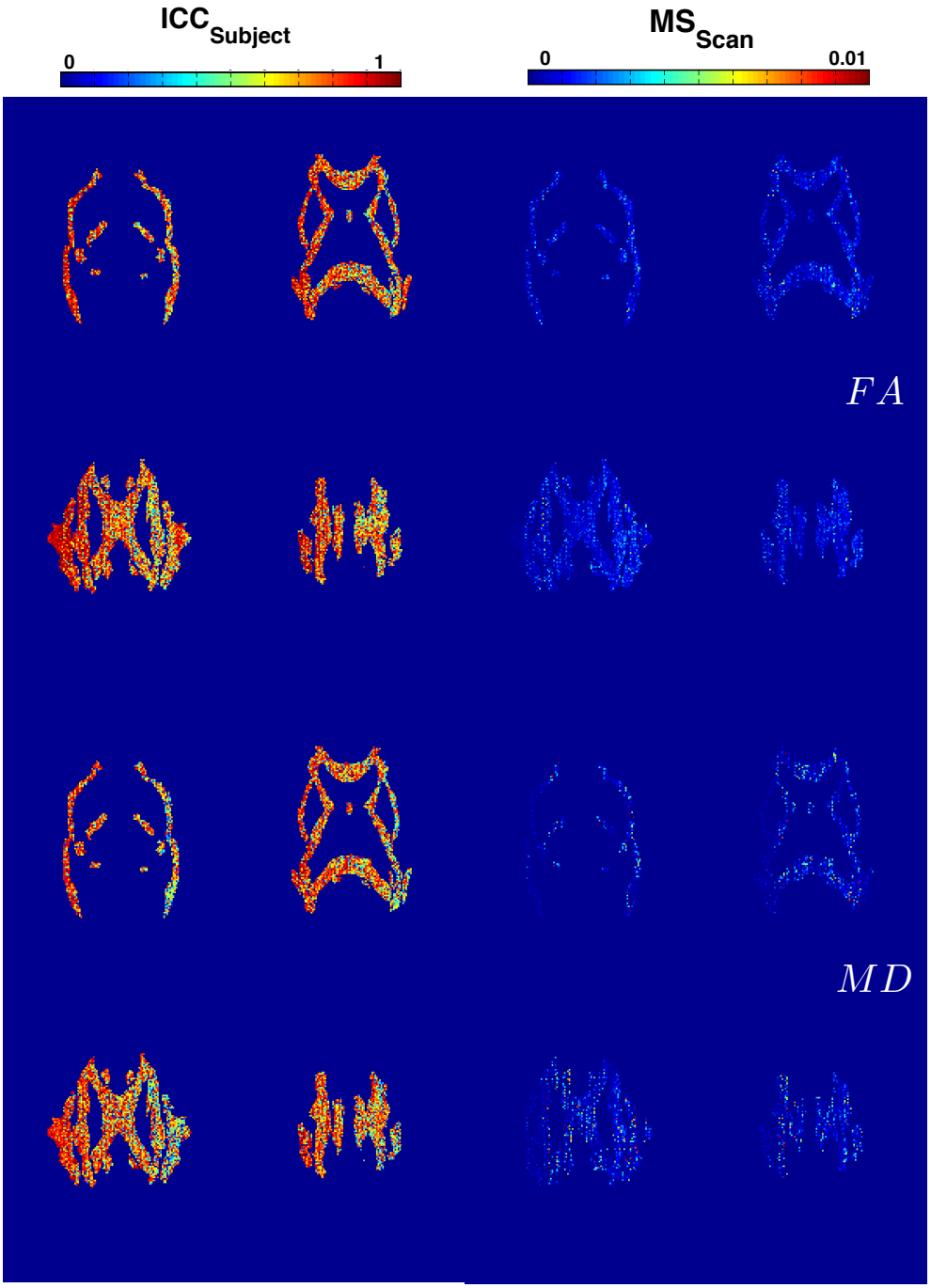

Figure 12.12: Maps of the $ICC_{Subject}$ and the MS_{Scan} for the DTI metrics of FA (top) and MD (bottom), in WM ROIs for four slices of the brain.

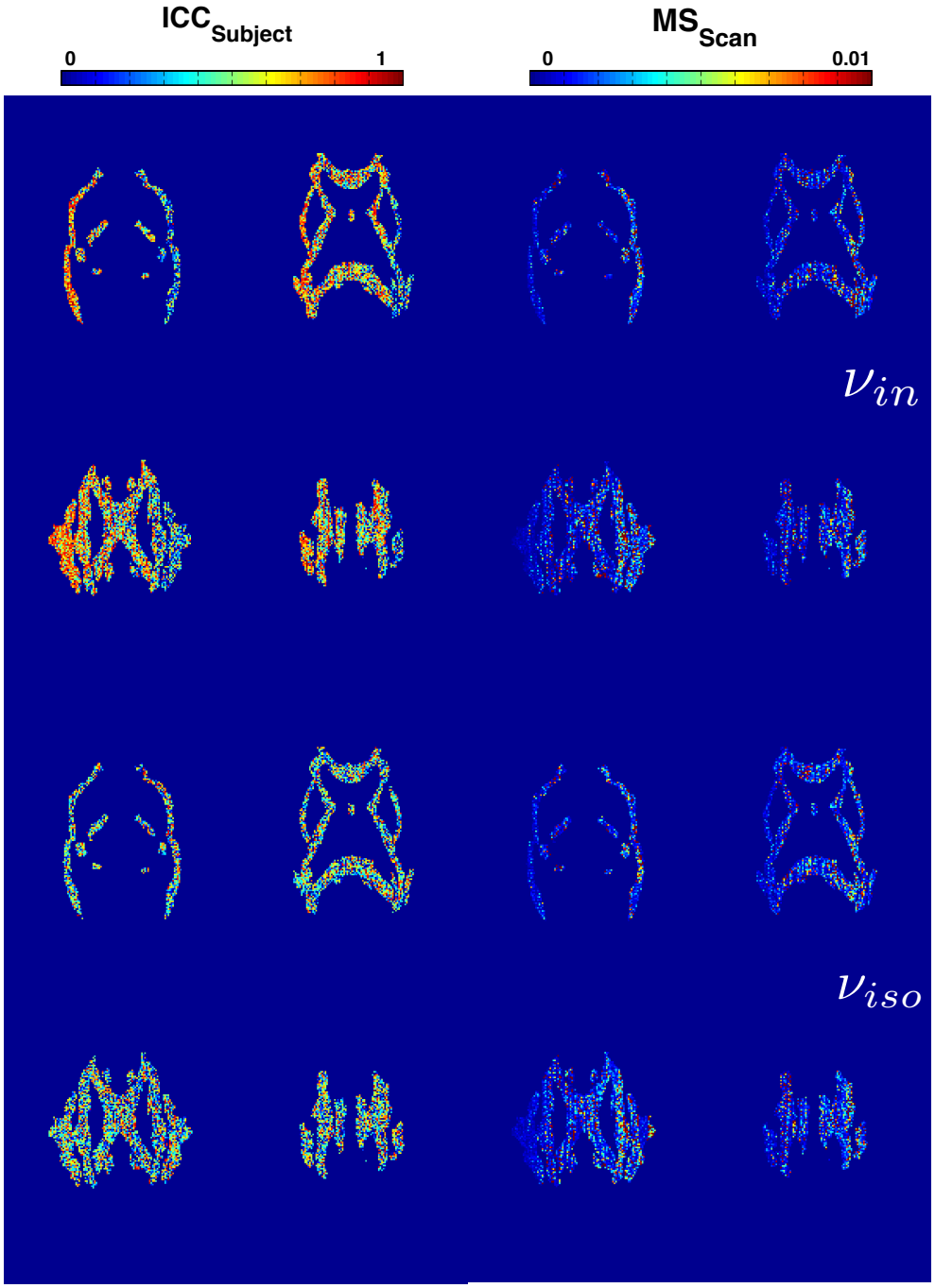

Figure 12.13: As Figure 12.12, but for ν_{in} (top) and ν_{iso} (bottom) indices of Bingham-NODDI.

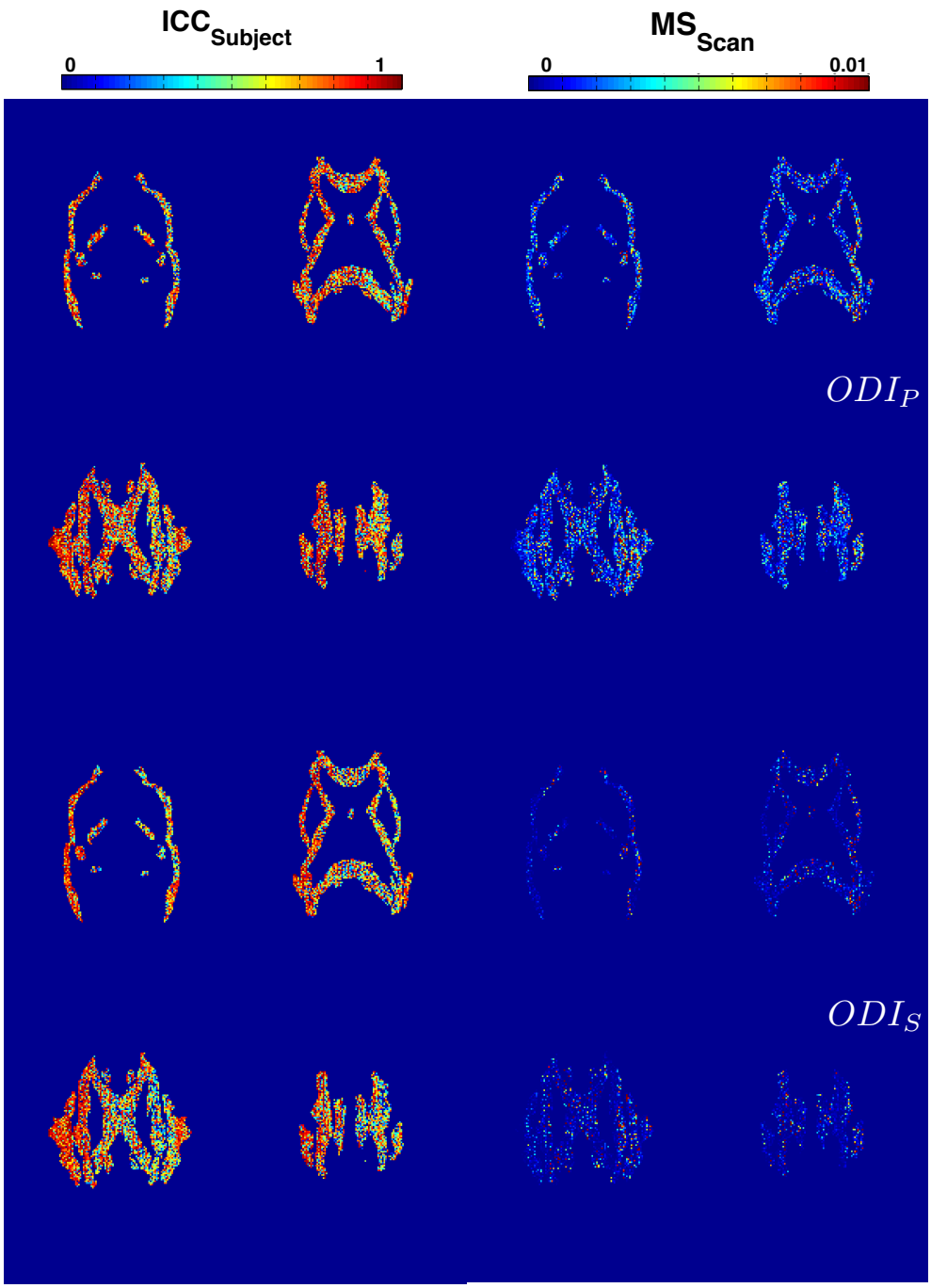

Figure 12.14: As Figure 12.12, but for ODI_P (top) and ODI_S (bottom) indices of Bingham-NODDI.

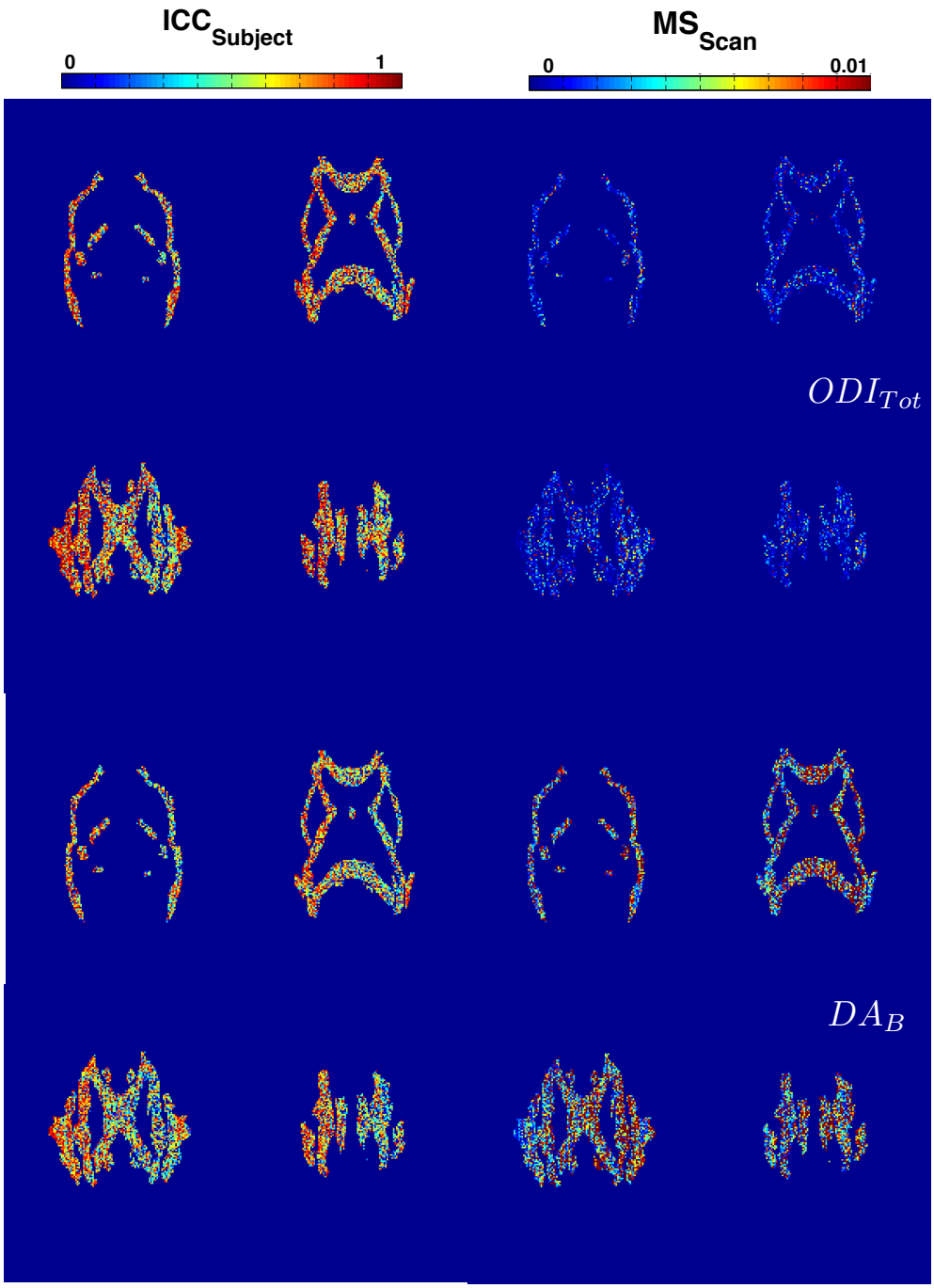

Figure 12.15: As Figure 12.12, but for $\mathrm{ODI_{Tot}}$ (top) and $\mathrm{DA_B}$ (bottom) indices of Bingham-NODDI.

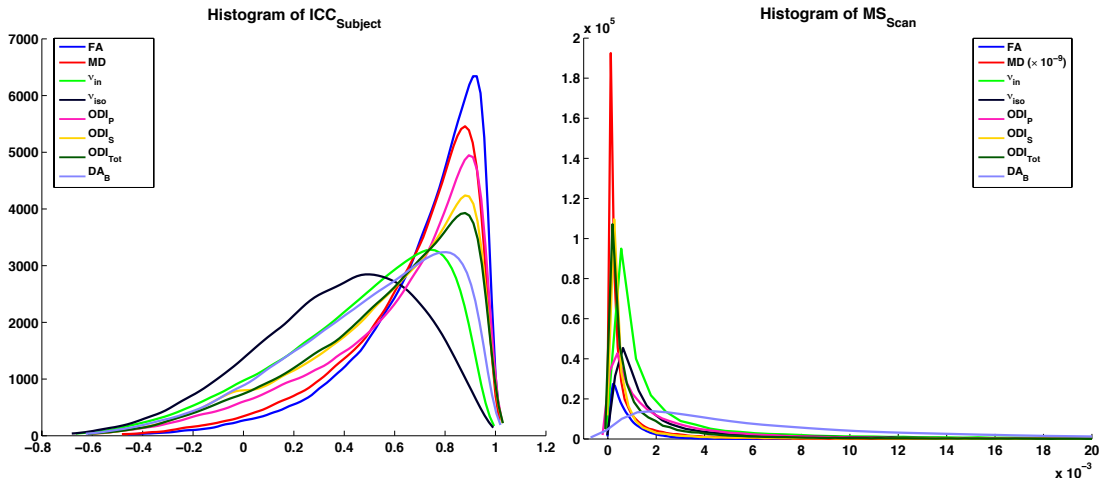

Figure 12.16: Histograms showing the distributions of $\mathrm{ICC}_{\mathrm{Subject}}$ (left) and the $\mathrm{MS}_{\mathrm{Scan}}$ values (right) for each of the parameters of Bingham-NODDI and DTI, in the WM ROIs.

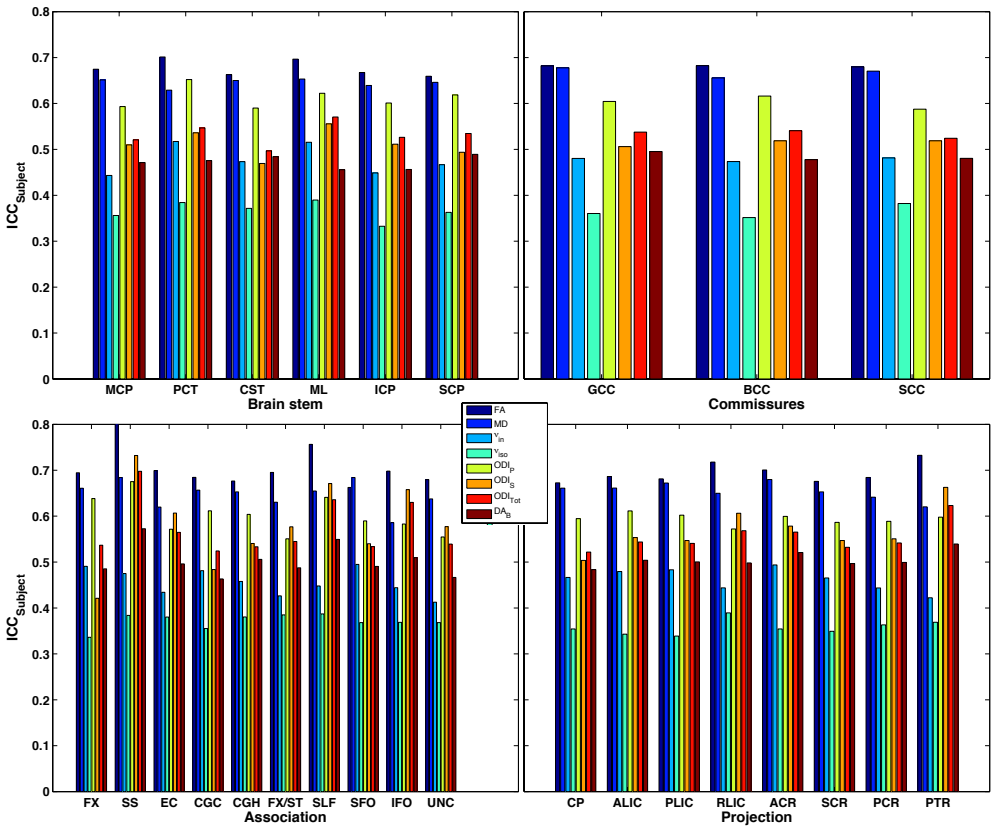

Figure 12.17: Variation of the reliability metric, $\mathrm{ICC}_{\mathrm{Subject}}$ for the parameters of Bingham-NODDI and DTI, across several groups of WM tracts.

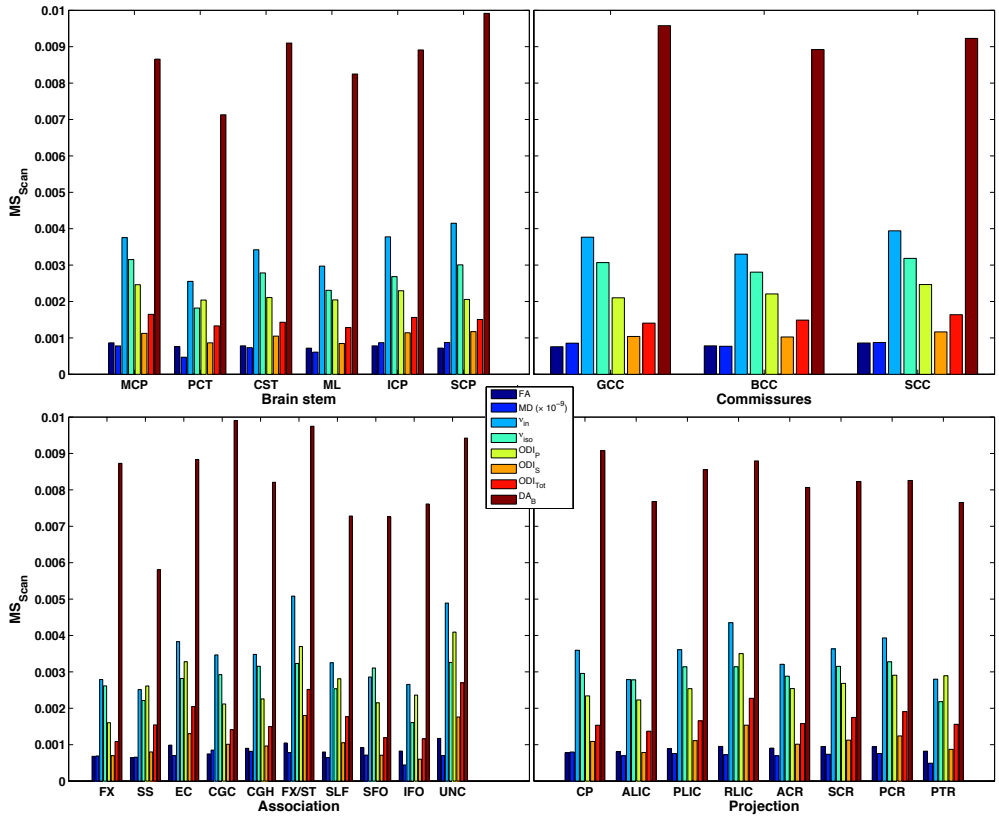

Figure 12.18: As 12.17, but for the MS_{Scan}.

12.5 DISCUSSION

12.5.1 *Reliability of Bingham-NODDI*

We find that the reliability of Bingham-NODDI metrics is less than that of the DTI metrics, consistent with the findings in Chung et al. 2016. The higher variability of the Bingham-NODDI metrics, compared to those of the DTI, indicates that they are not as robust. This is expected as Bingham-NODDI is a more complex model compared to the DTI, requiring several model assumption and a nonlinear optimisation scheme to find the optimum parameters. This however also highlights the sensitivity of Bingham-NODDI metrics to the changes in the DW-MRI signal, which would mean higher sensitivity to the changes in microstructure.

Analysing the raw images (DW-MRI), we see that the contrast is greatly different between two scans of one of the subjects (subject 10). In this case, the Bingham-NODDI parameters are found to be highly variable between the two scans of the same subject, but DTI ones are fairly constant (see the comparison in Appendix E).

While it is expected that DTI metrics are very robust to noise, the fact that they do not even change correspondingly to actual changes in the images acquired is not good as it might mean that the metrics may not be sensitive to the subtle changes in microstructure, which could be captured by Bingham-NODDI. This is a hypothesis based on the dataset used here and needs to be confirmed with further analysis, with a bigger cohort. From the many applications of DTI to several clinical and neuroscience studies, the sensitivity has been shown to be very good. A future study comparing the statistics of reliability for Bingham-NODDI and DTI using a clinical population, with a bigger cohort would shed more light into this.

12.6 FUTURE WORK AND LIMITATIONS

The study presented here provides a preliminary analysis of reproducibility of the proposed model. However, the analysis consists only of two scans for each subject acquired 40mins apart and further time points would provide a more comprehensive analysis, as for example done by Grech-Sollars et al. 2015.

The acquired data is not ideal as there are significant intensity differences between the two scans for some of the subjects (Appendix F). This results in very different estimates for the two scans of the same subject for Bingham-NODDI but seems to hardly impact the DTI metrics. This is expected as DTI is a very simple model to capture the complexity (multiple b-values and orientations sampled) of the acquired data. Nonetheless, the fact that Bingham-NODDI metrics have much lower reliability, and higher susceptibility to noise, compared to the DTI, is a disadvantage of the model.

The data used here seem to have some Gibbs ringing artifact, which was not corrected prior to analysis. Reducing such artifacts is expected to improve the performance of Bingham-NODDI metrics, especially for the kind of DW-MRI data that is typically acquired.

Another possible way to improve the analysis, specifically the parameters estimated for Bingham-NODDI is to improve the model fitting procedure. The fitting procedure is currently designed to provide very good estimates for the better quality data acquired (data in Chapters 8 and 11), but this data is clearly noisier than those and it would be interesting to see if the reliability of the metrics can be improved with a better fitting procedure.

It is also seen that while some of the Bingham-NODDI parameters have lower reliability, a few perform reasonably well, so it would be more informa-

tive to quantify the overall reliability of all the metrics and judge how good a model is based on all of its parameters.

13

CLINICAL TRANSLATION FEASIBILITY: DISCUSSION

The chapters in this part of thesis assess the relevance of the proposed model for use in neuroscience. This is done by presenting a pilot study establishing the normative values of the Bingham-NODDI parameters and a power analysis to compute the cohort requirements for using the model in group studies. This is followed by a prelimninary scan-rescan study to evaluate how reproducible the parameters of the model are. In both cases, comparisons are made to the indices of the DTI model, as it is the current standard in DW-MRI studies.

The first study utilises very high-quality data acquired on a state-of-the-art MRI scanner, while the second one uses one which has specifications typically found on clinical scanners. Both are useful as it is important to evaluate how reliable the model parameters are, with the type of data readily available, while the high-quality data provides an atlas of the most accurate and reliable values of these parameters, which are ideal to use as a reference.

We find that the CVs of the Bingham-NODDI metrics computed for the high-quality data in Chapter 11 are much less compared to those for the typical data (Chapter 12), despite the latter being a scan-rescan study. The DTI metrics, on the other hand, have comparable statistics of variation for both the datasets. This highlights the sensitivity of Bingham-NODDI metrics to changes in the intensity of the acquired data. So for Bingham-NODDI using higher quality data set is very important, while DTI metrics can be robustly estimated using the data from scanners that are widely being used. SNR was found to be important for estimation of anisotropic orientation dispersion for the Ball-Rackets model[147] as well.

It is expected that being a complex model, Bingham-NODDI parameters are susceptible to noise, but as noted also by Chung et al. 2016, it could also be an indication of better sensitivity of the NODDI metrics compared to the DTI ones.However, further analysis, with a big cohort is required to verify this, as well as a clinical application.

For the HCP data, we find modest inter-subject variability in the Bingham-NODDI metrics, which means that we can utilise the model for interesting clinical and neuroscience applications. We also report the range of microstructure indices in key WM regions, which show expected variation due to the heterogeneity of WM microstructure. The power calculations show that the minimum cohort requirements for the Bingham-NODDI indices of neurite morphology are comparable to those for the indices of standard DTI. The variability of the Bingham-NODDI metrics is also comparable to the DTI indices, specifically for the neurite density and the dispersion anisotropy indices.

The results of the power calculations show that the Bingham-NODDI can be used to differentiate populations using a reasonable number of subjects, based on the values of the metrics in the core WM tracts. Smaller WM structures like the fornix and uncinate fasciculus have the highest inter-subject variability and thus require the biggest cohort to find statistically significant differences, in group comparison studies.

Part V

ASSESSMENT OF BINGHAM-NODDI IN THE GREY MATTER

In this part of the thesis we assess how well the proposed model can estimate orientation dispersion anisotropy in the grey matter of the brain, given high-quality diffusion-weighted MRI data. This includes assessment of the Bingham-NODDI metrics estimated using high-quality ex vivo and in vivo data.

14

BINGHAM-NODDI: *EX-VIVO* DATA EXPERIMENTS

In this chapter, we assess the indices of Bingham-NODDI in neurites in the GM of the human brain, specifically the fibres present in the cortex, using high-quality *ex vivo* DW-MRI data.

14.1 ORIENTATION DISPERSION ANISOTROPY IN THE CORTEX

The assessment of GM in the *in vivo* data of Chapter 8 showed that for standard quality data (in terms of image resolution and amount of data acquired), Bingham-NODDI does not provide any extra information compared to Watson-NODDI. But it is known that fibres in the GM exhibit patterns of anisotropic orientation dispersion, for e.g. fibres that terminate into the cortex have a characteristic fanning pattern[32]. Here we present the results of the application of Bingham-NODDI to *ex-vivo* data, to explore if the proposed model can capture the expected complex microstructure in the cortical GM, using very high-resolution data, acquired with a very rich protocol.

We also establish whether the proposed metric of orientation dispersion anisotropy is consistent with the patterns of orientation dispersion in the underlying microstructure, by comparing imaging results to the histology of the same sample. The data used here was acquired for Kleinnijenhuis et al. 2013, which has corresponding 2D histology and the comparison of the imaging results to histological data presented here is qualitative only. The DW-MRI data and the histological data is acquired for Kleinnijenhuis et al. 2013 (detailed report in Kleinnijenhuis 2014). In this chapter, we analyse the acquired DW-MRI data using the Bingham-NODDI model.

14.2 SAMPLE

The sample is from the human primary visual cortex (V1), which is a very well-characterised region Kleinnijenhuis et al. 2013 of the neocortex, with a diverse cytoarchitecture including fibres fanning/bending into cortical layers, making it suitable for this work.

The samples were extracted from around the calcarine sulcus and include the cortex as well as some underlying WM. Relatively straight gyri were selected and cut to a length and diameter of 10 mm The sample was fixed in 10% formalin at 4°C and was immersed in phosphate buffered saline (PBS) for at least 72hrs at 4°C, to restore the R_2 relaxation rate[95].

The sample is imaged using high-resolution *ex vivo*, for which corresponding histology is also acquired, as described below.

14.2.1 *Data*

The *ex Vivo* DW-MRI data is acquired on a 9.4T Bruker small animal scanner. A 1x2 Bruker CryoProbe coil-array cooled to 20-30 K transmitted the RF pulses and received the signal.

The acquisition consists of mutliple b-values at $b = [0, 1000, 4000, 8000, 12000, 16000, 20000] s/mm^2$ with 60 diffusion directions ($\hat{\boldsymbol{G}}$) for each. Other parameters include $TE = 27ms, \delta = 8.4ms, \Delta = 12.8ms$ The acquired data has an isotropic resolution of $0.2mm$.

The histological sample we compare the results of the Bingham-NODDI to is shown in Figures 14.3 (left). It has myelin staining (LFB dye), which shows the myelinated axons of the cortex as darker regions. The myelin stain highlights the main WM tract extending towards the crown of the gyrus, as well as the *stria of Genari*. We can clearly see the various layers of the cortex, going from the WM tract to the pial surface (P), which includes the infra-granular layer (I), consisting of some of the myelinated fibres, the granular (G) and the supra-granular (S) layers. The granular layer coincides with the highly myelinated fibres of the stria of Gennari and thus has a different contrast to surrounding cortical layers.

A 2D structure tensor analysis[32] on the myelin stained images is shown in Figure 14.1 (left) and provides an estimate of the orientation distribution (ODF) of the neurites in the sample. We see very coherently organised WM fibres, projecting towards the gyral crown, and higher dispersion with bending fibres, at the GM/WM interface. The fibres clearly fan outwards, towards the gyral

crown. We also see the highly dispersed orientations at the stria of Gennari, which is expected due to the known presence of crossing fibres.

14.3 MODEL FITTING AND DATA ANALYSIS

Model fitting is carried out using Watson-NODDI, the estimates from which are used as a starting point for Bingham-NODDI fit (described in Chapter 9). An isotropic restriction compartment (with volume fraction ν_{ir}) is added to the two models, to account for *ex vivo* imaging as proposed in Alexander et al. 2010. The two NODDI models are compared using BIC, a standard model comparison metric.

The main results are shown for the model fitting procedure where the diffusivities are also fitted, as we see from simulations (Chapter 9) that diffusivity can be estimated from the acquisition used here. We also compare this to model fitting where the difusivities are fixed to empirical values for *ex vivo* data ($d_i = 6 \times 10^{-10} m^2/s$ and $d_{iso} = 2 \times 10^{-9} m^2/s$).

14.4 RESULTS

We show the results of fitting Bingham-NODDI to the high-resolution DW-MRI data. The LFB provides a reference for the ν_{in} and the orientation dispersion indices, while the derived ODF for the DA_B and orientation estimated.

14.4.1 *Dispersion anisotropy in the cortex*

We first assess if Bingham-NODDI can capture the complex configurations, present in the cortical layers. Figure 14.1 shows the maps of the orientations ($\hat{\mu}_1$ and $\hat{\mu}_2$), which are shown as 2D projections here and the dispersion anisotropy (DA_B) estimated by Bingham-NODDI, while Figure 14.2 the maps of its orientation dispersion indices.

The projections of the orientations point towards the gyral crown in the main WM, bending outwards at the WM/GM boundary and fanning towards the gyral crown in layer I (red circle), consistent with the histological ODF. The main WM shows high coherence, with a high level of dispersion at the WM/GM boundary (blue arrows), and highest dispersion at the stria of Gennari (red arrows).

We find that in general, the trends across the sample are consistent with histology in the orientation dispersion and orientation dispersion anisotropy maps. The DA_B maps show highest values in WM, which gradually get lower as the WM fibres disperse into the cortical GM areas, signifying the presence of fanning and bending fibres in the cortical areas. ODI_{Tot} is slightly higher and DA_B value high in the WM/GM interface region and the region of fanning (red circle), while both are the highest in the stria of Gennari (red arrows).

ODI_P and ODI_S have expected values, with lowest values in the main WM regions, higher in the layers I and S, and the highest values in the regions of crossings (red arrows). The presence of anisotropy is captured by the greater difference between the two dispersion indices in the fanning (red circle) and bending (blue arrows) regions.

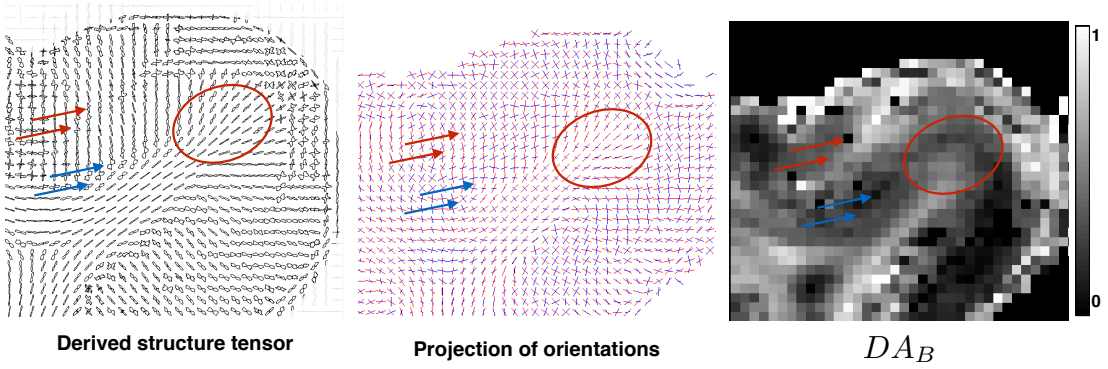

Figure 14.1: Bingham-NODDI estimation of dispersion anisotropy in the *ex vivo* cortical sample. The maps of DA_B and the primary and secondary dispersion orientations give expected patterns, consistent with the histological information (left image), as highlighted.

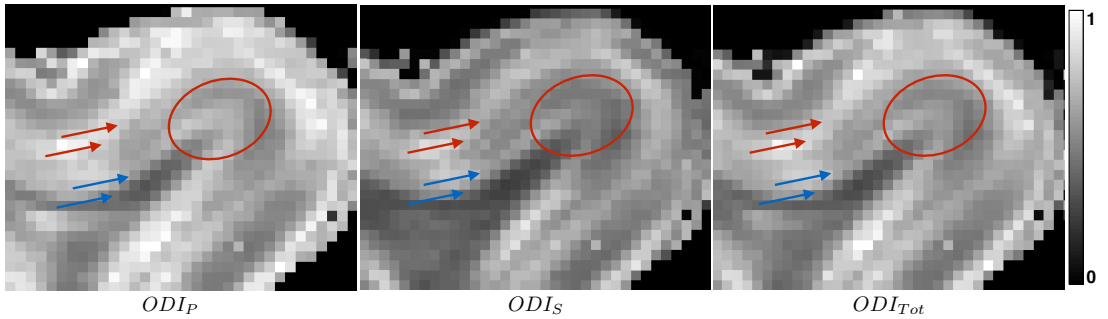

Figure 14.2: Bingham-NODDI estimation of orientation dispersion indices in the *ex vivo* cortical sample. The maps shown are for the primary and secondary orientation dispersion indices, ODI_P and ODI_S, and the overall dispersion, ODI_{Tot}.

14.4.2 *Neurite density*

The quantification of ν_{in} is same as for Watson-NODDI, but we assess it to make sure the results are consistent. We find that the neurite density map coincides very well to the regions of high myelin (red circle), seen in histology, including high values in the main WM tract and the stria of Gennari (red arrows). This is consistent with the findings in Kleinnijenhuis et al. 2013.

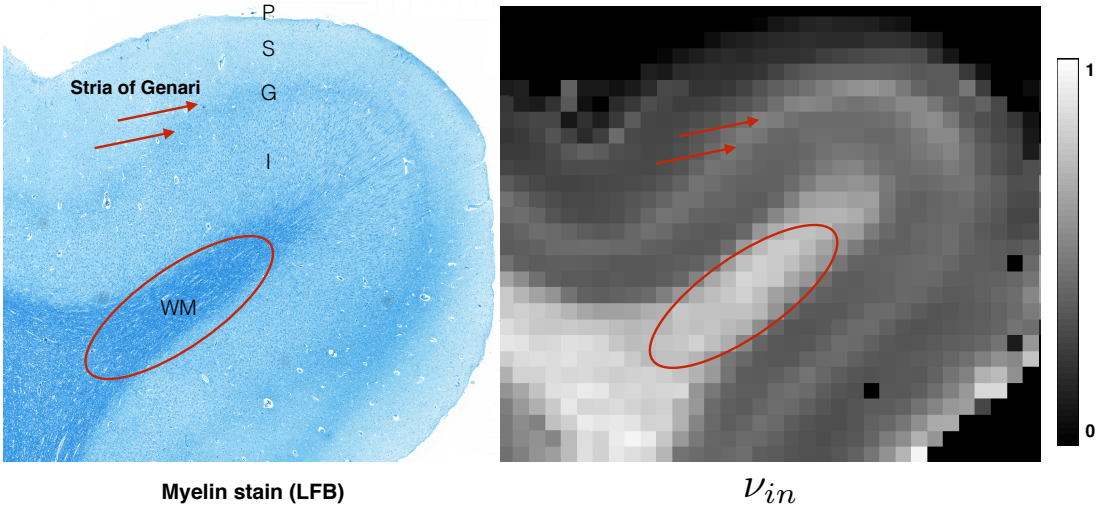

Figure 14.3: Comparison of the myelin stained histology (left) to the Bingham-NODDI index of neurite density, ν_{in} (right). The high neurite density values match well with the regions of high myelin content, as highlighted. *Key: P- pial surface, S - supragranular layer, G - granularlayer, I - infragranular layer, WM - white matter.*

14.4.3 *Comaprison with Watson-NODDI*

We assess whether Bingham-NODDI performs better than Watson-NODDI in the sample, as Watson-NODDI has been shown to delineate the laminar structure of the cortex much better than DTI with this dataset[95]. We compare the quality of fit of the two models with BIC, shown in Figure 14.4. This demonstrates that Bingham-NODDI explains the data better than Watson-NODDI. Watson-NODDI fits the data particularly poorly in the WM regions, especially near the WM/GM boundary, the areas where dispersion anisotropy is expected due to the fanning and bending of the WM fibres towards the cortical regions.

We see that Watson-NODDI performs worst than Bingham-NODDI but even Bingham-NODDI is not fitting the data very well. This highlights the need for further work to be done to enable more stable fitting of Bingham-NODDI.

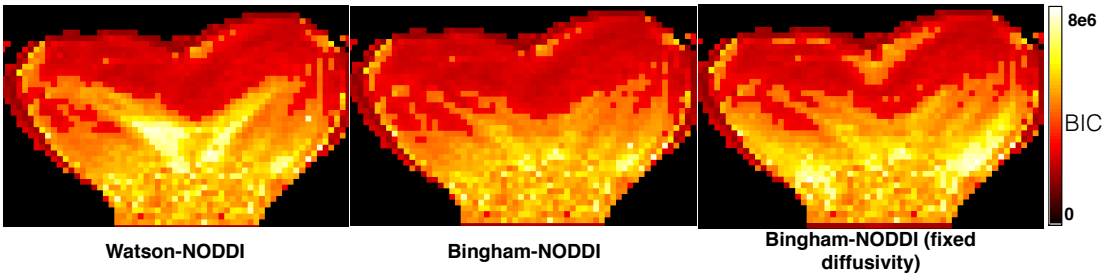

Figure 14.4: Comparison of the quality of fit in terms of the *BIC*, between Watson-NODDI (left), Bingham-NODDI (middle) and Bingham-NODDI with diffsivity fixed in the fitting procedure (right). The smaller the values, the better the model explains the data.

We also compare the estimates of κ for the two models, as it was found for assessment of Watson-NODDI[95] that κ is underestimated. Figure 14.5 shows that κ estimated by Bingham-NODDI is overall higher than that by Watson-NODDI. This suggests that Bingham-NODDI estimate of κ may be closer to the actual coherence of the neurites.

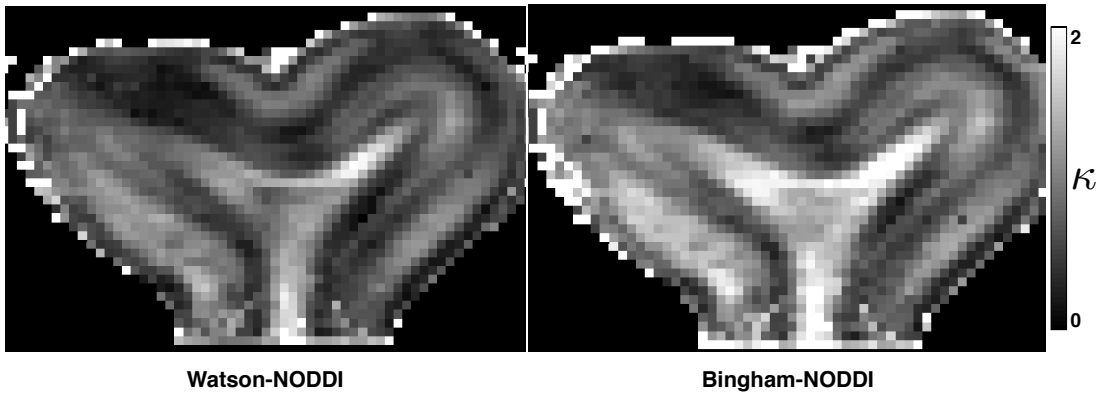

Figure 14.5: Comparison of the esitmation of the concentration parameter κ, estimated by Watson-NODDI (left) and Bingham-NODDI (right).

14.4.4 *Comparison with fixed diffusivity*

We compare Bingham-NODDI fitting with the diffusivity fixed, as is typically done for the model. The comparison of the two model fitting procedures, in terms of the BIC, is shown in Figure 14.4 and shows that fitting for the diffusivity gives a better fit for the data, which is expected as the diffusivity value used may not correspond to the actual diffusivity (due to fixation). Comparison of the actual model parameters shows that the estimated values are different for the two procedures (results not shown).

14.5 DISCUSSION

The results demonstrate that Bingham-NODDI is able to capture the fibres projecting deep into the cortex, by accounting for fanning/bending fibres. This has implications not only to enable a better understanding of the organisation of the human brain microstructure but also to enable fibres obtained from tractography to extend all the way into the cortical regions.

It is also shown that fitting for diffusivity gives a better fit to the data than when it is fixed. This is expected as when the diffusivity is fixed and connected in the intra- and extra-neurite compartments (tortuosity assumption), the parameters estimates are biased.

The diffusivities in the Bigham-NODDI model are fixed to typical values for *in vivo* data, for a stable estimate of the parameters, as done with Watson-NODDI. This has implications for the estimation of the model parameters, as discussed in details in Chapter 16 (Section 16.2.1).

14.5.1 *Limitations*

The biggest limitation of this work is that it presents a qualitative comparison only, which is sufficient to see if Bingham-NODDI can capture anisotropic orientation dispersion with DW-MRI data, but does not quantitatively compare the estimates of Bingham-NODDI to the histological data.

The comparison made here is to 2D histology, which cannot fully characterise the 3D ODF estimated by Bingham-NODDI, so it is not possible to directly compare the dispersion anisotropy index. But an indirect verification of the model is presented by comparison to Watson-NODDI metrics, which shows that Bingham-NODDI explains the data better and gives an overall higher value of the concentration parameter, that is shown to be underestimated by Watson-NODDI[95].

14.5.1.1 *Future work*

Future work will involve a direct comparison of the Bingham-NODDI indices and the histological measurements from these samples. Quantitative assessment will be beneficial, specifically to see how the profiles of various indices of the model vary across the laminar layers (Pial surface to the Infragranular layers). It would be particularly useful to compare the profiles of the indices of

Bingham-NODDI to see if any extra delineation of the layers can be obtained by a richer characterisation of the ODF.

15

BINGHAM-NODDI IN THE GM USING *IN VIVO* DATA

It is expected that dispersion anisotropy is present in the GM, specifically in the cortical GM where the fibres of the WM terminate, as discussed in Chapter 14. However, as seen in Chapter 8, the currently available clinical data do not have sufficient resolution or SNR in the GM to capture this.

In this chapter, we assess the performance of Bingham-NODDI in the cortical GM of the high-resolution *in vivo* data used in Chapter 11. We show a very basic comparison of the quality of the estimated values of Bingham-NODDI in this dataset to those for standard imaging (Chapter 8).

15.1 QUALITY OF FIT COMPARISON

We produce BIC maps, as done for the standard quality DW-MRI data in Chapter 8 (Figure 8.7). The results in Figure 15.1 show that Bingham-NODDI fits the data much better than Watson-NODDI, even in the GM. The regions in which Bingham-NODDI explains the data better than Watson-NODDI extends into the cortical GM regions for this data, showing the importance of high-quality data for the estimation of anisotropic orientation dispersion, demonstrated also by Sotiropoulos et al. 2012.

We also provide a quantitative assessment of the quality of fit of Bingham-NODDI in a few exemplary regions of the brain tissue, in Figure 15.2. Bingham-NODDI model fitting is superior to that of Watson-NODDI, particularly in the fanning WM regions. In comparison to the quality of fit for the GM in the standard quality images, the benefit of using Bingham-NODDI compared to Watson-NODDI is seen.

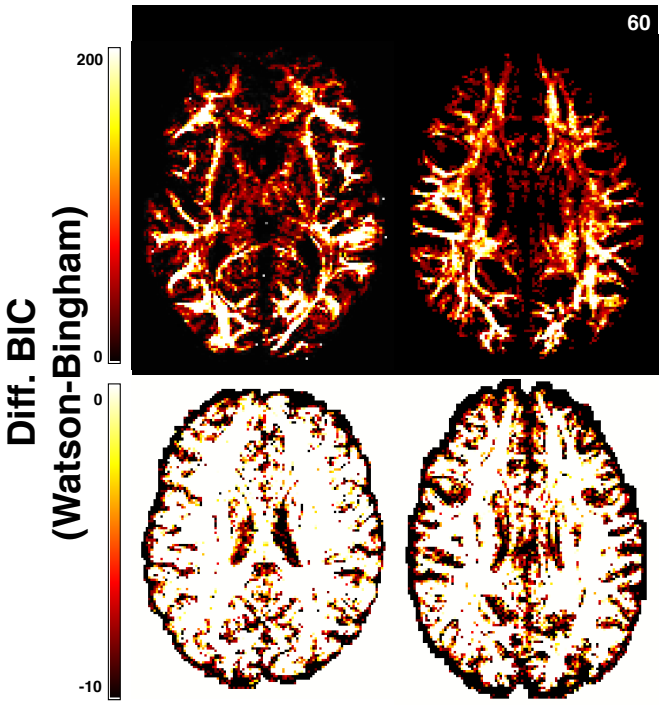

Figure 15.1: BIC difference maps to highlight the areas where Watson-NODDI performs worse than Bingham-NODDI (1st row) and those where Watson-NODDI is sufficient (2nd row). For clarity, the BIC difference map has been modified to show the positive and negative intensities separately. Each column shows the results for a different subject.

15.2 MAPPING OF DISPERSION ANISOTROPY INDEX

To visualise how the DA_B varies in the GM, we generate RGB images of the orientations μ_1 and μ_2 weighted by DA_B and the FA_{OT} (FA derived from the ODF of the Bingham distribution (Section 6.3.2)). The generated images are shown in Figures 15.3 and 15.4.

The figures show a clear advantage of using high-resolution data as the anisotropy FA_{OT} as well as the dispersion anisotropy DA_B have characteristic patterns in the cortex.

15.3 DISCUSSION

Here we show the results of the Bingham-NODDI fitting in the GM of the healthy human brain, using very high-quality DW-MRI data. We qualitatively compare the results to Watson-NODDI to see if including a more complex model for the ODF has any advantages in the GM. The maps of the dispersion anisotropy index (DA_B) of the Bingham-NODDI, derived from this high-quality data, in Figure 11.2 show contrast in the GM, at the individual as well

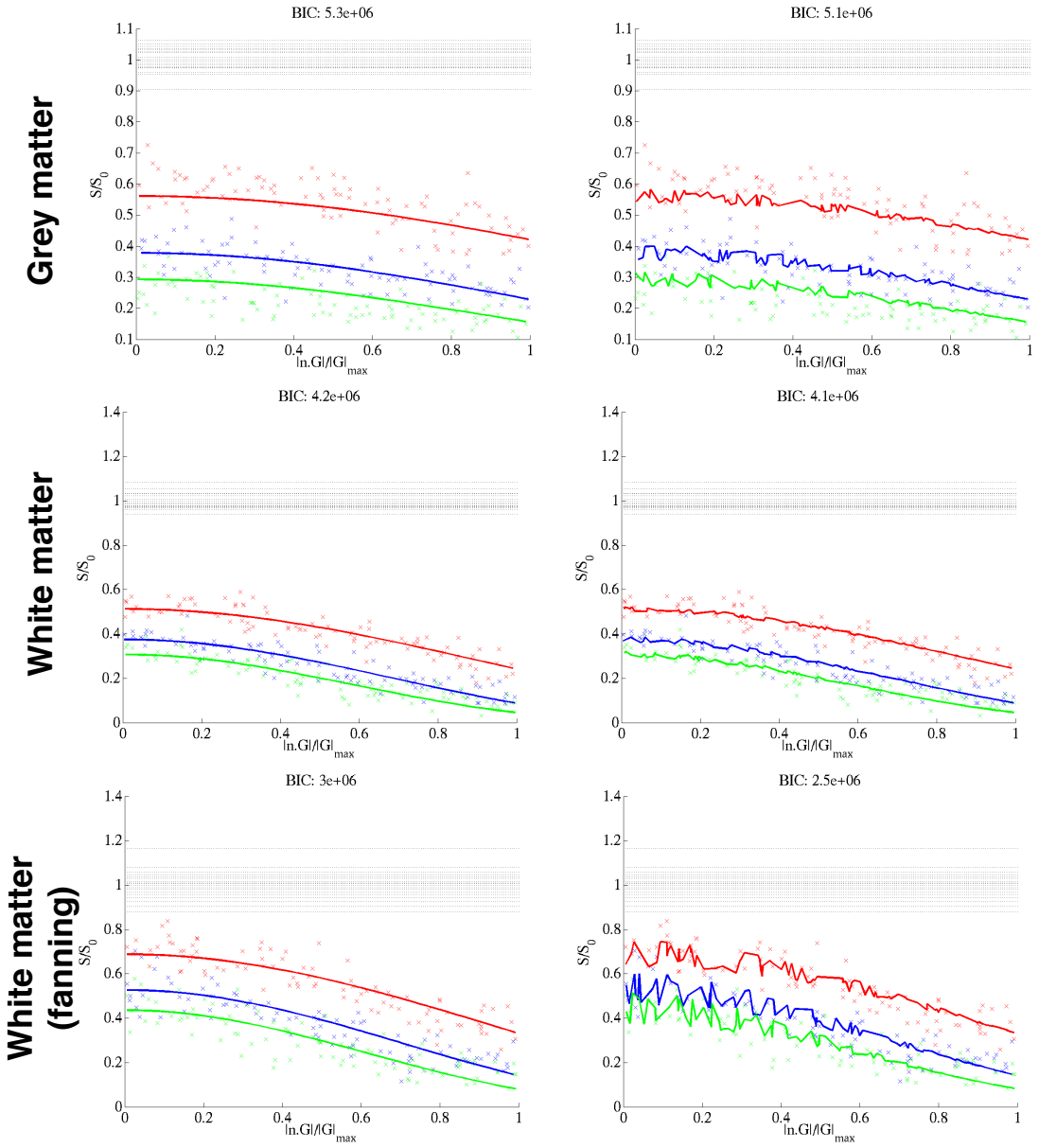

Figure 15.2: Quality of fit plots for a few voxels from specific regions of the brain tissue. The Watson-NODDI fits are shown on the left and Bingham-NODDI on the right.

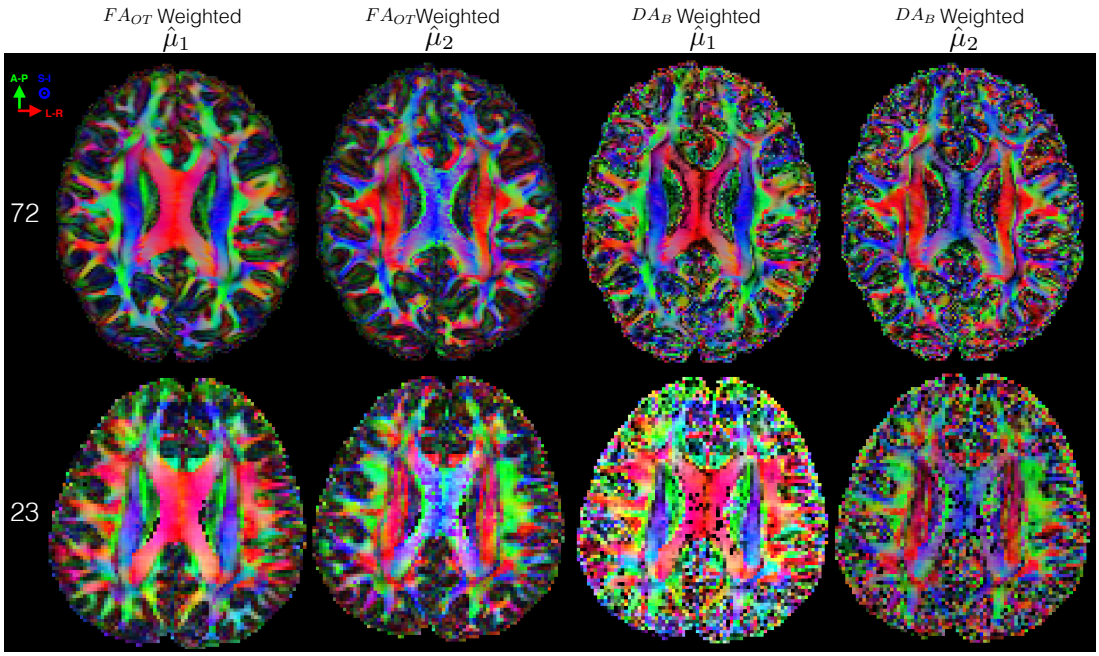

Figure 15.3: DA_B and FA_{OT} weighted RGB images of the dominant orientation $\hat{\mu}_2$ and primary dispersion orientation $\hat{\mu}_2$. The top row shows a slice for a subject from the HCP cohort, while the bottom row shows a slice from the datset used in Chapter 8.

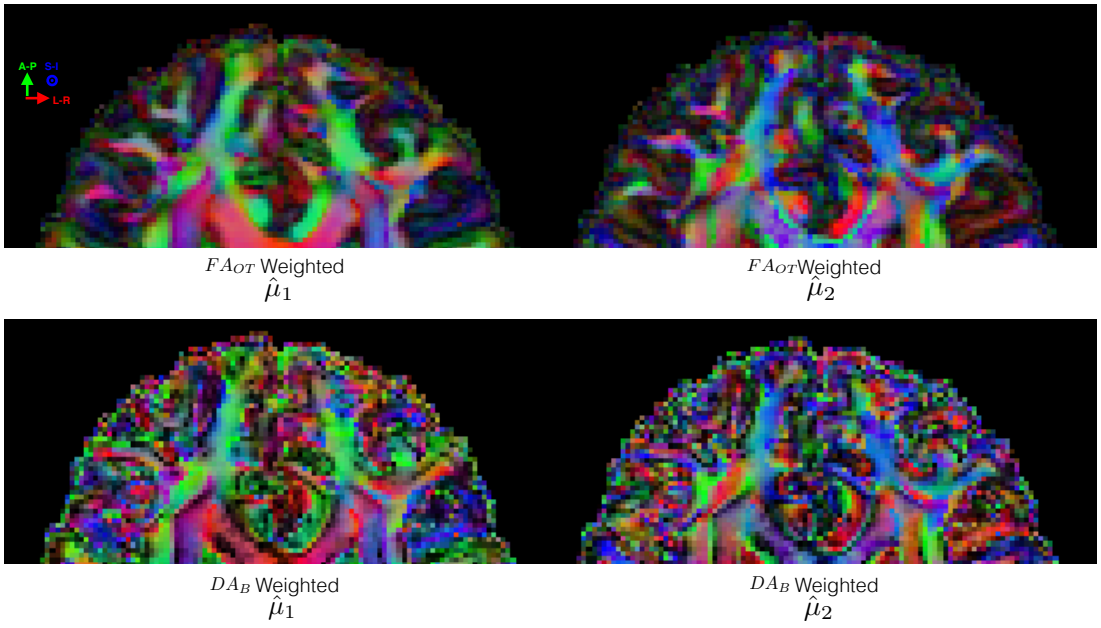

Figure 15.4: Zoomed in maps of DA_B and FA_{OT} weighted RGB images of the dominant orientation $\hat{\mu}_2$ and primary dispersion orientation $\hat{\mu}_2$, for the HCP subject.

as population level (normative values). For the standard DW-MRI data used in Chapters 8 and 12, however, the DA_B is very noisy in the GM, highlighting the need for better quality data for estimating this parameter. Here we carry out analysis to confirm this by showing that including the Bingham distribution in the NODDI model, improves the quality of fit to the data when the data is of sufficient SNR.

15.3.1 *Future work*

Here we show that the high-quality HCP data is sufficient for the estimation of Bingham-NODDI parameters in the cortex. We only show very preliminary and qualitative findings and a detailed assessment of the indices of Bingham-NODDI in the high-quality data should be carried out to fully assess their estimated values.

It would be very beneficial to estimate the normative values of the Bingham-NODDI metrics in the GM and carry out a reproducibility analysis, as done for WM in Chapters 11 and 12. But as discussed in Section 11.4.1 this requires an alignment method more suitable for the GM regions. Another challenge for this would be to obtain segmentations of the various GM regions, which are usually available for the T_1-weighted images and require registration with the DW-MRI, which is typically of lower resolution and has a different contrast.

Part VI

DISCUSSION AND FUTURE OUTLOOK

Here we summarise the main findings of the work presented in this thesis and discuss the various limitations associated with it as well as the potential use of it in neuroimaging. We then detail the potential future work to carry the work forward.

16

DISCUSSION

16.1 SUMMARY OF THE THESIS

The work presented here proposes Bingham-NODDI, an advance DW-MRI method to characterise complex neurite configurations. The proposed model presents a novel marker of the morphology of neurites (collective term for axons & dendrites), which specifically quantifies anisotropic orientation dispersion. Bingham-NODDI is the first technique to enable a specific *in vivo* quantification of this feature of neurites. This work provides an exciting development for better research in neuroscience, that can help making key links between the precise changes in microstructure that result in brain development, ageing, and pathology.

Bingham-NODDI characterises anisotropic orientation dispersion by utilising the Bingham distribution to model neurite orientation distribution. The proposed model estimates the extent of dispersion about the dominant orientation, separately along the primary and secondary dispersion orientations. These estimates are subsequently used to estimate the overall dispersion about the dominant orientation and the dispersion anisotropy index. A specific quantification of dispersion anisotropy has not been demonstrated with any other *in vivo* technique.

The proposed method is based on an existing microstructure imaging technique called neurite orientation dispersion and density imaging (NODDI), which provides indices of neurite morphology using Diffusion-Weighted Magnetic Resonance Imaging (DW-MRI) data. NODDI provides a suitable framework to get an *in-vivo* quantification of anisotropic orientation dispersion with standard clinical imaging as it has been shown to be clinically feasible and successfully used for a wide range of neuroscience applications. NODDI relies on a mathematical model that relates the microstructure features of interest to the measured DW-MRI data, which is sensitive to the microstructure. But NODDI

in its standard form can not quantify anisotropic orientation dispersion, due to the assumptions made in the mathematical model. So the work presented here extends the NODDI model to enable characterisation of anisotropic orientation dispersion.

In the first part of the thesis, the proposed technique is described, including the precise mathematical framework to enable the modelling of anisotropic orientation dispersion of neurites. The modified NODDI model for quantification of anisotropic orientation dispersion is described along with the indices that can be extracted from it which specifically quantify neurite morphology. These indices include a specific quantification of the level of orientation dispersion anisotropy, the *dispersion anisotropy index*. The indices of the proposed model are evaluated using *in silico* and *in vivo* data to establish their estimability using clinically feasible data and compared to the original NODDI model. The experiments show that the indices of the proposed method are estimable with a clinically feasible protocol and the proposed model provides a better fit for the acquired data, specifically in regions with complex fibre configurations, compared to the standard NODDI model. Anisotropic orientation dispersion is expected to be present in the grey matter (GM) as well as white matter (WM), but it is found that with standard quality data such configurations are not estimable in the GM. The first part is concluded with simulations to assess some assumptions of the proposed model and to find a model fitting procedure to get more stable parameter estimates from the model. The optimal model fitting procedure obtained here is used for the analysis in all the subsequent work.

The second part of the thesis is concerned with experiments to facilitate clinical translation of the proposed method. Here the proposed technique is applied to a larger cohort of a normal adult population to demonstrate its applicability to a greater number of subjects and to report the values of its indices across the normal human population. This is followed by a study to establish repeatability and reliability of the indices of the proposed model. The results show that plausible and sensible values of the indices of the proposed model can be obtained for normal adult subjects, using high-quality as well as standard acquisitions. It is found that the indices of the proposed model have similar inter-subject variability to the indices of the standard neuroimaging model of DW-MRI, the DTI, but are less reliable. The indices of the proposed model are more sensitive to noise so using state-of-the-art acquisitions are preferable for the proposed model.

In the third part, the focus is on using high-resolution DW-MRI data to assess if anisotropic orientation dispersion is estimable in the grey matter (GM), using Bingham-NODDI. We by assessing if the indices of the proposed model reflect underlying microstructure features. This involves using high-resolution *ex vivo* data acquired on a sample of the human visual cortex, which has corresponding histology. Additionally, some high-resolution *in vivo* data is used which is acquired on a state-of-the-art MRI system. The work shows that the dispersion anisotropy index is estimable with Bingham-NODDI in the GM and reflects the fanning and bending fibres in the cortex in expected areas. The results provide preliminary verification of the novel index of anisotropic orientation dispersion of neurites in the cortical GM and show that it reflects the underlying complex neurite configurations. But no direct comparisons are made to histology or quantitative analysis comparing to other techniques to characterise the ODF, which are very important to verify the utility of Bingham-NODDI in the GM. The study thus only provides a preliminary validation of the proposed method by assessing whether the estimated parameters reflect actual microstructure and how it performs compared to the DTI and Watson-NODDI.

More advanced systems are fast becoming common for neuroimaging research and provide higher quality images than possible until now and an immense amount of work is going towards getting better imaging, with fewer artifacts. All these advancements are very relevant and timely for the proposed technique, as it provides more sophisticated measures of microstructure morphology than the standard in DW-MRI, the DTI, but is not as robust to noise and artefacts.

16.2 LIMITATIONS OF BINGHAM-NODDI

Bingham-NODDI requires a nonlinear optimisation procedure to estimate its parameters from the DW-MRI data and has two extra parameters to be estimated, compared to Watson-NODDI. So the parameter estimates are slightly more variable than even the Watson-NODDI ones, as seen in parameter evaluation in Chapters 7 and 8.

Other limitations of the model relate mainly to the various assumptions made in the tissue model, but some also to the acquisition protocol and the noise sensitivity of the parameters estimated.

16.2.1 *Assumptions made in Bingham-NODDI*

The assumptions made in Bingham-NODDI tissue model are the same as those for Watson-NODDI, listed in Section 5.6, as only the quantification of the orientation dispersion is different between the two. These assumptions allow us to obtain stable estimates of neurite morphology using a clinically feasible acquisition. These include assumptions on the substrate being modelled as well as their diffusion properties.

As discussed in Chapter 10, a key assumption made in Bingham-NODDI is that it models only one population of neurites per voxel, which limits its use in regions of fibre crossings. We find that the regions of crossing can have high orientation dispersion, as well as high orientation dispersion anisotropy value, which we confirm with synthetic experiment, where we explicitly model crossing fibres, in the presence of dispersion, using the Bingham-NODDI model (Section 9.2). But modelling one a single neurite population provides more stable estimates from Bingham-NODDI, as it has been found that estimating microstructure while modelling multiple fibre populations is very unreliable[147].

Recent work shows that orientation dispersion and anisotropic orientation dispersion is more widespread in the human brain WM than multiple fibre populations[68], so it is important to characterise such configurations of neurites. Although higher levels of crossing fibres are shown in other work (e.g. Jeurissen et al. 20010) there is no clear consensus on the proportion of complex configurations in the brain. Specific characterisation of multiple-fibre populations is not of utmost importance in the work presented here, as the aim here was to infer subtle geometric features of brain microstructure. Future work can explore estimating indices of the microstructure along with connectivity analysis, as discussed in Chapter 17.

In the presented results, the diffusivity of the intra-neurite and the CSF compartments are fixed to empirically estimated values, and the intrinsic diffusivity is assumed to be the same in all tissue compartments ($d_i = d_\parallel$), as with the original model[185]. This gives robust estimates of tissue microstructure with a clinical imaging protocol, specifically the orientation dispersion parameter, but also introduces a bias to the estimated parameters as discussed by Jelescu et al. 2015. This may not be a practical concern as the estimates made with these assumptions correlate well with histology, as shown by Kleinnijenhuis et al. 2013 and Tariq et al. 2015a. However, it has been shown[103] that fixing diffusivity results in confounding effects in the estimation of neurite density estimate made by NODDI (possibly due to the tortuosity assumption). This

means that the estimate is no longer specific to the density of the neurites. Lampinena et al. 2017 also show that the value fixed for the diffusivity in the GM is not correct for NODDI and results in incorrect parameters. This is particularly important for clinical applications, where the correct diffusivity values must be used to ensure correct characterisation of the microstrucutre[74].

To compute the hindered diffusivity in the extra-neurite space the tortuosity model is used, which has been shown to be valid for randomly packed parallel cylinders at long diffusion times[154] but is known to break down at high neurite (or cell) density[4,65]. Using the tortuosity assumption has been shown to be a problem for the estimation of neurite density, especially in the GM, for the Watson-NODDI model[103]. From the analysis in Lampinena et al. 2017, it follows that a better assumption would be to equate the mean diffusivities in the two tissue compartments of the NODDI model, rather than the intrinsic diffusivities. This can be a good alternative assumption to assess in future studies. It would also be very beneficial for the utility of NODDI (both Watson and Bingham) to apply the models to high-quality data, like the HCP, and assess if such assumptions can be relaxed and how it impacts the estimation of the indices of the model.

Another assumption in the NODDI tissue model is that neurites are modelled as zero radius cylinders, which is used to ensure wider applicability of the technique. Many techniques aim to measure axon radii[6,11], but it has been found that it is a very hard parameter to estimate and requires very comprehensive protocols, with high diffusion weighing (b-values), which are not clinically feasible. It is also shown in subsequent work that if the neurites are modelled as arbitrarily oriented cylinders, rather than parallel cylinders, the estimation of their density and axon radii improves[87,183]. However, the techniques still lack clinical feasibility due to the non-standard acquisition protocol and long scan times they require. Recent work shows the non-sensitivity of standard MRI hardware to the majority of the axon radii ($1-2\mu m$[3]) present in the human brain[52].

Lastly, the T_2 relaxation effects, which are expected to be different in each NODIDI compartment, are not explicitly accounted for in the model. While the normalisation with the $b = 0$ measurement accounts for the overall impact of T_2 decay, the volume fractions of individual compartments are actually relaxation-weighted (see Appendix B.1). This can be accounted for by estimating the relaxation time, but requires extra acquisitions, with multiple echo times, which is currently not clinically feasible with existing NODDI protocol.

To relax the various assumptions in the NODDI tissue model, advances in standard MRI systems need to be made to allow *in vivo* acquisition of the rich data required to estimate the extra parameters, as concluded also from the experiments in Jelescu et al. 2015. This is generally an issue affecting all the *in vivo* microstructure imaging techniques in DW-MRI, which all rely on several assumptions to gain specificity to microstructure (Chapter 4).

16.2.2 *Model fitting procedure*

The computational efficiency of the current model fitting implementation is a concern, which requires nonlinear optimisation to estimate the microstructure parameters. The NODDI Matlab toolbox takes approximately 60 hours to fit the Bingham-NODDI model to the whole brain data used in Chapter 8 (using the fitting procedure proposed in Chapter 9 is much faster, but still takes a long time). This can be addressed with the convex optimisation procedure proposed by Daducci et al. 2015, which converts the nonlinear fitting into a linear optimisation problem, dramatically reducing the processing speed. A preliminary work extends this framework to allow robust estimation of multiple fibre populations, as well as microstructure indices[15].

16.2.3 *Reliability of parameter estimation*

The parameters estimated from Bingham-NODDI are not as robust to the measurement and other sources of noise, as compared to the standard DTI parameters, as indicated by the reproducibility results (Chapter 12). DTI is expected to be very robust for the data in Chapter 12, given that it a very simple model being used to estimate parameter from multi-shell data. Results from the analysis on the *HCP* data (Chapter 11) show comparable results for Bingham-NODDI and DTI models. So to get more reliable estimates from the proposed model requires DW-MRI data with high quality and fewer distortions. Such data is increasingly becoming available in neuroscience research field, but not in the clinical neuroscience. A potential way to improve the robustness of Bingham-NODDI estimates is using some form of machine learning techniques, like that proposed by Alexander et al. 2017, as discussed in Chapter 17.

16.2.4 *Acquisition protocol*

The optimised acquisition protocol for NODDI is feasible for standard hardware, but estimation of its indices requires multi-shell data with a high b-value. This is only a concern for utilising the NODDI model for retrospective studies, which usually consist of single b-value data acquired at $1000 s/mm^2$. Recent developments are working towards establishing techniques to enable estimation of microstructure indices from biophysical models like NODDI, with single-shell data, using machine learning techniques[7]. This would result in more studies utilising the technique, which is great for the advancement in the field of microstructure imaging and thus research in neuroscience.

16.3 DISCUSSION OF THE CLINICAL UTILITY

As detailed in the motivation for developing Bingham-NODDI, characterising anisotropic orientation dispersion can provide useful indices of neurite morphology, that can be utilised in clinical and neuroscience studies. The index of orientation dispersion anisotropy, which specifically quantifies this, can capture very subtle changes in neurite orientation configurations, which may not change the overall dispersion. This can provide an earlier marker of brain disease, which is the key to a better prognosis for brain disorders and diseases. Recent work applying Watson-NODDI to clinical application provides promising results for this. For example, recent work by Grussu et al. 2017 shows that Watson-NODDI estimation of orientation dispersion is an earlier marker of the onset of multiple sclerosis (MS). Traditionally it was thought that axonal breakdown, including loss of myelination, is the first marker of MS, but this study shows it may be orientation dispersion. Similarly, Bingham-NODDI may be able to provide earlier markers of brain disease like MS, in terms of the dispersion anisotropy index, which could be the first sign of a pathology.

Quantification of orientation dispersion anisotropy can be beneficial to understand the developing brain where features like dendritic arborization and fanning/bending of bundles of axons are key markers of normal brain development as they undergo significant changes in their configurations. For example, the cortical fibres go from having a highly anisotropic orientation dispersion to isotropic as the brain develops in the early years of life, while the development of axonal pathways together with their pruning result in an increase in this anisotropy[172]. These features characteristics have been shown to be altered in the preterm brain[85] and can be identified using the proposed

model, allowing early detection of developmental disorders in the preterm brain.

While there is still a very long way to go, before making the model proposed here feasible for such applications, due to various technical issues (e.g. small brain size and low neurite density for preterm infants, which reduces the SNR as well as the precision of the estimates), recent applications utilising Watson-NODDI are showing great promise in this regard.

17

FUTURE WORK

In this chapter, we discuss the main areas of future work to further this work in terms of the development and application of the proposed model, specifically addressing the limitations of the presented work in Chapter 16.

17.1 MODELLING CROSSING FIBRES WITH BINGHAM-NODDI

A potential future work would be to investigate the possibility of incorporating crossing fibres using Bingham-NODDI. Riffert et al. 2014 estimate the Bingham distribution for each peak of the estimated fibre ODF, avoiding the instability of estimating the mixture of Bingham distributions directly from the data[147]. It would be interesting to explore a similar approach, to first estimate the number of fibre populations (using for e.g. constrained spherical deconvolution (CSD)[166]) and then fitting Bingham-NODDI as a mixture of Bingham distributions, with the already estimated orientations, for stable estimates. This will allow estimation of microstructure specific indices while accounting for the existence of both crossings and anisotropic orientation dispersion.

17.2 RELAXING THE ASSUMPTIONS OF BINGHAM-NODDI

The rapid advancements in the MRI technology mean that it is now possible to acquire very high-resolution and quality DW-MRI data, in reasonable acquisition time. This is possible with the high field and gradient strength systems being increasingly adapted at many research centres (e.g. the 7T human scanners at HCP[1] and Cubric centre[2]), which use techniques like multi-band imaging[60] to accelerate the acquisition protocol. This provides a great op-

1 HCP: http://www.humanconnectome.org/
2 Cubric: http://sites.cardiff.ac.uk/cubric/research-2-2/microstructural-imaging/

portunity to get even better results from microstructure imaging techniques, including Bingham-NODDI, as the various assumptions made in the models, can be relaxed when used with a rich data set acquired in a reasonable acquisition time.

Improved quality of the data will also have an impact on the reproducibility of Bingham-NODDI indices, as seen from the analysis in Part (iv) of the thesis, giving greater confidence in the conclusions drawn in terms of microstructure morphology from the estimated parameters.

A lot of work has also recently gone into advanced acquisition sequences like the double pulse field gradient (d-PFG) and oscillating gradient spin echo (OGSE). Such sequences provide a further opportunity to resolve microstructure features that are hard to estimate with current clinical hardware, e.g. axon radii and diffusivity characteristics. While these sequences don't usually require a hardware upgrade, the translation of such techniques to clinical set up has been slow due to the complexity of implementing the sequences to scanners and is not usually supported by the manufacturers.

17.3 ACQUISITION PROTOCOL

The acquisition protocols used to evaluate Bingham-NODDI are the ones used in the original paper[185] and the two-shell protocol optimised for Watson-NODDI performs the best. However, it will be beneficial to carry out a protocol optimisation procedure specifically for Bingham-NODDI. This will enable us to determine the specific protocol required to reliably estimate the parameters of Bingham-NODDI, specifically the ones that are harder to estimate. Results presented here suggest that the estimation of the orientation dispersion and the dispersion anisotropy indices would improve (more accurate and precise) if greater orientations were probed in the DW-MRI protocol (more $\hat{\boldsymbol{G}}$ samples).

17.4 VALIDATION OF BINGHAM-NODDI

Bingham-NODDI requires 3-D histological data for validation of its indices, as it characterises the anisotropic orientation dispersion of neurites, which can only be fully evaluated in three dimensions. Recent 3D histological techniques like *Clarity*[58] and *PLI*[51] are showing promising results for the brain microstructure. The preliminary assessment of Bingham-NODDI in the cortical fibres shows promising results (Chapter 14), specifically compared to Watson-

NODDI, but it would be very informative to do a more thorough, quantitative analysis of the data. While the corresponding histology for the data is 2D (data as used in Kleinnijenhuis et al. 2013), it would be interesting as a quick assessment to see how the 2D fibre distributions compare between the histology and those estimated from fitting Bingham-NODDI to the *ex vivo* data.

17.5 CLINICAL APPLICATION OF BINGHAM-NODDI

To show the clinical utility of the Bingham-NODDI metrics, a clinical study using the model needs to be carried out. Such a study will be beneficial in determining how specific the indices are to a certain pathology and thus how useful the model is in practice. This will help to evaluate if including the Bingham distribution, a more complex model for the ODF of neurites, improves the diagnosis and/or prognosis of the disease, compared to Watson-NODDI. This can also reveal how useful ODI_P, ODI_S and DA_B are compared to the corresponding indices derived from the second order approximation of the ODF, which is more robust to noise. We find the errors and variability of the Bingham-NODDI metrics to be moderate, but a clinical study will help determine if they can distinguish normal and pathological tissue, and thus show how reasonable the statistics of estimation are in practice.

We do take the first step towards the clinical utility of Bingham-NODDI by establishing the cohort requirements for group studies (Chapter 11) and a reproducibility analysis (Chapter 12), but a study with a significant cohort of subjects, where the Bingham-NODDI parameters of a clinical and control population can statistically be differentiated, needs to be carried out.

17.6 FUTURE DIRECTIONS FOR MICROSTRUCTURE IMAGING

A great opportunity for microstructure imaging is the fast development of modelling in using other MRI modalities, paving way for use of multi-modal imaging techniques. This includes techniques like Multi-parametric mapping (MPM) that are extremely important as they utilise the various contrasts available with MRI and provide better modelling of the various microstructure features of interest, simultaneously. The rapid progression of techniques for faster and higher-quality MRI acquisitions, with fewer distortions, is also an area that will help the field of microstructure imaging, as currently, the main

limitation is that the data that can be acquired as a standard is not very rich enable accurate *in vivo* estimation of sophisticated measures of microstructure.

18

CONCLUSION

We have developed a noninvasive imaging technique that can quantify complex configurations of brain microstructure, feasible with standard neuroimaging technology. Our work demonstrates that the proposed model provides sensible estimates of neurite morphology and can enhance the characterisation of WM orientation dispersion, with measures that are accurate and reliable. We present an atlas of the metrics of the proposed model in the WM of the healthy adult brain, to serve as a reference for future neuroscience studies. However, the indices of the proposed method are not as robust and reproducible, in images acquired with clinical scanners, as the current standard in DW-MRI of the brain, DTI. But with the emergence of high-quality MRI systems, this difference will become less prominent, as the reliability and accuracy of BN indices improves significantly with better quality data

The exciting recent developments in microstructure imaging using MRI mean the acquisition is getting better in terms of quality and have fewer artifacts, which will make techniques such as the proposed one more relevant in the near future. This will help relax some of the assumptions made in the model, that have been known to cause its estimates to be biased.

Part VII

APPENDIX

A

DIFFUSION-WEIGHTED MAGNETIC RESONANCE IMAGING

A.1 NMR

$^1H^+$ nucleus has a net charge and a quantum spin of $1/2$, which gives rise to a magnetic moment, $\boldsymbol{\mu}$. [1] In the presence of an external magnetic field ($\boldsymbol{B}_0$), the $^1H^+$ spin take one of its two discrete energy states, *up* or *down*.

The difference in the occupation of the two energy states creates the equilibrium magnetization $\boldsymbol{M}_0$ in the direction of $\boldsymbol{B}_0$[2], as there are more nuclei in the spin-up than spin-down energy state. For N protons per unit volume,

The distribution of nuclei in the two energy states is dictated by the Boltzmann distribution

$$\boldsymbol{M}_0 = \frac{N\hbar^2\gamma^2\boldsymbol{B}_0}{4kT} \,, \tag{A.1}$$

Where $k = 1.38 \times 10^{-23} JK^{-1}$ and $\hbar = 1.05 \times 10^{-34} Js$ are the Boltzmann and Planck constants, respectively. Conventionally $\boldsymbol{B}_0$ is applied along the z-axis, which is also called the longitudinal plane and the plane perpendicular (x-y plane) is called the transverse plane.

$$\frac{N_+}{N_-} = \exp^{\frac{\Delta E}{kT}} = \exp^{\frac{\gamma\hbar\boldsymbol{B}_0}{kT}} \,. \tag{A.2}$$

Here ΔE is the difference in two energy states, T is the temperature and N_+ and N_- denote the number of nuclei in parallel and anti-parallel energy state, respectively. The constants in the equation are the Boltzmann $k = 1.38 \times$

1 $\boldsymbol{\mu} = \gamma \boldsymbol{I}$, where $\gamma = 2.68 \times 10^8 s^{-1} T^{-1}$, the gyromagnetic ratio for $^1H^+$ and $\boldsymbol{I}$ is the angular momentum of the nucleus.

2 there is no net magnetisation in the plane perpendicular to the axis of application of $\boldsymbol{B}_0$, as the precession of individual nuclei are not in phase

$10^{-23}JK^{-1}$ and Planck $\hbar = 1.05 \times 10^{-34}Js$. The number of nuclei in the N_+ always outnumber those in the N_- state, as N_- is a higher energy state. So the net magnetization of an ensemble of nuclei, in equilibrium is parallel to $\boldsymbol{B}_0$

A.2 THE BLOCH EQUATIONS

In the presence of an external magnetic field, the evolution of the net magnetisation, $\boldsymbol{M} = (M_x, M_y, M_z)$, which is the signal measured in MRI, can be explained by classical mechanics. This evolution is mathematically described by the Bloch equations.

According to Bloch's equation, the change in magnetization $\boldsymbol{M}(t)$ over time, in the presence of an external (static) magnetic field $\boldsymbol{B_0}$ is

$$\frac{d\boldsymbol{M}(t)}{dt} = \gamma \boldsymbol{M}(t) \times \boldsymbol{B_0} \, . \tag{A.3}$$

Here the $\times$ denotes a cross product.

In the presence of a static field along the longitudinal axis, $\boldsymbol{B_0}$, and a oscillating field in the transverse plane, $\boldsymbol{B_1}(t)$, this equation becomes:

$$\frac{d\boldsymbol{M}(t)}{dt} = \gamma \boldsymbol{M}(t) \times \begin{bmatrix} B_1 \cos \omega_1 t \\ B_1 \sin \omega_1 t \\ B_0 \end{bmatrix} \, . \tag{A.4}$$

When including the effects of the relaxation over time of $\boldsymbol{M}(t)$, which has been excited by an oscillating pulse $\boldsymbol{B_1}(t)$, the Bloch eqautions become:

$$\frac{d\boldsymbol{M}(t)}{dt} = \gamma \boldsymbol{M}(t) \times \boldsymbol{B}(t) - \boldsymbol{R}\left(\boldsymbol{M}(t) - \boldsymbol{M}_0\right) \, , \tag{A.5}$$

where $\boldsymbol{B}(t) = \boldsymbol{B_0} + \boldsymbol{B_1}(t)$, $\boldsymbol{M}_0$ is the equilibrium magnetization and $\boldsymbol{R} = diag(\frac{1}{T_2}, \frac{1}{T_2}, \frac{1}{T_1})$ represents the total relaxation effects on $\boldsymbol{M}(t)$, due to the spin-lattice (T_1) and spin-spin (T_2) relaxation. This describes the precession of $\boldsymbol{M}(t)$ about $\boldsymbol{B}(t)$ with $\omega(t) = -\gamma \boldsymbol{B}(t)$, while it returns to its equilibrium magnetization $\boldsymbol{M}_0$.

Including the diffusion into the Bloch equations, gives the *Bloch-Torry* equation

$$\frac{d\boldsymbol{M}(t)}{dt} = \gamma \boldsymbol{M}(t) \times \boldsymbol{B}(t) - \boldsymbol{R}\left(\boldsymbol{M}(t) - \boldsymbol{M}_0\right) + D\nabla^2 M_\perp \,. \tag{A.6}$$

A.3 SPINE ECHO SEQUENCE

At time $t = 0$ when the spins are excited with the rf pulse, the spins are all in phase and precessing coherently. But as time passes they slowly start de-phasing due to: $\vec{B}_0$ inhomogeneities and dipolar interactions between the neighbouring spins. This de-phasing of the spins causes a decay in the net-magnetisation of the spins in the transverse plane M_{xy} and the *longitudinal* magnetic field M_z starts to recover due to the spins losing energy and going back to their preferred low energy state along the longitudinal plane.

Mathematically, the recovery of M_z and the decay of M_{xy} is given by the solution of the *Bloch Equations* (Equation (A.5)), which gives the Equations (3.7) and (3.8) for the recovery of longitudintal magnatization M_z and the deacy of the transverse component of magnetization (M_{xy}), respectively.

After a time $t = \tau$, another rf pulse is applied to the system of spins, this time of 180^o, which reverses the phase of each spin by πradians. But since the spins are still precessing with their original frequencies, the 'faster' spins 'catch-up' with the slower ones and the phases are aligned. This results in the 're-appearance' of the maximum magnitude in the transverse plane as all the spins are coherent, which is called *Spin-echo*.

The time at which the echo appears is $t = 2\tau$ (since the time it takes the spins to go from being completely coherent at $t = 0$, to $t = \tau$, is the same time it takes them to go back to being coherent again, after 180^o rf pulse is applied). The reason that the 180^o pulse is applied is that the time at which the signal will re-appear, i.e. $TE = 2\tau$, can be controlled by changing the time between the application of the first and the second pulse.

Figure 3.3 shows the signal measured (or voltage induced) if a receiver coil is placed perpendicular to the transverse plane. The first signal is the *Free Induction Decay - FID* signal which appears when the first rf pulse is applied. The second signal is the echo signal which appears at time $t = 2\tau$ after the first pulse application. The frequency of both the signals is ω_0. The magnitude of the second signal is less than the magnitude for the **FID** signal due to the interactions with the neighbouring spins (the $\vec{B}_0$ inhomogeneity is static w.r.t

time and thus can be recovered, but the spin-spin interactions are time-variant and thus may be different before and after the application of the second rf, and thus can't be fully recovered). This decrease in the amplitude of the signal is described by the following equation:

$$SE_{max} = FID_{max}(e^{-\frac{TE}{T_2}}) \tag{A.7}$$

A.4 DIFFUSION THEORY

Fick's first law of diffusion describes the *diffusion flux* - $\boldsymbol{J}$ (the amount of particles diffusing per unit area, per unit time) in terms of the concentration:

$$\boldsymbol{J}(\boldsymbol{r}, t) = -D\nabla c(\boldsymbol{r}, t) \tag{A.8}$$

As indicated by the minus sign, the movement of particles is against the concentration gradient. D is the *diffusion coefficient*, an inherent property of the diffusing molecule, which depends on the temperature and the fluid viscosity. Using conservation of mass to apply the continuity theorem, and using Equation A.8, one can derive the equation for Fick's second law of diffusion[131]:

$$\frac{\partial c(\boldsymbol{r}, t)}{\partial t} = D\nabla^2 c(\boldsymbol{r}, t) \tag{A.9}$$

which states that the concentration of particles over time is a function of the second derivative of their concentration. These expressions (Equation (A.8) and (A.9)) assume *isotropic diffusion*, i.e. the diffusion is orientation independent. More generally the diffusion coefficient can be represented by a *cartesian tensor*, resulting in equations:

$$\boldsymbol{J}(\boldsymbol{r}, t) = -\boldsymbol{D}\nabla c(\boldsymbol{r}, t) \ . \tag{A.10}$$

and

$$\frac{\partial c(\boldsymbol{r}, t)}{\partial t} = \nabla \cdot \boldsymbol{D}\nabla c(\boldsymbol{r}, t) \ , \tag{A.11}$$

where $\boldsymbol{D}$ is a symmetric and positive 3×3 matrix, given by $\begin{pmatrix} D_{xx} & D_{xy} & D_{xz} \\ D_{xy} & D_{yy} & D_{yz} \\ D_{xz} & D_{yz} & D_{zz} \end{pmatrix}$, and the spatial gradients and flux $\boldsymbol{J}$ are measured along the three orthogonal axes. Such a description of diffusion is necessary when the diffusion is dependent on the orientation.

$$\frac{\partial P(\boldsymbol{r}_0, \boldsymbol{r}_1, t)}{\partial t} = \nabla \cdot \boldsymbol{D} \nabla P(\boldsymbol{r}_0, \boldsymbol{r}_1, t) \, . \tag{A.12}$$

For *self-diffusion*, i.e. in absence of a net concentration gradient, the probability of finding a particle $\boldsymbol{r}_1$ at time t, given by:

$$P(\boldsymbol{r}_1, t) = \int \rho(\boldsymbol{r}_0) P(\boldsymbol{r}_0, \boldsymbol{r}_1, t) d\boldsymbol{r}_0 \, , \tag{A.13}$$

where $\rho(\boldsymbol{r}_0)$ is the particle density and $P(\boldsymbol{r}_1, t)$ describes the probability of particles at initial position $\boldsymbol{r}_0$, moving to position $\boldsymbol{r}_1$, in time t, for all possible starting positions. $P(\boldsymbol{r}_1, t)$ is equivalent to the concentration (for a single particle), as it is the probability of finding a certain particle in a certain position at time t.

The diffusion equation (Equation (3.1)), describes the motion of particles from regions of high concentrations to low, as a rate of change of their concentration over time. For self-diffusion, a similar equation can be derived

$$\frac{\partial P(\boldsymbol{r}_0, \boldsymbol{r}_1, t)}{\partial t} = D \nabla^2 P(\boldsymbol{r}_0, \boldsymbol{r}_1, t) \, . \tag{A.14}$$

Equation A.11 gives an expression for $P(\boldsymbol{r}_0, \boldsymbol{r}_1, t)$, the *diffusion propagator* in terms of the diffusivity of the particles, undergoing self-diffusion.

B

BINGHAM-NODDI MATHEMATICAL DERIVATIONS

In the following sections we provide details of the simplifications and the derivations related to the tissue model of Bingham-NODDI, including the orientation distribution function.

B.1 VOLUME FRACTIONS IN THE NODDI MODEL

The volume fractions estimated by NODDI model are relaxation-weighted. This is due to the T_2 weighting which is not completely cancelled by normalising the diffusion weighted signal by the non-diffusion weighted signal. T_1 affect can be assumed to be negligible as for typical diffusion MR experiments, $TR >> T_1$ (for brain imaging, $T_1 = 0.5 - 2sec$ and for diffusion MRIs $TR = 10 - 12sec$)

As described in Section 5.2, NODDI is a multi-level compartment model mathematically described by Equation (5.1). But A in this equation is also a function of T_2 relaxation time due to non-zero echo time (TE)

$$\begin{aligned} A(\vec{q}, b, TE) &= (1 - \nu_{iso}) A_{tissue}(\vec{q}, b, TE) + \nu_{iso} A_{iso}(\vec{q}, b, TE) \\ &= (1 - \nu_{iso}) exp\left(-\frac{TE}{T_{2tissue}}\right) \widetilde{A}_{tissue}(\vec{q}, b) + \nu_{iso} exp\left(-\frac{TE}{T_{2iso}}\right) \widetilde{A}_{iso}(\vec{q}, b) \\ &= c_1 \widetilde{A}_{tissue}(\vec{q}, b) + c_2 \widetilde{A}_{iso}(\vec{q}, b) \ , \end{aligned} \tag{B.1}$$

where $\widetilde{A}_{\{..\}}$ denotes the normalised signal for the compartment. A non-diffusion weighted image is typically obtained to normalise by the T_2 weighting in the diffusion signal, by taking a measurement without diffusion weighting:

$$S_0(TE) = A(\vec{q}, 0, TE) = (1 - \nu_{iso})A_{tissue}(\vec{q}, 0, TE) + \nu_{iso}A_{iso}(\vec{q}, 0, TE)$$
$$= (1 - \nu_{iso})exp\left(-\frac{TE}{T_{2tissue}}\right) + \nu_{iso}exp\left(-\frac{TE}{T_{2iso}}\right)$$
$$= c_1 + c_2 \quad \text{(B.2)}$$

We then compute the normalised signal as:

$$\widetilde{A}(\vec{q}, b) = \frac{A(\vec{q}, b, TE)}{A(\vec{q}, 0, TE)} \, . \quad \text{(B.3)}$$

Substituting the values from Equation (B.1) and (B.2) we get:

$$\widetilde{A}(\vec{q}, b) = \frac{c_1}{c_1 + c_2}\widetilde{A}_{tissue}(\vec{q}, b) + \frac{c_2}{c_1 + c_2}\widetilde{A}_{iso}(\vec{q}, b) \, , \quad \text{(B.4)}$$

which shows that in NODDI model the volume fractions are relaxation-weighted.

B.2 EXPRESSION FOR THE PROBABILITY OF BINGHAM DISTRIBUTION

The probability of an orientation along $\hat{n}$, in Bingham distribution, is:

$$f(\hat{n}; \mathbf{B}) = \frac{1}{c_B} exp\left(\hat{n}^T \mathbf{B} \hat{n}\right) \, . \quad \text{(B.5)}$$

Substituting for $\mathbf{B}$ we get:

$$f(\hat{n}; \mathbf{B}) =$$
$$\frac{1}{c_B} exp\left(\hat{n}^T \left[\begin{pmatrix} \hat{\mu}_1 & \hat{\mu}_2 & \hat{\mu}_3 \end{pmatrix} \begin{pmatrix} \kappa_1 & 0 & 0 \\ 0 & \kappa_2 & 0 \\ 0 & 0 & \kappa_3 \end{pmatrix} \begin{pmatrix} \hat{\mu}_1^T \\ \hat{\mu}_2^T \\ \hat{\mu}_3^T \end{pmatrix}\right] \hat{n}\right) \, . \quad \text{(B.6)}$$

Multiplying out the expression in the exponential term, we get:

$$\hat{n}^T \left[\kappa_1(\hat{\mu}_1\hat{\mu}_1^T) + \kappa_2(\hat{\mu}_2\hat{\mu}_2^T) + \kappa_3(\hat{\mu}_3\hat{\mu}_3^T)\right] \hat{n} = \kappa_1(\hat{\mu}_1^T \hat{n})^2 + \kappa_2(\hat{\mu}_2^T \hat{n})^2 + \kappa_3(\hat{\mu}_3^T \hat{n})^2 \,, \quad \text{(B.7)}$$

as

$$\hat{v}^T (\hat{u}\hat{u}^T) \hat{v} = (\hat{v}^T \hat{u})(\hat{u}^T \hat{v}) = (\hat{v}^T \hat{u})(\hat{v}^T \hat{u}) = (\hat{v}^T \hat{u})^2 \,. \quad \text{(B.8)}$$

Thus the probability along $\hat{n}$ in a Bingham distribution can be written as:

$$f(\hat{n}; \mathbf{B}) = \frac{1}{c_B} exp\left(\kappa_1(\hat{\mu}_1 \cdot \hat{n})^2 + \kappa_2(\hat{\mu}_2 \cdot \hat{n})^2 + \kappa_3(\hat{\mu}_3 \cdot \hat{n})^2\right) \,, \quad \text{(B.9)}$$

where $(\hat{\mu}_i \cdot \hat{n}) = \hat{\mu}_i^T \hat{n}$ denotes the dot product of two vectors.

B.3 DEGREES OF FREEDOM OF THE BINGHAM MATRIX **B**

The property in Equation (6.2) implies that **B** has only two free variables (or degrees of freedom). This can be proved by rewriting the exponential part of Equation (6.4):

$$\begin{aligned}
&\kappa_1(\hat{\mu}_1 \cdot \hat{n})^2 + \kappa_2(\hat{\mu}_2 \cdot \hat{n})^2 + \kappa_3(\hat{\mu}_3 \cdot \hat{n})^2 \\
&= (\kappa_1 - \kappa_3 + \kappa_3)(\hat{\mu}_1 \cdot \hat{n})^2 + (\kappa_2 - \kappa_3 + \kappa_3)(\hat{\mu}_2 \cdot \hat{n})^2 + \kappa_3(\hat{\mu}_3 \cdot \hat{n})^2 \\
&= \kappa_3\left[(\hat{\mu}_1 \cdot \hat{n})^2 + (\hat{\mu}_2 \cdot \hat{n})^2 + (\hat{\mu}_3 \cdot \hat{n})^2\right] + (\kappa_1 - \kappa_3)(\hat{\mu}_1 \cdot \hat{n})^2 + (\kappa_2 - \kappa_3)(\hat{\mu}_2 \cdot \hat{n})^2 \,.
\end{aligned} \quad \text{(B.10)}$$

The expression $\left[(\hat{\mu}_1 \cdot \hat{n})^2 + (\hat{\mu}_2 \cdot \hat{n})^2 + (\hat{\mu}_3 \cdot \hat{n})^2\right] = 1$ as $\hat{n}$ is a unit vector and the sum of its projections along the three orthogonal axes is simply its magnitude. Thus κ_3 in **B** has no dependence on the orientation, and can be taken out of the integral of Equation (6.2) as a constant. So

$$\mathbf{B} = \begin{pmatrix} \hat{\mu}_1 & \hat{\mu}_2 & \hat{\mu}_3 \end{pmatrix} \begin{pmatrix} \kappa_1 - \kappa_3 & 0 & 0 \\ 0 & \kappa_2 - \kappa_3 & 0 \\ 0 & 0 & 0 \end{pmatrix} \begin{pmatrix} \hat{\mu}_1^T \\ \hat{\mu}_2^T \\ \hat{\mu}_3^T \end{pmatrix} = \begin{pmatrix} \hat{\mu}_1 & \hat{\mu}_2 & \hat{\mu}_3 \end{pmatrix} \begin{pmatrix} \kappa & 0 & 0 \\ 0 & \beta & 0 \\ 0 & 0 & 0 \end{pmatrix} \begin{pmatrix} \hat{\mu}_1^T \\ \hat{\mu}_2^T \\ \hat{\mu}_3^T \end{pmatrix}, \quad \text{(B.11)}$$

and the probability density function for Bingham distribution can be rewritten as

$$f(\hat{n}; \mathbf{B}) = \frac{1}{c_B} exp\left(\kappa(\hat{\mu}_1 \cdot \hat{n})^2 + \beta(\hat{\mu}_2 \cdot \hat{n})^2\right) . \quad \text{(B.12)}$$

B.4 BINGHAM, A SPHERICAL ANALOGUE OF THE 2D GAUSSIAN DISTRIBUTION

Bingham distribution is the spherical analogue of a 2D Gaussian probability density function. We draw on this observation to derive Equation (6.7) in Section 6.2.1, as we demonstrate below.

A 2D Gaussian distribution represents the probability of a random variable, $\vec{x}$ as

$$f(\vec{x}; \boldsymbol{\Sigma}) = c_G \exp\left(-\frac{(\vec{x} - \vec{\mu})^T \boldsymbol{\Sigma}^{-1} (\vec{x} - \vec{\mu})}{2}\right) , \quad \text{(B.13)}$$

where $\vec{\mu} = \begin{pmatrix} \mu_1 \\ \mu_2 \end{pmatrix}$ is the mean and $\boldsymbol{\Sigma} = {\sigma_1}^2 \hat{e}_1 \hat{e}_1^T + {\sigma_2}^2 \hat{e}_2 \hat{e}_2^T$ the variance of the distribution, expressed in terms of σ_i and $\hat{e}_i$, which represent the i-th eigenvalue and eigenvector of the distribution. This expression can be simplified to

$$f(\vec{x}; \boldsymbol{\Sigma}) = c_G \exp\left(-\left[\frac{\hat{e}_1 \cdot (\vec{x} - \vec{\mu})}{\sqrt{2}\sigma_1}\right]^2 - \left[\frac{\hat{e}_2 \cdot (\vec{x} - \vec{\mu})}{\sqrt{2}\sigma_2}\right]^2\right) . \quad \text{(B.14)}$$

To express Bingham distribution in a form equivalent to Equation (B.2), we can rewrite the exponential part of equation of Equation (B.12) as

$$\kappa(\hat{\mu}_1 \cdot \hat{n})^2 + (\beta - \kappa + \kappa)(\hat{\mu}_2 \cdot \hat{n})^2 + (\kappa - \kappa)(\hat{\mu}_3 \cdot \hat{n})^2 \,, \tag{B.15}$$

which simplifies to

$$\kappa - (\kappa - \beta)(\hat{\mu}_2 \cdot \hat{n})^2 - \kappa(\hat{\mu}_3 \cdot \hat{n})^2 \,, \tag{B.16}$$

since $(\hat{\mu}_1 \cdot \hat{n})^2 + (\hat{\mu}_2 \cdot \hat{n})^2 + (\hat{\mu}_3 \cdot \hat{n})^2 = 1$. Equation (B.4) is used to rewrite Equation (B.12) as

$$f(\hat{n}; \boldsymbol{B}) = \frac{e^{\kappa}}{c_B} \exp\left(-\frac{(\hat{\mu}_2 \cdot \hat{n})^2}{1/(\kappa - \beta)} - \frac{(\hat{\mu}_3 \cdot \hat{n})^2}{1/(\kappa)}\right) \,, \tag{B.17}$$

which has the same form as the probability density function in Equation B.2. The dispersion parameters of this equation are $1/(\kappa - \beta)$ and $1/(\kappa)$, which are proportional to ${\sigma_1}^2$ and ${\sigma_2}^2$ in Equation B.2. Since $\kappa \geqslant (\kappa - \beta) \geqslant 0$, the dispersion extent along $\hat{\mu}_3$ is less than that along $\hat{\mu}_2$.

C

BINGHAM-NODDI VS WATSON-NODDI

The following results show how well the two NODDI models estimate the respective concentration parameters, for various ground truth values. The data used here has been synthesised using the same model parameters as in Chapter 7, but with anisotropic orientation dispersion and a high neurite density. The results show that the Bingham-NODDI estimation of the primary orientation dispersion is more accurate compared to that of Watson-NODDI, but also more variable.

C.1 ESTIMATION OF THE CONCENTRATION PARAMETERS

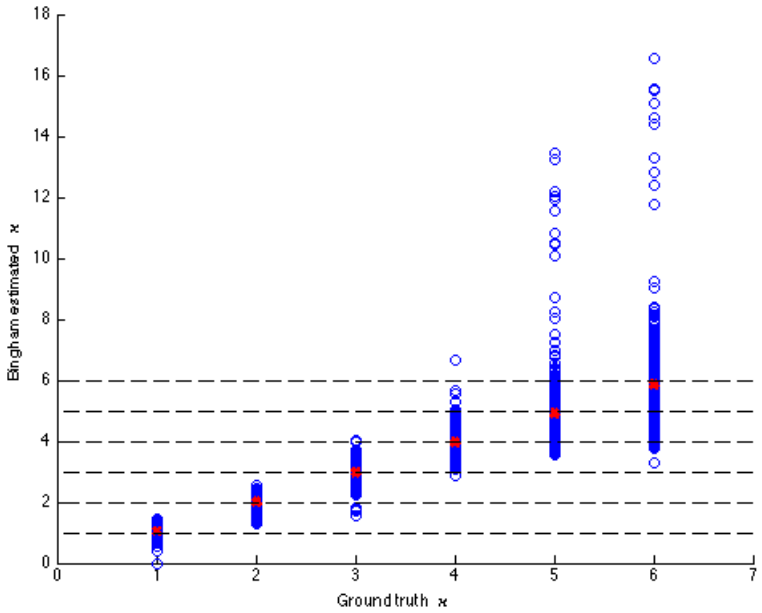

Figure C.1: Bingham-NODDI estimation of κ for high ν_{in}. The blue circles represent individual estimates, while the red cross is the mean for estimates for each ground truth value.

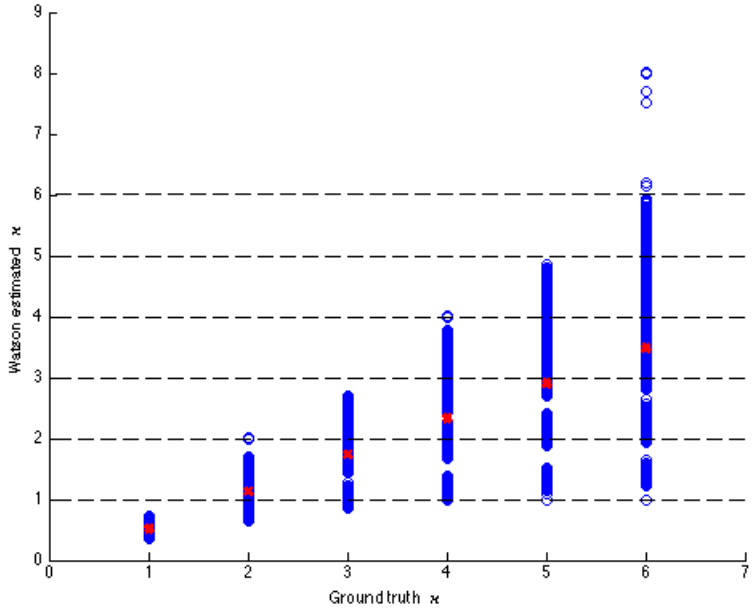

Figure C.2: As Figure C.1, but for Watson-NODDI estimation of κ.

As expected we see that Bingham-NODDI estimates the primary concentration parameter (κ) accurately, unlike Watson-NODDI. Watson-NODDI estimates are bad, specifically for higher values of κ, i.e. when the dispersion about the dominant orientation is very low.

It is found that the β estimates made by fitting Bingham-NODDI are accurate, but very unreliable, as they have very high variability.

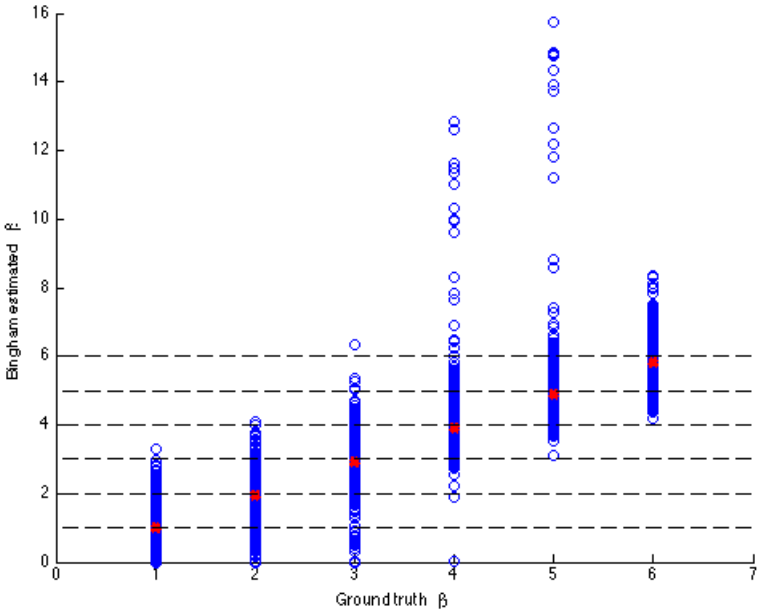

Figure C.3: As Figure C.1, but for Bingham-NODDI estimation of β.

D

NORMATIVE VALUES OF BINGHAM-NODDI INDICES IN THE WM - FURTHER RESULTS

D.1 QUALITY OF FIT

We do some quality of fit analysis on the new fitting procedure, to make sure that it improves the model fitting in the GM, with minimum impact on that in the WM of the brain.

With the new fitting procedure, the number of voxels with negative BIC values, signifying areas where Watson-NODDI is sufficient reduces, as shown in Table D.1.

D.2 VARIABILITY RESULTS

The following Table D.2 details the CV values obatined for the parameters of BIngham-NODDI.

D.3 POWER CALCULATION RESULTS

The following figures show the power calculation results for the three models compared here.

Subject	Original fit	New fit
Subject1	3.96%	1.92%
Subject2	5.51%	3.45%

Table D.1: The modified model fitting procedure reduces the percentage of voxels where Watson-NODDI is sufficient (mainly CSF regions). These results are computed over a slice of the DW-MRI data for two subjects.

	ν_{in}	ν_{iso}	ODI_P	ODI_S	ODI_{Tot}	DA_B
MCP	4.387	9.278	4.595	9.032	6.591	4.430
PCT	6.874	15.393	11.169	11.798	12.193	7.551
GCC	5.789	10.248	5.486	9.951	7.071	8.507
BCC	5.730	11.979	5.190	9.499	6.920	8.030
SCC	4.832	13.728	5.602	12.422	8.313	4.692
FX	8.543	30.594	28.613	38.383	35.624	9.419
CST	5.906	15.297	9.921	17.191	13.690	5.402
ML	6.216	24.442	11.372	16.830	14.582	10.312
ICP	5.776	26.639	7.793	10.918	9.552	4.850
SCP	5.334	12.696	10.078	17.126	14.293	5.627
CP	3.539	10.042	5.789	12.048	9.050	7.173
ALIC	4.452	23.362	5.420	9.948	7.152	7.752
PLIC	3.798	19.387	5.963	10.211	6.746	6.553
RLIC	6.031	17.571	5.411	13.409	7.818	7.967
ACR	4.822	10.908	5.245	7.928	5.558	6.454
SCR	3.869	13.116	5.955	7.511	5.976	5.976
PCR	4.702	14.675	7.013	9.208	7.751	5.177
PTR	4.867	14.359	5.462	11.349	7.238	6.191
SS	5.766	12.186	7.993	15.240	10.047	8.438
EC	5.131	26.215	4.229	7.241	5.466	3.550
CGC	6.036	18.377	7.446	11.478	9.358	4.947
CGH	8.578	26.728	9.777	16.550	13.810	7.309
FX/ST	6.698	15.732	8.075	14.839	11.695	8.944
SLF	3.920	11.227	3.783	6.838	5.503	2.822
SFO	5.527	16.521	6.498	7.950	6.865	7.637
IFO	5.674	40.304	9.043	9.941	9.403	6.369
UNC	8.529	35.499	12.879	24.936	19.756	10.328

Table D.2: Coefficient of variation of the Bingham-NODDI metrics, across all the subjects, for the various WM ROIs.

	10%							5%							2%						
	Vin	Viso	ODIp	ODIs	ODItot	DAb	DAt	Vin	Viso	ODIp	ODIs	ODItot	DAb	DAt	Vin	Viso	ODIp	ODIs	ODItot	DAb	DAt
MCP	4	9	4	9	6	4	6	9	30	9	28	16	9	14	39	217	71	226	132	58	102
PCT	6	21	12	13	14	7	10	17	77	42	46	49	20	33	94	433	399	322	413	233	371
GCC	5	11	5	10	7	8	9	13	35	12	34	18	25	29	66	284	77	264	122	189	226
BCC	5	14	5	10	6	8	8	13	48	11	31	18	23	24	67	356	80	248	127	157	214
SCC	5	17	5	15	8	4	10	10	62	12	51	24	10	30	51	459	146	488	237	49	288
FX	8	76	67	118	102	10	28	25	296	259	465	401	30	104	128	3041	1897	4578	3533	244	1095
CST	5	21	10	26	17	5	8	14	76	33	95	61	12	25	66	628	273	896	537	102	245
ML	6	49	13	25	19	11	11	15	190	43	91	69	36	34	73	1296	471	1029	794	337	341
ICP	5	58	7	12	10	5	7	13	225	22	40	31	10	20	65	1925	246	477	376	65	212
SCP	5	15	11	26	19	5	7	12	53	34	95	67	13	21	60	439	436	1285	864	69	279
CP	4	11	5	14	9	7	8	7	34	13	48	28	19	24	27	241	118	494	250	148	288
ALIC	4	45	5	10	7	7	9	9	174	12	34	19	21	28	39	955	68	269	131	129	166
PLIC	4	32	6	11	6	6	11	7	120	14	35	17	16	34	31	830	116	340	141	99	267
RLIC	6	27	5	17	7	8	11	14	99	12	59	22	22	36	79	619	93	460	157	164	297
ACR	5	12	5	8	5	6	10	10	40	11	22	12	16	31	49	243	61	144	62	113	243
SCR	4	16	6	7	6	6	9	7	56	14	20	14	14	27	32	376	81	125	75	85	187
PCR	5	19	7	9	7	5	8	10	70	18	29	21	11	25	49	461	131	200	140	76	210
PTR	5	19	5	13	7	6	8	10	67	12	43	19	15	26	55	416	93	339	152	104	215
SS	5	14	8	21	11	8	13	13	49	23	75	34	25	43	62	307	189	749	327	227	388
EC	5	56	4	7	5	4	5	11	218	8	19	12	7	11	55	1321	55	151	85	39	82
CGC	6	29	7	13	9	5	7	14	108	20	44	30	10	19	83	658	209	465	313	101	222
CGH	8	59	10	24	17	7	6	26	227	32	88	62	19	15	175	1275	444	1029	785	203	154
FX/ST	6	22	8	20	13	9	8	17	80	23	72	45	28	25	84	607	212	589	358	296	314
SLF	4	12	4	6	5	3	4	7	42	7	17	12	5	7	35	249	58	159	106	29	59
SFO	5	24	6	8	6	7	11	12	88	16	22	17	21	35	50	514	105	161	125	116	204
IFO	5	130	9	10	10	6	11	13	512	28	33	30	15	34	71	3126	229	313	262	118	279
UNC	8	101	16	51	33	11	12	25	398	55	198	125	36	39	137	3645	284	802	484	242	340

Figure D.1: Power calculations for Bingham-NODDI indices, for the various effect sizes.

	10%					5%					2%				
	Vin_WN	Viso_WN	ODI_WN	FA	MD	Vin_WN	Viso_WN	ODI_WN	FA	MD	Vin_WN	Viso_WN	ODI_WN	FA	MD
MCP	4	11	6	6	3	8	36	18	17	6	36	211	96	94	21
PCT	6	20	15	12	3	17	71	53	40	4	93	431	316	240	12
GCC	5	14	6	4	4	12	48	14	10	8	60	288	74	46	38
BCC	5	16	6	4	4	12	57	18	6	6	64	346	97	26	24
SCC	4	20	8	4	4	9	72	25	7	7	45	438	144	27	28
FX	8	125	90	18	12	23	493	354	65	39	130	3067	2203	391	234
CST	5	27	17	13	4	12	100	60	42	6	61	614	364	252	24
ML	6	52	23	10	3	14	200	83	32	4	72	1239	506	187	13
ICP	5	77	12	9	5	12	301	41	30	10	64	1869	243	172	47
SCP	5	19	25	8	4	11	70	91	22	9	56	423	559	127	41
CP	4	12	8	4	4	6	41	23	9	6	25	245	133	42	21
ALIC	4	40	6	5	3	8	151	15	12	5	37	929	81	61	16
PLIC	4	35	6	4	3	7	133	14	9	5	27	818	73	41	19
RLIC	5	24	5	5	4	13	87	13	11	6	69	534	68	52	22
ACR	5	12	5	5	3	10	39	11	12	5	48	233	53	63	20
SCR	4	16	5	4	3	7	58	10	7	5	31	350	47	28	14
PCR	5	19	6	5	3	10	70	16	13	6	48	424	85	65	20
PTR	5	18	6	4	4	11	65	16	8	6	58	393	85	37	22
SS	5	13	9	6	3	12	46	27	15	5	60	272	158	83	19
EC	5	52	5	5	3	11	201	12	10	5	55	1245	60	46	15
CGC	6	27	12	6	4	15	101	40	14	7	77	621	236	73	32
CGH	9	48	25	14	4	29	186	91	48	7	168	1151	558	290	29
FX/ST	6	25	12	7	4	15	93	39	18	7	78	569	228	100	29
SLF	4	12	5	4	3	7	39	11	7	5	32	233	55	30	18
SFO	5	22	7	5	3	10	82	19	13	5	50	500	107	69	15
IFO	5	114	10	6	3	14	450	32	18	6	71	2802	185	97	20
UNC	8	143	14	15	11	24	565	50	54	35	137	3517	300	325	206

Figure D.2: Power calculations for Watson-NODDI and DTI indices, for the various effect sizes.

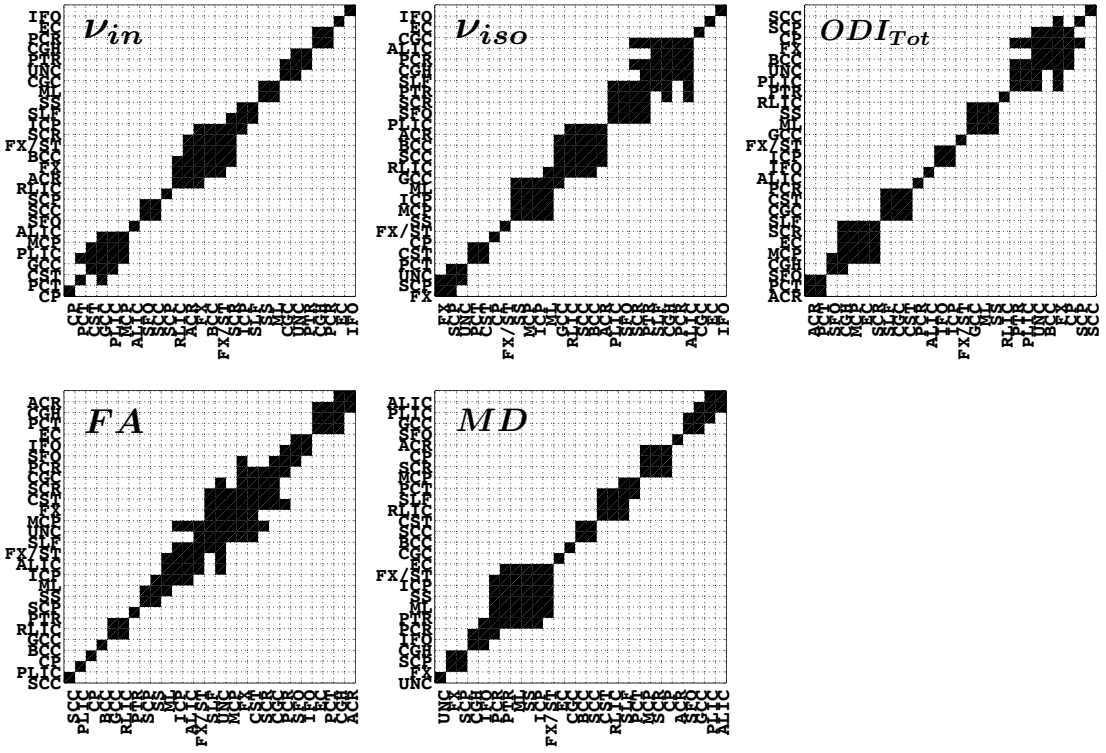

Figure D.3: Plot indicating whether each pair of ROI being compared is statistically the different (white) or not (black).

D.4 RESULTS OF THE ANALYSIS FOR WATSON-NODDI AND DTI

Here we present the normative values and inter-subject variability computed for the Watson-NODDI and DTI models for the HCP data.

D.4.1 *Watson-NODDI*

D.4.2 *DTI*

D.4.3 *Regional variability analysis for Watson-NODDI and DTI metrics*

	ν_{in}	ν_{iso}	ODI_{Tot}
MCP	0.836 ± 0.035	0.181 ± 0.016	0.280 ± 0.016
PCT	0.863 ± 0.059	0.227 ± 0.035	0.309 ± 0.033
GCC	0.842 ± 0.047	0.159 ± 0.016	0.201 ± 0.011
BCC	0.746 ± 0.042	0.155 ± 0.018	0.175 ± 0.010
SCC	0.790 ± 0.036	0.156 ± 0.021	0.151 ± 0.009
FX	0.750 ± 0.064	0.331 ± 0.101	0.172 ± 0.052
CST	0.854 ± 0.049	0.224 ± 0.034	0.259 ± 0.030
ML	0.704 ± 0.044	0.175 ± 0.042	0.200 ± 0.024*
ICP	0.729 ± 0.042	0.179 ± 0.047	0.227 ± 0.018*
SCP	0.778 ± 0.041*	0.328 ± 0.041	0.160 ± 0.018*
CP	0.882 ± 0.030	0.209 ± 0.021*	0.172 ± 0.012*
ALIC	0.817 ± 0.036	0.126 ± 0.029*	0.242 ± 0.014*
PLIC	0.842 ± 0.030*	0.138 ± 0.027*	0.182 ± 0.009*
RLIC	0.758 ± 0.043*	0.163 ± 0.027*	0.192 ± 0.010*
ACR	0.751 ± 0.036*	0.154 ± 0.017*	0.313 ± 0.016
SCR	0.740 ± 0.028*	0.136 ± 0.017*	0.275 ± 0.013
PCR	0.633 ± 0.029	0.131 ± 0.018*	0.249 ± 0.015*
PTR	0.659 ± 0.033*	0.137 ± 0.019*	0.183 ± 0.010*
SS	0.706 ± 0.040	0.187 ± 0.021*	0.198 ± 0.014
EC	0.621 ± 0.032	0.087 ± 0.022	0.279 ± 0.013*
CGC	0.681 ± 0.040	0.108 ± 0.019*	0.259 ± 0.022
CGH	0.634 ± 0.053*	0.130 ± 0.033	0.282 ± 0.034
FX/ST	0.744 ± 0.048*	0.199 ± 0.030*	0.212 ± 0.020
SLF	0.725 ± 0.028*	0.133 ± 0.014*	0.262 ± 0.010*
SFO	0.797 ± 0.044	0.136 ± 0.022*	0.291 ± 0.018*
IFO	0.558 ± 0.032	0.050 ± 0.019*	0.234 ± 0.018*
UNC	0.666 ± 0.056*	0.297 ± 0.104	0.177 ± 0.027

Table D.3: Mean and standard deviation of the normative values of the parameters of Watson-NODDI, across the all subjects, for the various WM ROIs.

	ν_{in}	ν_{iso}	ODI_{Tot}
MCP	4.232	9.123	5.820
PCT	6.809	15.307	10.781
GCC	5.571	10.252	5.709
BCC	5.622	11.747	5.979
SCC	4.594	13.347	5.968
FX	8.547	30.539	30.328
CST	5.746	15.106	11.785
ML	6.181	24.020	12.221
ICP	5.711	26.232	7.944
SCP	5.219	12.496	11.524
CP	3.435	10.104	6.882
ALIC	4.350	23.086	5.993
PLIC	3.611	19.252	4.892
RLIC	5.693	16.414	5.043
ACR	4.758	10.722	5.107
SCR	3.804	12.695	4.774
PCR	4.658	14.105	6.041
PTR	4.974	13.928	5.307
SS	5.632	11.425	7.068
EC	5.128	25.532	4.634
CGC	5.875	17.795	8.360
CGH	8.419	25.484	11.935
FX/ST	6.496	15.199	9.247
SLF	3.809	10.830	3.953
SFO	5.491	16.305	6.344
IFO	5.701	38.210	7.857
UNC	8.461	34.968	15.434

Table D.4: As Figure D.2, but for Watson-NODDI metrics.

	FA	$MD \times 10^{-9} m^2/s$
MCP	0.397 ± 0.025	0.504 ± 0.016
PCT	0.333 ± 0.034	0.509 ± 0.011
GCC	0.474 ± 0.022	0.474 ± 0.020
BCC	0.505 ± 0.016	0.528 ± 0.018
SCC	0.568 ± 0.017	0.525 ± 0.019
FX	0.393 ± 0.064	0.668 ± 0.081
CST	0.392 ± 0.041	0.516 ± 0.015*
ML	0.426 ± 0.037	0.554 ± 0.013
ICP	0.420 ± 0.033*	0.552 ± 0.023*
SCP	0.443 ± 0.034	0.651 ± 0.027*
CP	0.522 ± 0.023*	0.500 ± 0.017*
ALIC	0.417 ± 0.023	0.467 ± 0.012*
PLIC	0.539 ± 0.023	0.470 ± 0.014*
RLIC	0.472 ± 0.022*	0.515 ± 0.015*
ACR	0.318 ± 0.018*	0.494 ± 0.015*
SCR	0.385 ± 0.014*	0.501 ± 0.012*
PCR	0.373 ± 0.020*	0.558 ± 0.016*
PTR	0.461 ± 0.018	0.555 ± 0.017*
SS	0.433 ± 0.024	0.553 ± 0.016*
EC	0.337 ± 0.015*	0.543 ± 0.014
CGC	0.380 ± 0.021*	0.532 ± 0.018*
CGH	0.325 ± 0.033*	0.569 ± 0.019*
FX/ST	0.414 ± 0.030*	0.550 ± 0.020*
SLF	0.404 ± 0.013	0.511 ± 0.013*
SFO	0.365 ± 0.020*	0.476 ± 0.013*
IFO	0.357 ± 0.023*	0.564 ± 0.017*
UNC	0.400 ± 0.060*	0.701 ± 0.078

Table D.5: Mean and standard deviation of the normative values of the parameters of DTI, across all the subjects, for the various WM ROIs. *Abbreviations: CC - Corpus Callosum, CST - Corticospinal tract, ALIC - Anterior limb of internal capsule, PLIC - Posterior limb of internal capsule, ACR - Anterior corona radiata, SCR - Superior corona radiata, PCR - Posterior corona radiata, PTR - Posterior thalamic radiation, EC - External capsule, SLF - Superior longitudinal fasciculus*

	FA	*MD*
MCP	6.246	3.100
PCT	10.076	2.174
GCC	4.637	4.259
BCC	3.227	3.387
SCC	3.051	3.664
FX	16.347	12.162
CST	10.483	2.912
ML	8.632	2.270
ICP	7.800	4.078
SCP	7.639	4.183
CP	4.405	3.341
ALIC	5.474	2.618
PLIC	4.183	2.893
RLIC	4.751	2.997
ACR	5.548	2.957
SCR	3.626	2.326
PCR	5.386	2.893
PTR	3.974	3.129
SS	5.458	2.864
EC	4.411	2.513
CGC	5.464	3.386
CGH	10.126	3.360
FX/ST	7.132	3.630
SLF	3.311	2.573
SFO	5.610	2.696
IFO	6.466	2.945
UNC	14.899	11.155

Table D.6: As Figure D.2, but for DTI metrics.

E

STATISTICAL METHODS FOR REPRODUCIBILITY ANALYSIS

In this section, we describe the various statistical tools used to evaluate the reproducibility of neuroimaging methods and explain when each is suitable/relevant and what they allow us to evaluate.

E.1 RELIABILITY

Reliability is a measure associated with reproducibility studies, and is defined in Bartlett and Frost[20] as a measure that relates the *measurement error* to variability in true value due to differences *between subjects*. This is in contrast to *agreement* between two measurements which is a quantification of how close two measurements on *same subject* are. Both concepts are important in neuroimaging as agreement evaluates how *precise* the measurements made on the same subject are, while *reliability* is the ability of a method to distinguish between subjects and is population specific.

Reliability of a measurement method can be quantified as the *Intra-class correlation coefficient*:

$$\text{ICC} = \frac{\text{Variance of subject's true values}}{\text{Variance of subject's true values} + \text{Variance of measurement error}} \tag{E.1}$$

which is the estimate reported in general for reproducibility studies.

Reliability entails the concept that the discriminative ability of a parameter is related to the inherent differences *between-subjects* and the measurement error, which is the variance in measurements made on the same subject (*within-subject variability*). The variation in measurements made on the same subject can be due to actual changes in the variable being measured between the mea-

surements, measurement error due to the method's variability, random noise or due to the variance of measurement from an *observer/rater* (i.e. someone who reads the measurement).

It is also highlighted in Bartlett and Frost[20] that it is important to report the *between-subject variance* and the *within-subject variance*, as well as the ICC. This is because the ICC value is dependent on the *heterogeneity* of the population in the study and is thus study-specific. ICC has been defined in many forms in various studies[145]. The appropriate ICC for a certain study can be chosen based on some underlying decisions, as detailed by Shrout and Fleiss[145]; (a) Is a one-way or two-way *analysis of variance (ANOVA)* appropriate?; (b) Differences between raters' mean measurement are relevant?. In order to make these decisions, we need to understand which sources of variance we are interested in measuring and which of those are actually feasible with our experimental design.

In the following sections of this chapter, we explain the theory behind some of the statistical analysis tools that can be utilised for assessing the reproducibility of NODDI. In section E.1.1 we explain the framework of analysis of variance (ANOVA), and describe the analysis using the assumption of *random-effects*, with one- and two-way model. In the subsequent sections, we describe some of the other most commonly used statistical models; paired t-test and coefficient of variation and explain their relevance to our study.

E.1.1 *Analysis of Variance - ANOVA*

Analysis of variance is a very useful statistical method for a reproducibility study. It is a collection of statistical models in which the variance of a certain measured variable is *partitioned* into components which relate to various sources of variance. Any ANOVA test has some underlying assumptions on the distribution of the data being analysed. It assumes that the measurement errors are statistically independent of the true value (i.e. the error-free value), so the *standard deviations SDs* σ^2 is constant throughout the range of true values. Such a dependency of errors on the true value can be checked by obtaining a Bland-Altman plot[27], where the paired differences between two measurements are plotted against their mean, to look for any correlation or bias between the measurements, and can be corrected by transforming the measurements such that the error associated with the transformed values have no dependency on the mean, as shown in Bartlett and Frost[20]. An ANOVA test also assumes that difference between the measurements is normally dis-

tributed. It is important to check before carrying out an ANOVA on a set of measurements that these assumptions hold.

There are several classes of an ANOVA test, which depend on the assumptions made on the underlying experiment design, i.e. which sources of variances are neglected, or measured as a combination of another source.

E.1.1.1 *Fixed-effects model*

In a Fixed-effects model, only the within-subject variability is taken into account, since the subjects are treated as a fixed-effect and so the differences between them are not of interest. No inferences are made about the population, but the experiment is treated as a *case study* where we are just interested in the measurements or response from a specific set of subjects.

E.1.1.2 *Random-effects model*

In the Random-effects model we treat the subjects as being drawn from a population, i.e. the subject variable is a *random effect*. This allows us to make inferences about the population from which the subjects are drawn, by taking the sampling variability into account. Thus in a random effect analysis, we take into account the within-subject as well as between-subjects variability.

E.1.1.3 *Mixed-effects model*

A mixed-effect contains experimental factors of both fixed and random-effects.

E.1.2 *ANOVA for scan-rescan experiment of NODDI*

For purposes of our study, we are interested in finding the variance within-subjects (which may be attributed to measurement error), as well as the differences between-subjects. This is because we want to see if it is possible to distinguish subjects drawn from different populations (i.e. patient or normal) on basis of the parameters estimated by NODDI. Depending on how we want to analyse our data, and how many random-effects we are interested in, we can carry out a *one-way* or a *two-way* ANOVA test.

E.1.2.1 *One-way Random-effects model*

If we want to see the effect of within-subject variance on a measurement, we separate the variance into between-subject and within-subject variance (i.e. measurement error) and we are thus carrying out a one-way ANOVA. Here

we assume that our measurement only has two sources of variability and we would have the following equation describing the sources of variability in the measurement made:

$$Y_{ij} = \mu + \alpha_i + \epsilon_{ij} \tag{E.2}$$

Where $1 \leqslant i \leqslant n, 1 \leqslant j \leqslant k$, where n is the number of subjects and k the number of measurements/scans on each subject. The error and the between-subject effect are normally distributed as: ϵ_{ij} $N(0, \sigma^2)$ and α_i $N(0, {\sigma_n}^2)$. Y_{ij} is the j^{th} measurement (scan) made on the i^{th} subject, and μ is the population mean. Here we are only interested in the between-subject variance, which can be obtained by partitioning the *sum-squares*, the sum of squared differences from the mean, as follows[187]:

$$SSn = \sum_{i=1}^{n} k(\bar{Y}_{i.} - \bar{Y}_{..})^2 \tag{E.3}$$

$$SSk = \sum_{i=1}^{n} \sum_{j=1}^{k} (Y_{ij} - \bar{Y}_{i.})^2 \tag{E.4}$$

where $\bar{Y}_{..}$ is the grand mean of the data, and $\bar{Y}_{i.}$ and $\bar{Y}_{.j}$, the means across the first and the second effect of interest, respectively. The corresponding degrees of freedom for the ANOVA analysis for Equation (E.3) are $(n-1)$ and for Equation (E.4) are $(k-1)n$. The expectance of the *mean-sum squares* for each expression is then given by:

$$E(MSn) = \frac{SSn}{n-1} = \sigma^2 + k{\sigma_n}^2 \tag{E.5}$$

$$E(MSk) = \frac{SSk}{(k-1)n} = \sigma^2 \tag{E.6}$$

Thus the between-subject variance ${\sigma_n}^2$ can be obtained by:

$${\sigma_n}^2 = \frac{E(MSn) - E(MSk)}{k} \tag{E.7}$$

Here the within-subject variability σ^2 is the measurement error and is simply given by the $E(MSk)$. We can then derive the corresponding Intra-class correlation coefficient (ICC), from the definition given in Equation (E.1) to be:

$$ICC = \frac{{\sigma_n}^2}{({\sigma_n}^2 + \sigma^2)} = \frac{E(MSn) - E(MSk)}{E(MSn) + (k-1)E(MSk)} \tag{E.8}$$

E.1.2.2 *Two-way Random-effects model*

It is however known that two diffusion MR images, taken on the same subject and the same scan are not always the same, due to various artifacts from eddy currents, magnetic susceptibility gradients, noise as well as cardiac pulsation. So it would be desirable to treat the *scan effect* as a random variable too and separate it from the measurement error. If we treat both the subjects and the scans as a random effect, we obtain a two-way ANOVA test, whereby each measurement is given by:

$$Y_{ij} = \mu + \alpha_i + \beta_j + (\alpha\beta)_{ij} + \epsilon_{ij} \tag{E.9}$$

Where $1 \leqslant i \leqslant n, 1 \leqslant j \leqslant k$ and the random effects we are interested in are: $\alpha_i \ N(0, {\sigma_n}^2)$ the affect due to subjects and $\beta_j \ N(0, {\sigma_k}^2)$, the effect due to scans. If we assume that the effects have random distributions without any interaction between subjects and scans, we can circumvent the need to separate this interaction effect, i.e. $(\alpha\beta)_{ij}$ from the noise ϵ_{ij}. In order to separate this *interaction* affect, we would have to take multiple scans for each subject, on each day. Thus the variance of the interaction term, ${\sigma_I}^2$ and the variance of the noise, σ^2 wouldn't be separable in our experiment design, without multiple scans during each session on each subject. The sum-squares for this case are given by Zhang [187]:

$$SSn = \sum_{i=1}^{n} k(\bar{Y}_{i.} - \bar{Y}_{..})^2 \tag{E.10}$$

$$SSk = \sum_{j=1}^{k} n(\bar{Y}_{.j} - \bar{Y}_{..})^2 \tag{E.11}$$

$$SSnk = \sum_{i=1}^{n}\sum_{j=1}^{k}(Y_{ij} - \bar{Y}_{i.} - \bar{Y}_{.j} + \bar{Y}_{..})^2 \tag{E.12}$$

Thus we leave the contribution of the interaction between the subject and scans in the random noise. The corresponding degrees of freedom are then: $(n-1)$ for the subject effect, $(k-1)$ for the scan effect and $(n-1)(k-1)$ for the noise. The expectance of the *mean-sum squares* for each expression is then:

$$E(MSn) = \frac{SSn}{(n-1)} = k{\sigma_n}^2 + \sigma^2 + {\sigma_I}^2 \tag{E.13}$$

$$E(MSk) = \frac{SSk}{(k-1)} = n{\sigma_k}^2 + \sigma^2 + {\sigma_I}^2 \tag{E.14}$$

$$E(MSnk) = \frac{SSnk}{(n-1)(k-1)} = \sigma^2 + {\sigma_I}^2 \tag{E.15}$$

The between-subject variance ${\sigma_n}^2$ can then be obtained by the same analogy as in E.4, but using the $E(MSnk)$:

$${\sigma_n}^2 = \frac{E(MSn) - E(MSnk)}{k} \tag{E.16}$$

We are now able to separate the scan effect as follows:

$${\sigma_k}^2 = \frac{E(MSk) - E(MSnk)}{n} \tag{E.17}$$

Thus by obtaining sum-squares for each effect, one can easily compute the corresponding variances for it. The ICC is then given by:

$$ICC = \frac{{\sigma_n}^2}{({\sigma_n}^2 + {\sigma_k}^2 + {\sigma_I}^2 + \sigma^2)} = \frac{E(MSn) - E(MSnk)}{E(MSn) + (k-1)E(MSnk) + k(E(MSk) - E(MSnk))/n} \tag{E.18}$$

We can also now compute the *within-subject variation coefficient* using the expression:

$$WSC = \frac{{\sigma_k}^2}{({\sigma_n}^2 + {\sigma_k}^2 + {\sigma_I}^2 + \sigma^2)} = \frac{E(MSk) - E(MSnk)}{E(MSn) + (k-1)E(MSnk) + k(E(MSk) - E(MSnk))/n} \tag{E.19}$$

And the random noise variation coefficient:

$$Noise = \frac{({\sigma_I}^2 + \sigma^2)}{({\sigma_n}^2 + {\sigma_k}^2 + {\sigma_I}^2 + \sigma^2)} = \frac{E(MSnk)}{E(MSn) + (k-1)E(MSnk) + k(E(MSk) - E(MSnk))/n} \tag{E.20}$$

E.1.2.3 *Confidence intervals on ANOVA estimates*

The values of variability and ICC obtained using the ANOVA test, as described in Section E.1.2, are estimates, and thus have a variation associated with them. Thus like any estimates, the *confidence intervals*, representing the predicted variability with their values must also be reported. As given in[145], a formula exists for one-way random-effects ANOVA but needs to be approximated for the two-way ANOVA.

E.1.3 *Coefficient of variation*

Coefficient of variation is a commonly used statistic for reproducibility studies in neuroimaging[29,46,104]. It is a measure of the dispersion of the variables about the mean, given by:

$$CV = \frac{{\sigma_k}^2}{\mu} \times 100 \tag{E.21}$$

It is a useful quantity to measure as it allows to compare the degree of variation of one measurement to another, even if the values are significantly different from each other. Thus we can compare the CVs of NODDI and DTI measures directly.

E.1.4 *Paired t-test*

A paired t-test is a suitable way to analyse the statistical significance of the differences across paired measurements, for many subjects. A paired t-test is used to test the *Null* hypothesis that the difference in means of the repeated measurements is zero, i.e. the two samples are drawn from the same population. The assumption made in a t-test is that the samples are drawn from a normal distribution and the standard deviations of the two sets of measurements are the same. Thus a paired t-test is a very simple test of obtaining the statistically significant differences between the scans across the two imaging sessions.

A t-statistic is computed as a ratio of the mean of differences across the repeated measurements, $\bar{(}x_{i1} - x_{i2})$, and the standard error of those differences, SE:

$$t = \frac{(x_{i1} - x_{i2})}{SE} \tag{E.22}$$

where standard error is related to the standard deviation, s_d of the paired differences as: $SE = \frac{s_d}{\sqrt{n}}$, and n is the number of subjects.

In order to obtain the value of t corresponding to a statistically significant difference between the groups, a *significance level* α is defined and the value of t-statistic corresponding to this significance level T_α is obtained from a t-statistic table. If $t > T_\alpha$, then the NULL hypothesis is rejected.

E.1.5 *Pearson's correlation*

Pearson's correlation coefficient is computed measures the quality of the least square fit of two sets of measurements[177]. It is measured as a ratio of the *sum squares* of the two quantities

$$r^2 = \frac{SS^2{}_{xy}}{SS_{xx}SS_{yy}} \tag{E.23}$$

Where $SS^2{}_{xy}$ represents the covariance of the independent data X and the dependent variable Y, and SS_{xx} and SS_{yy} are respective variances of the two variables.

F

REPRODUCIBILITY AND RELIABILITY OF BINGHAM-NODDI INDICES IN THE WM - FURTHER RESULTS

F.1 WITHIN SUBJECT DIFFERENCES IN SCAN-RESCAN DATA

F.1.1 *Differences in data intensities*

Figures F.1-F.2 show differences in intensities of resgistered data for subjects 1 and 10, while Figures F.3-F.4 summarise how different these values are for some of the estimated parameters of the three models (Bingham-NODDI, Watson-NODDI and DTI). It is clear from these plots that despite some significant changes in the intensities of the two scans in subject 10, the DTI metrics are still very similar in the two scans, highlighting the insensitivity of the model to underlying changes in intensity.

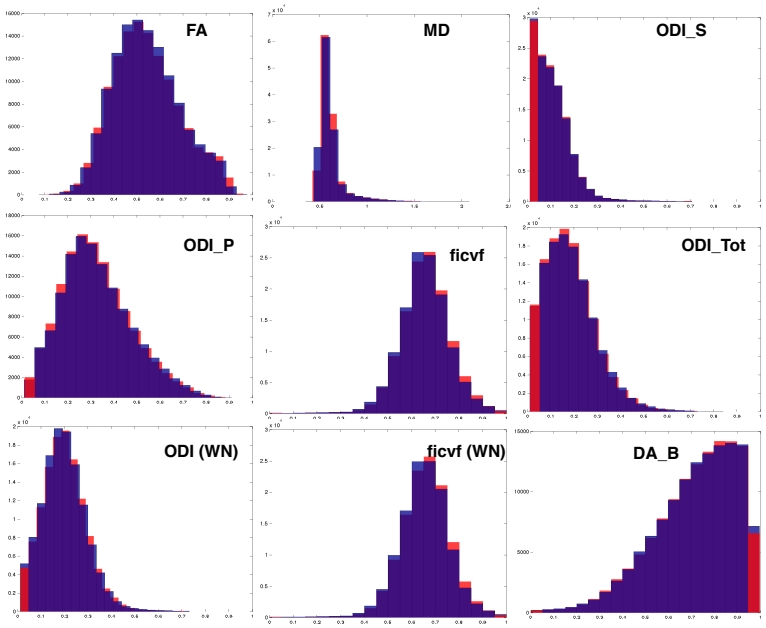

Figure F.1: Subject 1

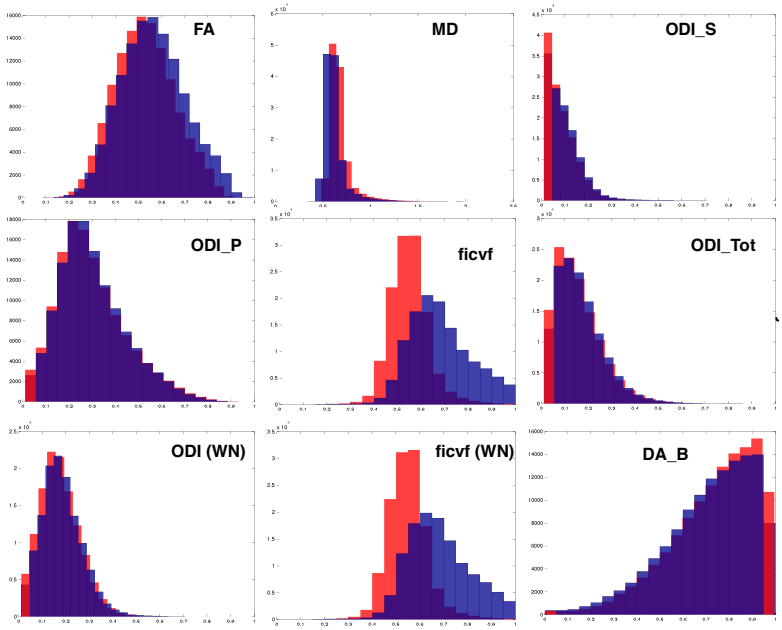

Figure F.2: Subject 10

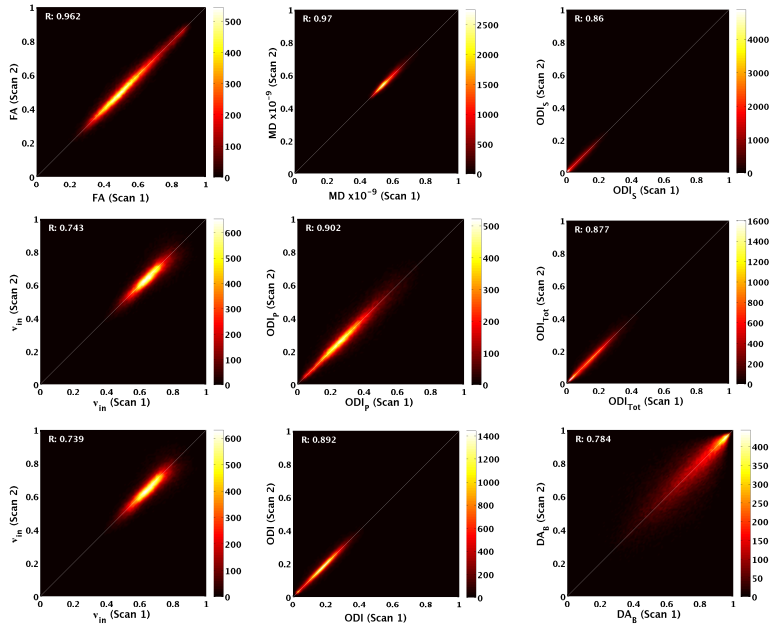

Figure F.3: Subject 1

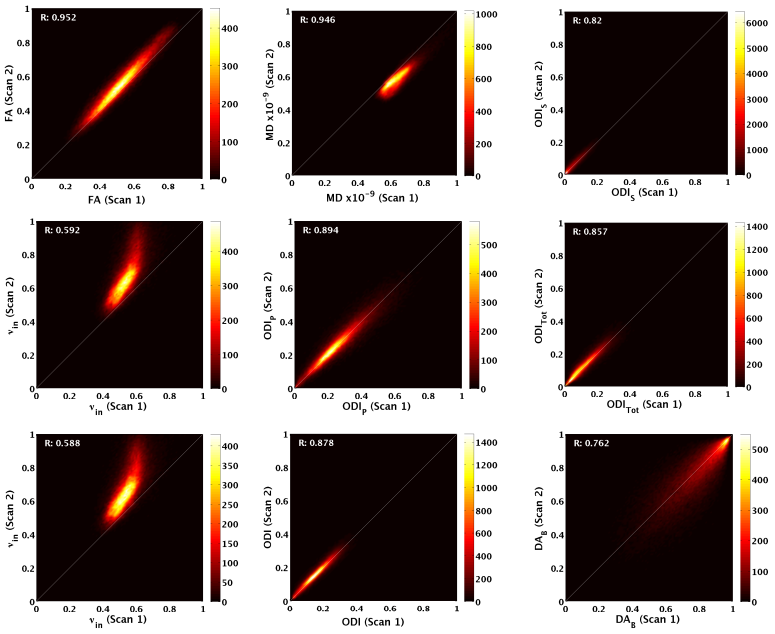

Figure F.4: Subject 10

BIBLIOGRAPHY

[1] Aguirre, G., 2012. Number of neurons in a voxel. https://cfn.upenn.edu/aguirre/wiki/public:neurons_in_a_voxel. [Online; accessed 29-August-2017].

[2] Alexander, D.C., 2005. Maximum entropy spherical deconvolution for diffusion MRI, in: Proc. IPMI, Springer: LNCS 3565, Fort Collins. pp. 76–87.

[3] Alexander, D.C., 2006. An Introduction to Computational Diffusion MRI: the Diffusion Tensor and Beyond.. Springer Berlin Heidelberg. pp. 83–106.

[4] Alexander, D.C., 2008. A general framework for experiment design in diffusion MRI and its application in measuring direct tissue-microstructure features. Magnetic Resonance in Medicine 60, 439–448.

[5] Alexander, D.C., 2009. Modelling, Fitting and Sampling in Diffusion MRI.. Springer Berlin Heidelberg. pp. 3–20.

[6] Alexander, D.C., Hubbard, P.L., Hall, M.G., Moore, E.A., Ptito, M., Parker, G.J.M., Dyrby, T.B., 2010. Orientationally invariant indices of axon diameter and density from diffusion MRI. NeuroImage 52, 1374–1389.

[7] Alexander, D.C., Zikic, D., Ghosh, A., Tanno, R., Wottschel, V., Zhang, J., Kaden, E., Dyrby, T.B., Sotiropoulos, S.N., Zhang, H., Criminisi, A., 2017. Image quality transfer and applications in diffusion MRI. NeuroImage 152, 283–298.

[8] Anderson, A.W., 2005. Measurement of fiber orientation distributions using high angular resolution diffusion imaging. Magnetic Resonance in Medicine 54, 1194–1206.

[9] Andersson, J.L.R., Sotiropoulos, S.N., 2016. An integrated approach to correction for off-resonance effects and subject movement in diffusion mr imaging. Neuroimage 125, 1063–1078.

[10] Assaf, Y., Basser, P.J., 2005. Composite hindered and restricted model of diffusion (CHARMED) MR imaging of the human brain. NeuroImage 30, 1100–1111.

[11] Assaf, Y., Blumenfeld-Katzir, T., Yovel, Y., Basser, P.J., 2008. AxCaliber: a method for measuring axon diameter distribution from diffusion MRI. Magnetic Resonance in Medicine 59, 1347–1354.

[12] Assaf, Y., Cohen, Y., 2000. Assignment of the water slow-diffusing component in the central nervous system using q-space diffusion MRS: implications for fiber tract imaging. Magn. Reson. Med. 43, 191–199.

[13] Assaf, Y., Cohen, Y., 2009. Inferring microstructural information of white matter form diffusion MRI, in: Johansen-Berg, H., Behrens, T.E.J. (Eds.), Diffusion MRI: from quantitative measurement to in vivo neuroanatomy. Academic Press, pp. 127–146.

[14] Assaf, Y., Freidlin, R.Z., Rohde, G.K., Basser, P.J., 2004. New modelling and experimental framework to characterize hindered and restricted water diffusion in brain white matter. Magnetic Resonance in Medicine 52, 965–978.

[15] Auria, A., Canales-Rodriguez, E., Wiaux, Y., Dirby, T., Alexander, D.C., Thiran, J.P., Daducci, A., 2015. Accelerated microstructure imaging via convex optimization AMICO in crossing fibers, in: Proc. 23rd Annual Meeting of the ISMRM, ISMRM, Toronto, Ontario, Canada.

[16] Bach, M., Laun, F.B., Leemans, A., Tax, C.M., Biessels, G.J., Stieltjes, B., Maier-Hein, K.H., 2014. Methodological considerations on tract-based spatial statistics (TBSS). NeuroImage 100, 358–369.

[17] Ball, G., Boardman, J.P., Aljabar, P., Pandit, A., Arichi, T., Merchant, N., Rueckert, D., Edwards, A.D., Counsell, S.J., 2013a. The influence of preterm birth on the developing thalamocortical connectome. Cortex 49, 1711–1721.

[18] Ball, G., Boardman, J.P., Rueckert, D., Aljabar, P., Arichi, T., Merchant, N., Gousias, I.S., Edwards, A.D., Counsell, S.J., 2012. The effect of preterm birth on thalamic and cortical development. Cerebral Cortex 12, 1016–1024.

[19] Ball, G., Srinivasan, L., Aljabar, P., Counsell, S.J., Durighel, G., Hajnal, J.V., Rutherford, M.A., Edwards, A.D., 2013b. Development of cortical microstructure in the preterm human brain. Proceedings of the National Academy of Science (PNAS) 110, 9541–9546.

[20] Bartlett, J.W., Frost, C., 2008. Reliability, repeatability and reproducibility: analysis of measurement errors in continuous variables. Ultrasound Obstet Gynecol 31, 466–475.

[21] Basser, P., Ozarslan, E., 2009. Introduction to diffusion MRI, in: Johansen-Berg, H., Behrens, T.E.J. (Eds.), Diffusion MRI: from quantitative measurement to in vivo neuroanatomy. Academic Press.

[22] Basser, P.J., Matiello, J., Le Bihan, D., 1994. MR diffusion tensor spectroscopy and imaging. Biophysical Journal 66, 259–267.

[23] Beaulieu, C., 2009. Introduction to diffusion MRI, in: Johansen-Berg, H., Behrens, T.E.J. (Eds.), The Biological Basis of Diffusion Anisotropy. Academic Press.

[24] Behrens, T.E.J., Woolrich, M.W., Jenkinson, M., Johansen-Berg, H., Nunes, R.G., Clare, S., Matthews, P.M., Brady, J.M., Smith, S.M., 2003. Characterization and propagation of uncertainty in diffusion-weighted MR imaging. Magnetic Resonance in Medicine 50, 1077–1088.

[25] Billiet, T., Vandenbulcke, M., Mädler, B., Peeters, R., Dhollander, T., Zhang, H., Deprez, S., den Bergh, B.R.V., Sunaert, S., Emsell, L., 2015. Age-related microstructural differences quantified using myelin water imaging and advanced diffusion MRI. Neurobiology of Aging 36, 2107–2121.

[26] Bingham, C., 1974. An antipodally symmetric distribution on the sphere. Annals of Statistics 6, 1201–1225.

[27] Bland, J., Altman, D., 1986. Statistical methods for assessing agreement between two methods of clinical measurement. Lancet 1, 307–310.

[28] Bloch, F., Hansen, W.W., Packard, M., 1946. Nuclear induction. Physical Review 70(7,8), 460–474.

[29] Bonekamp, D., Nagae, L.M., Degaonkar, M., Matson, M., Abdalla, W.M.A., Barker, P.B., Mori, S., Horská, A., 2007. Diffusion tensor imaging in children and adolescents: Reproducibility, hemispheric, and age-related differences. NeuroImage 34, 733–742.

[30] Brown, R., 1928. A brief account of microscopical observations made in the months of June, July, and August, 1827, on the particles contained in the pollen of plants; and on the general existence of active molecules in organic and inorganic bodies. Philos Mag. 4, 161–173.

[31] Bruijn, L., Miller, T., Cleveland, D., 2004. Unraveling the mechanisms involved in motor neuron degeneration in als. Annual Review Neuroscience 27, 723–749.

[32] Budde, M.D., Annese, J., 2013. Quantification of anisotropy and fiber orientation in human brain histological sections. Frontiers in Integrative Neuroscience 7, 1–8.

[33] Bürgel, U., Amunts, K., Hoemke, L., Mohlberg, H., Gilsbach, J., Zilles, K., 2006. White matter fiber tracts of the human brain: Three-dimensional mapping at microscopic resolution, topography and intersubject variability. Neuroimage 29, 1092–1105.

[34] Buxton, R.B., 2009. Introduction to Functional Magnetic Resonance Imaging, Principles and Techniques. Second ed., Cambridge University Press.

[35] Callaghan, P.T., 2011. Physics of Diffusion. Diffusion MRI: Theory, Methods and Applications. Oxford University Press.

[36] Chang, Y.S., Owen, J.P., Pojman, N.J., Thieu, T., Bukshpun, P., Wakahiro, M.L.J., Berman, J.I., Roberts, T.P.L., Nagarajan, S.S., Sherr, E.H., Mukherjee, P., 2015. White matter changes of neurite density and fiber orientation dispersion during human brain maturation. PLoS ONE 10, e0123656.

[37] Chung, A.W., Seunarine, K.K., Clark, C.A., 2016. NODDI reproducibility and variability with magnetic field strength: A comparison between 1.5 T and 3 T. Human brain mapping 37, 4550–4565.

[38] Clark, C., Hedehus, M., Moseley, M., 2001. Diffusion time dependence of the apparent diffusion tensor in healthy human brain and white matter disease. Magnetic Resonance in Medicine 24, 1126–1129.

[39] Clark, C.A., Hedehus, M., Moseley, M.E., 2002. In vivo mapping of the fast and slow diffusion tensors in human brain. Magnetic Resonance in Medicine 47, 623–628.

[40] Conel, J.L., 1939. The postnatal development of the human cerebral cortex. Harvard University Press, Cambridge, USA.

[41] Cook, P.A., Alexander, D.C., Parker, G.J.M., 2004. Modelling noise-induced fiber-orientation error in diffusion-tensor MRI, in: Proc. ISBI, IEEE, Arlington. pp. 332–336.

[42] Cook, P.A., Bai, Y., Nedjati-Gilani, S., Seunarine, K.K., Hall, M.G., Parker, G.J., Alexander, D.C., 2006. Camino: Open-Source Diffusion-MRI Reconstruction and Processing, in: Scientific Meeting of the International Society for Magnetic Resonance in Medicine, Magenetic Resonance in Medicine, Seattle, WA, USA. p. 2759.

[43] Counsell, S.J., Ball, G., Edwards, A.D., 2014. New imaging approaches to evaluate newborn brain injury and their role in predicting developmental disorders. Current Opinion in Neurology 27, 168–175.

[44] Crank, J., 1975. in: The Mathematics of Diffusion. Oxford University Press.

[45] Daducci, A., Canales-Rodríguez, E.J., Zhang, H., Dyrby, T.B., Alexander, D.C., Thiran, J.P., 2015. Accelerated microstructure imaging via convex optimisation (AMICO) from diffusion MRI data. NeuroImage 105, 32–44.

[46] Danielian, L.E., Iwata, N.K., Thomasson, D.M., Floeter, M.K., 2010. Reliability of fiber tracking measurements in diffusion tensor imaging for longitudinal study. NeuroImage 49, 1572–80.

[47] Davies, D.L., Smith, D.E., 1981. A golgi study of mouse hippocampal CA1 pyramidal neurons following perinatal ethanol exposure. Neuroscience Letters 26, 49–54.

[48] Decanniere, C., Eleff, S., Davis, D., VanZijl, P.C.M., 1995. Correlation of rapid changes in the average water diffusion constant and the concentrations of lactate and atp breakdown products during global ischemia in cat brain. Magn. Reson. Med 34, 343–352.

[49] Delakis, I., 2008-09. Introduction to MRI. Lecture notes, Medical Imaging.

[50] Dell'Acqua, F., Rizzo, G., Scifo, P., Clarke, R.A., Scotti, G., Fazio, F., 2007. Model-based deconvolution approach to solve fiber crossing in diffusion-weighted MR imaging. IEEE Trans. Biomedical Engineering 54, 462–472.

[51] Dohmen, M., Menzel, M., Wiese, H., Reckfort, J., Hanke, F., Pietrzyk, U., Zilles, K., Amunts, K., Axer, M., 2015. Understanding fiber mixture by simulation in 3D polarized light imaging. NeuroImage 111, 464–475.

[52] Drobnjak, I., Zhang, H., Ianuş, A., Kaden, E., Alexander, D.C., 2015. PGSE, OGSE, and sensitivity to axon diameter in diffusion MRI: Insight from a simulation study. Magnetic Resonance in Medicine 75, 688–700.

[53] Dyrby, T.B., Søgaard, L.V., Hall, M.G., Ptito, M., Alexander, D.C., 2013. Contrast and stability of the axon diameter index from microstructure imaging with diffusion MRI. Magnetic Resonance in Medicine 70, 711–721.

[54] Eaton-Rosen, Z., Melbourne, A., Orasanu, E., Cardoso, M.J., Modat, M., Bainbridge, A., Kendall, G.S., Robertson, N.J., Marlow, N., Ourselin, S., 2015. Longitudinal measurement of the developing grey matter in preterm subjects using multi-modal MRI. NeuroImage 111, 580–589.

[55] Edgar, J.M., Griffiths, I.R., 2009. White matter structure: a microscopist's view, in: Johansen-Berg, H., Behrens, T.E.J. (Eds.), Diffusion MRI: from quantitative measurement to in vivo neuroanatomy. Academic Press.

[56] Einstein, A., 1906. On the theory of brownian movement. Annalen der Physik 19, 371–381.

[57] Elster, A.D., 1993. Gradient echo imaging: techniques and acronyms. Radiology 186, 1–8.

[58] Epp, J.R., Niibori, Y., Hsiang, H.L.L., Mercaldo, V., Deisseroth, K., Josselyn, S.A., Frankland, P.W., 2015. Optimization of CLARITY for clearing whole-brain and other intact organs. eNeuro 2, 1–15.

[59] Evanglou, N., Esiri, M., Smith, S., Palace, J., Matthews, P., 2000. Quantitative pathological evidence for axonal loss in normal appearing white matter in multiple sclerosis. Annual Neurology 47, 391–395.

[60] Feinberg, D., Moeller, S., Smith, S., Auerbach, E., Ramanna, S., Gunther, M., Glasser, M., Miller, K., Ugurbil, K., , Yacoub, E., 2010. Multiplexed echo planar imaging for sub-second whole brain fMRI and fast diffusion imaging. PLoS One 5, e15710.

[61] Ferizi, U., 2014. Compartment models and model selection for *in vivo* diffusion MRI of human brain white matter. Ph.D. thesis. University College London.

[62] Ferizi, U., Schneider, T., Panagiotaki, E., Nedjati-Gilani, G., Zhang, H., Wheeler-Kingshott, C.A.M., Alexander, D.C., 2013a. Compartment models of the diffusion mr signal in brain white matter: A taxonomy and comparison. Magnetic Resonance in Medicine 72, 1785–1792.

[63] Ferizi, U., Schneider, T., Tariq, M., Wheeler-Kingshott, C.A.M., Zhang, H., Alexander, D.C., 2013b. The importance of being dispersed: A ranking of diffusion mri models for fibre dispersion using in vivo human brain data, in: Proceedings of the Annual Meeting of the Medical Image Computing and Computer Assisted Intervention (MICCAI), Boston, USA.

[64] Fiala, J., Spacek, J., Harris, K., 2002. Review: Dendritic spine pathology: Cause or consequence of neurological disorders. Brain Research Reviews 39, 29–54.

[65] Fieremans, E., De Deene, Y., Delputte, S., Özdemir, M.S., D'Asseler, Y., Vlassenbroeck, J., Deblaere, K., Achten, E., Lemahieu, I., 2008. Simulation and experimental verification of the diffusion in an anisotropic fiber phantom. Journal of Magnetic Resonance 190, 189–199.

[66] Fieremans, E., Jensen, J.H., Helpern, J.A., 2011. White matter characterization with diffusional kurtosis imaging. NeuroImage 58, 177–188.

[67] Fisher, N.I., Lewis, T., Embleton, B.J.J., 1987. Bingham distribution, in: Statistical Analysis of Spherical Data. Cambridge Univ. Press.

[68] Ghosh, A., Alexander, D.C., Zhang, H., 2015. Crossing versus fanning: Model comparison using hcp data, in: Proceedings CDMRI 2014 - MICCAI 2014 workshop on computational diffusion MRI, Cambridge, MA, USA.

[69] Glasser, M.F., Sotiropoulos, S.N., Wilson, J.A., Coalson, T.S., Fischl, B., Andersson, J.L., Xu, J., Jbabdi, S., Webster, M., Polimeni, J.R., Essen, D.C.V., Jenkinson, M., 2013. The minimal preprocessing pipelines for the human connectome project. NeuroImage 80, 105–124. Mapping the Connectome.

[70] Graham, M.S., Drobnjak, I., Zhang, H., 2016. Realistic simulation of artefacts in diffusion mri for validating post-processing correction techniques. Neuroimage 125, 1079–1094.

[71] Grech-Sollars, M., Hales, P.W., Miyazaki, K., Raschke, F., Rodriguez, D., Wilson, M., Gill, S.K., Banks, T., Saunders, D.E., Clayden, J.D., andThomas R. Barrick, M.N.G., Morgan, P.S., Davies, N.P., Rossiter, J., Auer, D.P., Grundy, R., Leach, M.O., Howe, F.A., Peet, A.C., , Clark, C.A., 2015. Multi-centre reproducibility of diffusion mri parameters for clinical sequences in the brain. NMR in Biomedicine 28, 468–485.

[72] Grussu, F., Schneider, T., Tur, C., Yates, R.L., Tachrount, M., Ianuş, A., Yiannakas, M.C., Newcombe, J., Zhang, H., Alexander, D.C., DeLuca, G.C., Wheeler-Kingshott, C.A.M.G., 2017. Neurite dispersion: a new marker of multiple sclerosis spinal cord pathology? Annals of Clinical and Translational Neurology 4, 1–17.

[73] Gudbjartsson, H., Patz, S., 1995. The Rician distribution of noisy MRI data. Magnetic Resonance in Medicine 34, 910–914.

[74] Guerrero, J.M., Adluru, N., Kecskemeti, S.R., Davidson, R.J., Alexander, A.L., 2016. Investigating the effects of intrinsic diffusivity on neurite orientation dispersion and density imaging (NODDI), in: Proc. ISMRM, ISMRM, Singapore.

[75] Hahn, E.L., 1950. Spin-echoes. Phys Rev 80 (4), 580–594.

[76] Henkelman, R.M., 1985. Measurement of signal intensities in the presence of noise in MR images. Medical Physics 12, 232–233.

[77] Hoy, A.R., Koay, C.G., Kecskemeti, S.R., Alexander, A.L., 2014. Optimization of a free water elimination two-compartment model for diffusion tensor imaging. NeuroImage 103, 323–333.

[78] Huang, H., Jeon, T., Sedmak, G., Pletikos, M., Vasung, L., Xu, X., Yarowsky, P., Richards, L.J., Kostović, I., Sestan, N., Mori, S., 2013. Coupling diffusion imaging with histological and gene expression analysis to examine the dynamics of cortical areas across the fetal period of human brain development. Cerebral Cortex 23, 2620–2631.

[79] Innocenti, G.M., Caminiti, R., Aboitiz, F., 2015. Comments on the paper by horowitz et al. (2014). Brain structure and function 220, 1789–1790.

[80] Jacobs, B., Driscoll, L., Schall, M., 1997. Life-span dendritic and spine changes in areas 10 and 18 of human cortex: A quantitative golgi study. Journal of comparative neurology 386, 661–680.

[81] Jacobs, B., Schall, M., Prather, M., Kapler, E., Driscoll, L., Baca, S., Jacobs, J., Ford, K., Wainwright, M., Treml, M., 2001. Regional dendritic and spine variation in human cerebral cortex: a quantitative golgi study. Cerebral Cortex 11, 558–571.

[82] Jelescu, I.O., Veraart, J., Adisetiyo, V., Milla, S.S., Novikov, D.S., Fieremans, E., 2015. One diffusion acquisition and different white matter models: How does microstructure change in human early development based on WMTI and NODDI? NeuroImage 107, 242–256.

[83] Jenkinson, M., F., B.C., Behrens, T.E., Woolrich, M.W., Smith, S.M., 2012. Fsl. Neuroimage 62, 782–790.

[84] Jensen, J.H., Helpern, J.A., Ramani, A., Lu, H., Kaczinsky, K., 2005. Diffusional kurtosis imaging: The quantification of non-Gaussian water diffusion by means of magnetic resonance imaging. Magnetic Resonance in Medicine 53, 1432–1440.

[85] Jespersen, S., Leigland, L., Cornea, A., Kroenke, C., 2012. Determination of axonal and dendritic orientation distributions within the developing

cerebral cortex by diffusion tensor imaging. IEEE Transactions in Medical Imaging 31, 16–32.

[86] Jespersen, S.N., Bjarkam, C.R., Nyengaard, J.R., Chakravarty, M.M., Hansen, B., Vosegaard, T., Østergaard, L., Yablonskiy, D.A., Chr. Nielsen, N., Vestergaard-Poulsen, P., 2010. Neurite density from magnetic resonance diffusion measure- ments at ultrahigh field: comparison with light microscopy and electron microscopy. NeuroImage 49, 205–216.

[87] Jespersen, S.N., Kroenke, C.D., Østergaard, L., Ackerman, J.J.H., Yablonskiy, D.A., 2007. Modeling dendrite density from magnetic resonance diffusion measurements. NeuroImage 34, 1473–1486.

[88] Jeurissen, B., Leemans, A., Tournier, J.D., Jones, D.K., Sijbers, J., 20010. Estimating the number of fiber orientations in diffusion mri voxels: a constrained spherical deconvolution study., in: Proc. ISMRM, ISMRM, Stockholm, Sweden. p. 573.

[89] Johansen-Berg, H., Behrens, T.E.J., 2009. Diffusion MRI: from quantitative measurement to in vivo neuroanatomy. Academic Press.

[90] Jones, D.K., 2009. Gaussian modeling of the diffusion signal, in: Johansen-Berg, H., Behrens, T.E.J. (Eds.), Diffusion MRI: from quantitative measurement to in vivo neuroanatomy. Academic Press.

[91] Jones, D.K., Basser, P.J., 2004. Squashing peanuts and smashing pumpkins: How noise distorts diffusion-weighted MR data. Magnetic Resonance in Medicine 52, 979–993.

[92] Jovicich, J., Czanner, S., Greve, D., Haley, E., van der Kouwe, A., Gollub, R., Kennedy, D., Schmitt, F., Brown, G., Macfall, J., Fischl, B., Dale, A., 2006. Reliability in multi-site structural mri studies: effects of gradient non-linearity correction on phantom and human data. NeuroImage 30, 436–443.

[93] Kaden, E., Knösche, T.R., Anwander, A., 2007. Parametric spherical deconvolution: Inferring anatomical connectivity using diffusion MR imaging. NeuroImage 37, 474–488.

[94] Kelly, C., Thompson, D., Chen, J., Leemans, A., Adamson, C., Inder, T., Cheong, J., Doyle, L., Anderson, P., 2016. Axon density and axon orientation dispersion in children born preterm. Human Brain Mapping , 3080–3102.

[95] Kleinnijenhuis, M., 2014. Imaging fibres in the brain. Ph.D. thesis. Radboud University.

[96] Kleinnijenhuis, M., Zhang, H., Wiedermann, D., Küsters, B., Norris, B.G., van Cappellen van Walsum, A.M., 2013. Detailed laminar characteristics of the human neocortex revealed by noddi and histology, in: Proc. 19th Annual Meeting of the OHBM, OHBM, WA, USA. p. 3815.

[97] Kochunov, P., Thompson, P., Lancaster, J., Bartzokis, G., Smith, S., Coyle, T., Royall, D., Laird, A., Fox, P., 2007. Relationship between white matter fractional anisotropy and other indices of cerebral health in normal aging: Tract-based spatial statistics study of aging. NeuroImage 35, 478–487.

[98] Kodiweeraa, C., Wu, Y.C., 2016. Data of NODDI diffusion metrics in the brain and computer simulation of hybrid diffusion imaging (HYDI) acquisition scheme. Journal data in brief 7, 1131–1138.

[99] Koev, P., Edelman, A., 2006. The efficient evaluation of the hypergeometric function of a matrix argument. Mathematics of computation 75, 833–846.

[100] Kostović, I., Jovanov-Milošević, N., Radoš, M., Sedmak, G., Benjak, V., Kostović-Srzentić, M., Vasung, L., Culjat, M., Radoš, M., Hüppi, P., Judaš, M., 2014. Perinatal and early postnatal reorganization of the subplate and related cellular compartments in the human cerebral wall as revealed by histological and MRI approaches. Brain Structure and Function 219, 231–253.

[101] Kostović, I., Vasung, L., 2009. Insights from in vivo fetal magnetic resonance imaging of cerebral development. Seminars in perinatology 33, 220–232.

[102] Kunz, N., Zhang, H., Vasung, L., R., O.K., Assaf, Y., Lazeyras, F., Alexander, D.C., Hüppi, P.S., 2014. Assessing white matter microstructure of the

newborn with multi-shell diffusion MRI and biophysical compartment models. NeuroImage 96, 288–299.

[103] Lampinena, B., Szczepankiewicza, F., Martenssonb, J., van Westenc, D., Sundgrenc, P.C., Nilsson, M., 2017. Neurite density imaging versus imaging of microscopic anisotropy in diffusion MRI: A model comparison using spherical tensor encoding. NeuroImage 147, 517–531.

[104] Landman, B.A., Huang, A.J., Gifford, A., Vikram, D.S., Lim, I.A.L., Farrell, J.A.D., Bogovic, J.A., Hua, J., Chen, M., Jarso, S., Smith, S.A., Joel, S., Mori, S., Pekar, J.J., Barker, P, B., Prince, J.L., van Zijl, P.C.M., 2011. Multiparametric neuroimaging reproducibility: A 3-t resource study. NeuroImage 54, 2854–2866.

[105] Lazar, M., Lee, J.H., Alexander, A.L., 2005. Axial asymmetry of water diffusion in brain white matter. Magnetic Resonance in Medicine 54, 860–867.

[106] Le Bihan, D., 2010. Magnetic resonance diffusion imaging: Introduction and concepts, in: Jones, D.K. (Ed.), Diffusion MRI: Theory, Methods, and Applications. Oxford University Press.

[107] Le Bihan, D., 2014. Diffusion MRI: what water tells us about the brain. EMBO Molecular Medicine 6 (5), 569–573.

[108] Le Bihan, D., Breton, E., Lallemand, D., Grenier, P., Cabanis, E., Laval-Jeantet, M., 1986. MR imaging of intravoxel incoherent motions: application to diffusion and perfusion in neurologic disorders. Radiology 161, 401–407.

[109] Le Bihan, D., Mangin, J.F., Poupon, C., Clark, C., Pappata, S., Molko, N., Chabriat, H., 2001. Diffusion tensor imaging: Concepts and applications. Journal of Magnetic Resonance Imaging 13, 534–546.

[110] Leisman, G., Machado, C., Melillo, R., Mualem, R., 2012. Intentionality and "free-will" from a neurodevelopmental perspective. Frontiers in Integrative Neuroscience 6, 1–12.

[111] Lemkaddem, A., Daducci, A., Kunz, N., Lazeyras, F., Seeck, M., Thiran, J.P., Vulliémoz, S., 2014. Connectivity and tissue microstructural

alterations in right and left temporal lobe epilepsy revealed by diffusion spectrum imaging. NeuroImage: Clinical 5, 349–358.

[112] Liewald, D., Miller, R., Logothetis, N., Wagner, H.J., Schüz, A., 2014. Distribution of axon diameters in cortical white matter: an electron-microscopic study on three human brains and a macaque. Biological Cybernetics 108, 541–557.

[113] Mardia, K., Jupp, P., 1990. Directional statistics. John Wiley & Sons, Ltd.

[114] Modat, M., Daga, P., Clarkson, M.J., Ourselin, S., 2010. NiftyReg: (version 1.3). [software]. http://sourceforge.net/projects/niftyreg/.

[115] Mori, S., Oishi, K., Jiang, H., Jiang, L., Li, X., Akhter, K., Hua, K., andAsif Mahmood, A.V.F., Woods, R., Toga, A., Pike, B., Rosa-Neto, P., Evans, A., Zhang, J., Huang, H., Miller, M.I., van Zijl, P., Mazziotta, J., 2008. Stereotaxic white matter atlas based on diffusion tensor imaging in an ICBM template. NeuroImage 40, 570–582.

[116] Moseley, M.E., Cohen, Y., Mintorovitch, J., 1990. Early detection of regional cerebral ischemic injury in cats: evaluation of diffusion and T2-weighted MRI and spectroscopy. Magnetic Resonance in Medicine 14, 330–346.

[117] Moseley, M.E., Kucharcz, J., Asgari, H.S., Norman, D., 1991. Anisotropy in diffusion-weighted MRI, in: ISMRM Workshop on Future Directions in MRI of Diffusion and Microcirculation, Magnetic Resonance in Medicine, Bethesda. pp. 321–326.

[118] Müller, R., Büttner, P., 1994. A critical discussion of intraclass correlation coefficients. Statistics in medicine 13, 2465–2476.

[119] Naidich, T.P., Krayenbühl, N., Kollias, S., Bou-Haidar, P., Bluestone, A.Y., Carpenter, D.M., 2016. White matter. URL: https://radiologykey.com/white-matter/.

[120] Nazeri, A., Chakravarty, M.M., Rotenberg, D.J., Rajji, T.K., Rathi, Y., Michailovich, O.V., Voineskos, A.N., 2015. Functional Consequences of Neurite Orientation Dispersion and Density in Humans across the Adult Lifespan. The Journal of Neuroscience 35, 1753–1762.

[121] Neuman, C.H., 1974. Spin echo of spins diffusing in a bounded medium. Journal of Chemical Physics 60, 4508–4511.

[122] Nicholson, C., 2001. Diffusion and related transport mechanisms in brain tissue. Reports on progress in physics 64, 815–884.

[123] Oishi, K., Zilles, K., Amunts, K., Faria, A., Jiang, H., Li, X., Akhter, K., Hua, K., Woods, R., Toga, A.W., Pike, B., Rosa-Neto, P., Evans, A., Zhang, J., Huang, H., Miller, M.I., van Zijl, P.C., Mazziotta, J., Mori, S., 2008. Human brain white matter atlas: identification and assignment of common anatomical structures in superficial white matter. NeuroImage 43, 447–457.

[124] O'Shea, M., 2005. The Brain: A Very Short Introduction (Very Short Introductions). Oxford University Press.

[125] Owen, J.P., Chang, Y.S., Pojman, N.J., Bukshpun, P., Wakahiro, M.L., Marco, E.J., Berman, J.I., Spiro, J.E., Chung, W.K., Buckner, R.L., Roberts, T.P., Nagarajan, S.S., Sherr, E.H., Mukherjee, P., 2014. Aberrant white matter microstructure in children with 16p11.2 deletions. The Journal of Neuroscience 34, 6214–6223.

[126] Panagiotaki, E., Schneider, T., Siow, B., Hall, M.G., Lythgoe, M.F., Alexander, D.C., 2012. Compartment models of the diffusion mr signal in brain white matter: A taxonomy and comparison. Neuroimage 59, 2241–2254.

[127] Paula-Barbosa, M., Mota Cardoso, R., Guimaraes, M., Cruz, C., 1980. Dendritic degeneration and regrowth in the cerebral cortex of patients with alzheimer's disease. J. Neurol. Sci 45, 129–134.

[128] Pierpaoli, C., Basser, P.J., 1996. Toward a quantitative assessment of diffusion anisotropy. Magnetic Resonance in Medicine 36, 893–906.

[129] Pierpaoli, C., Jezzard, P., Basser, P.J., Barnett, A., Di Chiro, G., 1996. Diffusion tensor MR imaging of the human brain. Radiology 201, 637–648.

[130] Pipe, J., 2009. Pulse sequences for diffusion-weighted mri., in: Johansen-Berg, H., Behrens, T.E.J. (Eds.), Diffusion MRI: from quantitative measurement to in vivo neuroanatomy. Academic Press.

[131] Price, W.S., 1997. Pulsed-field gradient nuclear magnetic resonance as a tool for studying translational diffusion: Part 1. basic theory. Concepts in Magnetic Resonance 9, 299–336.

[132] Provenzale, J.M., Isaacson, J., Chen, S., Stinnett, S., Liu, C., 2010. Correlation of apparent diffusion coefficient and fractional anisotropy values in the developing infant brain. AJ. Am. J. Roentgenol. 195, W456–W462.

[133] Purcell, E.M., Torrey, H.C., Pound, R.V., 1946. Resonance absorption by nuclear magnetic moments in a solid. Physical Review 69, 26—44.

[134] Richardson, S., Siow, B., Panagiotaki, E., Schneider, T., Lythgoe, M.F., Alexander, D.C., 2014. Viable and fixed white matter: Diffusion magnetic resonance comparisons and contrasts at physiologicaltemperature. Magnetic Resonance in Medicine 72, 1151–1161.

[135] Riffert, T.W., Schreiber, J., Anwander, A., Knösche, T.R., 2014. Beyond fractional anisotropy: Extraction of bundle-specific structural metrics from crossing fiber models. NeuroImage 100, 176–191.

[136] Roberts, R.E., Anderson, E.J., Husain, M., 2013. White matter microstructure and cognitive function. The Neuroscientist 19, 8–15.

[137] Rowe, M., 2014. New tractography methods based on parametric models of white matter fibre dispersion. Ph.D. thesis. University College London.

[138] Rowe, M.C., Zhang, H., Oxtoby, N., Alexander, D.C., 2013. Beyond crossing fibers: Tractography exploiting sub-voxel fibre dispersion and neighbourhood structure. Information Processing in Medical Imaging, Lecture Notes in Computer Science 7917, 402–413.

[139] Saksena, S., Rathore, R.K., Gupta, R.K., 2008. Clinical applications of diffusion tensor imaging. Magnetic Resonance Insights 2, 7–24.

[140] Schwarz, G., 1978. Estimating the dimension of a model. The Annals of Statistics 6, 461–464.

[141] Seunarine, K.K., Alexander, D.C., 2009. Multiple fibres: Beyond the diffusion tensor, in: Johansen-Berg, H., Behrens, T.E.J. (Eds.), Diffusion MRI:

from quantitative measurement to in vivo neuroanatomy. Academic Press, pp. 56–74.

[142] Shmueli, K., 2011-12. Magnetic resonance imaging. Lecture notes, MPHYGB10.

[143] Shoemake, K., 1992. Graphics gems iii, Academic Press Professional, Inc., San Diego, CA, USA. chapter Uniform Random Rotations, pp. 124–132.

[144] Shrout, P.E., Fleiss, J.L., 1979a. Intraclass correlations: uses in assessing rater reliability. Psychological bulletin 86, 420–428.

[145] Shrout, P.E., Fleiss, J.L., 1979b. Intraclass correlations: Uses in assessing rater reliability. Psychological Bulletin 86 (2), 420–428.

[146] Sorensen, A., Buonanno, F., G., G.R., Schwamm, L.H., Lev, M.H., Huang-Hellinger, F.R., Reese, T.G., Weisskoff, R.M., Davis, T.L., Suwanwela, N., Can, U., Moreira, J.A., Copen, W.A., Look, R.B., Finklestein, S.P., Rosen, B.R., Koroshetz, W.J., 1996. Hyperacute stroke: evaluation with combined multisection diffusion-weighted and hemodynamically weighted echo-planar MR imaging. Radiology 199, 391–401.

[147] Sotiropoulos, S.N., Behrens, T.E.J., Jbabdi, S., 2012. Ball and rackets: Inferring fiber fanning from diffusion-weighted MRI. NeuroImage 60, 1412–1425.

[148] Sotiropoulos, S.N., Jbabdi, S., Xu, J., Andersson, J.L., Moeller, S., Auerbach, E.J., Glasser, M.F., Hernandez, M., Sapiro, G., Jenkinson, M., Feinberg, D.A., Yacoub, E., Lenglet, C., Essen, D.C.V., Ugurbil, K., T. E. J, B., 2013. Advances in diffusion MRI acquisition and processing in the human connectome project. NeuroImage 80, 125–143.

[149] Stanisz, G.J., Szafer, A., Wright, G.A., Henkelman, M., 1997. An analytical model of restricted diffusion in bovine optic nerve. Magnetic Resonance in Medicine 37, 103–111.

[150] Stejskal, E.O., 1965. Use of spin echoes in a pulsed magnetic-field gradient to study anisotropic, restricted diffusion and flow. J Chem Phys 43 (10), 3597–3603.

[151] Stepisnik, J., 1999. Validity limits of gaussian approximation in cumulant expansion for diffusion attenuation of spin echo. Physica B 270, 110–117.

[152] Stiles, J., Jernigan, T.L., 2010. The basics of brain development. Neuropsychology Review 20, 327–348.

[153] Stuart, G.J., Spruston, N., 2015. Dendritic integration: 60 years of progress. Nature Neuroscience 18 (12), 1713–1721.

[154] Szafer, A., Zhong, J., Gore, J.C., 1995. Theoretical model for water diffusion in tissues. Magnetic Resonance in Medicine 33, 697–712.

[155] Tariq, M., Kleinnijenhuis, M., van Cappellen van Walsum, A.M., Zhang, H., 2015a. Validation of NODDI estimation of dispersion anisotropy in V1 of the human neocortex, in: Proc. 23rd Annual Meeting of the ISMRM, Berkeley, USA: ISMRM, Toronto, Canada.

[156] Tariq, M., Kleinnijenhuis, M., van Cappellen van Walsum, A.M., Zhang, H., 2015b. Validation of NODDI estimation of dispersion anisotropy in V1 of the human neocortex, in: Proceedings of 21st Annual Meeting of the Organization for Human Brain Mapping (OHBM), Honolulu, Hawaii.

[157] Tariq, M., Schneider, T., Alexander, D., Wheeler-Kingshott, C., Zhang, H., 2013. Assessing scan-rescan reproducibility of the parameter estimates from NODDI, in: Proc. 21st Scientific Meeting of the ISMRM, Utah, USA: ISMRM, Salt Lake City.

[158] Tariq, M., Schneider, T., Alexander, D.C., Wheeler-Kingshott, C.A.G., Zhang, H., 2016a. *Bingham-NODDI:* mapping anisotropic orientation dispersion of neurites using diffusion MRI. NeuroImage 133, 207–223.

[159] Tariq, M., Schneider, T., Alexander, D.C., Wheeler-Kingshott, C.A.M., Zhang, H., 2012. Scan-rescan reproducibility of neurite microstructure estimates using NODDI, in: Proceedings of Medical Image Understanding and Analysis, MIUA, Swansea. pp. 255–261.

[160] Tariq, M., Schneider, T., Alexander, D.C., Wheeler-Kingshott, C.A.M., Zhang, H., 2014a. *In vivo* estimation of dispersion anisotropy of neurites

using diffusion MRI, in: Proceedings of the Annual Meeting of the Medical Image Computing and Computer Assisted Intervention (MICCAI), Boston, USA. pp. 241–248.

[161] Tariq, M., Schneider, T., Alexander, D.C., Wheeler-Kingshott, C.A.M., Zhang, H., 2014b. NODDI with dispersion anisotropy, in: Proceedings of 22nd Annual Meeting of the International Society for Magnetic Resonance in Medicine (ISMRM), Milan, Italy.

[162] Tariq, M., Schneider, T., Alexander, D.C., Wheeler-Kingshott, C.A.M., Zhang, H., 2014c. NODDI with dispersion anisotropy, in: Proceedings of 20th Annual Meeting of the Organization for Human Brain Mapping (OHBM), Hamburg, Germany.

[163] Tariq, M., Zhang, J., Zhang, H., 2016b. Neurite morphology reveals rich regional microstructural variations in the human brain white matter, in: Proceedings of 22nd Annual Meeting of the Organization for Human Brain Mapping (OHBM), Geneva, Switzerland.

[164] Timmers, I., Zhang, H., Bastiani, M., Jansma, B.M., Roebroeck, A., Rubio-Gozalbo, M.E., 2014. White matter microstructure pathology in classic galactosemia revealed by neurite orientation dispersion and density imaging. Journal of Inherited Metabolic Disease , 1–10.

[165] Torrey, H.C., 1956. Bloch equations with diffusion terms. Physical Review 104, 563–565.

[166] Tournier, J.D., Calamante, F., Connelly, A., 2007. Robust determination of the fibre orientation distribution in diffusion MRI: Non-negativity constrained super-resolved spherical deconvolution. NeuroImage 35, 1459–1472.

[167] Tournier, J.D., Calamante, F., Gadian, D.G., Connelly, A., 2004. Direct estimation of the fiber orientation density function from diffusion-weighted MRI data using spherical deconvolution. NeuroImage 23, 1176–1185.

[168] Tuch, D.S., Reese, T.G., Wiegell, M.R., Makris, N., Belliveau, J.W., Wedeen, V.J., 2002. High angular resolution diffusion imaging reveals intravoxel white matter fiber heterogeneity. Magnetic Resonance in Medicine 48, 577–582.

[169] Türe, U., Yaşargil, M.G., Friedman, A.H., Al-Mefty, O., 2000. Fiber dissection technique: Lateral aspect of the brain. Neurosurgery 47, 417–426.

[170] Van Essen, D.C., Ugurbil, K., Auerbach, E., Barch, D., Behrens, T.E.J., Bucholz, R., Chang, A., Chen, L., Corbetta, M., Curtiss, S.W., Della Penna, S., Feinberg, D., Glasser, M.F., Harel, N., Heath, A.C., Larson-Prior, L., Marcus, D., Michalareas, G., Moeller, S., Oostenveld, R., Petersen, S.E., Prior, F., Schlaggar, B.L., Smith, S.M., Snyder, A.Z., Xu, J., Yacoub, E., WU-Minn HCP Consortium, 2012. The human connectome project: a data acquisition perspective. NeuroImage 62 (4), 2222–2231.

[171] Vasung, L., Fischi-Gomez, E., Hüppi, P.S., 2013. Multimodality evaluation of the pediatric brain: DTI and its competitors. Pediatric Radiology 43, 60–68.

[172] Vasung, L., Huang, H., Jovanov-Milošević, N., Pletikos, M., Mori, S., Kostović, I., 2010. Development of axonal pathways in the human fetal fronto-limbic brain: histochemical characterization and diffusion tensor imaging. Journal of anatomy 217, 400–417.

[173] Wang, Y., Gupta, A., Liu, Z., Zhang, H., Escolar, M.L., Gilmore, J.H., Gouttard, S., Fillard, P., Maltbie, E., Gerig, G., Styner, M., 2011. DTI registration in atlas based fiber analysis of infantile krabbe disease. NeuroImage 55, 1577–1586.

[174] Warach, S., Chien, D., Li, W., Ronthal, M., Edelman, R.R., 1992. Fast magnetic resonance diffusion-weighted imaging of acute human stroke. Neurology 42, 1717–1723.

[175] Wedeen, V.J., Hagmann, P., Tseng, W.Y.I., Reese, T.G., Weisskoff, R.M., 2004. Q-ball imaging. Magnetic Resonance in Medicine 52, 1358–372.

[176] Wedeen, V.J., Hagmann, P., Tseng, W.Y.I., Reese, T.G., Weisskoff, R.M., 2005. Mapping complex tissue architecture with diffusion spectrum magnetic resonance imaging. Magnetic Resonance in Medicine 54, 1377–1386.

[177] Weisstein, E.W., 2012. *Correlation Coefficient*, from MathWorld. URL: http://www.investopedia.com/terms/c/coefficientofvariation.asp.

[178] Werring, D.J., Clark, C.A., Barker, G.J., Thompson, A.J., Miller, D.H., 1999. Diffusion tensor imaging of lesions and normal-appearing white matter in multiple sclerosis. Neurology 52 (8), 1626–1632.

[179] Westin, C.F., Maier, S.E., Mamata, H., Nabavi, A., Jolesz, F.A., Kikinis, R., 2002. Processing and visualization for diffusion tensor MRI. Medical Image Analysis 6, 93–108.

[180] Winston, G.P., Micallef, C., Symms, M.R., Alexander, D.C., Duncan, J.S., Zhang, H., 2014. Advanced diffusion imaging sequences could aid assessing patients with focal cortical dysplasia and epilepsy. Epilepsy Research 108, 336–339.

[181] Yamasaki, F., Kurisu, K., Satoh, K., K., A., Sugiyama, K., Ohtaki, M., Takaba, J., Tominaga, A., Hanaya, R., Yoshioka, H., Hama, S., Ito, Y., Kajiwara, Y., Yahara, K., Saito, T., Thohar, M., 2005. Apparent diffusion coefficient of human brain tumors at MR imaging. Radiology 91, 235–985.

[182] Yushkevich, P.A., Piven, J., Hazlett, H.C., Smith, R.G., Ho, S., Gee, J.C., Gerig, G., 2006. User-guided 3D active contour segmentation of anatomical structures: Significantly improved efficiency and reliability. NeuroImage 31, 1116–1128.

[183] Zhang, H., Alexander, D.C., 2010. Axon diameter mapping in the presence of orientation dispersion with diffusion MRI, in: Proc. MICCAI, Springer, Beijing. pp. 640–647.

[184] Zhang, H., Hubbard, P., Parker, G., Alexander, D.C., 2011. Axon diameter mapping in the presence of orientation dispersion with diffusion MRI. NeuroImage 56, 1301–1315.

[185] Zhang, H., Schneider, T., Wheeler-Kingshott, C., Alexander, D., 2012. NODDI: Practical *in vivo* neurite orientation dispersion and density imaging of the human brain. NeuroImage 61, 1000–1016.

[186] Zhang, H., Yushkevich, P.A., Alexander, D.C., Gee, J.C., 2006. Deformable registration of diffusion tensor MR images with explicit orientation optimization. Medical Image Analysis 10, 764–785.